SAPIENZA UNIVERSITÀ DI ROMA

Department of Structural and Geotechnical Engineering

PhD Thesis in Geotechnical Engineering

XXXIII Cycle

Stress-deformation analysis of a zoned earth dam with elasto-plastic hardening soil models

Candidate	**Supervisor**
Laura Loprevite	Prof. Giuseppe Lanzo
	Co-supervisor
	Prof. Stavroula Kontoe

ABSTRACT

Zoned earth dams are challenging geotechnical structures for engineers due to the many uncertainties revolving around the behaviour of core and rockfill materials. This research focuses on validation of stress-deformation numerical analyses for better prediction of dam response during construction and first filling. The case study is Montedoglio dam, a 64 m high zoned earth-core dam located on the Tiber River at about 24 km from Arezzo (Central Italy). The construction of embankment dam started in 1977 and finished in 1986 and the reservoir was impounded in 1990. Numerical simulations are conducted using both the finite difference code FLAC 7.0 and the finite element code ICFEP which implement elasto-plastic hardening models. Specifically, two constitutive models were employed for the simulation of the construction and reservoir impounding phases: the Cysoil model (Cap-Yield) implemented in FLAC 7.0 and the Lade's Double-hardening model implemented in ICFEP. Model parameters for the core and the shoulders were calibrated using laboratory data. The numerical analyses of the construction phase of the dam were carried out with both codes and well captured the monitoring data recorded. The simulation of the reservoir impounding was conducted only using ICFEP with the Double-hardening model and reproduced with reasonable accuracy piezometers measurements and, consequently, stresses and deformations within the dam. The code ICFEP was used during a stage at Imperial College (London) under the supervision of the Professor Stavroula Kontoe.

ACKNOWLEDGMENTS

The research work exposed in this thesis was done under the supervision of Prof. Giuseppe Lanzo and Prof. Stavroula Kontoe, whose support is extremely appreciated.

I would like to thank the Soil Mechanics Section of the Civil Engineering Department of Imperial College, London, for a great hospitality and collaboration and the staff of the Structural and Geotechnical Engineering Department of La Sapienza, University of Rome, who shared their knowledge and experiences.

For the permission to publish the data of Montedoglio dam, Eng. Stefano Cola of EAUT (Ente Acque Umbre-Toscane) is gratefully acknowledged.

Index

Figure index

Table index

1. INTRODUCTION

1.1 Motivations of the study

Embankments dams are the most widely used dam type worldwide. In 2015 more than 70% of dams worldwide were earth and rockfill dams, according to the International Commission on Large Dams (ICOLD). In 2017 in Italy out of 538 dams, 164 were embankments dams, of which about 75% were zoned earth-rockfill and rockfill dams with upstream facing.

A key problem in the design, construction and operational lifetime of these large geotechnical structures is related to the deformation process. Many issues have been considerably investigated over the past fifty years, such as stability of dam body, deformations during construction and reservoir impounding, potential mechanisms of failure as well as seismic vulnerability. A crucial feature of these structures is that failure, expressed as a collapse or excessive movements, can lead to an uncontrolled release of the retained water with serious damages, especially in terms of human lives. A good understanding of the causes and mechanisms of the deformation process is therefore required and should be estimated realistically for an overall dam safety.

Since nineties, the use of the numerical analysis to study the deformation problems of embankment dams during construction and impoundment phases has increased substantially and nowadays this problem is extensively studied. Many authors have simulated the construction and reservoir filling stages and have investigated significant aspects of the numerical simulation, such as construction and excavation by layers or the appropriate choice of the constitutive model. The limitation of elastic constitutive models to simulate the deformation of rockfill dam during construction and first filling was highlighted. The application of advanced constitutive models such as elasto-plastic hardening models to account for pre-peak plasticity of rockfill behaviour, the effect of grain crushing and rearrangement, and the stiffness decrease connected with permanent deformations, was demonstrated. Further, a thorough simulation of the static stress and strain states of an embankment dam during construction and reservoir filling is a prerequisite for a reliable dynamic analysis.

Nowadays, the performance of embankment dams during construction, impoundment and service life can be evaluated reasonably well under static conditions by means of numerical methods. This happens when the results of the numerical simulations are comparable to the observed data from field measurements (topographic, piezometric, etc.). In this respect monitoring data are essential for the validation of the geotechnical model of the dam-foundation system. Nevertheless, the response of a dam is a rather complicated issue even under static conditions and the numerical results do not always match the observed behaviour. Therefore, well-documented case histories based on *ad-hoc* geotechnical data, especially on rockfill material which are generally lacking for the inherent difficulty in sampling, are still needed. Further, advanced numerical simulations need to be employed in order to better capture the actual behaviour of embankment dams. These advanced constitutive models do exist nowadays but they need to be validated against real well-documented case histories in order to obtain reliable results useful for the analysis of other existing dams and for gaining experience on future designs.

1.2 Goals

The main purpose of this study is to examine the deformation behaviour of an embankment dam through the numerical simulation of the construction and first filling using advanced constitutive models. To this aim, two elasto-plastic hardening models were selected for the numerical analyses. The Cysoil (or Cap-yield) model is a strain-hardening constitutive model implemented in FLAC 7.0, characterized by an elastic domain closed by a frictional and cohesive Mohr-Coulomb shear envelope and an elliptic volumetric cap. The Double Hardening model is a strain-hardening/softening model implemented in ICFEP (Imperial College Finite Element Programme), which is characterized, as well, by an elastic domain closed by two intersecting yield surfaces, the conical and the cap yield surfaces. The hardening rules of the models allow to account for the plasticity effect of grain crushing and rearrangement, permitting plastic deformations in response to an isotropic stress increase, and to capture the decrease in stiffness accompanied by irreversible deformation when the soil is subjected to deviatoric loading.

The Montedoglio zoned earth dam was selected as a case study. This is a 64 m high dam located in the Tuscany region (Central Italy). The vertical core is realized by compacted clayey silt while the upstream and downstream shoulders are characterized by alluvial material from the river bed. The shoulders are based on a 6 m layer of compacted alluvial soil, while the core is directly founded on a formation of ophiolitic rocks. High-quality geotechnical data are available for the core and the shells as well. The models parameters were derived from the results of standard laboratory tests on undisturbed samples retrieved in the core. Reconstituted shells samples were subjected to non-standard triaxial tests of large dimensions. Moreover, high-quality monitoring data are also available during the construction and impoundment phases. The Montedoglio dam, therefore, represents an excellent opportunity to validate the advanced numerical models previously described.

Plane-strain numerical analyses of the main cross-section of Montedoglio dam were carried out during the construction and first filling phases using both codes FLAC and ICFEP, and the corresponding advanced models Cysoil and Double Hardening Soil model. The calculated responses were compared to the recorded behaviour and in both cases a satisfactory agreement was found. Therefore, the capability of both advanced constitutive models to reproduce the observed deformation pattern was established. The comparison of calculated results in terms of vertical and horizontal stresses within the dam body were also carried out. Further, the superiority of these models in comparison to the more simple models (such as the elasto-plastic one) was also established. The differences between the results of the two advanced constitutive models were further commented and the possible reasons were put forward.

1.3 Thesis outline

The thesis is organised in Chapters as follows.

Chapter 2 reviews the literature studies on the possible mechanism of failure of earth dams and their deformation behaviour during construction and reservoir impounding. Particular attention is devoted to the constitutive models for dam materials, highlighting the benefits and limitation of simple models as well as the capabilities of the advanced ones in simulating the stress-deformation behaviour of embankment dams.

Chapter 3 describes the main features of the code Flac, which is a two-dimensional explicit finite difference program. The illustration of the strain-hardening constitutive model Cysoil implemented in FLAC 7.0 is also provided.

Chapter 4 deals with the main features of the code ICFEP. Specifically, the general principles of the finite element method (FEM) are outlined, and the Lade's elasto-plastic double hardening model implemented in ICFEP is illustrated in detail.

Chapter 5 describes the case-history considered, that is the Montedoglio earth zoned dam. The geotechnical characterization of dam's materials and its subsoil is described based on the results of extensive in-situ and laboratory tests. The monitoring data available during the construction and filling operations is also presented.

Chapter 6 and Chapter 7 describe the stress-deformation analysis of the Montedoglio dam carried out with FLAC and ICFEP, respectively. Calibration of the geotechnical model in both codes is presented. For FLAC, the determination of Cysoil model parameters is first described and then the results of the stress-deformation numerical analysis of the construction phase of the dam, are illustrated. Analogously, for ICFEP the calibration of the Lade's double hardening model is described first, followed by the examination of the numerical results of the dam construction and reservoir impounding of the dam.

Chapter 8 compare the numerical results obtained with the two models, figuring out the main differences and similarities.

The thesis leads to Chapter 9, in which the main conclusions of the research study are summarized.

2. LITERATURE REVIEW

2.1 INTRODUCTION

In this chapter the performance of embankment dams during construction and impoundment is reviewed. Information derived from literature are illustrated in the following five sections.

The classification of embankment dams is first presented as a function of the construction method and materials, height, type of structure and position of the waterproof element, with emphasis given to the behaviour of zoned dams. This is followed by a brief overview of the different mechanisms leading to the static of collapse of embankments dams, such as erosion by overtopping, rotational slips and internal erosion, which are important to understand and to avoid uncontrolled release of storage water. Subsequently, the deformation behaviour of zoned and rockfill dams is thoroughly discussed. Stress and deformation patterns within the dam area analysed during the construction phase and first impoundment. The interpretation of field measurements during the lifetime of dam is fundamental to keep some important variables under control and to understand the possible deformation mechanism within the dam. For this reason, some methods of interpretation of measurements are explained and commented. Simple procedures to estimate deformations and displacements are presented, which can be useful to get a feeling of the dam behaviour and to compare them with numerical analysis results. Finally, the numerical modelling of dam construction and reservoir filling is reviewed, which is essential if a good reproduction of the stress and strain states would be achieved. To this aim, particularly important is the choice of the constitutive model, because some models of the class of hardening plasticity are capable to capture aspects of the soil behaviour which can definitively improve the simulation results (e.g., plasticity effect of grain crushing and rearrangement, plastic deformations in response to an isotropic stress increase, decrease in stiffness accompanied by irreversible deformation when the soil is subjected to deviatoric loading, etc.). A brief overview of the most common constitutive models used in practice for embankment dams numerical analysis and a series of numerical analysis and their results of the phases of construction and reservoir impounding with advanced constitutive models are therefore illustrated in some detail.

2.2 EMBANKMENT DAM CLASSIFICATION

There are several types of embankment dams and many classifications exist which depend on several aspects such as: (i) the construction material, (ii) the kind of structure and (iii) the position of the waterproof element (Tanchev, 2014). According to the construction material, embankment dams can be divided in: (i) earth dams, essentially formed (by more than 50%) of fine-grained materials (clay, sand or sandy gravels), (ii) earth–rockfill dams, whose main body is made of coarse-grained gravel or rock materials with a core made of fine-grained material, and (iii) rockfill dams, constructed from coarse-grained soil while waterproofing is provided by a facing of some artificial material. The earth and rockfill dams are homogeneous, while the earth–core rockfill dams are defined as zoned, because of the presence of two different materials. The homogeneous rockfill dams are also defined by the type of facing, which generally are concrete or bituminous. The rockfill material of homogeneous or zoned dams can be placed compacting about 2 m thick material layers by vibrating rollers or without compaction; in this latter case it is called dumped rockfill. The zoned dams are characterized by a central earth or bituminous core with function of retaining water and a lateral rockfill shoulders with the function of stability, filter layers are added between these two materials to prevent internal erosion. In Figure 2.1 a schematic representation of earthfill dams (E), earth-core rockfill dams (ECRD) and rockfill dams with concrete facing (CFRD) or bituminous facing (BFRD), is provided.

The International Commission on Large Dams (ICOLD) divides dams according to their size, in large or small. Large dams include structures higher than 15 metres or having a height between 10 and 15 metres, provided they fulfil at least one of the following conditions: the length of dam’s crest should not be smaller than 500 m; the volume of the impounding reservoir, formed by the dam should not be smaller than 1 million m^3; the maximum quantity of flood water which could be evacuated from the reservoir should not be smaller than 2000 m^3/s; the conditions for founding the dam are particularly difficult; and the dam has an unusual construction (Tanchev, 2014).

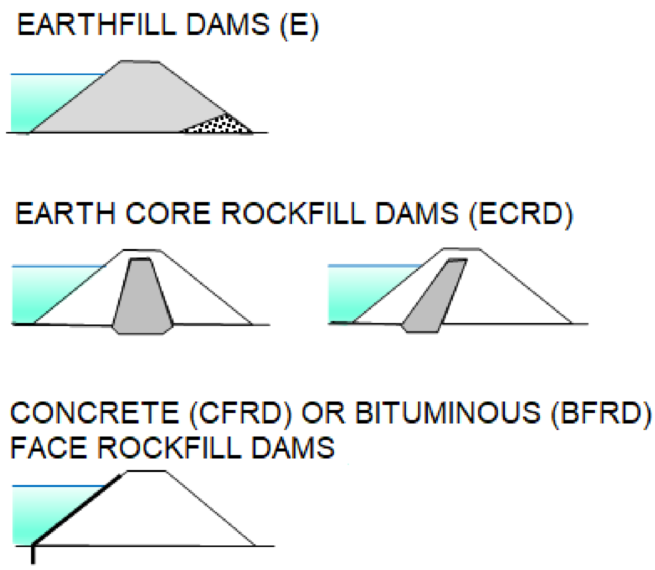

Figure 2.1 Main types of embankment dams.

2.3 MECHANISMS OF FAILURE

Embankment dams are large significant structures, whose failure due to the presence of a large volume of retained water can lead to an uncontrolled release of water and, consequently, can bring to major disasters and loss of human life. The comprehension of dam failure is a significant issue in the processing of assessment of new or existing dams. The failure can be described as a collapse or excess movement of a part or a full embankment dam. Penman (1986) has defined the possible static causes of failure of embankment dams: rotational slips, erosion by overtopping and internal erosion.

The rotational slips are caused by upstream or downstream slope instability, which are often related to the construction phase of the embankment dams, therefore, the water is not yet in the reservoir and the failure risk is less dangerous (Penman, 1986). Foster (1998) reported 124 incidents of slope instability in embankment dam, 12 of which took place with an uncontrolled release of water from reservoir. He defined some factors influencing the phenomenon of slope instability of embankment dams: the type of dam, the homogeneous earthfill dam is more susceptible to instability; the soil foundation, rock foundation soil is usually better to prevent the phenomenon; the kind of embankment soil, sand and gravels are preferable to high plasticity clay and silt; the placement, compacted material are more suitable. For assessment of the stability of rockfill dams, deformations are of crucial importance. In particular, those occurring in the thin water-impermeable element, and through it, indirectly, of the entire structure (Tanchev, 2014). The slope instability is identified in the United States as a secondary cause of failure of embankment dams (USACE, 2004).

The overtopping could be caused by an inadequate spillway facility or an insufficient reservoir storage capacity. The overtopping risks were reduced through improved hydrological studies and methods of predicting flood flows, but several old dams are still pretty inadequate to overcome a predicted maximum flow without overtopping. The primary cause of failure of embankment dams in the United States is identified in overtopping, as a result of inadequate spillway capacity, while the next most frequent cause is seepage and piping (USACE, 2004). The seepage through the foundation and abutments is more dangerous than through the dam, hence it is recommended to insert instrumentation in the abutments and foundation.

The mechanical erosion was defined by Tanchev (2014) as the phenomenon due to the fine earth particles carrying by seepage water from foundation or from dam body, which can lead to weakening of embankment dam, to start the process of piping and to reach dam failure. The failure by internal erosion is very dangerous because it can occur suddenly with a full reservoir (Penman, 1986). To prevent this effect, drainages can be employed. McCook (2004) defined the seepage erosion as a phenomenon which occurs when the water flowing through cracks or defect erodes the soil from the walls of the crack or defect. Internal erosion and piping can be divided into four phases: initiation and continuation of erosion, progression to form a pipe and formation of a breach (Fell et al., 2003).

Foster et al. (1998, 2000a, 2000b) used the ICOLD (1974, 1995) data and information on the dams which had experienced incidents to develop historic performance data for dams constructed up to 1986, showing that about 1 out of 25 large embankment dams constructed before 1950 and about 1 out of 200 constructed after 1950 failed (Fell et al., 2005). The statistics of Foster et al. (1998, 2000a, 2000b) of failure of embankment dams during operation, excluding failures during construction, show that after overtopping, internal erosion and piping are the most important failure modes: slope instability accounts for only 5.5% of failures and only 1.6% for dams built after 1950. Their data shows that for dams in Australia, USA, Canada and New Zealand designed and constructed after 1930, about 90% of failures were related to internal erosion and piping. The failure data reflect the fact that it is possible to reliably assess the factor of safety of a dam, that modern criteria for acceptable factors of safety are reasonably conservative, and that most dams will show excessive deformation if they are marginally stable, allowing remedial works or lowering of the reservoir water level before failure occurs (Fell et al., 2005).

The erosion failure mechanisms by overtopping and by internal cracking are consequently the most common, and the most dangerous, for the presence of full reservoir. Some serious historical dam incidents caused by overtopping and internal erosion are briefly presented below with the aim to highlight the type and the frequency of occurred mechanisms; no other detailed aspects which could influence the failure are introduced and explained for the case-histories examined.

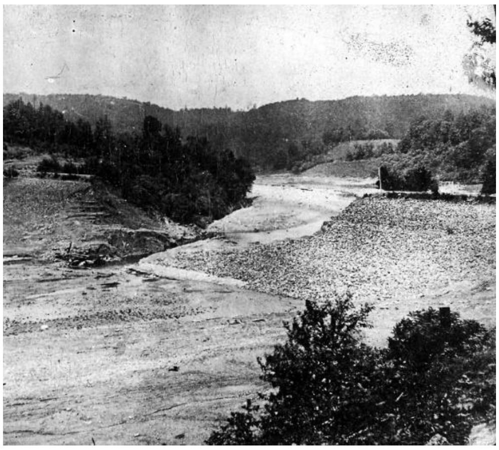

Figure 2.2 South Fork Dam after failure in 1889 (Photo source: www.damfailures.org/case-study/south-fork-dam-pennsylvania-1889)

Figure 2.3 The ruptured embankment viewed from inside the reservoir of Dale Dyke dam, few days after the disaster (Photo source: www.mick-armitage.staff.shef.ac.uk/sheffield/photogal/picflud1.html)

Penman (1986) reported the following dam accidents: Estrecho de Rientes was a 45.7 m high dam built in Spain from 1755 to 1789, the first reservoir impounding was in February 1802, after which the dam breached releasing a great amount of water destroying part of the town of Lorca without knowing the exact cause; South Fork was a 21.9 m high embankment dam built in 1852 in Pennsylvania using an upstream earthfill and a downstream rockfill shoulders, and overtopping occurred during the day on 31 May 1889 causing a great loss of human lives (in Fig. 2.2 an image of the dam after failure is showed); Dale Dyke was a puddle clay core dam with a height of 29 m built in England, which failed during first filling in March 1864 (Fig. 2.3); Teton dam was a 93 high embankment dam constructed in Idaho and the dam failure (Fig. 2.4) was on first filling due to internal erosion when the reservoir level was 9.2 m below the crest.

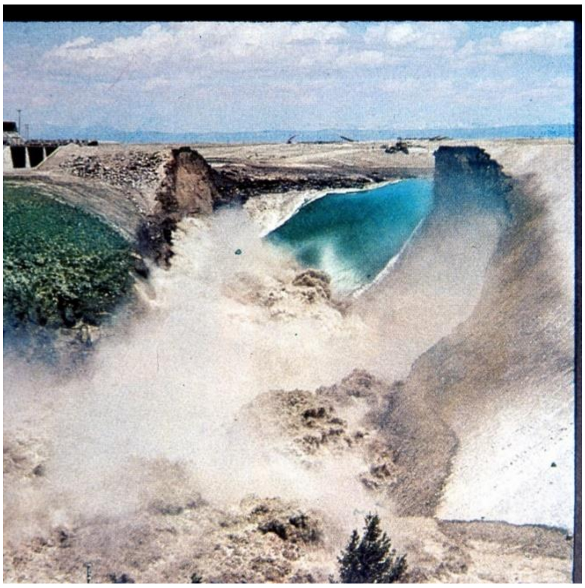

Figure 2.4 The Teton Dam collapse on the 5 of June 1976 (Photo source: www.deseret.com/2016/6/5/20589697/40th-anniversary-of-the-collapse-of-the-teton-dam#the-teton-dam-collapsed-june-5-1976)

Sharma and Kumar (2013) also presented some case histories of embankment dam failure due to overtopping and internal erosion: the Belci dam was a 18.5 m high clay core earthfill dam with a concrete upstream facing built in 1962 in Romania, which was characterized by a first overtopping and a partial erosion during 1970, a secondly and catastrophic overtopping in 1990 due to a severe rainfall causing a breach of 112 m long and 15 m deep; the Tous dam was a 70 m high clay core zoned dam built in Spain in 1958, which was overcome by water reaching about 1.10 m above the crest in 1982 and eroding a greater part of the shoulders (Fig. 2.5), after the incident the dam was reconstructed; the Baldwin Hills Dam was a 71 m high homogeneous earthfill built in California, it breached in 1963 due to internal erosion releasing the major part the reservoir water.

Figure 2.5 Original Tous Dam after overtopping failure (Photo source: Alcrudo, 2003).

As it was shown (Figures 2.2, 2.3, 2.4 and 2.5), the damages of real failure mechanisms caused by erosion, by overtopping and by internal cracking, are catastrophic, especially because the dams were already impounded. The slope instability instead, usually occurs during dam construction and it is a less widespread mechanism as statistics revealed.

2.4 DEFORMATION OF EMBANKMENT DAMS

Deformation behaviour of embankment dams, both during and after construction, is of fundamental importance in understanding whether the future performance will be satisfactory. Analysis of deformation requires consideration of stress conditions and the constitutive relations of the materials utilized for the embankment construction; in case of zoned earth dams also the interaction between the different material zones have to be considered.

Early works by Poulos and coworkers (e.g., Poulos et al., 1972) estimated the deformations in earth dams and embankments using the elastic theory in order to determine stresses and strain in the soil. However, since the pioneering study carried out by Clough and Woodward (1967) it was demonstrated the potential of the numerical analyses, and specifically of the finite element method, to calculate stresses and movements in earth and rockfill dams. Eisenstein (1974) reported several cases described in the literature showing good agreement between measured and calculated movements in dams. Based on these indications, it appeared that quite reasonable values of displacements and stresses could be calculated using stress-strain and strength parameters determined from laboratory tests. Successively, Duncan (1992, 1994) showed the potential of finite element method to model many complexities of embankment dam behaviour which include nonlinear stress-strain behaviour, dependence of stiffness and strength on confining pressure, irrecoverable plastic deformations, volumetric strains caused by shear stresses, stress-path dependent strength, creep, stress relaxation, to cite some of them. In particular, he summarized 42 cases of embankment and dam analyses, all of these cases including comparisons of calculated and measured movements, pore pressures, or both. The wide use of advanced constitutive relationships based on parameters determined by means of results of conventional soil tests was also stressed. Since then, several finite element analyses have been used (Saboya and Byrne, 1993; Kovacevic, 1994; Naylor et al., 1997; Dounias et al., 1996; among others) to model the deformations caused by variation in stress conditions, commonly for deformation during construction and first filling. More recently, other examples of numerical analyses of embankment dams with the aim of assessing the deformation behaviour during various phases in dam's life (i.e., construction, first reservoir impounding, subsequent reservoir operations) are provided (Tschernutter et al., 2011; Pramthawee et al., 2011; Kovacevic & Potts, 2011 and Kovacevic et al., 2013; Qoreishi, 2013; Kim et al., 2014; Derakhshandi et al., 2014; Da Silva & de Assis, 2014; Sukkarak et al., 2017; Rezaee et al. 2017). The long term deformations of embankment dams, due to the seasonal reservoir level changes, were also analysed through the numerical modelling by some authors (Pelecanos et al., 2018; Ventrella et al., 2019).

Hunter and Fell (2003) reported the behaviour of several embankment dams around the world, considering the factors influencing the stress conditions, strength and compressibility of the embankment materials and the interaction between embankment zones. These field experiences have shown that there are some common important aspects at each stage of its life which must be considered when trying to model their behavior. Figure 2.6 shows the three main stages of the lifespan of an embankment dam as follows:

1. Construction of the dam: Simulation of the embankment construction by building up a series of discrete layers of material to the desired level. Mechanical properties of dam body materials have to be considered at this stage.

2. Filling of the reservoir: Rising the level of the water of the reservoir leads to flow of water through the dam body and subsequent stress adjustments. The hydro-mechanical interactions can be considered at this stage.

3. Dam Operation: Variation in reservoir level and possible seismic motions are the main features of this stage.

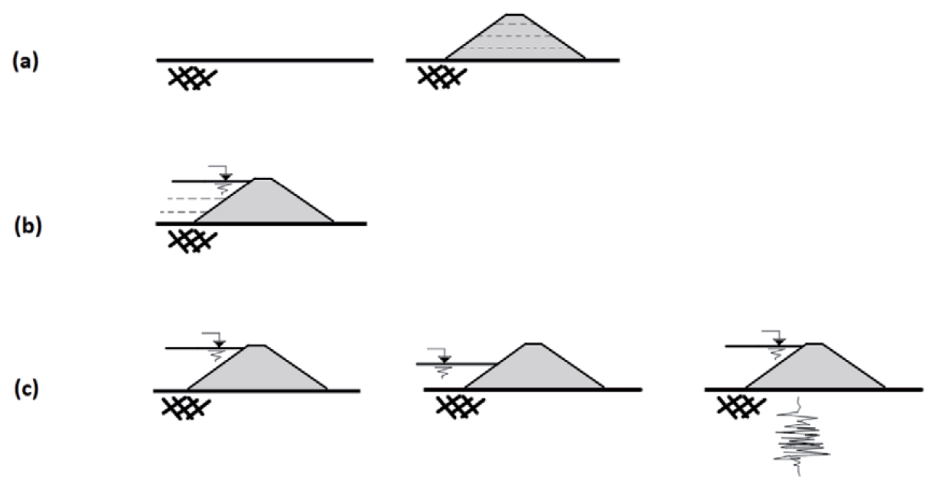

Figure 2.6 Different stages of a lifespan of an earth-core rockfill dam (ECRD): a) construction of the dam in layers; b) impoundment of the reservoir by increasing the level of water in several steps; c) service life: variation of ground water level in the reservoir, earthquake, etc (Qoreishi, 2013).

2.4.1 Stresses and deformations during construction

A thorough review of the general deformation behaviour of embankment dams has been conducted by Hunter and Fell (2003) who investigated a number of instrumented homogeneous earthfill, rockfill as well as zoned earth-core rockfill dams based on historical records of embankment performance. Most of the deformation data collected and analysed is represented by vertical deformation, usually from instrumentation installed in the core as construction proceeded, whereas data on horizontal deformation was less frequently monitored, even if was collected and analysed for a number of embankments. The main findings of this study will be summarized and discussed in the following.

In their work, Hunter and Fell (2003) before analysing the experimental data, first investigated the state of stresses in the dam's body through numerical analyses. Particular attention was devoted to zoned dam where the state of stress inside the dam's body could be influenced by a sort of load transfer from one element to another, which can lead to hydraulic fracturing, one of the causes of internal erosion into the dam. This unloading of the core and overloading of the shoulders is named "arching effect" and will be analysed more in detail later on (see Sect. 2.4.2). The Authors used an elastic finite difference analysis for homogeneous dams, for estimating the total vertical stress profiles during and at the end of construction for a variety of symmetrical embankment shapes. For zoned dam, in order to assess the general stress conditions and trend of deformation behaviour during construction and therefore to facilitate the understanding of the results of numerical simulations, first undertook the analysis of a simple plane strain finite difference model of a zoned embankment. In some cases, the homogeneous dam approach was used also for zoned embankment dams, but only in case where arching has a negligible influence on the vertical stress profile. Hunter and Fell (2003) considered valid this assumption only in two cases: (i) zoned embankments with broad central earthfill zones (e.g. for central core widths with a combined core slope greater than about 1.5 to 2H to 1V); (ii) zoned embankments where the compressibility properties of the central earthfill zone and gravelly or rockfill shoulders were similar.

The model used to study zoned dams consisted of a 100 m high central core earth and rockfill dam, of thin core width on a rigid foundation (Fig. 2.7), the construction was modelled in ten lifts each of 10 m height, and a Mohr-Coulomb linear-elastic perfectly plastic model was used for both the central core and rockfill. Three analyses were carried out each using the same properties for the rockfill and varying the properties of the core material (Table 2.1) as follows: in case 1, the core has similar shear strength properties to the rockfill and same Poisson's ratio, which corresponds to a well-compacted silty gravel core with non-plastic fines; case 2 is characterized by a very stiff core with Poisson's ratio much greater than that of the rockfill; case 3 represents a wet placed core, assuming an undrained behaviour of the core.

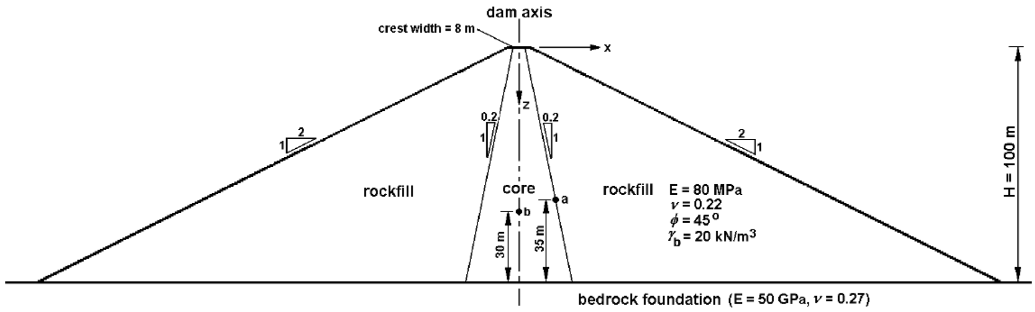

Figure 2.7 Embankment model for finite difference analysis during construction (Hunter & Fell, 2003)

Table 2.1 Properties of central core used in finite difference analyses (Hunter & Fell, 2003)

Analysed Case	E (MPa)	ν (-)	γ (kN/m^3)	c (kPa)	φ (°)
Case 1	100	0.22	20	0	45
Case 2	100	0.40	20	75	20
Case 3	100	0.48	20	30	5

Results of numerical analysis (Fig. 2.8) show the influence of the difference in shear strength and Poisson's ratio of the core on the stresses within the embankment and on the deformation behaviour. Where the properties of the core are similar to those of the rockfill (Case 1) the lateral stress distribution is similar to the homogeneous case and lateral displacements in the core and rockfill are small. Where the stress-strain properties of the core are different to those of the rockfill, such as for Cases 2 and 3, the stress profiles differ significantly from the homogeneous case with much higher lateral stresses developed during construction as well as arching across the core. The results also show that: (i) lateral stresses and strains increase with increasing Poisson's ratio of the core, reflecting yielding and plastic deformation of the core, particularly for Case 3; (ii) maximum lateral strains are observed at a depth below the crest of approximately 65% of the embankment height (h/H = 0.65); (iii) lateral strains, which occur largely as plastic deformation of the core, contribute significantly to the vertical strain observed in the core; (iv) arching occurs in the narrow core as a result of the large differential vertical deformation between the core and the shoulders. The horizontal stress and displacements distributions were strongly influenced by the choice of the Poisson ratio as shown in Fig. 2.8.

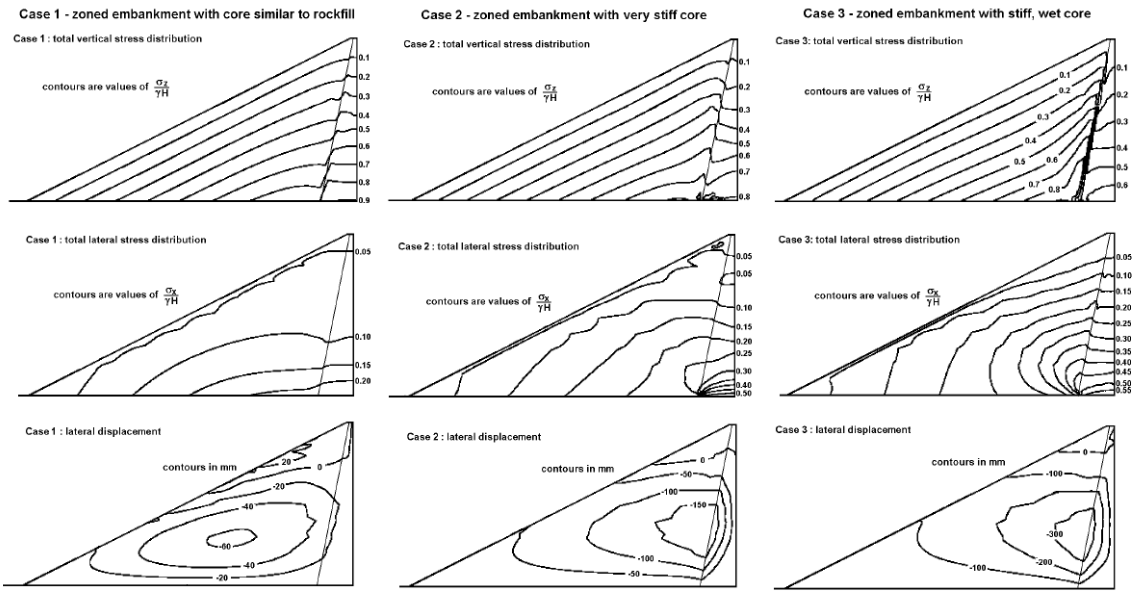

Figure 2.8 Total vertical stress, total lateral stress, and lateral (horizontal) displacement distributions at end of construction for zoned earthfill finite difference analysis (Hunter & Fell, 2003)

Hunter & Fell (2003) stated that the amount of deformations in rockfill and earth-core rockfill dams depends on different factors, such as the mechanical properties of both the materials which characterize the embankment dam, the embankment height, the valley shape and the stress-strain relationship of rockfill. The accuracy of prediction of rockfill deformation during construction for both numerical and empirical methods depends on the quality of representation of the stress-strain relationship of the rockfill, which is strongly dependent on the rockfill properties, in particular the intact strength of the rock, method of placement and particle size distribution after compaction. Many authors based on field observations (Mori and Pinto 1988; and others) and on results of large scale laboratory tests (Marsal 1973; Marachi, 1969; and others) indicate the compressibility properties of rockfill are affected by: i) degree of compaction of the rockfill; ii) applied stress conditions and stress path; iii) particle shape and particle size distribution, iv) intact strength of the rock used as rockfill (Hunter & Fell, 2003). Hunter and Fell (2003) identified the susceptibility of rockfill to collapse compression on wetting as a significant factor in the evaluation of the deformation behaviour, and they specified that the typical stress-strain relationships of rockfill from field measurements during construction (under the embankment centreline) is a non-linear relationship with a general trend of decreasing secant (and tangent) modulus with increasing applied stress. The compressibility properties of earthfill are dependent on the soil type, the degree of compaction, and the moisture content at placement relative to Standard optimum (Hunter & Fell, 2003). The earthfill material is a partially saturated with an amount of over-consolidation that is related to the compactive effort of the roller and the pore water suction, the result pore water suction is dependent on the moisture content at placement, the degree of saturation of the compacted earthfill and the material type (Hunter & Fell, 2003). Hunter and Fell (2003) also indicate as significant factors influencing the deformations, the embankment height, as a measure of the level of applied stress within the embankment, and the valley shape, for embankments constructed in narrow valleys due to the effects of cross-valley arching and resultant reduction in applied stresses.

Hunter and Fell (2003) indicated that during construction for a dry placed, well compacted earthfill, the settlements increases with the increase in effective stress, due to compression of pore air in the partially saturated soil which bring to an increase of the degree of saturation and a reduction of the pore water suction until positive pore water pressures is developed. In compacted earthfills placed close to or wet of optimum moisture content, the degree of saturation is relatively high at compaction (generally greater than 85 to 90%) and the matric suction relatively low compared with dry placed earthfills, hence positive pore water pressures are generally developed at low levels of confining stress. Considering the earthfill as low permeability soil, the conditions during construction are close to undrained, therefore, deformations largely occur as plastic type deformations due to yielding in undrained loading (Hunter & Fell, 2003).

Summarizing, the total and effective stress conditions established in an embankment during construction are dependent on the embankment geometry, the embankment zoning geometry, and the strength and compressibility properties of the embankment materials (Hunter & Fell, 2003).

In the analysis of the deformation behaviour during construction, Hunter and Fell (2003) grouped the embankment dams in two categories: dry placed earthfill core dams (i.e.

typically those placed at moisture content drier than about 0.5 to 1% dry of optimum standard) or other cases with small lateral deformations, and wet placed earthfill core dams and other cases with large lateral displacements. More specifically in the first group are: (i) zoned dam with relatively broad core widths and dry placed earthfill cores, typically those placed at moistures contents drier than about 0.5 to 1% dry of Standard optimum; (ii) zoned dam with cores of dominantly sandy to gravelly soil types with low plasticity silty fines or with low plasticity clayey fines of low fines content, and within which positive pore pressures during construction were relatively low; (iii) zoned embankments with thin cores where the compressibility properties of the core are similar to the shoulders. In Fig. 2.9 the vertical strain versus effective vertical stress at the end of the construction for all case studies of dry placed earthfills is presented. In the plots some bounds are defined, based on evaluation of the data, of the general limits of "normal" type deformation during construction (Hunter & Fell, 2003). The points which are located outside the bounds could be potentially "abnormal". This kind of representation is very helpful to find suspected abnormal deformations, as in Fig. 2.9b for the dry placed dominantly sandy and gravelly earthfills, where Naramata dam data shows a probable arching effect in the narrow, dry placed earthfill core.

In Table 2.2 the estimated values of confined secant moduli for well compacted dry placed earthfills are reported whereas in Figure 2.10 the variation of the moduli with the estimated vertical effective stress is also illustrated. It can be observed that the range of confined moduli within any core material is relatively broad, up to 0.5 to 2 times the mean value. According to Hunter and Fell (2003), this variation can partly be attributed to variations in material properties, variation in density due to compaction and inaccuracy in the measurement readings.

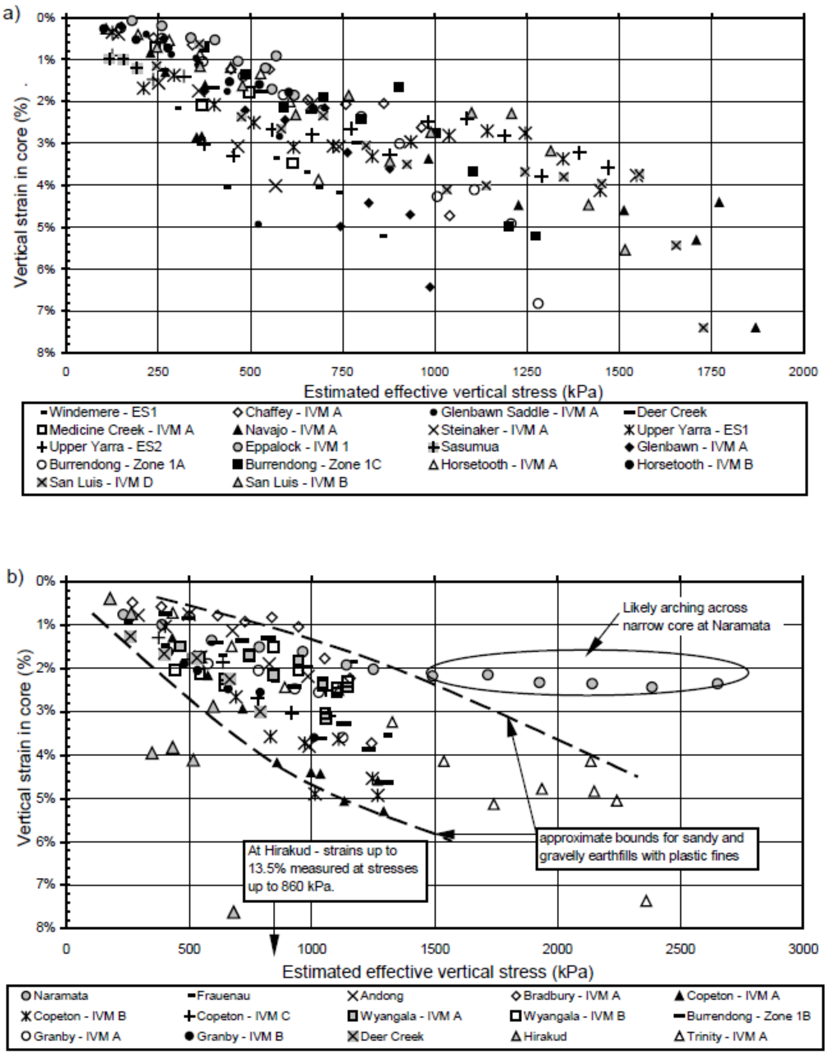

Figure 2.9 Vertical strain versus effective vertical stress in the core at end of construction for (a) dry placed clay earthfills and (b) dry placed dominantly sandy and gravelly earthfills (Hunter & Fell, 2003)

Core Material Type	No. Cases	Confined Secant Modulus (MPa)*[1]		
		Effective Vertical Stress Range (kPa)		
		500 to 700*[2]	1000	1500 to 2000
Clayey soil types (CL) – sandy clays and gravelly clays	20	15 to 45 (27)	15 to 50 (30)	25 to 42
Silty soils (ML), data from Gould.	3	30 to 60	-	-
Clayey Sands to Clayey Gravels (SC/GC), plastic fines, > 20% fines	11	20 to 65 (33)	30 to 65 (40)	25 to 65
Silty Sands to Silty Gravels (SM/GM), plastic fines, > 20% fines	9	35 to 65 (46)	45 to 65 (50)	35 to 65
Sandy and Gravelly soils - non-plastic fines or < 20% plastic fines	6	35 to 80 (60)	35 to 90 (60)	40 to 90

Notes *[1] Values represent range of confined secant moduli, values in brackets represent average
*[2] Includes Gould (1953, 1954) data.

Table 2.2 Confined secant moduli during construction for well compacted dry placed earthfills

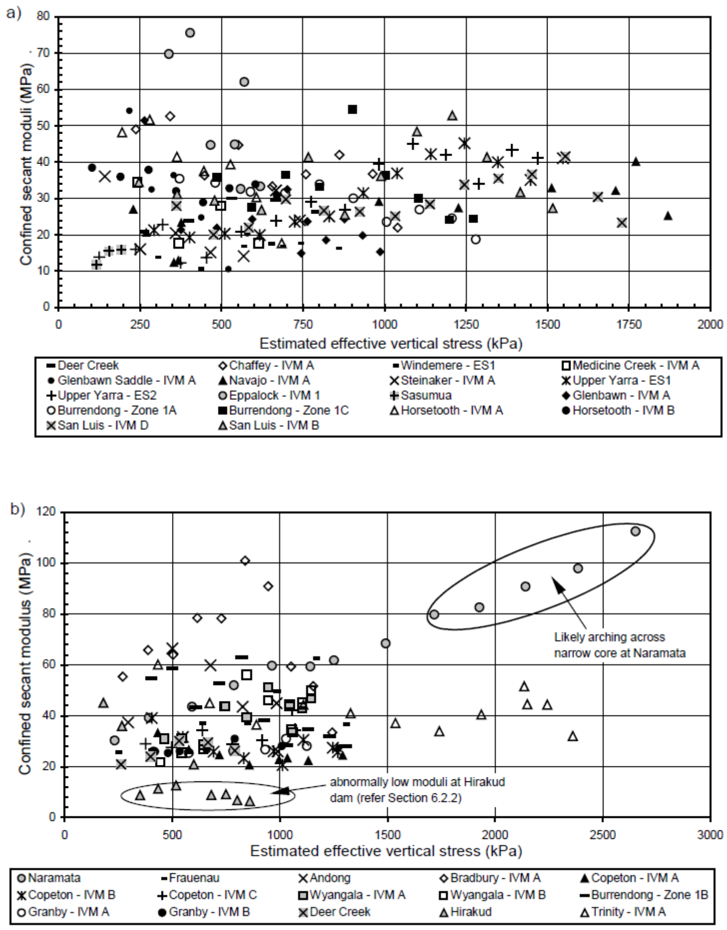

Figure 2.10 Confined secant moduli versus effective vertical stress in the core at end of construction for (a) dry placed clay earthfills and (b) dry placed dominantly sandy and gravelly earthfills (Hunter & Fell, 2003)

The embankment dams pertaining to the second group, that is where the lateral displacement of the core during construction is generally large and has a significant influence on the vertical deformation behaviour of the core, were modelled by the Authors case-by-case using finite element methods (Hunter & Fell, 2003). In Fig. 2.11 and 2.12 the vertical strain of the core at end of construction versus fill height is plotted for dominantly sandy and gravelly earthfill cores in Fig. 2.11 and for clay cores in Fig. 2.12, highlighting a very high vertical strain measured within some regions of the core of several zoned embankments including Blowering, Beliche, Tedorigawa and Chicoasen. In Fig. 2.12b it was also possible to identify an arching effect in the Talbingo dam. In the Figures some points fall outside the bounds, but it is not necessary that they are symptom of abnormal deformations, because they can be due to the inaccuracies or errors of measurement.

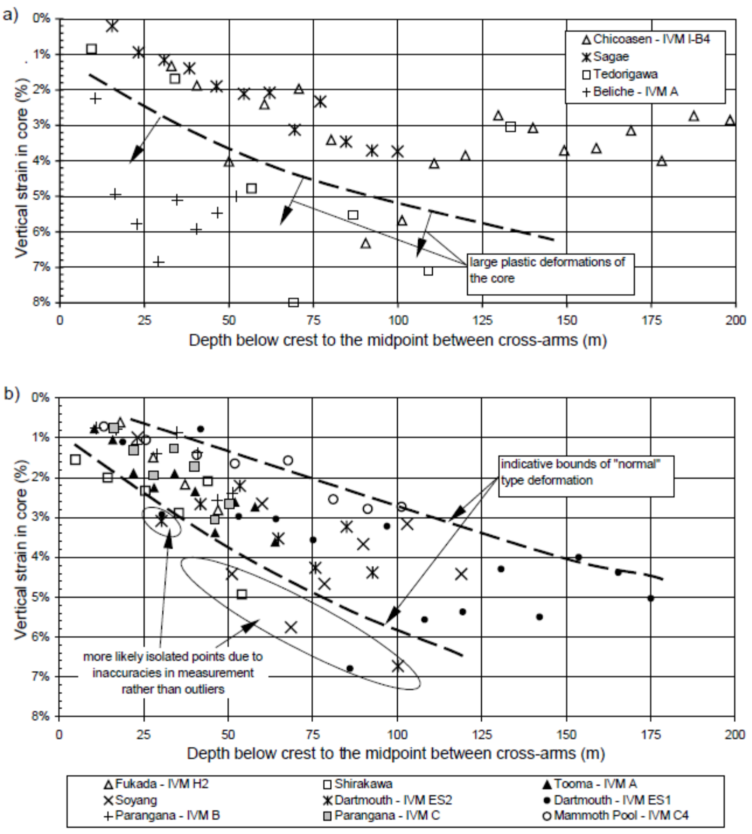

Figure 2.11 Vertical strain in the core versus fill height at end of construction for dominantly sandy and gravelly earthfills with plastic fines placed close to or wet of Standard optimum, for (a) thin cores (combined slopes less than 0.5H to 1V), and (b) medium to thick cores (combined slope ≥ 0.5H to 1V) (Hunter & Fell, 2003)

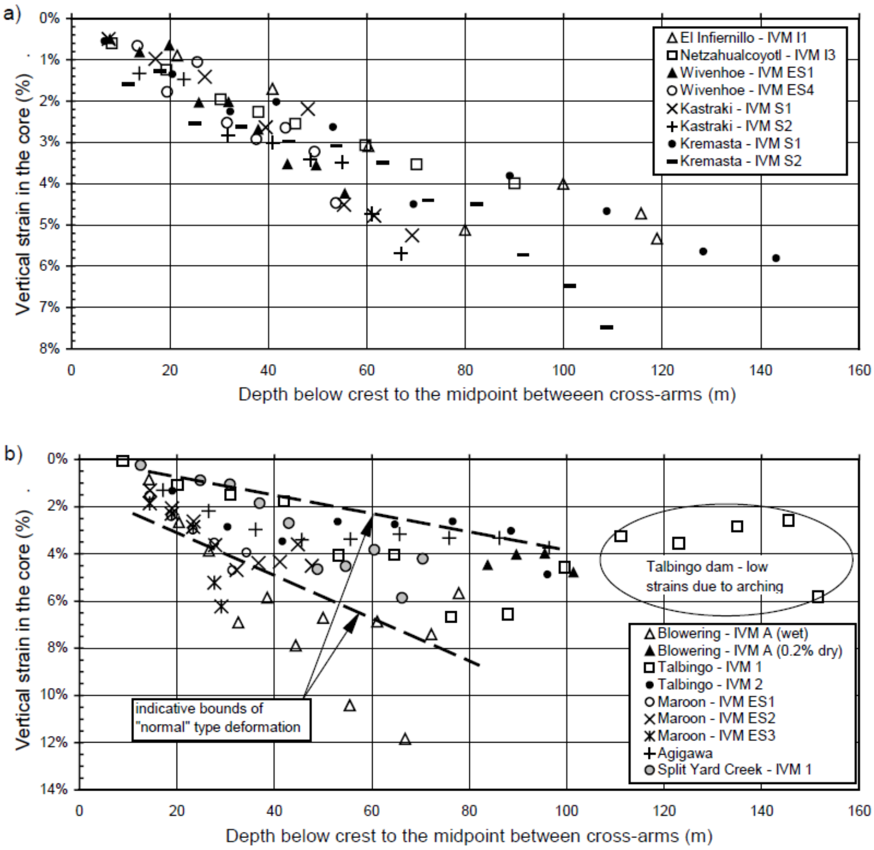

Figure 2.12 Vertical strain of the core versus fill height at end of construction for clay earthfills placed close to or wet of Standard optimum moisture content, for (a) thin core (combined slopes less than 0.5H to 1V), and (b) medium to thick cores (combined slope ≥ 0.5H to 1V) (Hunter & Fell, 2003)

The numerical analyses of Hunter and Fell (2003) on representative cases of zoned dams show that the deformation behaviour is strongly influenced by the differences of the stress-strain properties between the materials of core and shell, highlighting small lateral displacements in the core and rockfill when the properties are similar, and higher lateral stresses and arching across the core when the properties are pretty different. The dry placed earthfill core dams can be considered part of the first group, while the wet placed earthfill core dams part of the second one. The deformation behaviour is also influenced by the embankment height, the valley shape and quality of the representation of the stress-strain relationship of the materials.

2.4.2 Arching effect

One of the causes of erosion is internal cracking, which develops within zones of tensile stresses in zoned and earthfill dams due to differential settlement, filling of the reservoir, and seismic action. The cracks could be: transversal, which can be caused by tensile stresses related to differential embankment and foundation settlement; longitudinal, resulting from settlement of upstream transition zone or shell due to initial saturation by the reservoir or due to rapid drawdown; and horizontal, which occurs when the core material is much more compressible than the adjacent transition or shell material. A type of horizontal cracking is the hydraulic fracturing, which is a fissure of the core material. It can be due to an effect called arching and occurs when settlements between materials are non-uniform, which could be core and shoulder materials but also core and foundation materials. The former is characterized by the tendency of the core to arch across the less compressible adjacent zones, which could result in a reduction of the vertical stress in the core; the latter can occur if the foundation material below the core is very compressible. The hydraulic fissure can be formed inside the core when in some zone the force of the hydrostatic pressure or of pore water pressure exceeds the value of the total normal stress (Tanchev, 2014). Penman (1986) stated that hydraulic fracturing could occur when the value of pore water pressure is between the values of the total major principal stress σ_1 and the total minor principal stress σ_3 (Tanchev, 2014). Penman also (1986) indicated the presence of arching in a reduction in vertical total pressure which can occur in the core, and to avoid hydraulic fracture, the total pressure on any plane passing through the core must exceed the reservoir water pressure. Rezaei & Salehi (2011) indicated that a hydraulic crack could develop, when soil pressure (minor principal total stress) of core is less than the adjacent hydrostatic pressure. Derakhshandi et al. (2014) considered that decreased vertical stress, during construction and first impounding, due to arching phenomenon can make horizontal cracks, because water pressure is higher than vertical stress.

Rezaei & Salehi (2011) defined three kinds of arching effect: longitudinal (Fig. 2.13a), which can happen for the narrow shape of the valley; transverse (Fig. 2.13b), which occurs between core and shell due to the substantial different types of material and differential settlements; local (Fig. 2.13c), which occurs between two different stiffness materials such as foundation or other concrete structures like cut-off wall and culvert.

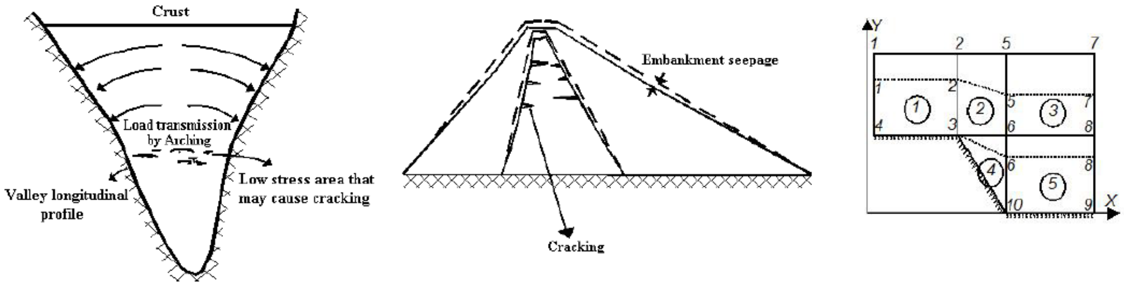

Figure 2.13 Types of arching: a) longitudinal b) transverse and c) local (Rezaei et al. 2011)

Rezaei & Salehi (2011) distinguished different modes of load transmission between core and shell in dams: stress transmission from the core to the shell due to more vertical core displacements compared to those of the shell, and load transmission from the shell to the core because the shoulders settled more than the core.

Pagano et al. (1998) discussed the arching effect caused by a load transfer because of the interaction between a fine-grained core and stiffer shells, whose intensity depends on the dam geometry and on the differences in stiffness. The effect of arching is to increase the horizontal minimum principal stress σ_x along the dam axis and to decrease the vertical maximum principal stress σ_z, compared to the overburden pressure at the same elevation (Pagano et al., 1998). Investigating the stress state inside the dam body is necessary to understand the possibility of the existence of arching effect, and for this purpose the numerical analysis is very useful.

In general arching due to the transmission of forces from core to shoulders caused by different stiffness could be defined through the arching degree, which is well represented by a coefficient defined Arching Ratio (AR):

$$AR = \frac{\sigma_v}{\gamma h} \tag{2.1}$$

where σ_v is the vertical total pressure, γh represents the overburden pressure, h is the embankment height and γ is the unit weight. The higher AR, the less the arching phenomenon in the core and the lower the probability of hydraulic fracturing would be (Derakhshandi et al., 2014). AR less than unit means that load transfer from core to shell occurs, and as the dam height increases AR decreases, resulting in a more pronounced arching effect in upper high dam. Derakhshandi et al. (2014) indicated the arching ratio as an important parameter which can evaluate the hydraulic fracturing at the end of construction.

Arching could be represented plotting the AR parameter along the core axis. To evaluate arching in zoned existing dams, total vertical stress measurements could be plotted with overburden pressure during construction. Two cases where it was possible to interpret measurements during construction are reported from Pagano et al. (1998): Kastraki dam (Fig. 2.14) and Beliche dam (Fig. 2.15). The Beliche dam was also subject of numerical analysis by Naylor et al. (1986; 1997).

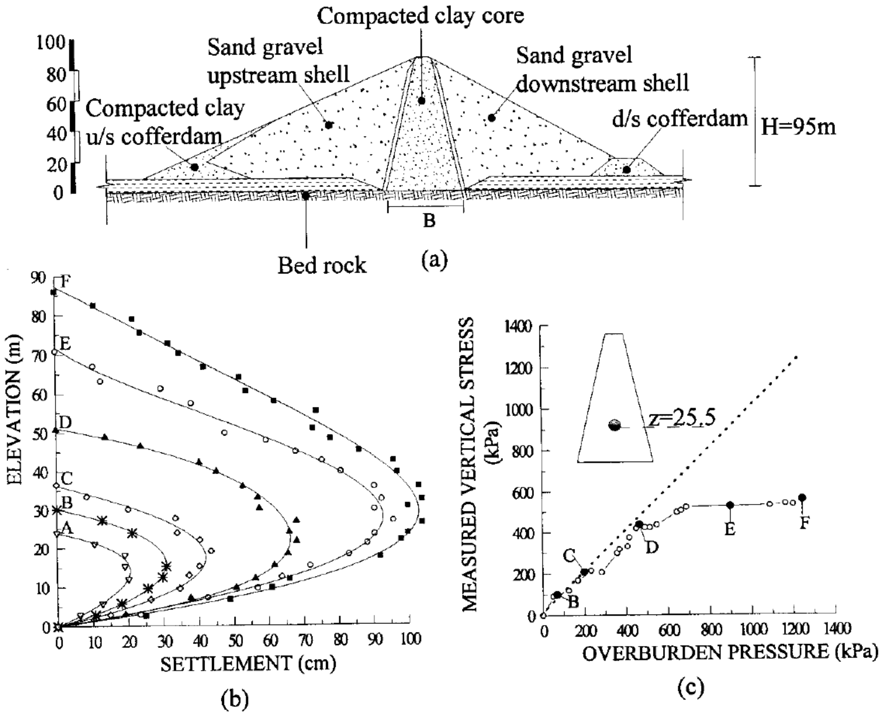

Figure 2.14 Kastraki dam: (a) main cross section; (b) settlement profiles during construction; (c) vertical total stresses in core at elevation of 25.5 m (Pagano et al., 1998)

The Kastraki dam is a 95 m high zoned dam, constructed from August 1967 to May 1969 with a clay core compacted around the optimum of the Standard Proctor Test and with shells of compacted river sand and gravel. Pagano et al. (1998) and Fontanella and Pagano (2008) plotted the measured total vertical stress of a point along the core axis of Kastraki dam against the overburden pressure during construction (Fig. 2.14c), pointing out that although at the beginning measured and overburden pressure are similar, as the dam height increases the total vertical stress becomes less than overburden pressure, which means that a load transfer occurs.

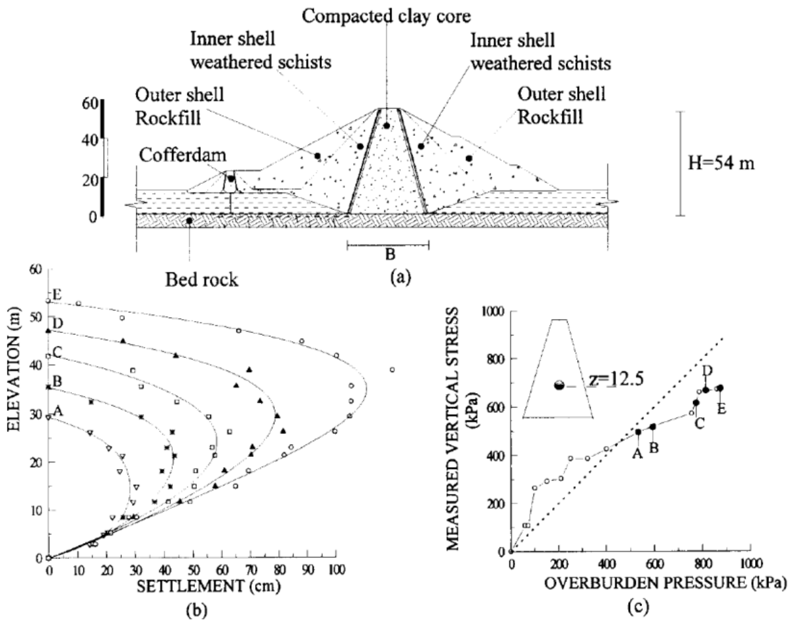

Figure 2.15 Beliche dam: (a) main cross section (b) settlement profiles during construction (c) vertical total stresses in core at elevation of 12.5 m (Pagano et al., 1998)

The Beliche dam is a 54 m high zoned dam constructed in Portugal from July 1983 to March 1985. The dam is characterized by a fine-grained core compacted around the optimum of the Standard Proctor Test and two types of rockfill shoulders, inner and outer (Fig. 2.15a). The inner shells present a high compressibility rockfill in order to ensure a higher vertical stress in the core, which could bring to a reverse load transfer from the shell to the core during construction and reservoir impounding, increasing, in this way, the margin of safety against internal erosion due to hydraulic fracture (Naylor et al., 1997). Pagano et al. (1998) analysed the settlement profiles (Fig. 2.15b) indicating that as the fill level increased, the effects related to the progressive lack of confinement prevailed on possible stress discharge. Naylor et al. (1986; 1997) studied the construction and reservoir impounding of the Beliche dam through a finite element back-analysis. Fig. 2.16 and 2.17 present calculated vertical stress profiles on horizontal sections at elevation of 12.5 and 22.5 m in comparison with the measured profiles, and they confirm the design intention of the high compressive effective stress in the core, which means reduced risk of internal erosion. Naylor et al. (1997), therefore, highlighted the importance of reproducing the correct stress distribution, which depends on the relative stiffness of different zones.

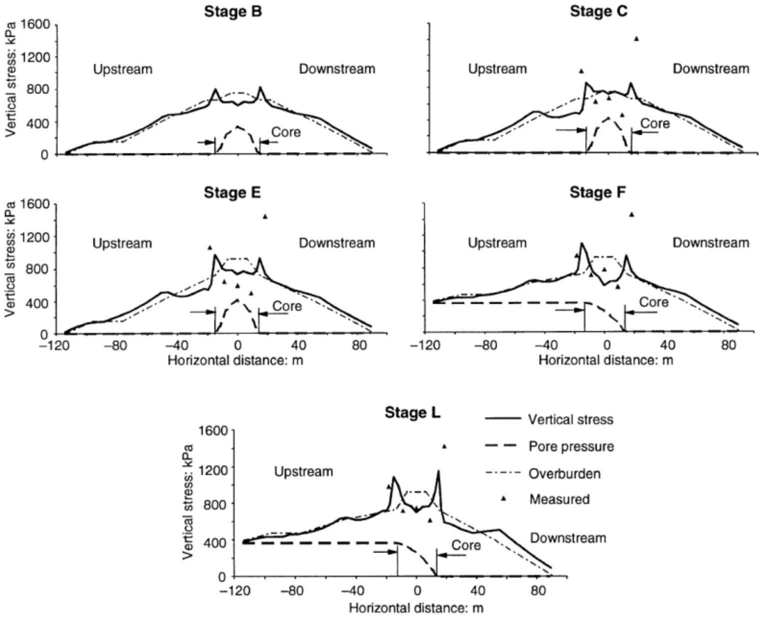

Figure 2.16 Vertical stress at elevation 12.5 m (Naylor et al., 1997)

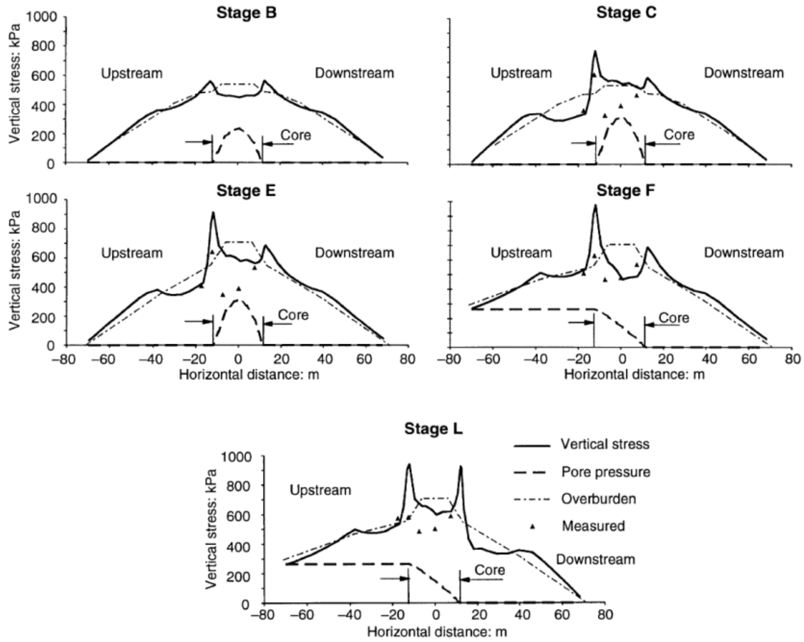

Figure 2.17 Vertical stress at elevation 22.5 m (Naylor et al., 1997)

Hunter and Fell (2003) through the numerical analysis previously reported, demonstrated that arching is developed in zoned embankments with narrow cores not only due to the core being more compressible than the supporting shoulders but also due to lateral spreading of the core. They compared vertical pressures measured during construction in the core of zoned embankments using pressure cells, to the vertical stress estimated for a homogeneous embankment allowing for the embankment shape (Fig. 2.18). The Kastraki, Thomson and Chicoasen dams present a measured vertical stress less than the homogeneous case, which means arching across the core.

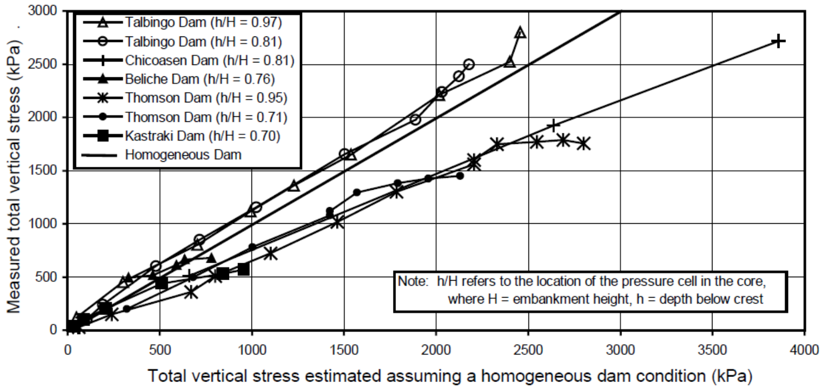

Figure 2.18 Estimated versus measured total vertical stresses during construction (Hunter & Fell, 2003)

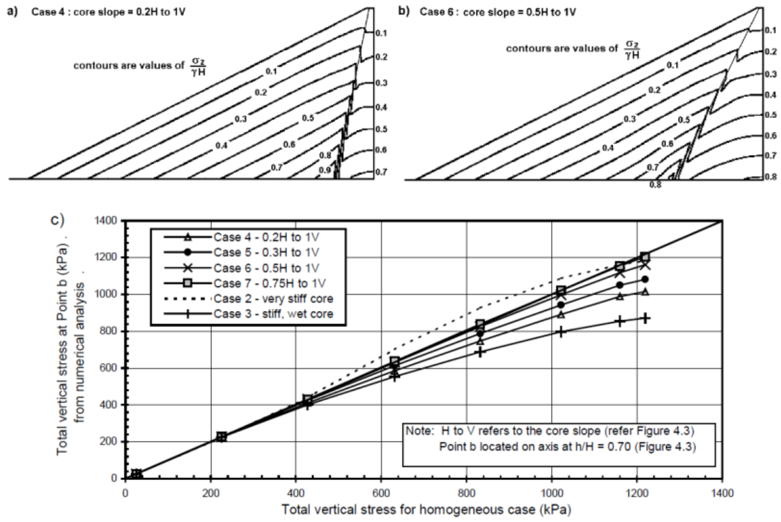

Figure 2.19 Total vertical stress profiles from the numerical analysis of construction for zoned embankments with different core slopes; (a) 0.2H to 1V case, (b) 0.5H to 1V case, and (c) total vertical stress at h/H = 0.70 with increasing embankment height (Hunter & Fell, 2003)

Hunter and Fell (2003) carried out other numerical analysis to investigate the effect of core width (Fig. 2.19). They changed the symmetrical core slopes from 0.2H, 0.3H, 0.5H and 0.75H to 1V using for the core Young's modulus half value of the rockfill one. The tendency of the total vertical stresses (Fig. 2.19) on the embankment centreline at Point b (Fig. 2.7) is to initially follow the homogeneous case at low stress levels and then curves away at higher stress levels, indicating the presence of arching. The results of the analysis also show that at end of construction the total vertical stresses on the embankment axis increase with increasing core width (Hunter & Fell, 2003).

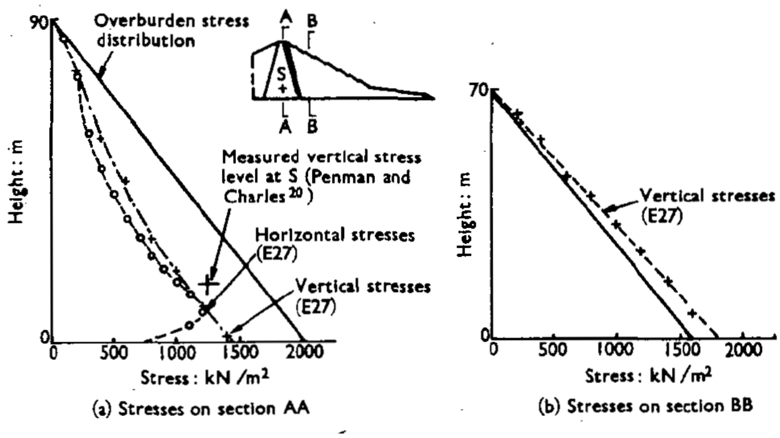

Figure 2.20 Computed stresses on two vertical sections of Llyn Brianne dam (Cathie and Dungar, 1978)

An earth-core dam was analysed by Cathie and Dungar (1978) using finite element approach showing arching, the Llyn Brianne dam, which is a 90 m high zoned dam with clay core and rockfill shoulders. The lateral stresses applied to the rockfill shoulders by the clay core were underestimated in the analysis (Cathie and Dungar, 1978), which do not account for arching. Comparison of predicted and measured stress distribution on the centreline of the core (Fig. 2.20a) and on the rockfill shoulder (Fig. 2.20b) highlighted a load transfer from the core, where horizontal and vertical stresses are less than the overburden pressure, to the shoulder, where vertical stresses is increased compared to overburden pressure.

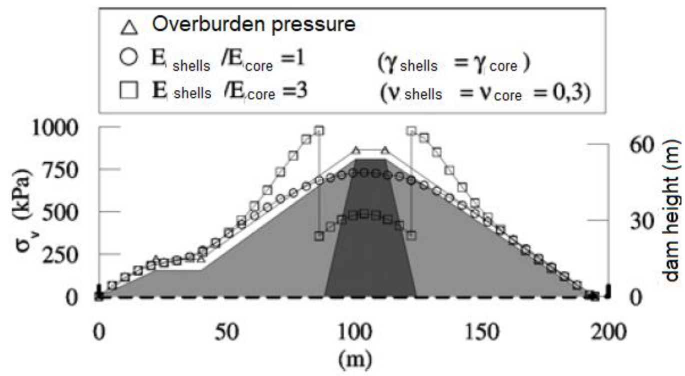

Figure 2.21 Beliche dam: theoretical distributions of total vertical stress along a dam horizontal axis (Fontanella and Pagano, 2008)

Fontanella and Pagano (2008) reported two numerical total vertical stress distribution along a dam horizontal axis, considering a linear elastic behaviour of the materials, and the distribution of the overburden pressure. Firstly, they modelled the dam as only one homogeneous soil characterized by a prescribed value of the Young's modulus, secondly, they gave to the shells a Young's modulus three times greater than core Young's modulus, obtaining (Fig. 2.21) a reduction of total vertical stress in the core and an increase in the shells.

Rezaei et al. (2011) conducted a series of numerical analyses using Drucker-Prager model, in order to define the characteristics on which arching depends. They concluded that: (i) the least amount of arching coefficient occurs in 50% to 80% of dam height; (ii) dam height and filter thickness have not great influence on stress transmission; (iii) higher dams and steep slope of dam body have more stress transmission and less arching coefficient; (iv) as the core slope increases, stress transmission is more and arching coefficient is less; (v) vertical core has more stress transmission than an inclined one; (vi) more compacted shell and cores with higher moisture content have much stress transmission and less arching coefficient.

The arching effect in zoned dams could be therefore explained as a stress transmission from the core to the shells, and it can be quantified through the arching ratio, defined as the total vertical stress during construction over the overburden pressure. The total vertical stress distribution obtained with numerical analyses could be employed if the measurements during construction are not available. Values of the arching ratio parameter less than unity indicate the presence of arching effects. The results of numerical analyses indicate that the arching effect is more pronounced in the upper high dam and that the greater the core slope, the greater the stress transmission.

2.4.3 Stresses and deformations during first impoundment

Nobari and Duncan (1972b) and Sherard (1973) investigated the effect of reservoir filling in a zoned embankment. It is considered that on first filling the core can be considered impermeable and that the water load acts on its upstream face. On the other hand rockfill zone upstream is considered permeable and therefore it will become saturated during first filling. Specifically, the effect of first reservoir filling on a zoned dam is illustrated in Figure 2.22 and can be summarized as follows (Hunter & Fell, 2003):

(i) hydrostatic water pressure on the upstream face of the core results in a net increase in the total stresses within and downstream of this zone; the resulting deformation is downstream and downward; successive seepage of water into the core, with a stationary seepage flow, will result in seepage forces which can cause additional deformations;

(ii) applied water load on the upstream foundation: this could cause differential foundation settlements, especially in the case when soil conditions differ under the dam;

(iii) buoyant uplift on upstream shell with a decrease of effective stresses in the permeable rockfill upstream shell, with the result of deformation upward and upstream which are likely to be small because of the high tangent modulus on unloading of rockfill material compared to their modulus during loading;

(iv) softening of the saturated non-cohesive granular material in the upstream shell with the consequence of additional settlement and horizontal deformations.

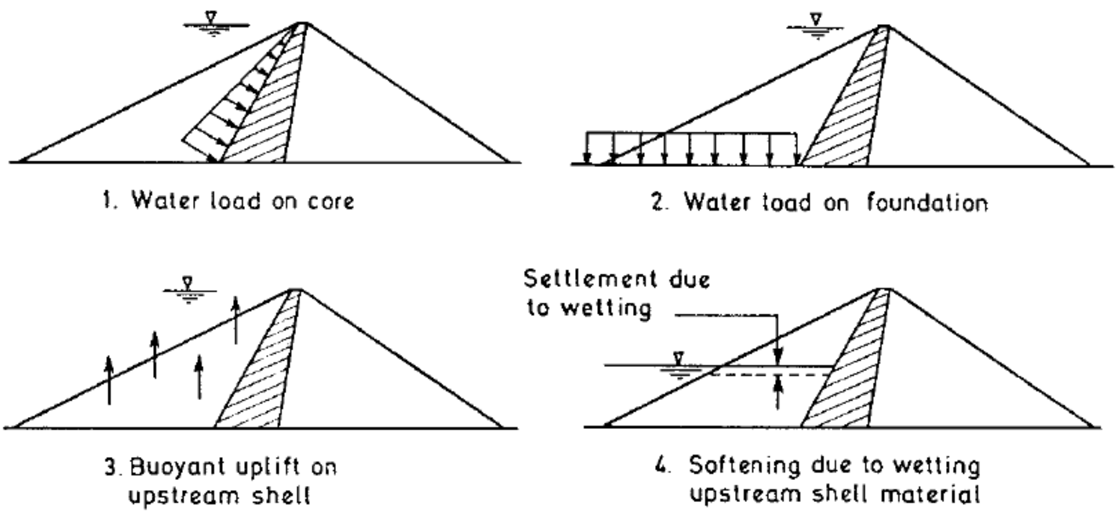

Figure 2.22 Effect of reservoir filling on a zoned embankment (Nobari and Duncan 1972b)

The effect of the water load on the core, assuming that it behaves in undrained conditions during first filling, is a net increase in total stress acting on the upstream face of the core, which depends on the magnitude, the location and the direction in which it acts as controlled by the orientation of the upstream face of the earthfill zone, and on the existing stresses within the embankment at end of construction (Hunter & Fell, 2003). In zoned embankment dams with near vertical narrow core the direction of the applied water load is near horizontal (Hunter & Fell, 2003). Hunter and Fell (2003) carried out numerical analyses to compare the lateral stress distributions also for the first filling, considering both the cases when the two materials of core and shells have same compressibility properties and when the core is wet placed with low undrained strength, obtaining that the change in total lateral stress in the core is greater in the first case. The main deformations resulting from the water load on core face are horizontal, because the horizontal component of the applied stress vector is higher compared to the vertical one. The observed settlements during first filling could be due to a combination of time dependent creep and consolidation. A consequence of the water load on the upstream core face during the reservoir impounding is a formation of a stationary seepage flow through the core, which is characterized by the development of pore water pressure in the part of the core below the seepage line and by seepage forces which cause additional deformations. Tanchev (2014) stated that distinguishing a clear boundary between the state following the first filling of the reservoir and the state of established stationary seepage flow is very difficult, and in practice, the process of seepage begins with the commencement of the raising of the water level.

The increase of water in the reservoir in the numerical approach should be simulated gradually in several increments (Tanchev, 2014), and for each increment the water should be raised up applying the corresponding hydrostatic pressure on both the upstream face and the upstream foundation of the dam and hydraulic boundary condition as permeable on the upstream face of the dam and as impermeable on the upstream face of the core.

Therefore, the factors affecting the deformation behaviour of a zoned dam during first impoundment are essentially the water load, the compressibility properties of the core material and the rockfill upstream shoulder and the susceptibility to collapse compression on wetting of the upstream rockfill zone. This latter aspect will be discussed more in detail in section 2.4.5.

2.4.4 Simplified method of interpreting settlement measurements

The monitoring of embankment dams is necessary to characterize the mechanical behaviour of the dam during construction and reservoir impounding. Representative measurements such as displacements, stress, strain and pore pressure are very helpful to understand the mechanical behaviour through the back-analysis of embankment dam. Several authors (e.g. Pagano et al. 1998) used measurements of vertical settlements in embankment dams in order to assess the in situ deformability properties exhibited by construction materials and to verify whether the observed mechanical behaviour was consistent with that predicted during the design stage. This verification procedure can be performed using numerical analysis or simple interpretation of the measurements.

A simple procedure to interpret vertical settlement profiles is the “theoretical curve” by Marsal (1958), which defines the settlement profile $s(z)$ along the dam axis z as a parabola with the maximum at mid-height:

$$s(z) = \frac{\gamma}{D} z(H - z) \tag{2.2}$$

where γ is the unit weight and H is the dam height. D is the vertical stiffness and it can be obtained from the maximum settlement at mid-height s_{max}:

$$D = \frac{\gamma}{s_{max}} \frac{H^2}{4} \tag{2.3}$$

This curve was obtained considering the material as homogeneous and linearly elastic, but if a non-linear elastic behaviour is considered a symmetry of the parabolic shape relative to the maximum settlement is respected, because the shape of settlement profiles is not affected by the assuming material behaviour (Pagano et al., 1998).

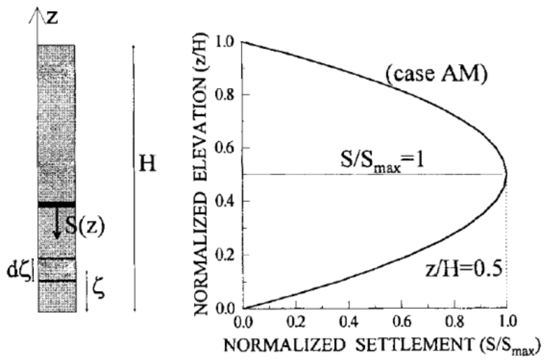

Figure 2.23 Vertical settlement profile for one-dimensional case and homogeneous fill (Pagano et al., 1998)

This type of one-dimensional approach does not account for the shape of dam's cross-section and does not consider geometrical effects, hence the real settlement profile could be really different. In fact, it was demonstrated that the measured vertical settlement profiles of embankment dams diverges from a parabola with the maximum at mid-height (Pagano et al., 1998). Naylor (1991) stated that the one-dimensional conditions are reliable enough to predict mechanical behaviour of a central part of a cross-section of large embankment dam, at least during the last construction stages. Although the limitations of the the one-dimensional approach, it could be helpful to model two or three-dimensional effects introducing artifices. Pagano et al. (1998) introduced some non-homogeneities in the one-dimensional condition to simulate geometrical effects, in order to facilitate the interpretation of results obtained from two-dimensional plane-strain analysis. A variation of confining stresses with elevation can be simulated by assuming the stiffness D to be a function of elevation ζ:

$$D = D_0 + \eta\, \zeta \qquad (2.4)$$

where D_0 is the stiffness at foundation level. If the stiffness D increases along the elevation ($\eta > 0$), the maximum settlement is located below mid-height (Case DM Fig. 2.24a: Down Mid-height), if D decreases along the elevation ($\eta < 0$), the maximum moves above mid-height (Case UM Fig. 2.24a: Up Mid-height).

To simulate vertical stress variations due to load transfer, it is possible to consider the assumption that the unit weight γ varies along elevation ζ:

$$\gamma = \gamma_0 - \lambda\zeta \tag{2.5}$$

where γ_0 is the unit weight at foundation level.

Assuming the stiffness D constant along the elevation, the unit weight γ could decrease with ζ ($\lambda > 0$) and the maximum is located below mid-height (Case DM Fig. 2.24b: Down Mid-height), or the unit weight γ could increase with ζ ($\lambda < 0$) and the maximum moves above mid-height (Case UM Fig. 2.24b: Up Mid-height).

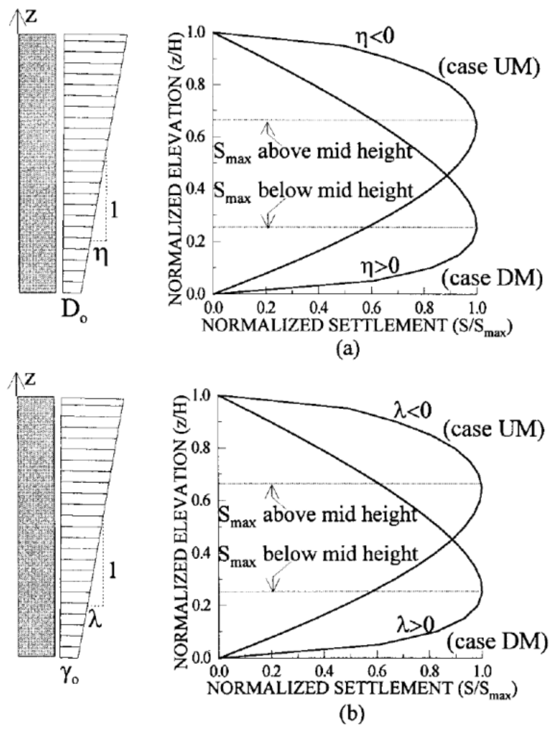

Figure 2.24 Vertical settlement profile for one-dimensional case and nonhomogeneous fill: (a) stiffness D varying along elevation and constant unit weight; (b) unit weight γ varying along elevation and constant stiffness (Pagano et al., 1998)

Pagano et al. (1998) also investigated the effects of changes in geometry and material properties in homogeneous fill dam and the effects of lack of confinement and arching in a zoned dam, through finite element analysis in plane-strain condition with linear elastic materials. For an ideal section of homogeneous earth dam (Fig. 2.25), they changed the geometry in terms of slopes (angle δ) and the material properties in terms of Poisson's ratio (ν) to understand how such as variations affect the vertical settlement distribution. The Young's modulus was not modified because it does not affect the shape of settlement profile but only the maximum value (Pagano et al., 1998). Fig. 2.25a shows that the maximum settlement elevation at the end of construction $(z_{Smax})_f$ moves up when the angle δ and the Poisson's ratio ν increase. The one-dimensional stiffness D can vary from a minim value D_{min}, which corresponds to unconfined conditions, to a maximum value D_{max}, which expresses oedometric conditions (Pagano et al., 1998). The ratio between D_{max} and D_{min} is close to unity until the Poisson's ratio ν becomes greater than 0.3, after that the ratio increases rapidly.

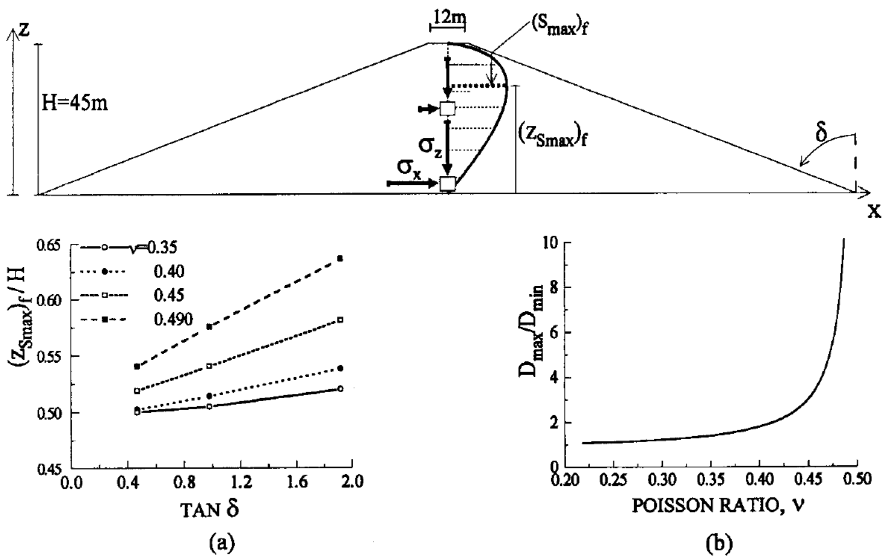

Figure 2.25 Effects of lateral slopes and conventional stiffness on maximum settlement elevation at the end of construction: (a) elevation of maximum settlement versus lateral slopes for different values of Poisson's ratio; (b) stiffness ratio versus Poisson's ratio (Pagano et al., 1998)

Pagano et al. (1998) indicated that the shape of settlements of central core zoned dams depends on different factors: (i) a reduction of conventional vertical stiffness D with elevation, caused by lateral confinement decrease; (ii) an increase of conventional vertical stiffness D with elevation, caused by arching; (iii) a reduction of vertical stress compared with the overburden pressure, caused by arching. The lack of lateral confinement and stress discharge moves the maximum settlement location in opposite directions, hence the maximum value likely occurs at mid-height (Pagano et al., 1998). They performed some numerical analysis to illustrate the influence of Young's modulus and of the thickness assigned to the core and shells on maximum settlement location. The value of Poisson's ratio was assumed equal to 0.3 to minimise effects related to lack of lateral confinement. In case the Young's modulus is the same for the core and the shells (homogeneous case) the maximum settlement occurs approximately at mid-height, while when the ratio (B_{core}/B_{shell}) between the thickness of the core and of the shell decreases or when the ratio (E_{shell}/E_{core}) between Young's moduli increases, as you can see in Fig. 2.26, the maximum settlement location moves downward due to arching.

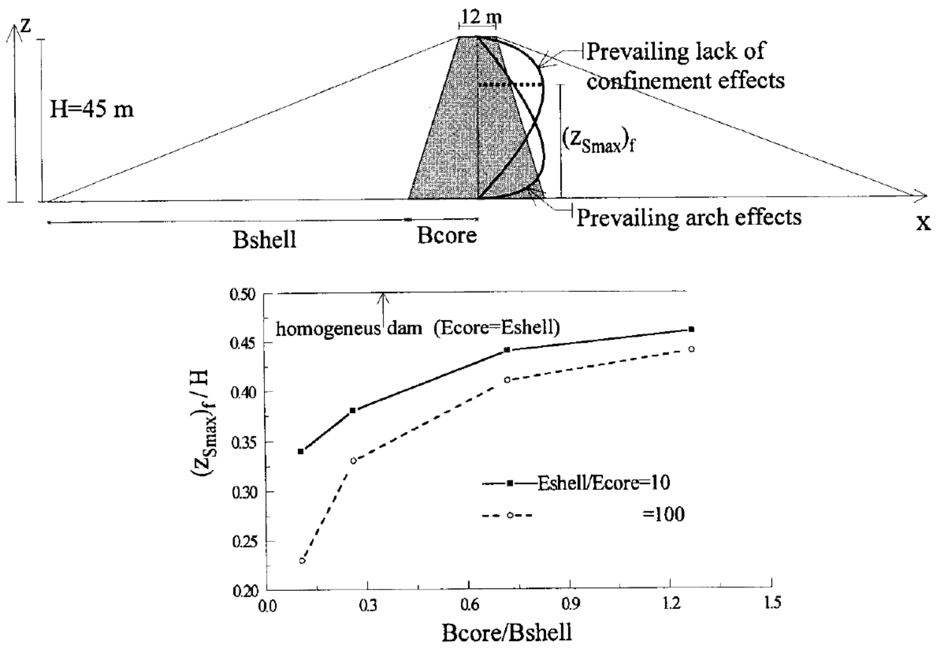

Figure 2.26 Effects of Young's moduli (Ecore/Eshell) and thickness ratio (Bcore/Bshell) on elevation of maximum settlement (Pagano et al., 1998)

Measurements from monitoring are therefore essential to understand the mechanical behaviour of embankment dams, especially during construction and reservoir impounding. A simple method (Marsal, 1958) to interpret the vertical settlement profiles is characterized by a one-dimensional approach and does not consider significant factors, such the shape of dam’s cross-section and geometrical effects. Pagano et al. (1998) simulated these two-dimensional effects considering a variation of confining stresses with elevation and a vertical stress variation due to load transfer, assuming for each case respectively, the stiffness and the unit weight as a function of elevation. Parametric numerical analyses of a homogeneous dam carried out by Pagano et al. (1998) show that the maximum settlement elevation at the end of construction, from the mid-height in one-dimensional conditions, moves up when the embankment slope decreases and the Poisson’s ratio increases. On the other hand, for a zoned dam the parametric numerical analyses indicate that when the ratio between the thickness of the core and of the shell decreases or when the ratio between Young's moduli increases, the maximum settlement location moves downward due to arching.

2.4.5 Collapse compression

The collapse compression of rockfill material is a consequence of reservoir impounding due to the softening of the saturated non-cohesive granular material in the upstream shell of zoned dams, which can lead to additional settlement, as mentioned in the preceding section. Hunter and Fell (2003) defined collapse compression or collapse settlement on wetting of embankment materials as an important factor in the deformation behaviour during first filling for a large number of embankments.

The effects of collapse compression are most noted for the upstream shoulder on initial impoundment, however, collapse compression has also been observed in the downstream shoulder following wetting due to rainfall, leakage or tail-water impoundment (Hunter & Fell, 2003). Evidence of collapse compression during first reservoir filling includes differential settlement across the dam crest with greater settlement of the upstream shoulder, crest spreading, and longitudinal crest cracking in some case studies. In most cases the amount of collapse compression and its effect on the overall deformation behaviour of the dam is rather limited, while in some cases it is very large (Tanchev, 2014).

Compaction results in the rearrangement of the granular particles or aggregates, and with the addition of water, the aggregates increase in volume and soften with the absorption of water to the clay particles, resulting in a volume change which depends on the pre-wetting dry density and stress state of the soil (Lawton et al., 1992). Alonso et al. (2013) highlighted that understanding the behaviour of compacted soils requires not only information on the as-compacted density and water content but also a proper consideration of microstructure, which controls the compressibility and collapse potential. Lawton et al. (1992) indicated the pre-wetting conditions of the soil as determinant factor of the collapse potential; they also found that collapse occurred in dams where the soils were compacted to relatively low dry densities and degrees of saturation, and that there is a critical degree of saturation above which negligible collapse occurs, the degree varies with overburden pressure and approximately follows the line of optimums found in Proctor compaction testing.

Hunter and Fell (2003) indicated factors that influence the susceptibility of a rockfill to collapse compression: the rock substance unconfined compressive strength and its reduction on saturation, moisture condition at placement (dry placed, water added or sluiced), degree of compaction, particle size distribution (coarser rockfills are potentially more susceptible) and applied stress levels prior to saturation. Case study and laboratory test data indicate that the potential for magnitude of collapse compression is: greater for dry-placed rockfills and for dumped rockfill, decreases with increasing compactive effort, and increases with increasing stress level (Nobari and Duncan, 1972a; Marsal, 1973; Alonso and Oldecop, 2000; Tanchev, 2014) (Hunter & Fell, 2003).

Two loading-wetting sequences have been used in the laboratory to study collapse compression. The more commonly used method consists of loading the compacted soil incrementally to a specific state of stress, allowing the sample to come to equilibrium under the applied stresses, and then providing the soil access to water, using laboratory tests as oedometer or triaxial test. The second load-wetting sequence is known as the double-oedometer procedure (Jennings and Knight, 1957), where two oedometer tests are performed using nominally identical samples, in one test the specimen remains at its compaction water content and in the other, the specimen, under a small seating load, is first inundated with water and allowed to come to moisture equilibrium (Lawton et al., 1992).

Results of dry and wet oedometer tests on rockfill samples are presented in Fig. 2.27, where the process that bring to collapse is shown: from a point of the compression curve for the initially dry material (1) water was added at constant stress state (3), obtaining the wet compression curve (4). Hunter and Fell (2003) stated that the collapse strain is equivalent to the difference in strain between the dry and wetted states at a given confining stress.

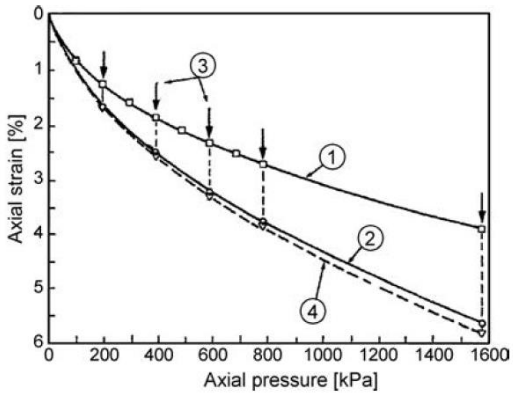

Figure 2.27 Compression curves for dry and wet states and collapse compression from the dry to wet state for gravel in the oedometer test (after Nobari & Duncan 1972a): (1) initially dry; (2) initially wet; (3) water added; (4) initially dry, then water added (Tanchev, 2014)

Several authors implemented the collapse compression of susceptible rockfills on wetting into modelling of embankment dams. Incorporating collapse compression into constitutive models adds further complexity and greater uncertainty in the estimation of material parameters between laboratory and field conditions due to the dependency of collapse compression on compaction moisture content, compacted density, applied stress conditions and material properties (Hunter & Fell, 2003). Justo (1991) and Naylor et al. (1989) proposed methods for incorporation of collapse compression of rockfill into constitutive models.

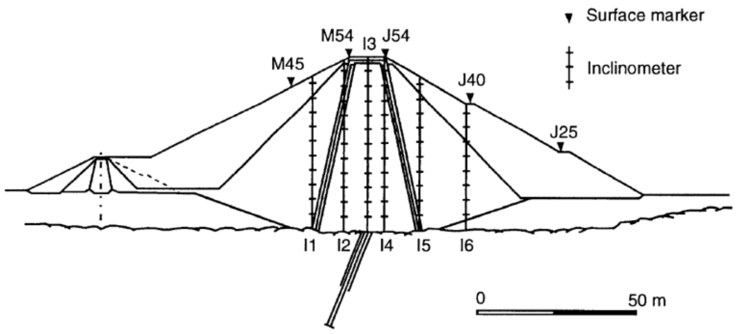

Figure 2.28 Section of Beliche dam with the positions of surface markers and inclinometers (Naylor, 1997)

Naylor (1997) during the back-analysis of the construction and reservoir filling of Beliche dam, introduced the effects of collapse settlements into an elasto-plastic critical state constitutive model through a procedure which is in the first instance a “material property change” analysis. It means that the response of the body of the dam is computed due to a change of the material properties between two chosen set of values: from a dry set to a wet set. In Fig. 2.28 a section of Beliche dam with the positions of inclinometers is shown. A reasonably good predictions of settlements in the centre of the dam was obtained by Naylor (1997) (Fig. 2.29), but the settlement on the crest and in the downstream part was underestimated (Fig. 2.30), which can be partly attributed to differences in relative density between that in the tests used for parameter determination and that in the dam, and to the effects of creep (Naylor, 1997).

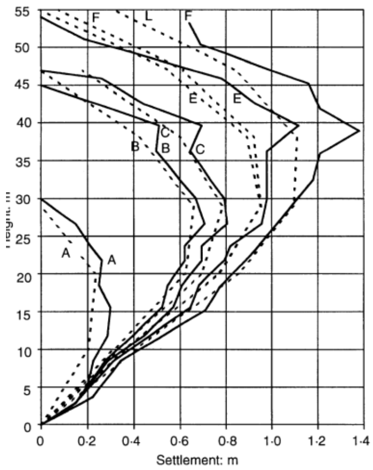

Figure 2.29 Vertical settlements at inclinometer I3 (full lines represent the measurements, broken lines represent the predictions) (Naylor, 1997)

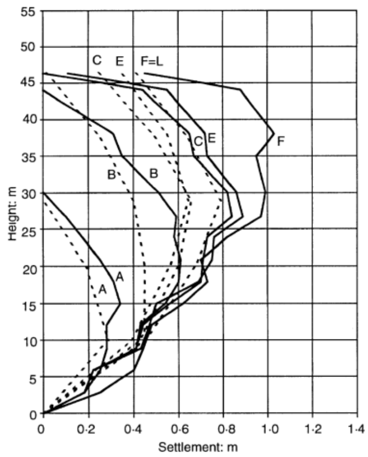

Figure 2.30 Vertical settlements at inclinometer I1 (full lines represent the measurements, broken lines represent the predictions) (Naylor, 1997)

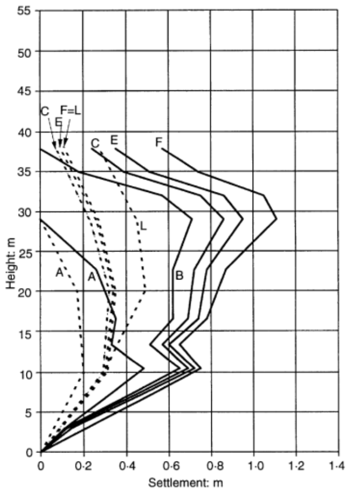

Figure 2.31 Vertical settlements at inclinometer I6 (full lines represent the measurements, broken lines represent the predictions) (Naylor, 1997)

The analysis of zoned earth dams has also been approached from the perspective of unsaturated soil mechanics. For instance, as Alonso et al. (2005) modelled the Beliche dam using two elasto-plastic constitutive models and considered the effect of development of strains as a consequence of suction or relative humidity changes. The question of the applicability of unsaturated soil analysis to rockfill behaviour was raised by Naylor et al. (1997), which not considered the effects of partial saturation in the Beliche dam analysis, because this effect is thought to be small in the rockfill. Alonso et al. (2005) explained their decision as probably due to the opinion that partial saturation has a small effect in the rockfill based on a capillary interpretation of suction effects in granular materials. In fact, approximate calculations of capillary induced stresses in rockfill and gravels (Alonso, 2003) indicate that their absolute values are extremely small, and therefore their reduction (due to wetting) may hardly affect gravel or rockfill behaviour. On the other side, introducing effects of partial saturation can lead to understand and reflect the dam behaviour under the effect of collapse compression (Alonso et al., 2005). Alonso et al. (2005) performed a coupled flow–deformation analysis of the history of construction, impoundment and the operational phase of Beliche Dam. The constitutive models for core and shells are different, in particular the shell model is capable of representing the effect that the compressibility of rockfill increases as the material is wetted, and the rockfill collapses, at constant confining stress, when the ambient relative humidity is increased (Alonso et al., 2005). In both types of materials, the role of suction or, alternatively, the prevailing relative humidity is a fundamental variable to explain the behaviour of the dam during construction, impounding and operation (Alonso et al., 2005). Alonso et al. (2005) defined a dam base case on the basis of the material parameters derived from the laboratory tests performed, whose numerical results are in agreement with measurements in the central core (Fig. 2.32b) and underestimate upstream (Fig. 2.32a) and downstream movements (2.32c). Despite the good agreement between predicted and observed vertical settlements, several reasons may be proposed to explain the discrepancies in the upstream and downstream shoulders, like the validity of scaled compacted samples and the uncertainty of the permeability value in the field.

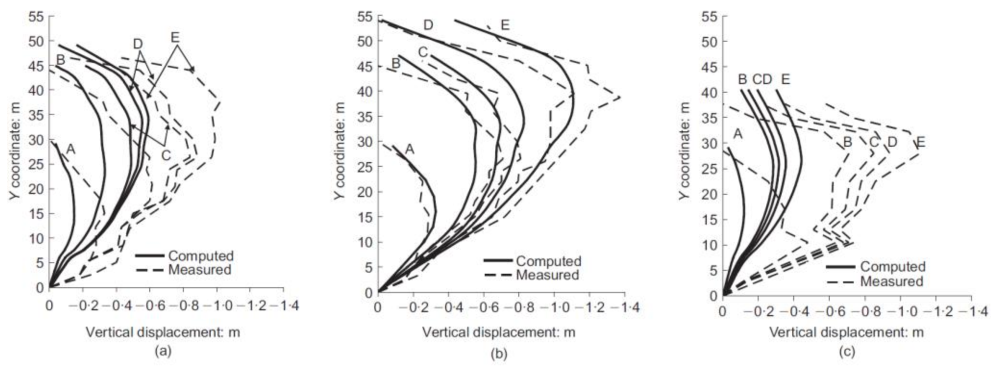

Figure 2.32 Calculated and measured vertical displacements at position of extensometers (a) I1, (b) I3 and (c) I6 during construction and impoundment for stages [A] to [E]: base case (Elevation 0 corresponds to bottom of clay core) (Alonso et al., 2005)

The mechanism of collapse compression is a result of adding water to the dry placed rockfill material and it appears in the upstream shell of zoned dams. The main influencing factors are: the moisture condition at placement, the degree of compaction, the particle size distribution and the stress levels prior to saturation. The potential collapse compression could be considered into constitutive models to carry out numerical analyses of zoned dams when the rockfill material of the shoulders is dry placed or dumped, low compacted and for high stress levels. The unsaturated soil analysis could be not considered because the effects are small in the rockfill material and also for the complexity of this type of analysis.

2.5 CONSTITUTIVE MODELS FOR EMBANKMENT DAM

The stress-strain relationship plays a key role to correctly represent the deformations of embankment dams during construction and impoundment. The classes of constitutive models useful for static geotechnical applications involve the elastic and the elasto-plastic models. The group of elastic models includes: (i) the linear isotropic elastic model, which defines the soil behaviour through two independent constants; (ii) the linear anisotropy elastic model, in which the characteristics of the stress-strain relationship depend on the direction; (iii) and the nonlinear elastic models, in which the material parameters vary with stress and strain levels (Potts & Zdravkovic, 1999). These elastic models are relativity simple, however they cannot capture many aspects of real soil behaviour, like the influence of the stress path and the presence of irreversible strains. Hence, they were extended with concepts of plastic yield, hardening and softening rules to develop the class of elasto-plastic models.

The elastic models can be employed when the soil is not stressed close to failure, but do not correctly model the undrained behaviour or problems where local failure occurs (Duncan, 1996). These stress-strain relationships sometimes cannot capture the deformation behaviour as well, for example when it needs to account for nonlinear behaviour and the variation of soil modulus with confining pressure. Kovacevic (1994) revealed the limitations of nonlinear elastic stress-strain relationships modelling the deformation of the face slab of concrete face rockfill dams during reservoir impoundment. During dam construction and impounding, a great variety of stress paths occurs, accompanied by a rotation of principal stresses, which cannot be accounted for by elastic constitutive models. In these cases, the constitutive models based on plasticity theory approximates better the real behaviour of the dam soils. Duncan (1996) indicated the difference between the two types of models is more evident at high stress levels, because plastic strains are heavily influenced by the stress history; an aspect which can be only modelled using elasto-plastic stress-strain relationships. Duncan (1996) suggests using elasto-plastic stress-strain relationships in undrained analysis in terms of effective stresses and marks the dependence of the accuracy of the analyses on predictions of the changes in pore pressures caused by changes in total stress. Naylor (1997) stated that the use of an elasto-plastic model is particularly appropriate for the post construction stages of the dam, since this class of model automatically provides the increased incremental stiffness, owing to the effective stress path moving from the yield surface into the elastic region during impounding.

The group of the elasto-plastic models could be divided in (i) elastic perfectly plastic, like the Tresca and Mohr-Coulomb models, and (ii) elastic strain hardening/softening plastic models. The use of hardening or softening rules and the development of the critical state models created a large improvement into describing the real soil behaviour. The introduction of the pre-peak plasticity is also included to model the dilatancy, the tendency of soils to change volume on sharing, with the advantage that plastic strains depend not only on the stress increment like elastic ones, but also on the accumulated stress (Potts & Zdravkovic, 2001). Both laboratory and field data suggest that dilatancy is unlikely to occur widely in rockfill dams, thus, the use of such models that account for the dilatancy alone is not enough to describe the deformation behaviour of embankment dams. Therefore, some elasto-plasticmodels were developed to take into account together the plastic deformations during consolidation, which are governed by crushing and yielding of interparticle contacts, and during shearing, which are developed also due to sliding and rolling. Hence, more complex elasto-plastic models emerged which combine the modelling of limited tensile capacity of soils, the hardening/softening plasticity theory and the presence of multiple yield and plastic potential surfaces which are simultaneously active. These types of constitutive models could be defined as the class of the advanced constitutive models. The last group includes elasto-plastic models with multi yield surfaces with isotropic hardening, like the double yield surface model (Lade, 1977), and with kinematic hardening, like the multi kinematic "bubble" models (Grammatikopoulou et al., 2006; Al-Tabbaa & Wood, 1989).

Kovacevic (1994) employed advanced elasto-plastic models of the critical state type to account for pre-peak plasticity of rockfill behaviour, demonstrating that they are more valuable to model the deformation behaviour under the stress path conditions imposed. The comparison of predicted and observed settlements of two studied dams proved the superior performance of the advanced elasto-plastic models (Kovacevic, 1994). Studies of Kovacevic (1994) and Kovacevic et al. (2008) reflect the superiority of this class of models to provide better prediction of stresses and strains in embankment dams. This class of models are not much used in practice because of the complexity and the great number of parameters, derived from laboratory tests like triaxial or oedometer tests. Laboratory tests are very difficult to be realized for rockfill materials due to the limitation of the tested material on the maximum particle size, which can lead to disagreement in material properties between the tested and the field soil (Hunter & Fell, 2003).

For the sake of conciseness, only a brief overview and the key aspects of the most common constitutive models employed in numerical analyses of embankment dams are presented below.

2.5.1 Linear elastic model

Though soils are far from being either linear or elastic (Potts & Zdravkovic, 2001), the isotropic linear elastic model was extensively employed in the past for numerical analyses of embankment dams for its inner simplicity (Clough and Woodward, 1967; Penman et al., 1971; Poulos et al., 1972; Cathie and Dungar, 1978; Penman and Charles, 1985; and others). The model is characterized by only two elastic parameters: a Young's modulus E, and a Poisson's ratio ν. The appropriate values of these two model parameters depend on confining pressure and deviator stress, hence, selecting the proper values is not straightforward. Thought the model was largely used in the past in the assessment of deformational behaviour of embankment dams, some difficulties have been found in deriving model parameters from available test data, and in producing displacement patterns which agree with field measurements (Kovacevic, 1994). The model could be used for low stress levels and small strains, conditions far from failure which usually prevail in rockfill dams. The elastic stress-strain models could be employed obtaining reasonably accurate displacements only when the stiffness between different embankment materials is not strongly different, like the case of stiff shell and soft core in a zoned dam (Duncan, 1996).

2.5.2 Non-linear elastic model

The non-linear elastic models are a good improvement from the simple linear elasticity, because the material parameters depend on stress and/or strain level. The main characteristics of three models widely employed in numerical modelling of embankment dams were briefly presented*: power law, K-G* and *hyperbolic* models.

2.5.2.1 Power law

The *power law* models were originally developed to fit the results of one-dimensional tests. The relation between volumetric strain ε_v and axial strain ε_a in one-dimensional test can be described by (Rowe, 1971):

$$\varepsilon_v = C\left(\frac{\sigma'_a}{Pa}\right)^D \tag{2.6}$$

Where Pa is the atmospheric pressure, C and D are dimensionless parameters. By differentiating the equation (2.6), the expression for the tangential Young's modulus E_t can be derived using the value of Poison's ratio ν estimated from theory of elasticity using the coefficient of lateral earth pressure at rest for normally consolidated soils K_0:

$$\nu = \frac{K_0}{1+K_0} \tag{2.7}$$

K_0 could be determined through the angle of sharing resistance ($K_0 = 1 - \sin\varphi'$) or directly from one-dimensional test ($K_0 = \sigma'_r/\sigma'_a$). Three model parameters are required to represent loading condition when K_0 is considered constant.

2.5.2.2 K - G

The *K-G* model is an extension of the bi-linear model and describes the soil behaviour using *K* and *G* moduli, instead of employing E and ν. The tangential bulk K_t and shear G_t moduli can be defined in terms of invariants (Potts et al., 2001):

$$K_t = K_{t0} + \alpha_k p' \tag{2.8}$$

$$G_t = G_{t0} + \alpha_G p' + \beta_G J \tag{2.9}$$

Where $K_{t0}, \alpha_k, G_{t0}, \alpha_G$ and β_G are the required five model parameters which should be derived to fit the available soil data. The values of cohesion c' and angle of sharing resistance φ' are therefore used when determining the values of the five model parameters (Potts et al., 2001).

2.5.2.3 Hyperbolic

The *hyperbolic model* is based on a hyperbolic function which approximates the strain-stress curve in a conventional triaxial tests (Potts et al., 2001). The original model was attributed to Kondner (1963), however, it was extensively developed by Duncan and Chang (1970). The original model was based on the following hyperbolic equation:

$$(\sigma_1 - \sigma_3) = \frac{\varepsilon}{a + b\varepsilon} \tag{2.10}$$

Where σ_1 and σ_3 are the major and minor principal stresses, ε the axial strain and a and b are material constants. Differentiating Equation (2.10), the variation of the tangent Young's modulus E_t with stress level $(\sigma_1 - \sigma_3)$ can be obtained. Using a Mohr-Coulomb failure criterion, the following expression for the tangent Young's modulus can be derived:

$$E_t = \left[1 - \frac{R_f(1 - \sin\varphi\prime)(\sigma_1' - \sigma_3')}{2c\prime\cos\varphi\prime + 2\sigma_3'\sin\varphi\prime}\right]^2 M_l Pa \left(\frac{\sigma_3'}{Pa}\right)^n \tag{2.11}$$

where R_f is the failure ratio with a value always less than unity, Pa is the atmospheric pressure, M_l is a modulus number and n is an exponent determining the rate of variation of the initial tangential modulus E_t with confining stress σ_3'. Duncan (1980) modelled the volume change behaviour of soils by an exponential relationship between the bulk tangent modulus K_t and the confining pressure σ_3', instead of using the tangent Poisson's ratio ν_t:

$$K_t = M_B Pa \left(\frac{\sigma_3'}{Pa}\right)^m \tag{2.12}$$

where M_B and m are dimensionless parameters. Seven parameters are necessary to characterize the model. The hyperbolic elastic relationship was widely employed to simulate the construction and impoundment of embankment dams (Chang and Duncan, 1970; Nobari and Duncan, 1972b; Cathie and Dungar, 1978; and many others). When the materials are not stressed to failure, linear elastic models are generally not suitable for accurate modelling of deformation behaviour due to the non-linear stress-strain relationship of earthfill and rockfill, and the use hyperbolic elastic models provide improved predictions of deformation (Hunter & Fell, 2003). Nevertheless, the hyperbolic elastic model has the limitation that the model parameters are typically derived from triaxial compression or oedometer laboratory tests and are therefore limited by the narrow range of stress paths covered in comparison to the broader range of stress paths imposed in the field (Hunter & Fell, 2003). The finite-element analysis of New Melones Dam, a 190.5 m high dam completely constructed in 1978 and characterized by compacted rockfill shells and an impervious clay core, was carried out by Duncan (1996). A finite-element mesh for New Melones Dam is represented in Fig. 2.33. The results, obtained using hyperbolic stress-strain relationships, show that nonlinear elastic analyses are not capable of representing volume changes caused by changes in shear stress, and they do not reflect the influences of stress path in the same way that an elasto-plastic stress-strain relationship would (Duncan, 1996).

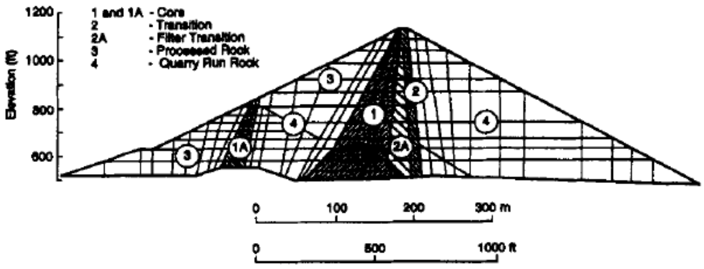

Figure 2.33 A finite-element mesh for New Melones Dam (Duncan, 1996)

2.5.3 Perfectly plastic model

The elastic perfectly plastic models include the Tresca and Von Mises models to describe the undrained behaviour in terms of total stresses, and the Mohr-Coulomb and Drucker-Prager to simulate the soil behaviour in terms of effective stresses.

2.5.3.1 Mohr-Coulomb

The Mohr-Coulomb model was extensively used in the past to analyse embankment dams for the simplicity and for the few model parameters to be characterized. Results of laboratory test plotted in terms of effective stresses show that in a certain stress range the tangent to the failure Mohr's circles, from several tests performed with different initial effective stresses, can be assumed to be straight and expressed by:

$$\tau_f = c' + \sigma'_{nf} \tan \varphi' \tag{2.13}$$

which represent the failure criterion and where c' and φ' are the cohesion and friction angle, τ_f and σ'_{nf} are the shear and normal effective stresses on the failure plane. This equation is often called the Mohr-Coulomb failure criterion and it can be rewritten in the principal stress space and adopted as a yield function:

$$F(\{\sigma'\},\{k\}) = \sigma'_1 - \sigma'_3 - 2c' \cos \varphi' - (\sigma'_1 + \sigma'_3) \sin \varphi' \tag{2.14}$$

For general stress state it is necessary to calculate all three principal stresses and determine the major σ'_3 and the minor σ'_1 values, however it is more convenient to rewrite Equation (2.14) in terms of stress invariants: p', which is the mean effective stress; J, which is deviatoric stress; θ, which is the Lode's angle.

$$p' = \frac{\sigma'_1 + \sigma'_2 + \sigma'_3}{3} \tag{2.15}$$

$$J = \frac{1}{\sqrt{6}} \sqrt{(\sigma'_1 - \sigma'_2)^2 + (\sigma'_2 - \sigma'_3)^2 + (\sigma'_3 - \sigma'_1)^2} \tag{2.16}$$

$$\theta = \tan^{-1} \left[\frac{1}{\sqrt{3}} \left(2 \frac{(\sigma'_2 - \sigma'_3)}{(\sigma'_1 - \sigma'_3)} - 1 \right) \right] \tag{2.17}$$

The Equation (2.14) can be replaced by the following relationship:

$$F(\{\sigma'\},\{k\}) = J - \left(\frac{c'}{\tan \varphi'} + p' \right) g(\theta) = 0 \tag{2.18}$$

$$g(\theta) = \frac{\sin \varphi'}{\cos \theta + \frac{\sin \theta \sin \varphi'}{\sqrt{3}}} \tag{2.19}$$

In Figure 2.34 the yield function plotted in the principal stress space is showed as an irregular hexagonal cone. The Mohr-Coulomb model is perfectly plastic and there is no hardening or softening law required, hence the state parameter $\{k\} = \{c', \varphi'\}^T$ is constant and independent of plastic strain or plastic work (Potts & Zdravkovic, 1999).

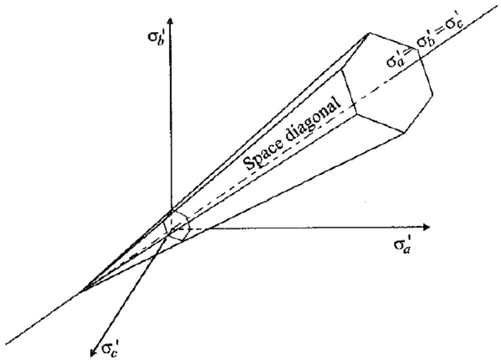

Figure 2.34 Mohr-Coulomb yield surface in principal stress space (Potts & Zdravkovic, 1999)

The problems of this approach are: (i) the magnitude of the plastic volumetric strain (dilation) is much larger than that observed in real soils; (ii) once the soil yields, it will dilate forever, while real soil dilates initially on meeting the failure surface and reaches a constant volume condition at large strains (Potts & Zdravkovic, 1999). The first problem could be solved assuming a non-associated flow rule, assuming a plastic potential function characterized by a similar form to the yield function where the friction angle φ' is replaced by a dilatation angle ψ obtaining the following relation:

$$G(\{\sigma'\},\{m\}) = J - \left(a_{pp} + p'\right) g_{pp}(\theta) = 0 \tag{2.20}$$

$$g_{pp}(\theta) = \frac{\sin\psi}{\cos\theta + \frac{\sin\theta \sin\psi}{\sqrt{3}}} \tag{2.21}$$

where a_{pp} is the distant of the apex of the plastic potential cone from the origin of principal effective stress space (see Fig. 2.35):

$$a_{pp} = \left(\frac{c'}{\tan\varphi'} + p'_c\right)\frac{g(\theta_c)}{g_{pp}(\theta_c)} - p'_c \tag{2.22}$$

where p'_c, θ_c are the stress invariants at the current state of stress, which assumed to be on the yield surface. The model requires 5 parameters: c', φ', ψ, E, ν.

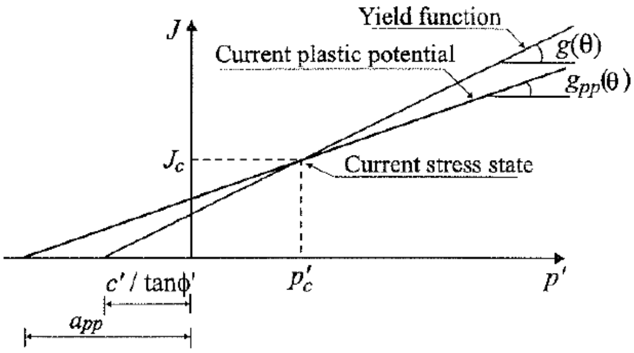

Figure 2.35 Relationship between the yield and plastic potential function (Potts & Zdravkovic, 1999)

Although the use of a non-associated flow rule enables the magnitude of the incremental plastic volumetric strain to be restricted, the model still predicts increasing volumetric strains, no matter how far the soil is sheared, producing unrealistic predictions in some conditions (Potts & Zdravkovic, 1999). The Mohr-Coulomb model could be improved using strain hardening or softening laws, varying the strength parameters with the accumulated plastic strains.

2.5.4 Hardening/softening plasticity model

The strain hardening or softening plasticity is an improved development of soil constitutive modelling. The Cam Clay (Roscoe et al., 1958) and the Modified Cam Clay (Roscoe and Burland, 1968) models were developed at the University of Cambridge for triaxial loading conditions of normally consolidated or lightly over-consolidated clay. Developed in the context of the critical state formulation, they are characterized by an isotropic hardening or softening and an associated flow rule which brings to the limitation of not predicting a peak in the deviatoric stress before the critical state is approached (Ti et al., 2009). The critical state models cannot also predict the observed softening and dilatancy of dense sands and the undrained response of very loose sands (Ti et al., 2009). These limitations were overcome by introducing elasto-plastic models with multiple yield and plastic potential surfaces.

2.5.4.1 Double yield surfaces

Including modelling of limited tensile capacity of soils, non-linear elastic stress-strain relationships and double yield surfaces with different plastic potential functions bring to a new class of models extensively employed in numerical analyses of embankment dams. The most common models of this class are the Lade's double hardening (Sect. 4.3), the Hardening Soil and the Cysoil (Sect. 3.3) models. The main feature is the presence of a non-linear elastic domain closed by two intersecting yield surfaces, generally a cap and a deviatoric surfaces (see Fig. 2.36 for Cysoil model as example) which isotropically harden or soften. There is a failure criterion, which could be the Mohr-Coulomb criterion, such for Hardening Soil and Cysoil models. An associated flow rule for the cap and a non-associated flow rule for the deviatoric surface are considered. The models take into account with the cap hardening the plastic deformations during consolidation, which are governed by crushing and yielding of interparticle contacts, and with the deviatoric hardening the irreversible strains during shearing, which are developed due to deviatoric loading and also due to sliding and rolling. They can account for the stress path dependency, the plasticity effect of grain crushing and rearrangement, shear-induced volume changes and the decrease in stiffness accompanied by irreversible deformation when the soil is subjected to deviatoric loading. The determination of the models parameters is based on the results of isotropic compression or one-dimensional tests and of triaxial tests.

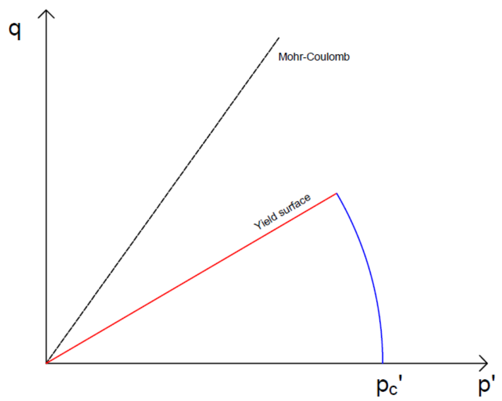

Figure 2.36 Double yield surfaces of the Cysoil Model: deviatoric yield surface (red) and the elliptical cap (blue)

2.6 NUMERICAL ANALYSIS OF EMBANKMENT DAMS

Several numerical analyses of embankment dams have been performed over the years, some of which are focused on deformation behaviour of zoned or rockfill dams during construction and reservoir impounding. The literature review highlighted the relevance of simulating construction aspects, such as construction by layers, the value of the appropriate choice of constitutive models, dependent on the purpose, and the agreement between real and simulated soil behaviour obtained employing elasto-plastic constitutive models. Duncan (1996), Kovacevic (1994) and Kovacevic et al. (2008; 2011; 2013) dealt widely with numerical analysis of the deformation behaviour of embankment dams, especially zoned and rockfill ones. They discussed the methods of analysis, their limitations, available constitutive models of stress-strain relationship and areas of uncertainty (Hunter & Fell, 2003). They highlighted the importance of simulating dam construction or excavation adding or removing layers, and the critical role of stress-strain relationships. Duncan (1996) indicated that the analysis should simulate as closely as possible the actual construction or loading sequence of the problem being analysed, adding elements to simulate fill placement, removing elements to simulate excavation, and applying loads in increments. Kovacevic (1994) pointed out that embankment dams should be built up in relatively thin horizontal layers. For the choice of stress-strain relationship, Duncan (1996) stated that selecting an appropriate soil stress-strain relationship is primarily involved with balancing simplicity and accuracy, the type of relationship suitable for a given case depends on the conditions being analysed and the purpose of the analysis. Kovacevic (1994) commented that to achieve reasonable accurate and useful predictions of stresses and deformations of rockfill dams, the rockfill stress-strain behaviour has to be represented by an appropriate constitutive law.

2.6.1 Numerical analyses with advanced constitutive models

Kovacevic (1994) and Kovacevic et al. (2008) examined the deformational behaviour of rockfill and zoned dams, and demonstrated the relevance of the use of adequate constitutive laws and, in particular, the importance of modelling the plastic behaviour of embankment fills during loading, unloading and re-loading (Kovacevic et al., 2008). They analysed and modelled some embankment dams constructed in the UK with advanced elasto-plastic constitutive models, simulating different phases as embankment construction, first reservoir impounding, subsequent reservoir operation and raising the crest level. The numerical results were compared with field measurements in terms of vertical and horizontal displacements within the dam body and settlements of the upstream membrane of rockfill dams. The numerical analyses were carried out with the computer code ICFEP (Potts & Zdravkovic, 1999) in plane strain, using eight noded isoparametric quadrilateral elements with 2x2 integration and a modified Newton-Raphson scheme, with an error controlled substepping algorithm. Two elasto-plastic models of Lade, one having a double (Lade, 1977) and the other one having a single yield surface (Kim and Lade, 1988; Lade and Kim, 1988a, 1988b), were implemented into ICFEP by Kovacevic (1994) to model the pre-peak plastic behaviour of rockfills. These models were originally developed for cohesionless soils (Lade, 1977), but because the observed compression curves for compacted fills have a similar trend to that of sands, it is possible to employ them for compacted fills as well. The models are based on concepts from non-linear elasticity and isotropic work-hardening plasticity theories, and both models are applicable to general three-dimensional stress conditions, while input parameters can be derived entirely from the results of standard laboratory tests (Kovacevic, 1994). They are employed in the finite element analyses of rockfill dams with an upstream asphaltic concrete membrane (Kovacevic, 1994) and of puddle core zoned dams (Kovacevic et al. 2008). These two models are called Lade’s single hardening and double hardening models, with a single yield surface (Kim and Lade, 1988; Lade and Kim, 1988a, 1988b) and with two intersecting yield surfaces (Lade, 1977), respectively. The kinematic hardening “bubble” model (Grammatikopoulou et al., 2006; Al-Tabbaa & Wood, 1989) was also used by Kovacevic et al. (2008) in some finite element analyses, where the Lade’s models seem to be not enough to describe the observed behaviour of the dams. The formulation of the models can be referred to the respective references, although the Lade’s double hardening model is described in the Sect. 4.3 of this thesis.

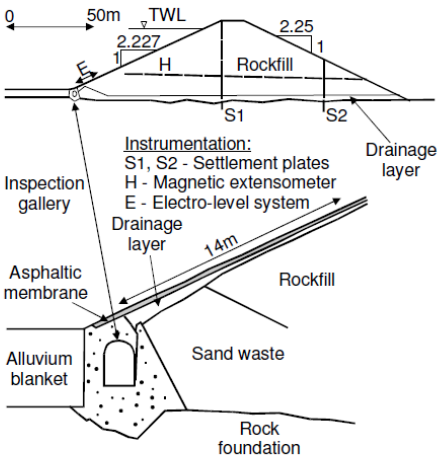

Figure 2.37 Cross-section of Roadford dam (Kovacevic et al., 2008)

Roadford Dam is a homogeneous 41m high rockfill dam (Fig. 2.37) in Devon completed in 1990. The dam is characterized by a layer of a less compressible sand-waste fill, in order to reduce differential movements between the asphaltic membrane and the stiff concrete block at the upstream toe. The analysis of Roadford dam was carried out considering three different constitutive models: a non-linear elastic perfectly plastic model of the Mohr-Coulomb type, which only accounts for the plastic behaviour when the peak strength is mobilised, and the two Lade's elasto-plastic constitutive models, both of which account for the plastic behaviour before and after the peak strength of the rockfill is mobilised. The model’s parameters for the rockfill fills were evaluated through laboratory tests, both large oedometer (d = 1 m) and triaxial (d = 250 mm) tests on the low grade rockfill which was used for the dam construction (Kovacevic, 1994). The models parameters were derived in a deterministic way and it was shown that they are capable of reproducing the full range of the observed rockfill behaviour in the available laboratory tests (Kovacevic, 1994). Numerical results obtained with all the three models show a good fit to the available test data, but the results achieved with the two Lade’s models are more appropriate (Fig. 2.38).

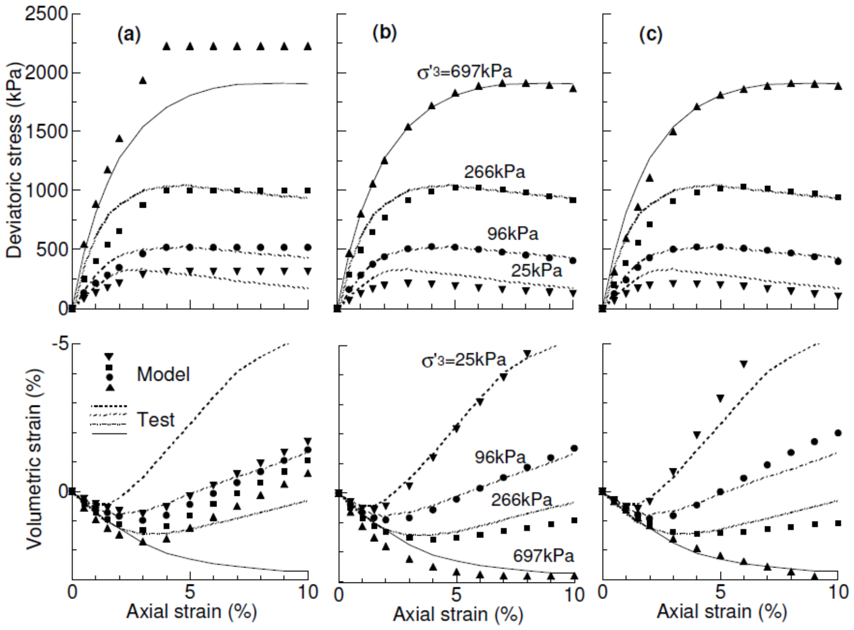

Figure 2.38 Predicted and measured behaviour in triaxial tests for Roadford Dam by (a) nonlinear elastic Mohr Coulomb model and (b) & (c) Lade’s elasto-plastic models (Kovacevic et al., 2008)

The observed and predicted settlements of the dam during construction along the vertical lines S1 and S2 (shown in Fig. 2.37) are presented in Fig. 2.39a, while measured and calculated lateral movements along the extensometer H (see Fig. 2.37) are shown in Fig. 2.39b. The predictions using both Lade's models are in reasonable agreement with the field data, while results from a nonlinear elastic Mohr Coulomb model overestimate both the settlements and the lateral movements during construction. The predictions could be improved by adjusting the non-linear elastic model parameters, but it could not fit the triaxial test results (Kovacevic et al., 2008). The likely cause for the difference between the above predictions is the ability of the Lade’s models to account for the plastic strains pre-peak, which are qualitatively quite different from the elastic strains predicted by the non-linear elastic model (Kovacevic et al., 2008).

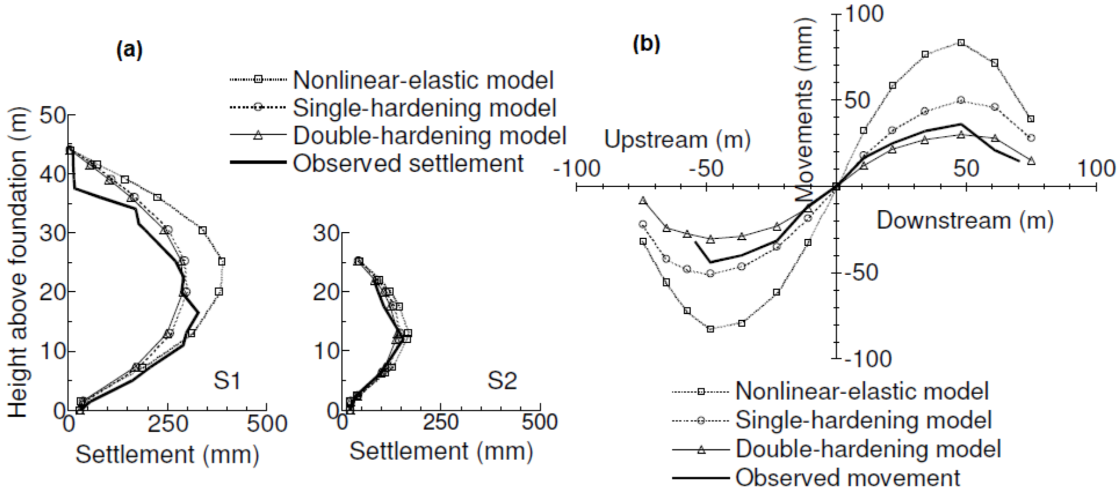

Figure 2.39 Predicted and observed settlements of Roadford dam during construction: (a) vertical and (b) lateral (Kovacevic et al., 2008)

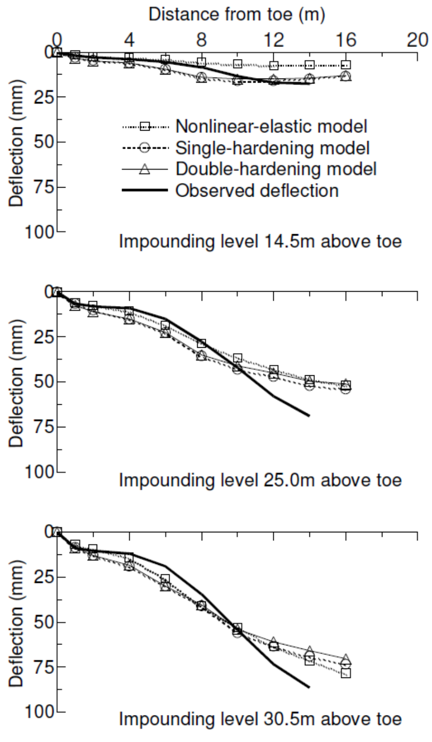

Figure 2.40 Predicted and observed deflections of asphaltic concrete membrane of Roadford dam during first impounding (Kovacevic et al., 2008)

Comparison of predictions and observed deflections of the asphaltic concrete membrane of Roadford dam at three reservoir impounding levels (Fig. 2.40) indicate that the Mohr Coulomb model underestimates the membrane deflections during the initial stages of reservoir impounding (Kovacevic, 1994). Considering only the two Lade's elasto-plastic constitutive models, it was shown by Kovacevic (1994) that the double hardening model is more suitable for the use in the finite element analyses of rockfill dams than the single hardening model, because the former is more sensitive to the changes in stress path directions which occur during reservoir impounding particularly at lower stress levels, which typically characterize rockfill dams. Unfortunately, the double hardening model is more complex and it needs more input parameters to be characterized than the single-hardening one.

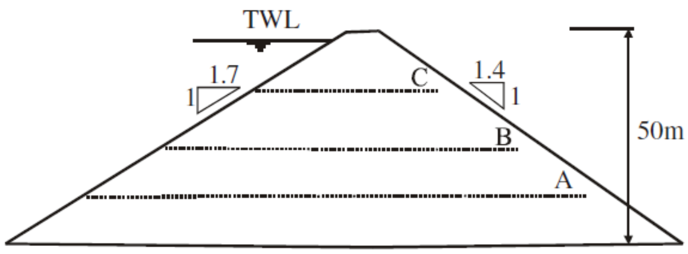

Figure 2.41 Cross-section of Winscar Dam (Kovacevic et al., 2008)

The Winscar dam is a 53m high rockfill dam and was the first dam in the UK to use an upstream asphaltic concrete membrane as the watertight element (Kovacevic et al., 2008). Three horizontal plate gauges were installed in the 50m high section of the dam during construction at positions A, B and C as indicated in Figure 2.41, hence the dam's performance during construction and subsequent impounding was monitored (Kovacevic, 1994). Large diameter oedometer and triaxial tests on rockfill fill were carried out. The Winscar dam was modelled by Kovacevic (1994) and Kovacevic et al. (2008) using the finite element approach and the Lade's double-hardening and single-hardening models for the sandstone rockfll. The predicted and observed movements at the end of construction are presented in Fig. 2.42. The comparison also includes an earlier numerical prediction performed by Penman & Charles (1985) using a linear elastic model and a second prediction obtained using the Lade's double-hardening elasto-plastic model. The results of the analysis with the single hardening model are very similar to those obtained with the double-hardening one, therefore, this prediction is omitted in Figure 2.42 (Kovacevic, 1994; Kovacevic et al. 2008). The finite element analyses using both linear elastic and elasto-plastic constitutive models underestimated the dam movements during construction, particularly at the higher dam elevations where the large observed settlements may well be due to creep in the sandstone rockfill (Penman & Charles, 1985).

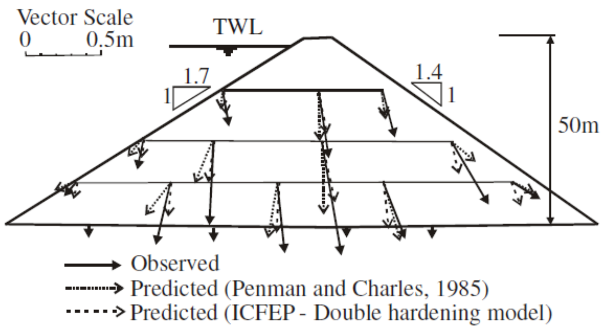

Figure 2.42 Comparison of predicted and observed movements during construction of Winscar Dam (Kovacevic et al., 2008)

Fig. 2.43 shows the comparison of the predicted and observed deflections of the upstream membrane during reservoir impounding, in particular, in Fig. 2.43a the prediction made by Penman & Charles (1985) and in Fig. 2.43b that obtained by Kovacevic (1994). Penman & Charles (1975) significantly overestimated the membrane movements, for this reason, subsequently they modified the employed model parameters to simulate the stress changes during reservoir impounding more closely and, as a result, smaller and more realistic membrane movements were obtained (Penman & Charles, 1985). The modified parameters, however, could not recover the observed movements during dam construction any longer (Kovacevic et al., 2008). The finite element analyses of Winscar dam with both Lade's constitutive models have confirmed their good performance, because reasonable dam movements were predicted during both construction and reservoir impounding without adjusting the input parameters derived from the available large laboratory test data. Furthermore, it was demonstrated that Lade's models are capable of predicting a pattern of membrane movement during reservoir impounding, although the Lade's models cannot predict with accuracy the rockfill response during large stress reversals which take place in the upstream toe area of a dam for the higher levels of reservoir impounding (Kovacevic, 1994).

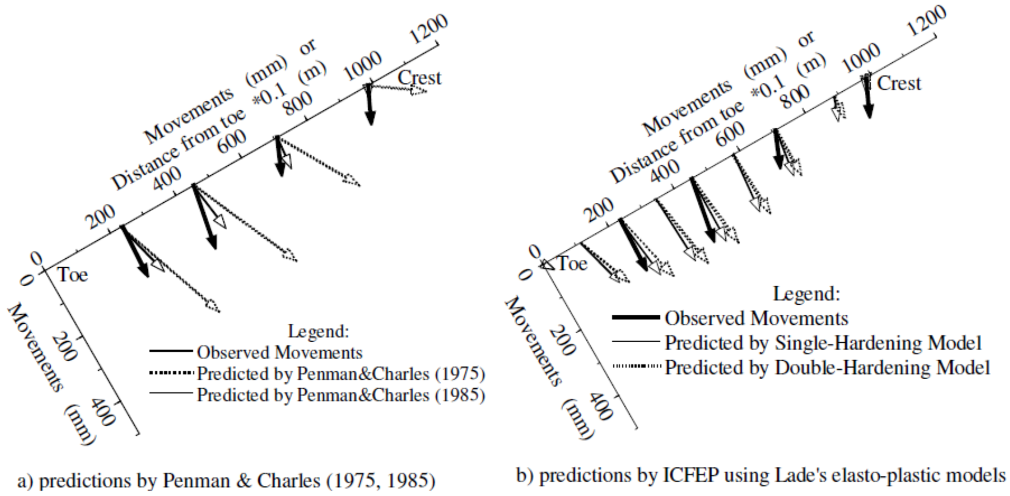

Figure 2.43 Predicted and observed movements of upstream membrane during reservoir impounding of Winscar Dam (Kovacevic et al., 2008)

Several old embankment dams with narrow central cores of puddle clay were built in the U.K. since the early 19th century and detailed inspections showed that they developed significant crest settlements, which could not be accounted for by standard creep theories (Kovacevic et al., 2008). Kovacevic et al. (1997; 2008) analysed a series of dams with puddle clay cores using Lade's single-hardening model and a kinematic hardening "bubble" model (Grammatikopoulou et al., 2006; Al-Tabbaa & Wood, 1989). In Fig. 2.44 the cross-sections of two analysed puddle clay core dams are presented.

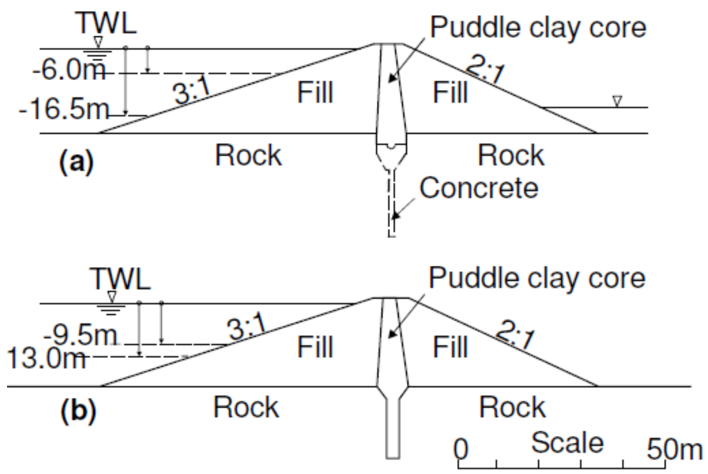

Figure 2.44 Cross-sections of (a) Ramsden and (b) Walshaw Dean Lower Dam (Kovacevic et al., 2008)

The 25m high Ramsden Dam is an old embankment dam with a central puddle clay core and a concrete filled cut-off trench (Fig. 2.44a). The previous success of using Lade's elasto-plastic models in predicting the behaviour of rockfill dams during construction and impoundment led Kovacevic et al. (2008) to analyse this old dam using the Lade's single-hardening model. In Fig. 2.45a the results of cyclic loading in an oedometer test on the dam shoulder fill are shown. In order to account for the observed permanent deformation after each operational cycle of drawdown and re-impounding, the non-linear elastic moduli in the Lade's model during unloading were made stiffer than during reloading (Kovacevic et al., 2008). The predictions were in reasonable agreement with observations during two reservoir drawdowns during 1988 (Fig. 2.46a) and 1989 (Fig. 2.46b), but the results showed a tendency for the predicted permanent displacements to be towards upstream, rather than downstream as the observations suggest (Kovacevic et al., 2008). It was suspected that a part of the problem was in the inability of the Lades's elasto plastic models to account for the hysteretic behaviour during unloading/re-loading cycles (Fig. 2.45b), for this reason, a kinematic hardening 'bubble' model (Grammatikopoulou et al., 2006; Al-Tabbaa & Wood, 1989) was employed to account for this hysteretic behaviour in the oedometer test (Fig. 2.45c) (Kovacevic et al., 2008).

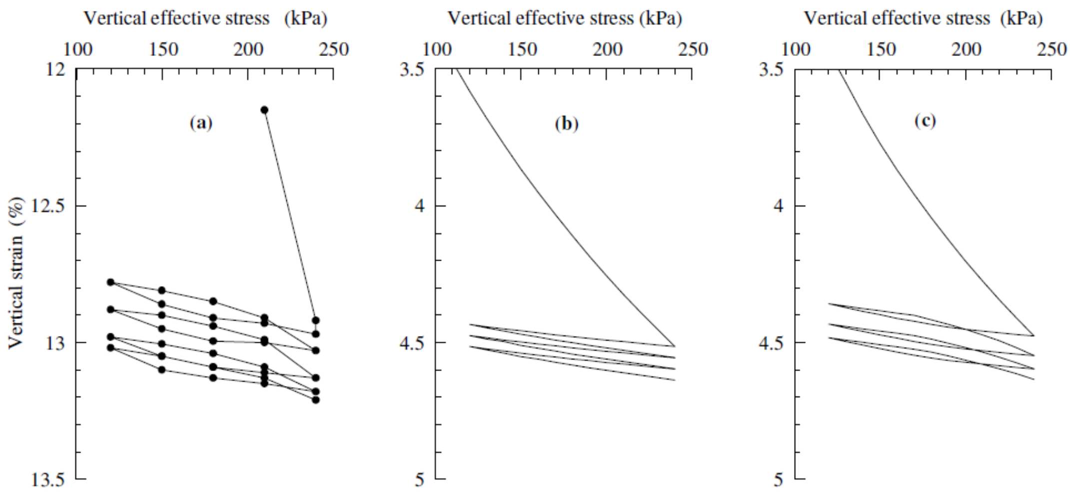

Figure 2.45 Behaviour of shoulder fill during cyclic loading in an oedometer test: (a) observed and predicted by (b) Lade's and (c) 'bubble' model (Kovacevic et al., 2008)

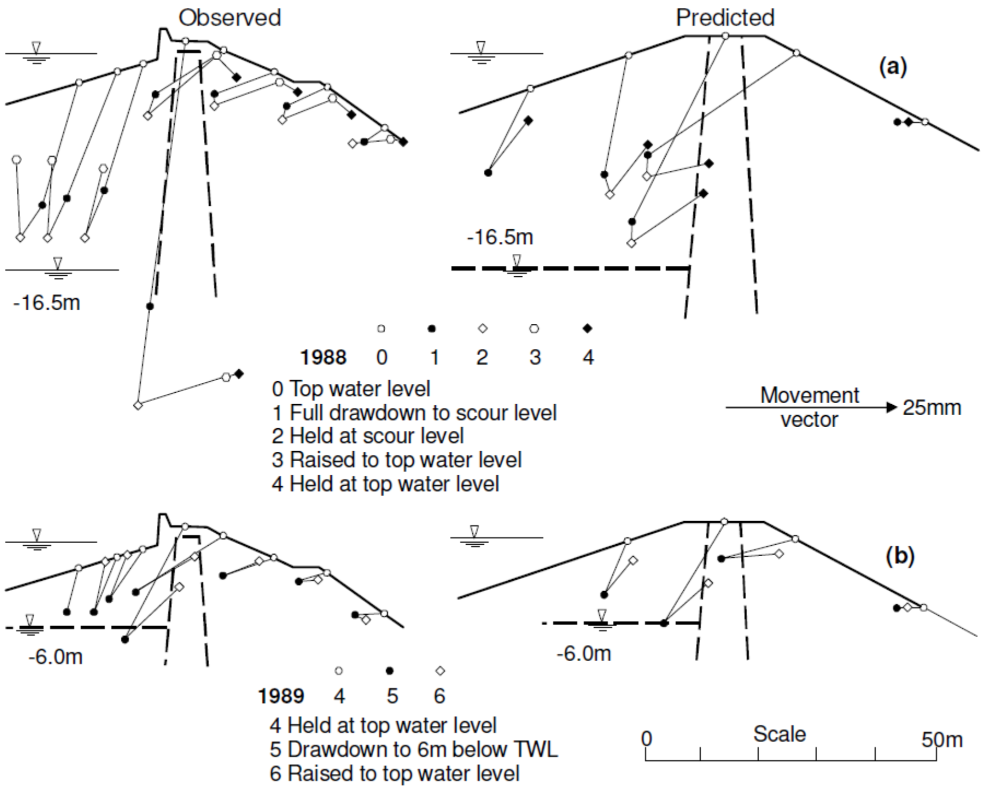

Figure 2.46 Observed and predicted behaviour of Ramsden Dam using Lade's single hardening model during (a) 1988 and (b) 1989 drawdowns (Kovacevic et al., 2008)

The Walshaw Dean Lower Dam is a 22 m high embankment dam with a narrow central puddle clay core and a 20m deep puddle clay filled cut-off trench (Fig. 2.44b). It was completed in West Yorkshire at the turn of the last century. The dam was analysed by Kovacevic et al. (2008) using both Lade's single hardening model and the kinematic hardening 'bubble' model (Grammatikopoulou et al., 2006; Al-Tabbaa & Wood, 1989) The results are presented in Fig. 2.47 compared with field measurements of horizontal and vertical displacements at the dam crest. Both models predicted well the observed settlements, but only the 'bubble' model successfully predicted the observed movements downstream, because the downstream movements seem a result of the plastic behaviour during unloading/re-loading loops which the Lade's model cannot account for (Kovacevic et al., 2008).

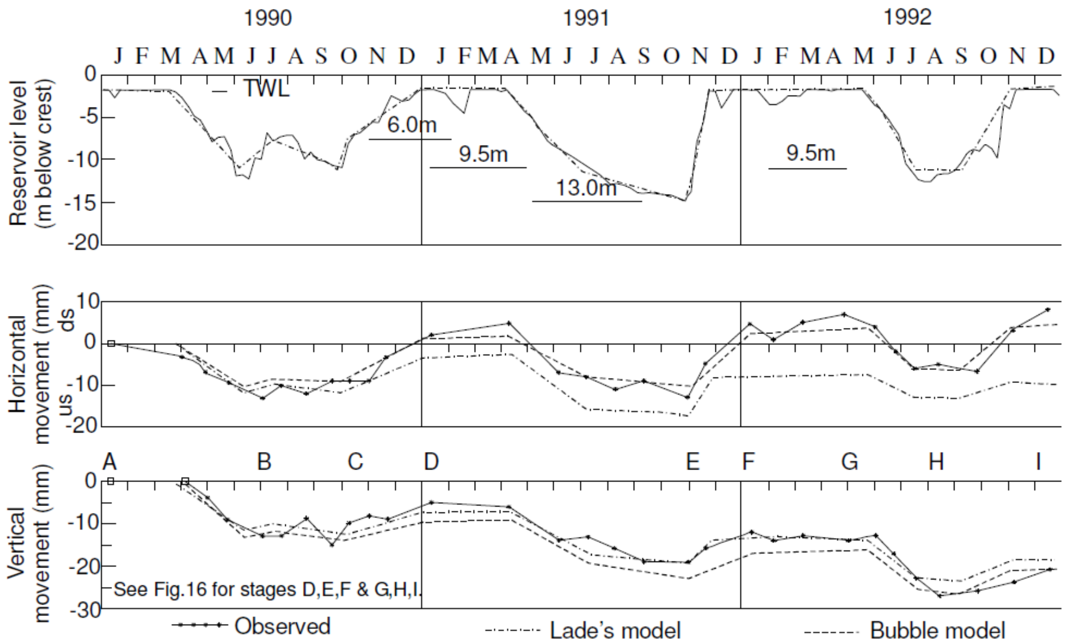

Figure 2.47 Observed and predicted displacements of the Walshaw Dean Lower Dam crest during three drawdowns (Kovacevic et al., 2008)

The Ladybower Dam is a 43m high dam built in Derbyshire during the Second World War and is characterized by a puddle clay core. During construction the dam settled significantly and it was decided to raise the dam by constructing new fill on the downstream shoulder (Fig. 2.48). Both the original dam and the reconstructed dam were analysed by Kovacevic et al. (2008) in order to provide an independent check on the cause of settlement for the original section, verified the stability of the reconstruction, and enabled a settlement prediction to be made for the modified section (Kovacevic et al., 2008).

Observed settlements and lateral displacements along the axis of the original dam are plotted against the level (height) of the new fill in Fig. 2.49 (Kovacevic et al., 2008). The observed movements only started to develop after 30m of fill had been placed. The prediction using the Lade's single hardening model overestimate the observed movements, while the 'bubble' model prediction was quite reasonable (Vaughan et al., 2004), proving that the 'bubble' model can be successfully used in characterising the behaviour of dams not only during operational cycles of draw-dawn and re-impounding but also crest raising (Kovacevic et al., 2008).

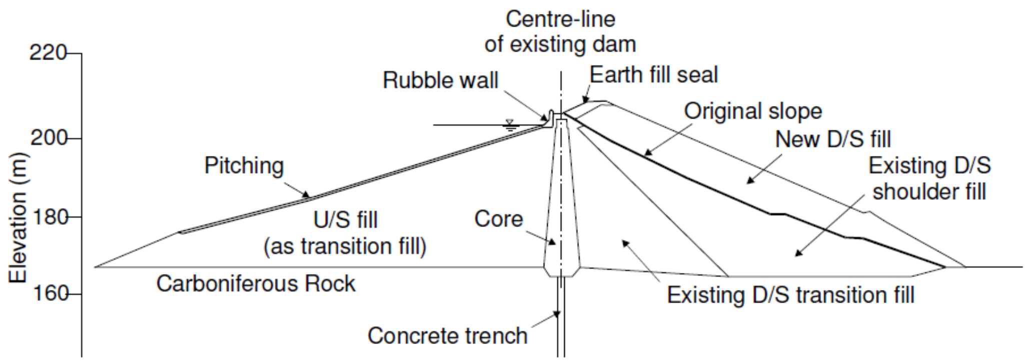

Figure 2.48 Typical cross-section of old and reconstructed Ladybower Dam (Kovacevic et al., 2008)

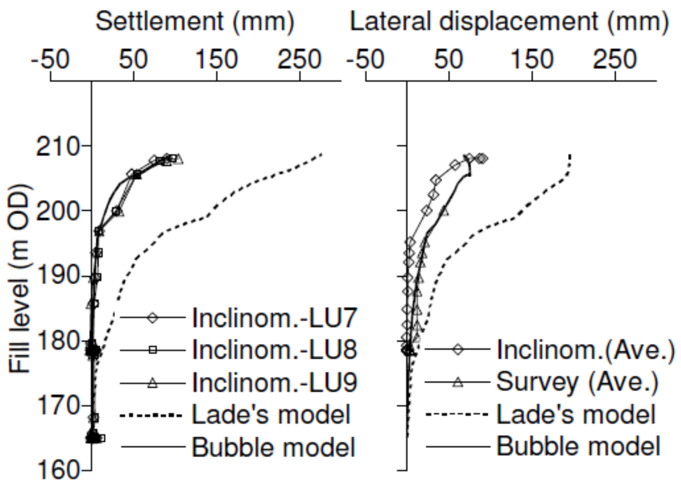

Figure 2.49 Observed and predicted (a) settlements and (b) lateral displacements of Ladybower Dam at original dam centerline (Kovacevic et al., 2008)

Pramthawee et al. (2011) performed numerical analyses with the finite element code ABAQUS of the construction phase of a concrete face rockfill dam with the hyperbolic elastic and the elasto-plastic hardening soil models, simulating the response of the rockfill dam realistically. The aim was to evaluate the efficiency of the elasto-plastic model with strain hardening to simulate the rockfill behaviour during construction. This model is well explained in Pramthawee et al. (2011) and it is based on the Mohr-Coulomb failure criterion with shear and volumetric hardening. The studied dam was constructed between 2006 and 2010 and is characterized by a height of 182.0 m. The results of the analyses were compared with the monitoring recordings, in terms of settlements (SG instrument in Figure 2.50) and horizontal displacements (PI instrument in Figure 2.50) for both constitutive models. It can be seen from Figure 2.50 that the predicted values from the elasto-plastic hardening soil model (HS) are in good agreement with measured data for the entire recorded elevations, while the predicted values from the hyperbolic elastic model (HB) overestimate the field data, especially for the horizontal displacements.

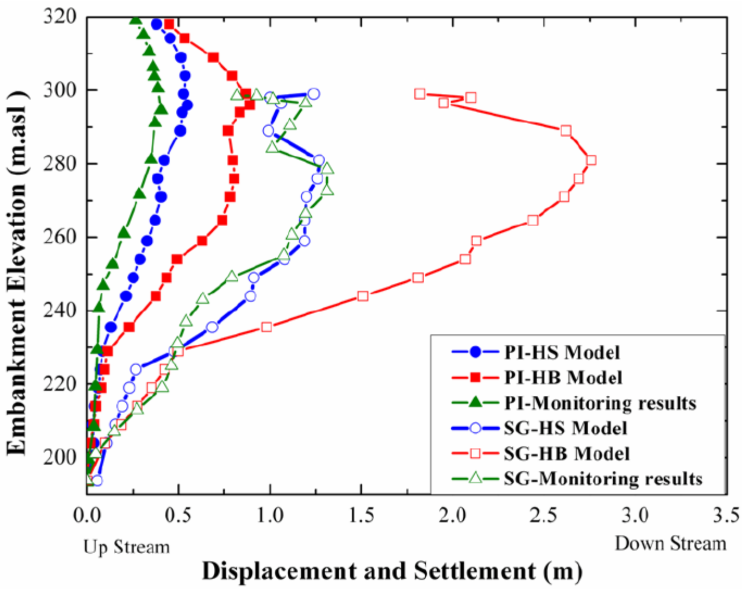

Figure 2.50 Settlements and horizontal displacement of rockfill varied level in embankment by SG and PI instruments sets, respectively (Pramthawee et al., 2011)

Tschernutter et al. (2011) analysed an existing embankment dam with a central concrete water barrier after heightening of the dam, with the Hardening soil constitutive model implemented in PLAXIS 2D. The Bockhartsee Dam is a 50 m high rockfill dam with a 60 cm thick central concrete membrane (diaphragm wall) as water barrier, constructed in the years between 1980 and 1982. It was heightened during 2006 and 2007 by placing an angular retaining wall on top of the existing dam crest downstream of the existing concrete membrane (Fig. 2.51) (Tschernutter et al., 2011). The numerical analyses were performed assuming 2-D plane strain conditions with the finite element code PLAXIS 2D using Mohr Coulomb´s model at the beginning with inadequate results. For this reason, it was decided to employ the Hardening Soil model implemented in PLAXIS (Plaxis 2D Manual), based on concept of soil dilatancy and with a yield cap (Tschernutter et al., 2011). The analysis included the following phases in chronological order: construction of the original dam; first impounding of the original dam; drawdown; construction of the heightening; first impounding of the heightened dam; drawdown. The measured vertical displacements of the settlement gauge SP1 (see Fig. 2.52) were compared in Figure 2.52 with the predicted values using the hardening soil model. The measurements refer to the first impounding (05.11.07) and to the drawdown (03.06.08) after the heightening. The measured horizontal displacements from inclinometer SP1 (see Fig. 2.53) were compared with the computed displacements for the first impounding (05.11.07) and the drawdown (25.06.08) after the heightening (Tschernutter et al., 2011). There is a good agreement between both the vertical and horizontal displacements obtained with the hardening soil model and the field data.

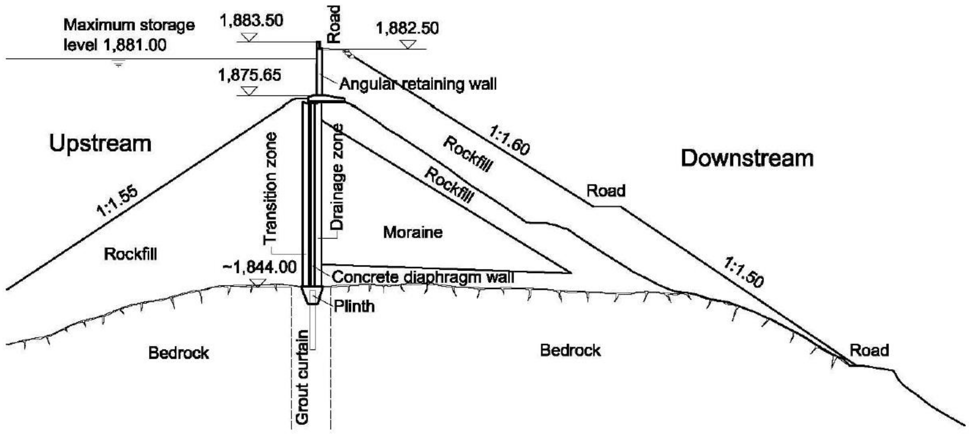

Figure 2.51 Cross section Bockhartsee Dam after heightening (Tschernutter et al., 2011)

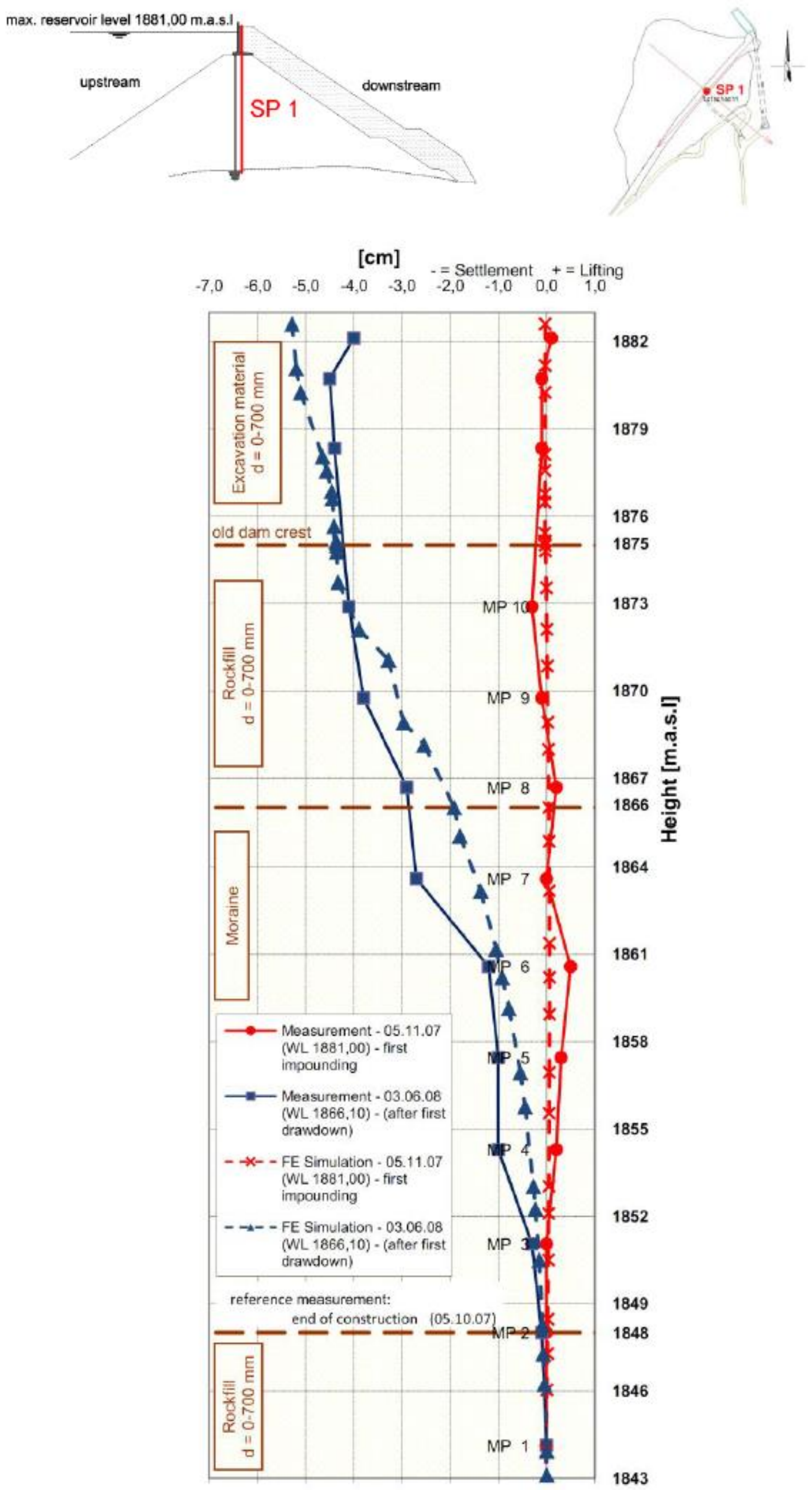

Figure 2.52 Comparison of measured and computed vertical displacements, downstream, settlement gauge SP1 (Tschernutter et al., 2011)

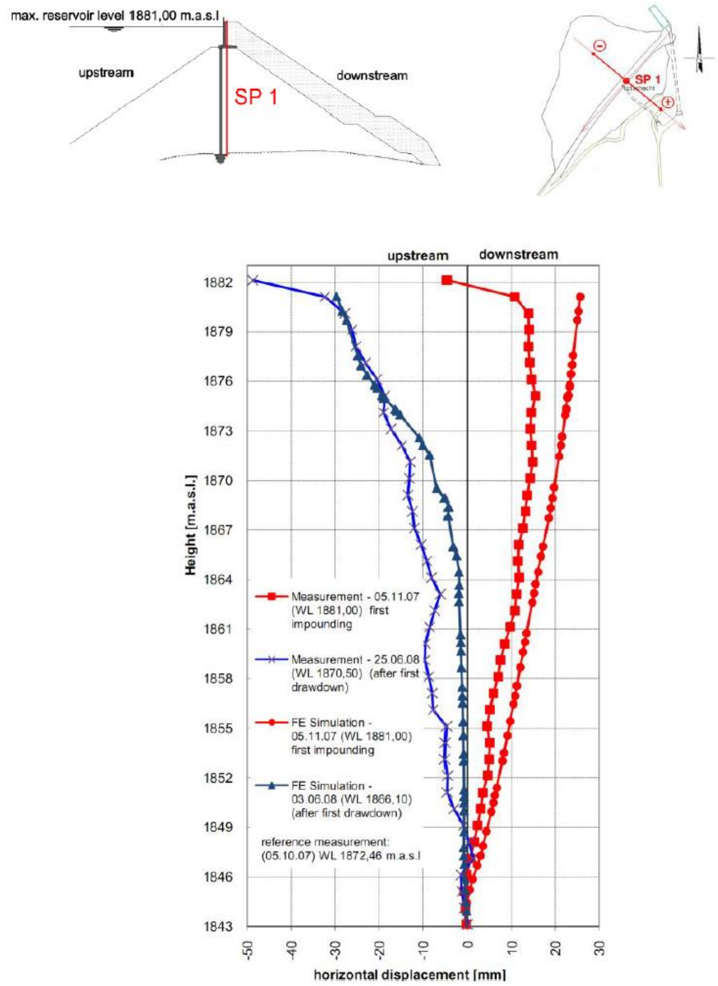

Figure 2.53 Comparison of measured and computed horizontal displacements, inclinometer SP1, downstream (Tschernutter et al., 2011)

Sukkarak et al. (2017) employed an elasto-plastic model with double yield surfaces to simulate the settlement behaviour during construction of the Nam Ngum 2 (Figure 2.54), a 182 m high rockfill dams with a three-dimensional finite element analysis. The constitutive model considered in the numerical analysis was the hardening soil model (Schanz et al., 1999), based on the theory of elasto-plasticity with double yield surfaces, with the presence of a yield cap and a stress-dependent stiffness and dilatancy. The model was modified by Sukkarak et al. (2017) to incorporate the effect of particle breakage on the dilatancy of rockfill materials changing the Rowe's stress-dilatancy equation. In addition, the stress-dependent stiffness values are modified to exhibit different degrees of evolution with changes in the stress state (Sukkarak et al., 2017). The comparisons between the predicted results and the monitoring data in terms of settlements at the end of construction (Fig. 2.55) highlight the capacity of the model to well predict the deformation behaviour of the rockfill dam.

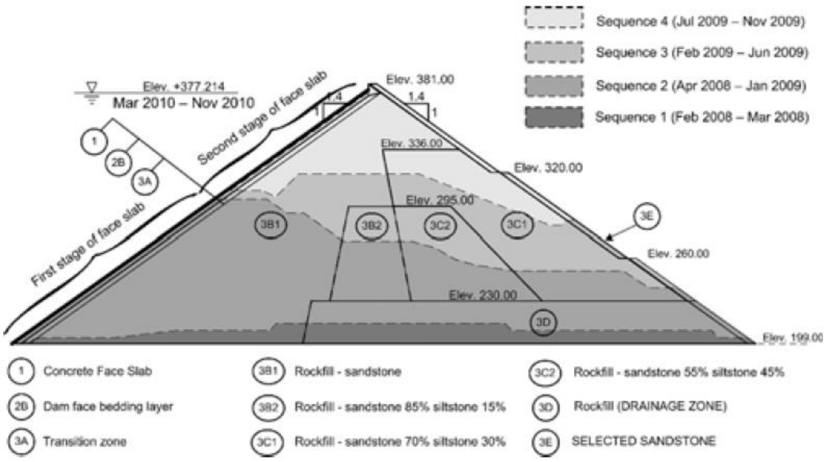

Figure 2.54 Typical Section of the Nam Ngum 2 CFRD (Sukkarak et al., 2016)

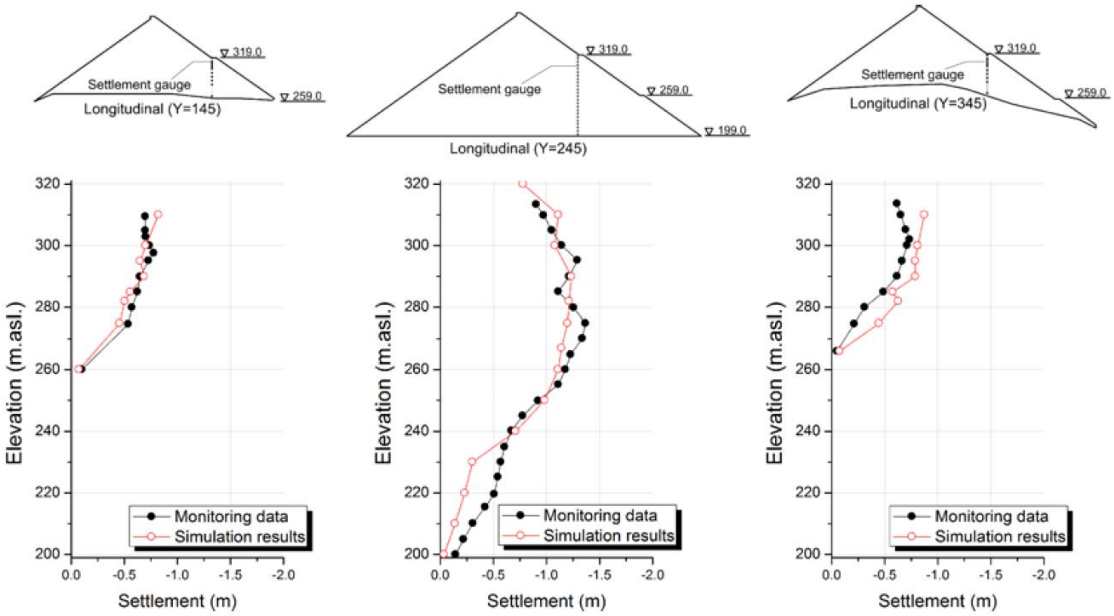

Figure 2.55 The predicted and measured settlements (Sukkarak et al., 2016)

In this section a brief description of selected numerical analyses of embankment dams using elasto-plastic hardening constitutive models has been presented. In general, an improved agreement between observed and predicted deformation using such models has been shown in comparison with simpler model.

It was well demonstrated that the elasto-plastic hardening soil models are more suitable to model the embankment dam behaviour during construction and reservoir impounding than simpler models, such as linear or non-linear elastic and Mohr-Coulomb type model. The advantages of these models are: the capacity to well describe deformational behaviour during construction and reservoir impounding; the improvement of representing the pre-peak plasticity of rockfill behaviour compared to elastic perfectly plastic models. On the other hand, these types of models are more complex and are characterized by many parameters, and often there are not available test data on rockfill due to limitation of the maximum grain size allowed.

Kovacevic (1994) and Kovacevic et al. (2008) pointed out the role of the Lade’s double hardening model to represent the pashes of construction and first filling of the analysed dams, and also stated that the double hardening model is more suitable, for the use in the finite element analyses of rockfill dams, than the single hardening model, because the former is more sensitive to the changes in stress path directions which occur during reservoir impounding particularly at lower stress levels, which typically characterize rockfill dams. However, both the Lades’s elasto plastic models are not capable to account for the hysteretic behaviour during unloading and re-loading cycles. For this reason, in some cases the kinematic hardening ‘bubble’ model (Grammatikopoulou et al., 2006; Al-Tabbaa & Wood, 1989) was employed obtaining great results.

3. THE FINITE DIFFERENCE CODE FLAC

3.1 INTRODUCTION

The finite difference method is very useful to perform numerical analysis of many types of geotechnical problem, and is perhaps the oldest numerical technique used for the solution of sets of differential equations, given initial values and/or boundary values; it is characterized by the assumption that every derivative in the set of governing equations is replaced directly by an algebraic expression written in terms of the field variables (e.g., stress or displacement) at discrete points in space; these variables are undefined within elements (FLAC Ver. 7.0 User's Manual). The materials can be simulated though elements or zones, which form a grid. The finite difference code employed in this thesis is FLAC (Fast Lagrangian Analysis of Continua), which is a two-dimensional explicit finite difference program for engineering mechanics computation and which uses an explicit, time-marching method to solve the algebraic equations.

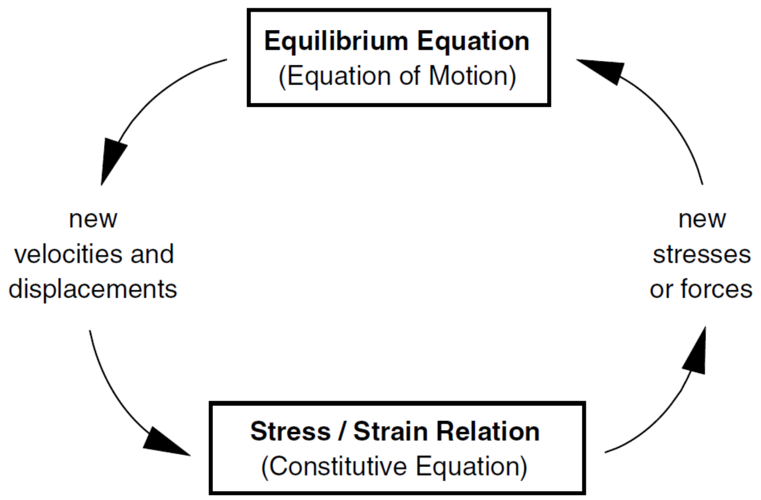

Figure 3.1 Basic explicit calculation cycle (FLAC Ver. 7.0 User's Manual)

The formulation in FLAC needs, even for static problems, the dynamic equations of motion to ensure that the numerical scheme is stable when the physical system to be modelled is unstable. The code FLAC is characterized by the general calculation scheme in Fig. 3.1, in which the equations of motion were invoked to derive new velocities and displacements from stresses and forces. From velocities strain rates are derived, and from strain rates new stresses, taking one time-step for every cycle around the loop. An important aspect of the method is that for each box in Fig. 3.1 the calculated new variables are based on known fixed values within the box. For example, the new stresses are calculated from the velocities already calculated, which are assumed to be frozen for the operation of the box. Although this assumption seems unreasonable because stress changes influence also velocity changes, choosing a small time-step allow to justify it. The most important advantage of this assumption is that no iteration process is necessary when computing stresses from strains in an element, even if the constitutive law is wildly nonlinear. The disadvantage of the explicit method is the presence of a small timestep, which means that large numbers of steps must be taken (FLAC Ver. 7.0 User's Manual). The term Lagrangian refers to the Lagrangian formulation, characterized by the assumption that the incremental displacements are added to the coordinates, hence the grid moves and deforms with the material it represents. This formulation is in contrast to the Eulerian formulation, in which the material moves and deforms relative to a fixed grid.

3.2 FORMULATION OF FINITE DIFFERENCE METHOD

The finite difference method involves the formulation of field equations, the numerical formulation, the mechanical damping and critical time step.

3.2.1 Field equations

The solution of geotechnical problems in FLAC invokes the equations of motion and constitutive relations. The equations of motion could be identified in the generalised Newton's law of motion for a continuous solid body, expressed as:

$$\rho \frac{\partial \dot{u}_i}{\partial t} = \frac{\partial \sigma_{ij}}{\partial x_j} + \rho g_i \tag{3.1}$$

Where ρ is the mass density, t is the time, x_i is the components of coordinate vector, σ_{ij} is the components of stress tensor, g_i is the components of gravitational acceleration, $\dot{u}_i$ is the velocity components, and the indices i denote the components in a Cartesian coordinate. The other set of equations that apply to a solid deformable body is the constitutive law, which could be expressed as follows:

$$\sigma_{ij} = M\left(\sigma_{ij}, \dot{e}_{ij}, \kappa\right) \tag{3.2}$$

Where M is the functional form of the constitutive law, κ is a history parameter which may or may not be present, depending on the particular law, and $\dot{e}_{ij}$ is the strain-rate components. The strain rate could be derived from velocity gradient as:

$$\dot{e}_{ij} = \frac{1}{2}\left[\frac{\partial \dot{u}_i}{\partial x_j} + \frac{\partial \dot{u}_j}{\partial x_i}\right] \tag{3.3}$$

From the old stress tensor and the strain rate, the new stress tensor could be estimated.

3.2.2 Numerical formulation

The finite difference method is characterized by a division of the solid body into small quadrilateral elements which define a mesh determined by the user. The code subdivides each element into two overlaid sets of constant-strain triangular elements (Fig. 3.2). The deviatoric stress components of each triangle are maintained independently, requiring sixteen stress components for each quadrilateral. The force vector exerted on each node is taken to be the mean of the two force vectors exerted by the two overlaid quadrilaterals, obtaining a symmetric response of the composite element for symmetric loading.

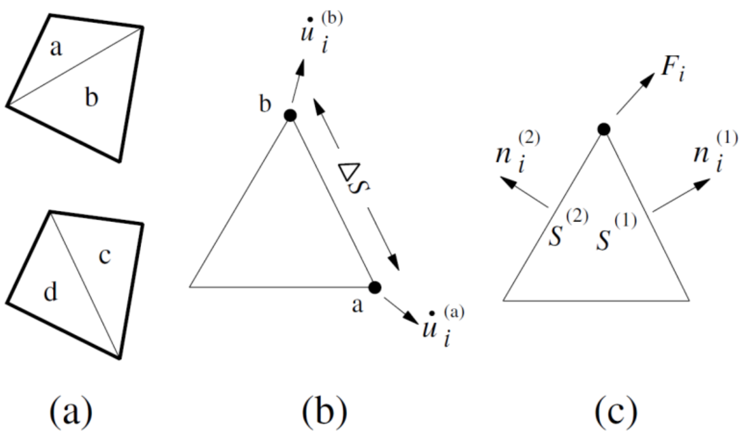

Figure 3.2 (a) Overlaid quadrilateral elements used in FLAC (b) Typical triangular element with velocity vectors (c) Nodal force vector (FLAC Ver. 7.0 User's Manual)

The difference equations for a triangle are derived from the generalized form of Gauss divergence theorem:

$$\int_s n_i \, f \, ds = \int_A \frac{\partial f}{\partial x_i} \, dA \tag{3.4}$$

Where $\int_s$ is the integral around the boundary of a closed surface, n_i is the unit normal to the surface s, f is a scalar, vector or tensor, x_i are position vectors, ds is an incremental arc length and $\int_A$ is the integral over the surface area A. Substituting the average velocity vector of each triangle side for f, it is possible to write strain rates in terms of nodal velocities for a triangular subzone:

$$\frac{\partial \dot{u}_i}{\partial x_j} \cong \frac{1}{2A} \sum_s \left(\dot{u}_i{}^{(a)} + \dot{u}_i{}^{(b)} \right) n_j \, \Delta s \tag{3.5}$$

$$\dot{e}_{ij} = \frac{1}{2} \left[\frac{\partial \dot{u}_i}{\partial x_j} + \frac{\partial \dot{u}_j}{\partial x_i} \right] \tag{3.3}$$

where the summation is over the sides of the triangular subzone, and (a) and (b) are two consecutive nodes on a side. Using Eq. (3.5) and Eq. (3.3) it is possible to derive the components of the strain rate tensor based on nodal velocities. From the strain rate tensor, using the constitutive law it is possible to derive a new stress tensor. Once the stresses have been calculated, the equivalent forces applied to each nodal point are determined. The stresses in each triangular subzone act as tractions on the sides of the triangle, which could be taken equivalent to two equal forces acting at the ends of the corresponding side (FLAC Ver. 7.0 User's Manual). Each triangle corner receives two force contributions, one from each side resulting in (Fig. 3.2c):

$$F_i = \frac{1}{2} \, \sigma_{ij} \left(n_j^{(1)} S^{(1)} + n_j^{(2)} S^{(2)} \right) \tag{3.6}$$

The quadrilateral element contains two sets of two triangles and within each set, the forces from triangles meeting at each node are summed. The forces from both sets are then averaged, to give the nodal force contribution of the quadrilateral. For each node, the forces from all surrounding quadrilaterals are summed to give the net nodal force vector $\sum F_i$, which includes contributions from applied loads and from body forces due to gravity. If the body is at equilibrium, or in steady-state flow, the net nodal force vector $\sum F_i$ on the node will be zero. Otherwise, the node will be accelerated according to the finite difference form of Newton's second law of motion:

$$\dot{u}_i^{\left(t+\frac{\Delta t}{2}\right)} = \dot{u}_i^{\left(t-\frac{\Delta t}{2}\right)} + \sum F_i^{(t)} \frac{\Delta t}{m} \tag{3.7}$$

Where the superscripts denote the time at which the corresponding variable is evaluated, m is the lumped gravitational mass at the node, defined as the sum of one-third of the masses of triangles connected to the node (FLAC Ver. 7.0 User's Manual).

3.2.3 Mechanical damping and critical time step

For solving static problems, the equations of motion must be damped to provide static or quasi-static solutions. FLAC uses a form of damping called local damping, which is a non-viscous damping. The damping force on each node is proportional to the magnitude of the unbalanced force, the direction of the damping force is such that energy is always dissipated. The Eq. (3.7) can be integrated with the local damping obtaining:

$$\dot{u}_i^{\left(t+\frac{\Delta t}{2}\right)} = \dot{u}_i^{\left(t-\frac{\Delta t}{2}\right)} + \left\{\sum F_i^{(t)} - (F_d)_i\right\} \frac{\Delta t}{m_n} \tag{3.8}$$

$$(F_d)_i = \alpha \left|\sum F_i^{(t)}\right| sign\left(\dot{u}_i^{\left(t-\frac{\Delta t}{2}\right)}\right) \tag{3.9}$$

Where F_d is the damping force, α is a constant (α = 0.8 in FLAC), and m_n is a fictitious nodal mass. The explicit-solution procedure is not unconditionally stable and the timestep must be chosen to satisfy the following condition for an elastic solid discretized into elements of size Δx:

$$\Delta t < \Delta t_c = \frac{\Delta x}{C_p} \tag{3.10}$$

Where Δt is the computational time step, Δt_c is the critical time step, and C_p is the maximum speed at which information can propagate, which can be assumed equal to p-waves velocity as follows:

$$C_p = \sqrt{\frac{K+\frac{4G}{3}}{\rho}} \tag{3.11}$$

Where K and G are the bulk and the shear modulus, respectively.

3.3 CAP-YIELD (CYSOIL) IMPLEMENTED IN FLAC

Several authors (Sect. 2.6) employed elasto-plastic hardening models to describe the construction and reservoir impounding of embankment dams, proving that this class of models is well-suited to simulate the deformational behaviour. In this context, from the family of hardening plasticity models, a model implemented in FLAC 7.0 was chosen to reproduce the stress and strain state of a zoned earth dam during construction and impoundment. The model's name is cap-yield or Cysoil, which is a strain-hardening constitutive model characterized by a frictional and cohesive Mohr-Coulomb shear envelope and an elliptic volumetric cap. A feature of the model is the presence of a cap in the (p', q) plane to account for the plasticity effect of grain crushing and rearrangement, permitting plastic deformations in response to an isotropic stress increase. Another important aspect which the model is capable to capture is the decrease in stiffness accompanied by irreversible deformation when the soil is subjected to deviatoric loading through a friction hardening law. The model is also characterized by a dilation hardening or softening law to introduce the shear-induced volume changes. The basic Cysoil model behaviour can be enhanced using three types of hardening laws (FLAC Ver. 7.0 User's Manual): a cap hardening law, to capture the volumetric power law behaviour observed in isotropic compaction tests; a friction-hardening law, to reproduce the hyperbolic stress-strain law behaviour observed in drained triaxial tests; and a compaction/dilation law to model irrecoverable volumetric strain taking place as a result of soil shearing. The model is characterized by three yield surfaces (Fig. 3.3): deviatoric (shear), volumetric (cap) and tension cut off.

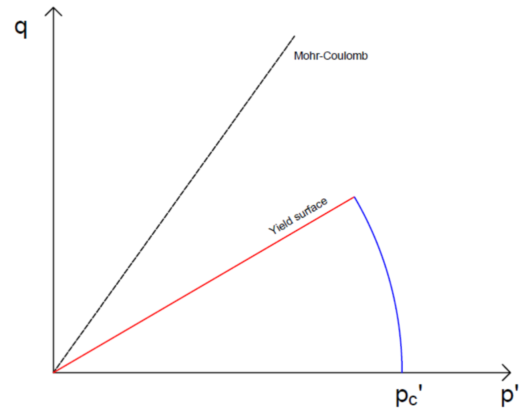

Figure 3.3 The yield surfaces of the Cysoil Material Model: deviatoric yield surface (red) and the elliptical cap (blue)

The deviatoric hardening mechanism is defined by a yield surface close to Mohr-Coulomb criterion:

$$f_s = Mp' - q + Nc' \tag{3.12}$$

Where

$$M = \frac{6\sin\varphi'_m}{3-\sin\varphi'_m} \tag{3.13}$$

$$N = \frac{6\cos\varphi'_m}{3-\sin\varphi'_m} \tag{3.14}$$

$$p' = \frac{\sigma'_1+\sigma'_2+\sigma'_3}{3} \tag{3.15}$$

$$q = -[-\sigma'_1 + (\delta - 1)\sigma'_2 - \delta\sigma'_3] \tag{3.16}$$

$$\delta = \frac{3+\sin\varphi'_m}{3-\sin\varphi'_m} \tag{3.17}$$

p' is the mean effective stress, q is a measure of shear stress, φ'_m is the mobilized friction angle and c' is the cohesion.

The deviatoric potential function is non-associated:

$$g_s = M^* p' - q^* \tag{3.18}$$

where

$$M^* = \frac{6\sin\psi_m}{3-\sin\psi_m} \tag{3.19}$$

$$q^* = -[-\sigma_1' + (\delta^* - 1)\sigma_2' - \delta^*\sigma_3'] \tag{3.20}$$

$$\delta^* = \frac{3+\sin\psi_m}{3-\sin\psi_m} \tag{3.21}$$

ψ_m is the mobilized dilatancy angle.

The flow rule is defined in terms of relationship between the plastic volumetric strain and plastic deviatoric strain through the mobilized dilatancy angle:

$$\dot{\varepsilon}_v^p = \sin\psi_m \;\dot{\varepsilon}_s^p \tag{3.22}$$

The mobilized dilatancy angle ψ_m is described through the Rowe stress-dilatancy theory (Rowe, 1962). The theory is based on a definition of a critical state friction angle φ_{cv}, below which the material contracts ($\varphi_m' < \varphi_{cv}$) and above which the material dilates ($\varphi_m' > \varphi_{cv}$).

$$\sin\psi_m = \frac{\sin\varphi_m' - \sin\varphi_{cv}}{1-\sin\varphi_m'\sin\varphi_{cv}} \tag{3.23}$$

where

$$\sin\varphi_{cv} = \frac{\sin\varphi_f' - \sin\psi_f}{1-\sin\varphi_f'\sin\psi_f} \tag{3.24}$$

φ_f' and ψ_f are ultimate (known) values of friction and dilation, respectively.

The friction-hardening behaviour is modelled using the following hyperbolic incremental law (Byrne et al. 2003), which links the mobilized friction angle φ_m' and plastic shear strain γ^P through the plastic shear modulus G^P:

$$d\,(\sin\varphi_m') = \frac{G^P}{p'}\,d(\gamma^P) \tag{3.25}$$

$$G^P = \beta G^e \left(1 - \frac{\sin\varphi'_m}{\sin\varphi'_f} R_f\right)^2 \tag{3.26}$$

where G^e is the elastic tangent shear modulus, β is a calibration factor, and R_f is the constant failure ratio, which is smaller than 1 (0.9 in most cases) and used to assign a lower bound for G^P. The elastic tangent shear modulus G^e could be expressed as a function of p':

$$G^e = G^e_{ref} \left(\frac{p'}{p_{ref}}\right)^{m_1} \tag{3.27}$$

where G^e_{ref} is the elastic tangent shear modulus at reference effective pressure, p_{ref} is the reference effective pressure, and m_1 is a constant.

The volumetric yield surface is an elliptic cap which close the elastic domain simulating the densification or compaction of the material and it is associated:

$$f_c = \frac{q^2}{\alpha^2} + p'^2 - {p_c}'^2 \tag{3.28}$$

where α is a dimensionless parameter defining the shape of the elliptical cap and p_c is the cap pressure which is the location of the intersection of this yield surface with the p axis. p'_c is the hardening parameter and depends on the volumetric plastic strain ε_v^P.

The Cysoil model is capable to reproduce the dependence of the soil stiffness with the level of confinement through a nonlinear relationship, which captures the isotropic volumetric behaviour of the soils:

$$\frac{dp'}{d\varepsilon_v} = K^{iso}_{ref} \left(\frac{p'}{p_{ref}}\right)^{m_2} \tag{3.29}$$

where K^{iso}_{ref} is the slope of the laboratory curve for p' versus ε_v at reference effective pressure p_{ref} and m_2 is a constant (m_2 < 1).

A typical result of an isotropic consolidation test, representative of this law, in terms of the variation of confining pressure versus volumetric strain, is presented in Fig. 3.4 with loading and unloading paths. The ratio between the rates of elastic and plastic volumetric strain represents a model parameter and is assumed to be constant:

$$R = \frac{d\varepsilon_v{}^p}{d\varepsilon_v{}^e} \tag{3.30}$$

The hardening rule can be expressed by the following relationship:

$$\frac{dp'_c}{d\varepsilon_v{}^p} = \frac{1+R}{R} K_{ref}^{iso} \left(\frac{p'}{p_{ref}}\right)^{m_2} \tag{3.31}$$

Based on these assumptions it is also possible to calculate the elastic tangent bulk modulus as follows:

$$K^e = (1+R) K_{ref}^{iso} \left(\frac{p'}{p_{ref}}\right)^{m_2} \tag{3.32}$$

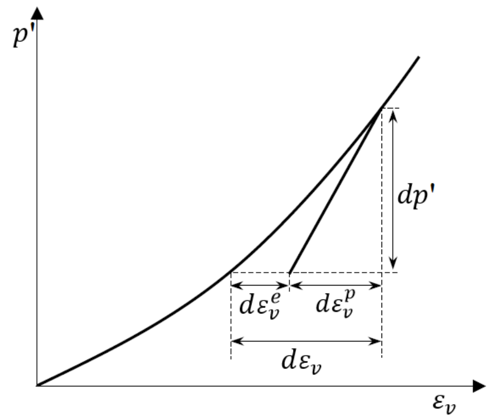

Figure 3.4 Isotropic consolidation test with loading and unloading paths: variation of confining pressure with volumetric strain (FLAC Ver. 7.0 User's Manual)

The tension cut off mechanism incorporate the tensile strength of the material to the model. The minor principal stress is limited to the tensile strength of the material and the flow rule is associated with no hardening.

$$f_t = \sigma^t - \sigma_3 \tag{3.33}$$

where σ^t is the tensile strength of the material.

4. THE FINITE ELEMENT CODE ICFEP

4.1 INTRODUCTION

The finite element method (FEM) is a numerical technique which can be used to solve a great range of geotechnical problems in approximate way (Kovacevic, 1994). The finite element code employed for the finite element analyses reported in this thesis is the "Imperial College Finite Element Program", also named ICFEP (Potts & Zdravkovic, 1999). This chapter presents a brief overview of the method, some related geotechnical considerations and details about the coupled consolidation. An advanced constitutive model with multiple yield and plastic potential surfaces named Lade's double hardening model (Lade, 1977) is also presented. The constitutive model was implemented in ICFEP in 1994 by Kovacevic (1994) and used in the numerical analysis of this thesis.

4.2 FORMULATION OF FINITE DIFFERENCE METHOD

4.2.1 Linear analysis

The finite element method for linear materials involves the following steps: element discretisation, primary variable approximation, element equations, global equations, boundary conditions and solution of global equilibrium equations (Potts & Zdravkovic, 1999) The element discretisation consists of discretizing the geometry of the problem in small regions called finite elements, which form the finite element mesh. The elements are characterized by triangular or quadrilateral shape and by key points defined nodes, which are on the corner for elements with straight sides and also at the midpoint of each side for elements with curved sides (Potts & Zdravkovic, 1999). ICFEP is a displacement based finite element method and the primary unknown quantity is the displacement field, which varies over the problem domain (Potts & Zdravkovic, 1999). The displacement components are expressed in terms of values at the nodes and varies over each element as a simple polynomial form (Potts & Zdravkovic, 1999). ICFEP includes quadrilateral isoparametric elements with either four or eight nodes, however in this thesis the eight nodes combination was employed. The basic procedure in the isoparametric finite element formulation is to express the element displacements and element geometry in terms of interpolation functions using the natural coordinate system (Potts & Zdravkovic, 1999). The element equations combine the conditions of compatibility, equilibrium and the employed constitutive model. To determine the element equations for linear material behaviour, the principle of minimum potential energy is invoked (Potts & Zdravkovic, 1999). The derived element equations are:

$$[K_E]\,\{\Delta d_E\} = \{\Delta R_E\} \tag{4.1}$$

Where $[K_E]$ is the element stiffness matrix, $\{\Delta d_E\}$ is the vector of incremental element nodal displacements and $\{\Delta R_E\}$ is the vector of incremental nodal forces (Potts & Zdravkovic, 1999).

Combining the element equations, the global equations are obtained:

$$[K_G]\,\{\Delta d_G\} = \{\Delta R_G\} \tag{4.2}$$

Where $[K_G]$ is the global stiffness matrix, $\{\Delta d_G\}$ is the vector of all incremental nodal displacements and $\{\Delta R_G\}$ is the vector of all incremental nodal forces (Potts & Zdravkovic, 1999).

The boundary conditions, as load and displacement conditions, define the problem completely. The loading conditions affect the right hand side vector of the global system of equations $\{\Delta R_G\}$, while the displacement conditions affect the vector $\{\Delta d_G\}$. The achieved system of equations needs to be solved to obtain the nodal displacements, using a mathematical technique, ICFEP adopts a technique based on Gaussian elimination (Potts & Zdravkovic, 1999).

4.2.2 Nonlinear analysis

When the constitutive model becomes elasto-plastic or nonlinear elastic, it is necessary to deal with nonlinear analysis. The constitutive matrix is not constant, but varies with stress or strain, therefore, this variation needs to be taken into account in the finite element analysis. The boundary conditions are applied incrementally and the global equilibrium equation is written and solved in incremental form:

$$[K_G]^i\,\{\Delta d_G\}^i = \{\Delta R_G\}^i \tag{4.3}$$

where $[K_G]^i$ is the incremental global stiffness matrix, $\{\Delta d_G\}^i$ is the vector of incremental nodal displacements and $\{\Delta R_G\}^i$ is the vector of incremental nodal forces and i is the increment number (Potts & Zdravkovic, 1999). The boundary conditions must be applied in small increments and the equation needs to be solved for each increment. The final solution is obtained by summing the results of each increment (Potts & Zdravkovic, 1999). Large number of solution strategies exists to solve the global incremental equations, however, the result depends on the solution increment size. Three methods to solve incremental equations are implemented in ICFEP: tangent stiffness, visco-plastic and modified Newton-Raphson scheme (Potts & Zdravkovic, 1999). The modified Newton-Raphson method was used in this thesis, because it is more accurate and less sensitive to increment size than the others and appears to be the most efficient solution strategy (Kovacevic, 1994). The method employ an iterative technique to solve the incremental global equation (Eq. 4.3). The first iteration involves the load vector ΔR_1 and the incremental global stiffness matrix $[K_G]^1$, which produce an incorrect solution. The predicted incremental displacements are used to calculate the residual load $\{\psi\}$, which is a measure of the error in the analysis (Potts & Zdravkovic, 1999). The incremental global equation (4.3) is then solved again with this residual load forming the right hand side vector (Potts & Zdravkovic, 1999):

$$[K_G]^i \left(\{\Delta d_G\}^i\right)^j = \{\psi\}^{j-1} \tag{4.4}$$

where the superscript j refers to the iteration number and $\{\psi\}^0 = \{\Delta R_G\}^i$. The process is repeated until the residual load is small and the incremental displacements are equal to the sum of the iterative displacements (Potts & Zdravkovic, 1999). The approach is illustrated in Figure 4.1 for a single degree freedom system (Kovacevic, 1994).

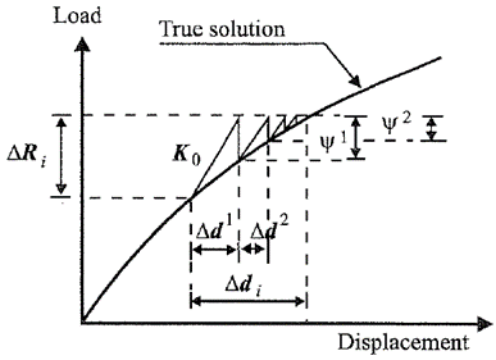

Figure 4.1 Modified Newton-Raphson method (Kovacevic, 1994)

Every solution increment needs more iterations, hence a convergence criterion requires to be fixed. The limits are imposed on the values of both the iterative displacements $\left(\{\Delta d_G\}^i\right)^j$ and the residual loads $\{\psi\}^j$. The norm of the iterative values of the parameters had to be less than typically 1 % of the norm of the incremental values (Potts & Zdravkovic, 1999; Kovacevic, 1994).From the incremental displacements at the end of each iteration, the incremental strains are estimated. The stress changes are derived integrating the constitutive model along the incremental strain paths through a method called "stress point algorithm", which can include different approaches (Potts & Zdravkovic, 1999; Kovacevic, 1994). In all the analysis of this thesis, the sub-stepping scheme using a modified Euler integration procedure with error control (Sloan, 1987) was used (Kovacevic, 1994). Then, the stress changes are added to the values of the stresses at the beginning of the increment and used to evaluate consistent equivalent nodal forces. The difference between these forces and the externally applied loads gives the residual load vector (Potts & Zdravkovic, 1999; Kovacevic, 1994).

4.2.3 Geotechnical considerations

In this Section a few geotechnical considerations, which are relevant for the case study, are discussed and explored by the finite element point of view. These geotechnical details contribute to perform more realistic numerical analyses. The most relevant aspects are: initial stresses, excavation, construction and compaction. The nonlinear finite element analysis requires the knowledge of initial stresses at the beginning because the material behaviour depends strongly on the stress history and because identifying the initial stress is necessary to calculate the unloading forces during excavation, also for a linear elastic analyses (Kovacevic, 1994). The development of the initial stress state in the ICFEP numerical analyses was specified directly through a subroutine, formulated specifically for the case study. The excavation of soil can be simulated in the finite element analysis by sequentially removing groups of elements (Kovacevic, 1994). The process of modelling the excavation involves the determination of the nodal forces resulted from the internal stresses acting in the soil mass before elements are removed, and applying equal and opposite forces to the new soil boundary (Potts & Zdravkovic, 1999). The construction can be modelled by sequentially adding groups of elements (Kovacevic, 1994). The simulation needs to respect some important properties: the elements must be present in the existent original mesh, but they should be deactivated before the excavation and reactivated incrementally during construction; the constitutive model of the elements, during construction, needs to be consistent with its behaviour; once constructed, the constitutive model can change to represent the behaviour of the material once placed; when an element is constructed, the addition of its weight to the finite element mesh is simulated by applying self-weight body forces to the constructed element (Potts & Zdravkovic, 1999). In ICFEP, the elements which are going to be constructed are characterized by a linear elastic constitutive model and by a very low stiffness ("ghost elements") (Potts & Zdravkovic, 1999; Kovacevic, 1994). During construction the vertical stresses becomes equal to the overburden pressure while the horizontal stresses can be determined by the value of Poisson's ratio $\nu = 0.45$ (Kovacevic, 1994). After construction, each layer is subject to mechanical compaction, an artificial process that induces a characteristic yield stress in the compacted soil mass similar to that exhibited by the soil masses subjected to natural processes of over consolidation during their geological life time (Prakash et al., 2014). As a result of compaction, the horizontal stresses in the soil and the lateral earth pressure increase (Massarsch, 2002, Potts et al., 2001). The effect of compaction stresses in the constructed layers during dam construction could be taken into account using a proper value of K_0.

4.2.4 Coupled consolidation

While many geotechnical applications can be solved with one or both the two extreme conditions of undrained and fully drained analysis, the real soil behaviour is often time related with the pore water pressure response dependent on soil permeability, the rate of loading and the hydraulic boundary conditions (Potts & Zdravkovic, 1999). The previous briefly described finite element method for linear and nonlinear materials needs to be integrated with seepage equations. The theory, which combines together the equations governing the flow of pore fluid through soil skeleton with the equation governing the deformation of the soil due to loading, is defined "coupled" (Potts & Zdravkovic, 1999). The new aspect is that the degrees of freedom are not only the displacements but also the pore fluid pressure, however, only the corner nodes are pore fluid pressure degrees of freedom.

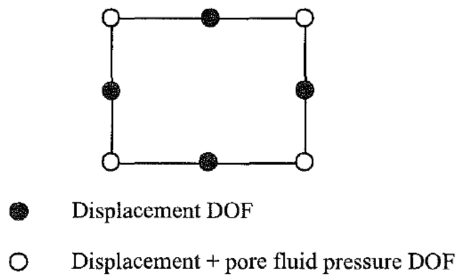

Figure 4.2 Degrees of freedom for an eight noded element (Potts and Zdravkovic, 1999)

The Biot's consolidation theory (Biot, 1941) is invoked to analyse the consolidation process: the equations of equilibrium, the constitutive behaviour, the equations of continuity, and the generalized Darcy's Law have to be satisfied for a soil saturated with an incompressible pore fluid (Potts & Zdravkovic, 1999). The principle of minimum potential energy and the principle of virtual work are invoked to derive the finite element equations associated with equilibrium and continuity:

$$[K_G]\,\{\Delta d_G\} + [L_G]\,\{\Delta p_f\} = \{\Delta R_G\} \tag{4.5}$$

$$[L_G]^T\,\left(\frac{\{\Delta d_G\}}{\Delta t}\right) - [\Phi_G]\{\Delta p_f\} = 0 \tag{4.6}$$

Where $[K_G]$ is the global stiffness matrix, $\{\Delta d_G\}$ is the vector of all incremental nodal displacements, $\{\Delta R_G\}$ is the vector of all incremental nodal forces, $\{\Delta p_f\}$ is the change in pore pressure, $[L_G]$ is the global coupling matrix, $[\Phi_G]$ is the global flux matrix (Potts & Zdravkovic, 1999; Kovacevic, 1994). To solve equations (4.5) and (4.6) a time marching process is adopted, using this approximation (Potts & Zdravkovic, 1999):

$$\int_{t_1}^{t_2}[\Phi_G]\{p_f\}\,dt = [\Phi_G]\left[\beta\left(\{p_f\}\right)_2 + (1-\beta)\left(\{p_f\}\right)_1\right]\Delta t \tag{4.7}$$

Where $(\{\Delta d_G\}, \{p_f\})_1$ is the solution at the time t_1, $(\{\Delta d_G\}, \{p_f\})_2$ is the solution at the time $t_2 = t_1 + \Delta t$, β is a parameter which must be $\beta \geq 0.5$ (Booker and Small, 1975) to avoid instability.

Substituting equation (4.7) in the continuity equation (4.6), and adding equation (4.5), the general incremental matrix form could be written:

$$\begin{bmatrix} [K_G] & [L_G] \\ [L_G]^T & -\beta\Delta t[\Phi_G] \end{bmatrix} \begin{Bmatrix} \{\Delta d_G\} \\ \{\Delta p_f\} \end{Bmatrix} = \begin{Bmatrix} \{\Delta R_G\} \\ [\Phi_G](\{p_f\})_1 \Delta t \end{Bmatrix} \tag{4.8}$$

This system of non-linear equations of a coupled consolidation problem can be solved using the modified Newton-Raphson method (Kovacevic, 1994).

4.2.5 Hydraulic Boundary Conditions

In the case of coupled consolidation, where the pore fluid pressure is a degree of freedom at nodes, it is important to consider the hydraulic boundary conditions for each node at the boundary and inside of the mesh, in terms of prescribed pore fluid pressure or a prescribed nodal flow (Potts & Zdravkovic, 1999). The default condition, if the hydraulic conditions are not specified for the boundaries, often prescribes zero nodal flow. To apply these conditions is possible to specify the prescribed pore fluid pressure at nodes, which can be defined as an incremental change or an accumulated value at the end of a particular increment. A briefly description of the hydraulic boundary conditions used in the numerical analysis are presented in this thesis: infiltration and precipitation. The infiltration is a hydraulic boundary condition which allows to prescribe pore fluid flows across a boundary of the finite element mesh for a defined increment of the analysis (Potts & Zdravkovic, 1999). The precipitation boundary condition prescribes a dual boundary condition to part of the mesh, because both the pore fluid pressure and infiltration flow rate are specified (Potts & Zdravkovic, 1999): for each node and each increment, there is a check if the pore fluid pressure is more compressive than that prescribed initially; when it happens, the boundary condition for that node is taken as a prescribed pore fluid pressure specified at the beginning; contrariwise, if the pore fluid pressure is more tensile than that prescribed or if the current flow rate at the node exceeds the nodal flow value corresponding to the total infiltration flow rate, this nodal flow value is taken as a boundary condition (Potts & Zdravkovic, 1999).

4.2.6 Permeability models

To solve the coupled analysis, it is necessary to give the value of the permeability as input. There are several options available in ICFEP to model the permeability variation. The simplest solution is to model the permeability k as linear isotropic function defined by a single scalar value in any direction, and the software allows also to vary this permeability with depth (Potts & Zdravkovic, 1999). Another option is to consider a linear anisotropic permeability, which means that the permeability is direction dependent and it is necessary to specify all values of the coefficient in each direction. There are also two nonlinear model in which the permeability is still isotropic and varies with void ratio or mean effective stress. In the following relation the coefficient of permeability k varies with the void ratio e, while a and b are material parameters (Potts & Zdravkovic, 1999):

$$\ln k = a + be \tag{4.9}$$

$$k = e^{(a+be)} \tag{4.10}$$

The negative aspects of previous model are that knowing void ratio is necessary at any stage of the analysis, hence it needs to consider the initial value of void ratio as input in the finite element program, and that determining parameters a and b is difficult due to few laboratory or field data available. Consequently, it is often convenient to adopt an expression in which k varies with the mean effective stress, according to the follow relation (Potts & Zdravkovic, 1999):

$$\ln\left(\frac{k}{k_0}\right) = -ap' \tag{4.11}$$

$$k = k_0\, e^{(-ap\prime)} \tag{4.12}$$

Where k_0 is the coefficient of permeability at zero mean effective stress and a is a constant, incorporating the initial void ratio at zero mean effective stress and the coefficient of volume compressibility m_v.

4.3 LADE'S ELASTO-PLASTIC DOUBLE HARDENING MODEL IMPLEMENTED IN ICFEP

The soil exhibits irreversible behaviour, yield phenomena and shear induced dilatancy (Potts & Zdravkovic, 1999). Advanced elasto-plastic constitutive models can in principle simulate real soil behaviour, but each model is capable of capture some features better than others. In this Section an elasto-plastic constitutive model with two intersecting yield surfaces called Lade’s double hardening model (Lade, 1977) is explained. The theory of this model is based on the behaviour observed in isotropic compression and triaxial compression tests on different cohesionless soils (Lade, 1977). The model is based on concepts from non-linear elasticity and isotropic work-hardening/softening plasticity theories and it was implemented in ICFEP in 1994 by Kovacevic (Potts & Zdravkovic, 1999; Kovacevic, 1994). It is applicable to general three-dimensional stress condition, but the input parameters can be derived entirely from the results of isotropic compression and conventional drained triaxial compression tests (Lade, 1977). The formulation of the model, in terms of elastic behaviour, failure criterion, yield function, plastic potential and hardening and softening rules, is described. This model is useful for representing the behaviour of fill materials, indeed it has been used extensively at Imperial College for modelling the behaviour of fill materials typical of embankment constructions (Potts & Zdravkovic, 1999).

4.3.1 Basic behaviour of cohesionless soils

To model the stress-strain behaviour of soils through the elasto-plastic theory, the total strain increment vector $\Delta\varepsilon$ can be divided into two components, an elastic component $\Delta\varepsilon^{e}$ and a plastic component $\Delta\varepsilon^{p}$:

$$\Delta\varepsilon = \Delta\varepsilon^{e} + \Delta\varepsilon^{p} \tag{4.13}$$

In the double hardening model the plastic component $\Delta\varepsilon^{p}$ is divided into two parts, a plastic collapse component $\Delta\varepsilon^{p,c}$ and a plastic expansive component $\Delta\varepsilon^{p,p}$ (Lade, 1977):

$$\Delta\varepsilon^{p} = \Delta\varepsilon^{p,c} + \Delta\varepsilon^{p,p} \tag{4.14}$$

These strain components are calculated separately, the elastic strains by Hooke's law, the plastic collapse strains by a plastic stress-strain theory involving a cap-type yield surface, and the plastic expansive strains by a stress-strain theory which involves a conical yield surface with apex at the origin of the stress space (Lade, 1977). Figure 4.3 shows a typical result of a triaxial test, in terms of variations of stress difference $(\sigma_1 - \sigma_3)$ and volumetric strain ε_v with axial strain. The total strain is considered to consist of elastic, plastic collapse, and plastic expansive components of strain. Both elastic (recoverable) and plastic (irrecoverable) deformations occur from the beginning of loading of a cohesionless soil, the stress-strain relationship is nonlinear, and a decrease in strength follows peak failure (Lade, 1977). The plastic strains are initially smaller than the elastic strains, but at higher values of stress the plastic strains dominate the response (Lade, 1977).

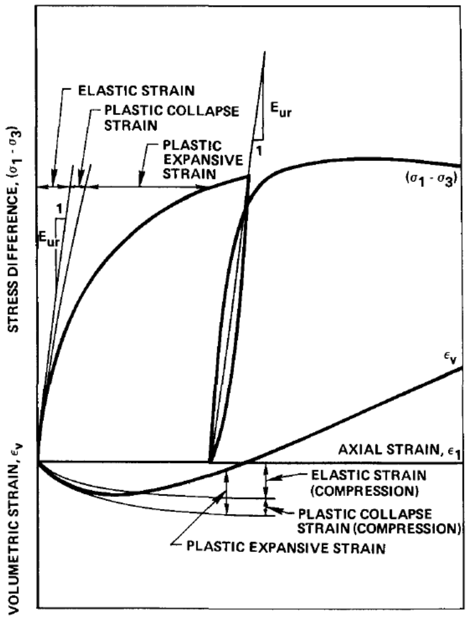

Figure 4.3 Schematic illustration of elastic, plastic collapse and plastic expansive strain components in drained triaxial compression test (Lade, 1977)

4.3.2 Overview of the model

The model is characterized by an elastic domain closed by two intersecting yield surfaces, the conical and the cap yield surfaces. There is a following representation of the yield surfaces in the $J - p'$ plane of invariant quantities (Fig. 4.4) where p' is the mean effective stress and J is the deviatoric stress.:

$$p' = \frac{\sigma_1' + \sigma_2' + \sigma_3'}{3} \tag{4.15}$$

$$J = \frac{1}{\sqrt{6}} \sqrt{(\sigma_1' - \sigma_2')^2 + (\sigma_2' - \sigma_3')^2 + (\sigma_3' - \sigma_1')^2} \tag{4.16}$$

If a soil is normally consolidated, it is plastic and its stress state is on both the yield surfaces, for example point “a” in Fig. 4.4 a (Potts & Zdravkovic, 1999). From that point, the behaviour depends on the direction of the stress path. If the stress path moves below both yield surfaces (into zone 1 in Fig. 4.4 b), the behaviour is nonlinear elastic and the soil becomes over consolidated. If it is directed into zone 2, the behaviour is elasto-plastic and only the cap yield surface is active, which expands following the work hardening rule, while the conical yield surface remains fixed. If the stress path is directed into zone 4, the behaviour is elasto-plastic as well with the dormant cap and the active conical surface, which expands or contracts depending on the work hardening/softening rules. If the stress path moves into zone 3, both yield surfaces are activated simultaneously, expanding the elastic domain (Potts & Zdravkovic, 1999).

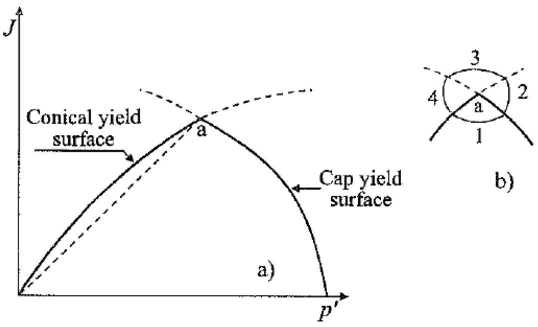

Figure 4.3 Yield surfaces for Lade’s double hardening model (Potts and Zdravkovic, 1999)

4.3.3 Elastic Behaviour

The elastic behaviour is characterized by isotropic elasticity, requiring two independent elastic parameters: a stress dependent Young's modulus E and a constant value of Poisson's ratio ν. Lade defined a relation between the unloading-reloading modulus and the effective confining pressure σ_3':

$$E = MPa\left(\frac{\sigma_3'}{Pa}\right)^n \tag{4.17}$$

Where the dimensionless and constant values at a given initial void ratio modulus number M and exponent n are determined from triaxial compression tests performed with various values of the confining pressure σ_3', and Pa is the atmospheric pressure expressed in the same units as E and σ_3' (Lade, 1977).

There are other two alternatives for this model in ICFEP to calculate the Young's modulus E. The first replaces the minor principal effective stress σ_3' by the mean effective stress p':

$$E = MPa\left(\frac{p'}{Pa}\right)^n \tag{4.18}$$

Where

$$p' = \frac{\sigma_1'+\sigma_2'+\sigma_3'}{3} = \frac{\sigma_x'+\sigma_y'+\sigma_z'}{3} \tag{4.19}$$

The above expressions of the Young's modulus are non-conservative and that energy could be extracted or generated from certain loading cycles (Zytinski *et al.*, 1978), but in practice this fact may not be important if monotonic loading is considered and may become significant if the loading involves many stress reversals (Kovacevic, 1994). The third expression of the Young's modulus was derived by Lade and Nelson (1987) from theoretical considerations based on the principle of conservation of energy (Kovacevic, 1994):

$$E = NPa\left[\left(\frac{I_1}{Pa}\right)^2 + R\left(\frac{J_2}{Pa}\right)^2\right]^\lambda \tag{4.20}$$

Where I_1 is the first invariant of the effective stress tensor (4.22), J_2 is the second invariant of the deviatoric stress tensor (4.23) and R is a constant (4.21).

$$R = \frac{6(1+\nu)}{1-2\nu} \tag{4.21}$$

$$I_1 = \sigma_1' + \sigma_2' + \sigma_3' = \sigma_x' + \sigma_y' + \sigma_z' \tag{4.22}$$

$$J_2 = J^2 = \frac{1}{6}[(\sigma_1'-\sigma_2')^2 + (\sigma_2'-\sigma_3')^2 + (\sigma_3'-\sigma_1')^2] =$$

$$= \frac{1}{6}\left[\left(\sigma_x'-\sigma_y'\right)^2 + \left(\sigma_y'-\sigma_z'\right)^2 + (\sigma_z'-\sigma_x')^2\right] + \tau_{xy}^2 + \tau_{yz}^2 + \tau_{zx}^2 \tag{4.23}$$

The parameter Pa is atmospheric pressure expressed in the same units as E, I_1 and $(J_2)^{\frac{1}{2}}$, and the modulus number N and the exponent λ are constant, dimensionless numbers (Kovacevic, 1994).

All of the above three expressions have been implemented in ICFEP by Kovacevic (1994), but only the first one is used in this thesis.

4.3.4 Failure Criterion

The failure surface is curved for most cohesionless soils and the friction angle decreases with increasing magnitude of the mean normal stress (Lade, 1977). To consider this aspect in a failure criterion, Lade (1977) studied data from triaxial compression tests on many different cohesionless soils obtaining a relationship between the stresses at failure in terms of the first and the third stress invariants I_1 and I_3:

$$\eta_1 = \left(\frac{I_1^3}{I_3} - 27\right)\left(\frac{I_1}{Pa}\right)^m \tag{4.24}$$

Where

$$I_3 = \sigma_1' \, \sigma_2' \, \sigma_3' = \sigma_x'\sigma_y'\sigma_z' + \tau_{xy}\tau_{yz}\tau_{zx} + \tau_{yx}\tau_{zy}\tau_{xz} -$$

$$-\left(\sigma_x'\tau_{yz}\tau_{zy} + \sigma_y'\tau_{zx}\tau_{xz} + \sigma_z'\tau_{xy}\tau_{yx}\right) \tag{4.25}$$

η_1 and m are dimensionless and constant parameters at a given initial void ratio.

The failure criterion has a curved shape in the $J - p'$ space (Fig. 4.5 a), and a rounded triangular shape in the deviatoric plane (Fig. 4.5 b) (Potts & Zdravkovic, 1999). The apex angle and the curvature of the failure surface increase with the values of η_1 and m respectively. For $m = 0$ the failure surface is straight in $J - p'$ space (Lade, 1977).

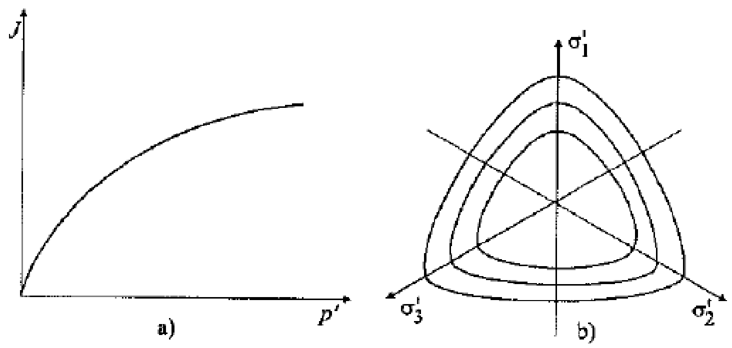

Figure 4.4 Failure criterion: a) in the J-p' space, b) in the deviatoric plane (Potts and Zdravkovic, 1999)

To introduce the effective cohesion and tensile strength, the principal stress space has been translated along the hydrostatic axis (Fig. 4.6) (Kovacevic, 1994). A constant value of $a\ Pa$ is added to the normal effective stresses σ' to obtain:

$$\underline{\sigma'} = \sigma' + aPa \tag{4.26}$$

Where a is a dimensionless parameter. The value of $a\ Pa$ represents the effect of the tensile strength of the material.

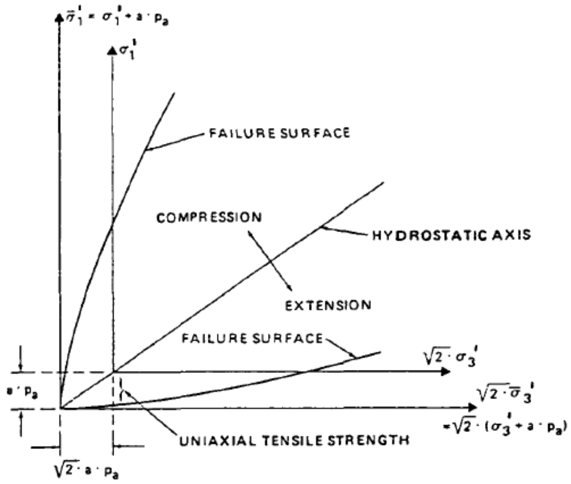

Figure 4.5 Translation of principal stress space along hydrostatic axis to include effect of tensile strength in failure criterion (after Lade, 1984)

4.3.5 Plastic Collapse Strains

During an isotropic compression test, an increase of isotropic stresses causes a partial collapse of the grain structure resulting in a volumetric compression, which is the reason of the plastic strains that occurs during the test. The elastic strains which are recoverable upon unloading can be calculated with good accuracy from Hooke's law, while the irrecoverable collapse strains can therefore be separated from the total strains observed in these tests by subtracting the elastic strains (Lade, 1977). Normally, for a general stress increment (not along the hydrostatic axis), it is complicated to divide the plastic strains into collapse strains and expansive strains, because both types of strain occur simultaneously for such a stress increment. It is therefore necessary to find the magnitudes of the collapse strains from isotropic compression, the only loading condition which does not produce plastic expansive strains (Lade, 1977, Kovacevic, 1994). To reproduce this behaviour, the chosen yield surface forms a cap on the open end of the conical yield surface (Fig. 4.7). The collapse yield criterion forms a sphere with centre at the origin of the principal effective stress space, which is connected with the conical yield surface

(Lade, 1977). The equation for the yield cap can be written in terms of the first and the second stress invariants I_1 and I_2, respectively (Kovacevic, 1994):

$$f_c = I_1^2 + 2\,I_2 - H_c = 0 \tag{4.27}$$

Where

$$I_2 = -(\sigma_1'\sigma_2' + \sigma_2'\sigma_3' + \sigma_3'\sigma_1') = \tau_{xy}\tau_{yx} + \tau_{yz}\tau_{zy} + \tau_{zx}\tau_{xz} -$$
$$-\left(\sigma_x'\sigma_y' + \sigma_y'\sigma_z' + \sigma_z'\sigma_x'\right) \tag{4.28}$$

As the value of f_c increases beyond its current value, the soil work-hardens and collapse strains are produced. According to the yield criterion yielding does not result in eventual failure, which is controlled entirely by the conical yield surface (Lade, 1977).

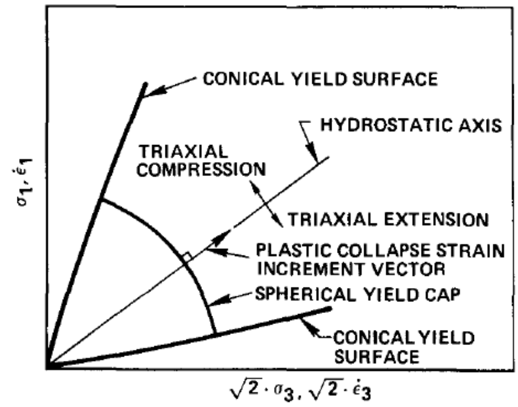

Figure 4.6 Location of yield cap relative to conical yield surface shown in triaxial plane (Lade, 1977)

H_c is the work-hardening parameter described by

$$H_c = Pa^2 \left[\frac{W_{p,c}}{C\,Pa}\right]^{\frac{1}{p}} \tag{4.29}$$

Where p and C are dimensionless material parameters and $W_{p,c}$ is the accumulated plastic work associated with the cap yield surface (Kovacevic, 1994):

$$W_{p,c} = \sum\left(\Delta W_{p,c}\right) = \sum\left(\sigma^T \Delta\varepsilon^{p,c}\right) \tag{4.30}$$

Isotropic compression of an isotropic soil results in equal linear strains in the three principal directions (Lade, 1977). Thus, for this condition the strain increment vector should be pointed in the direction outward from the origin and coincide with the hydrostatic axis, as shown in Fig. 4.7 (Lade, 1977). To allow this condition, the cap yield surface uses an associated flow rule:

$$f_c = g_c \tag{4.31}$$

4.3.6 Plastic Expansive Strains

The plastic expansive strains $\Delta\varepsilon^{p,p}$ are governed by a conical yield surface, the same shape of the failure surface with curved meridians in any plane containing the hydrostatic axis and a smoothly rounded triangular cross-section in the deviatoric plane (see Figure 4.8 b) (Kovacevic, 1994). The process of hardening is isotropic, because the conical yield surface expands symmetrically around the hydrostatic axis. This yield surface is expressed by the following relation

$$f_p = \left(\frac{I_1^3}{I_3} - 27\right)\left(\frac{I_1}{Pa}\right)^m - H_p = 0 \tag{4.32}$$

where m is a parameter describing the curvature of the surface meridians and H_p is a work-hardening parameter which defines the size of the surface. The ultimate value of H_p corresponds to the failure surface where $H_p = \eta_1$. During unloading and neutral loading, the yield surface remains in the same position corresponding to the highest value of H_p previously applied to the soil (Lade, 1977).

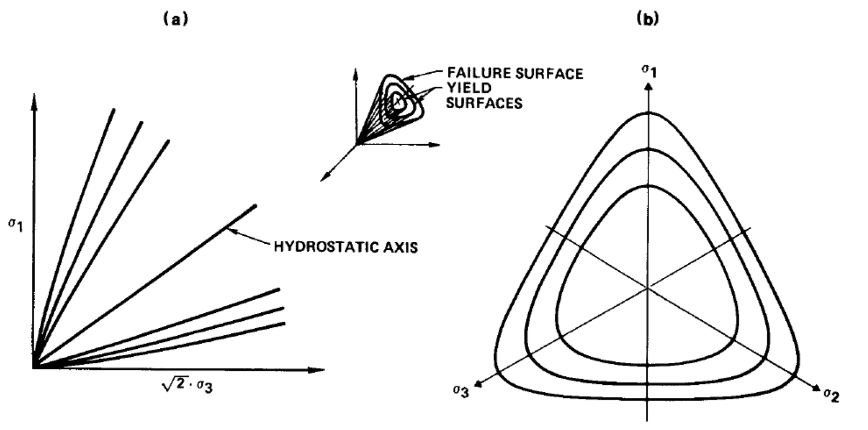

Figure 4.7 Characteristics of failure and yield surfaces shown in principal stress space: a) in triaxial plane, b) in deviatoric plane (Lade, 1977)

For the plastic expansive strains, the associated flow rule is not accurate, therefore, the plastic potential function differs from the yield function (Lade, 1977). The plastic potential surfaces are shaped like asymmetric bullets with their pointed apices at the origin of the stress space, their traces in octahedral planes are the same as those for the yield surfaces (Fig. 4.8 b) and their traces in triaxial planes resemble those of the yield surface (Fig. 4.8 a), but their apex angles are greater, they are more curved, they cut the yield surfaces, and they become asymptotic to the hydrostatic axis at a greater rate than the yield surfaces (Lade, 1977). The plastic potential is defined by the following expression:

$$g_p = I_1^3 - I_3\left[27 + \eta_2\left(\frac{Pa}{I_1}\right)^m\right] \tag{4.33}$$

Where the value of η_2 is a parameter which depends on H_p and on the minimum principal effective stress σ_3':

$$\eta_2 = \mathrm{S}\,H_p + R\left(\frac{\sigma_3'}{Pa}\right)^{1/2} + t \tag{4.34}$$

In which S, R and t are dimensionless parameters.

The work-hardening (or softening) parameter H_p is defined as:

$$H_p = a\,e^{-b\,W_{p,p}}\left(\frac{W_{p,p}}{Pa}\right)^{1/q} \tag{4.35}$$

Where $W_{p,p}$ is the accumulated plastic expansive work calculated from

$$W_{p,p} = \sum\left(\Delta W_{p,p}\right) = \sum(\sigma^T\Delta\varepsilon^{p,p}) \tag{4.36}$$

in which $(\sigma^T\Delta\varepsilon^{p,p})$ is the plastic work done per unit volume during the strain increment vector $\Delta\varepsilon^{p,p}$ (Kovacevic, 1994) The parameters a, b and q are dependent on the minimum principal effective stress σ_3':

$$a = \eta_1\left(\frac{e\,Pa}{W_{p.peak}}\right)^{1/q} \tag{4.37}$$

$$b = \frac{1}{q\,W_{p.peak}} \tag{4.38}$$

$$q = \alpha + \beta\frac{\sigma_3'}{Pa},\;\; q \geq 1 \tag{4.39}$$

Where e is the base for natural logarithms and $W_{p.peak}$ is the accumulated plastic work associated with the conical yield surface at peak strength, which depends on the minimum principal effective stress σ_3':

$$W_{p.peak} = Pa\ P \left(\frac{\sigma_3'}{Pa}\right)^I \tag{4.40}$$

Where P and I are dimensionless parameters.

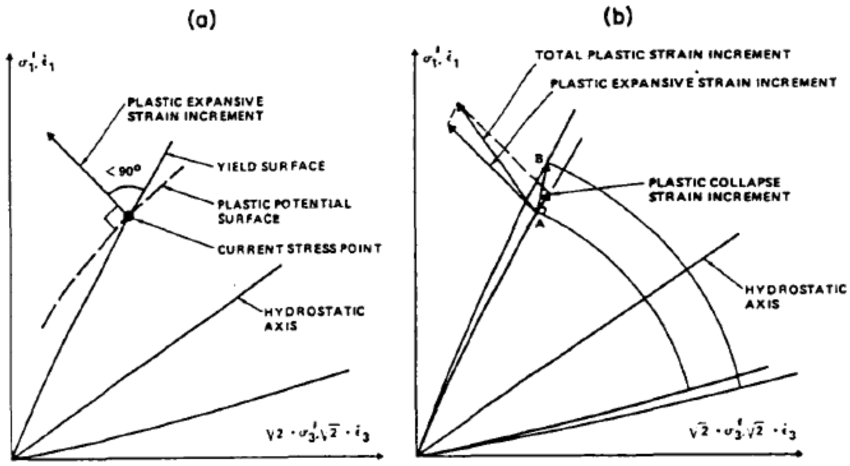

Figure 4.8 Schematic diagrams of a) yield and plastic potential surfaces for plastic expansive strains and (b) yielding process with both yield surfaces activated and combination of plastic strain increments (after Lade and Nelson, 1984)

In Figure 4.9 b the yielding process with both yield surfaces active is shown for the triaxial plane and all the vectors of total plastic strain increment, plastic expansive strain increment and plastic collapse strain increment are represented. The total plastic strain increment is calculated by summing the two components of the vector and the total strain increment is obtained by adding the elastic strain component (Kovacevic, 1994).

The model is characterized by fourteen (or fifteen, in the case of materials with effective cohesion) parameters. Three parameters determine the elastic response (M or N, n or λ, ν), two are connected with the plastic collapse strain component (C and p), and nine with the plastic expansive strain component ($\eta_1, m, S, R, t, \alpha, \beta, P, I$).

5. THE MONTEDOGLIO ZONED EARTH DAM

5.1 DESCRIPTION OF THE DAM

The Montedoglio dam is a 64 m high earth-core rockfill dam located on the Tiber River at about 24 km from Arezzo in the Tuscany region, with the function to provide irrigation water storage with a reservoir capacity of $153 \cdot 10^6$ m^3. Construction of the dam started in 1977 and was completed in 1986. The reservoir was first impounded in 1990 and finally reached its full capacity in 2010. The crest length and the crest width are 566 and 8 m, respectively. The vertical core is constituted by compacted clayey silt whereas the upstream and downstream shells are formed by river bed alluvial material. Drainage layers within both upstream and downstream shells and filters between the core and the shells are also present. The upstream slope is 2.6:1, the downstream shell is characterized by berms and the average slope is 2.4:1. The core width is 4.1 m, the core slope is 1:6 while in the foundation it becomes about 1:1.5. The shells rest on a 6 m layer of compacted alluvial soil, while the core is directly founded on a formation of ophiolitic rocks. The plain view and the main simplified cross-section of the embankment dam are presented in Fig. 5.1 and 5.2, respectively.

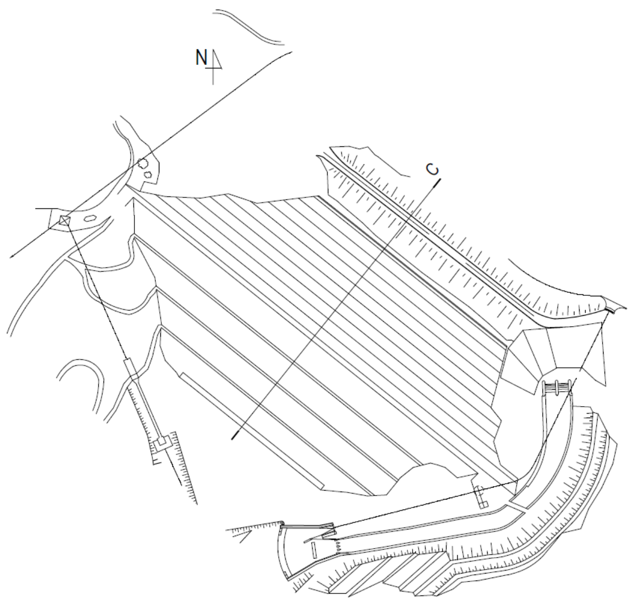

Figure 5.1 Plain view of Montedoglio dam

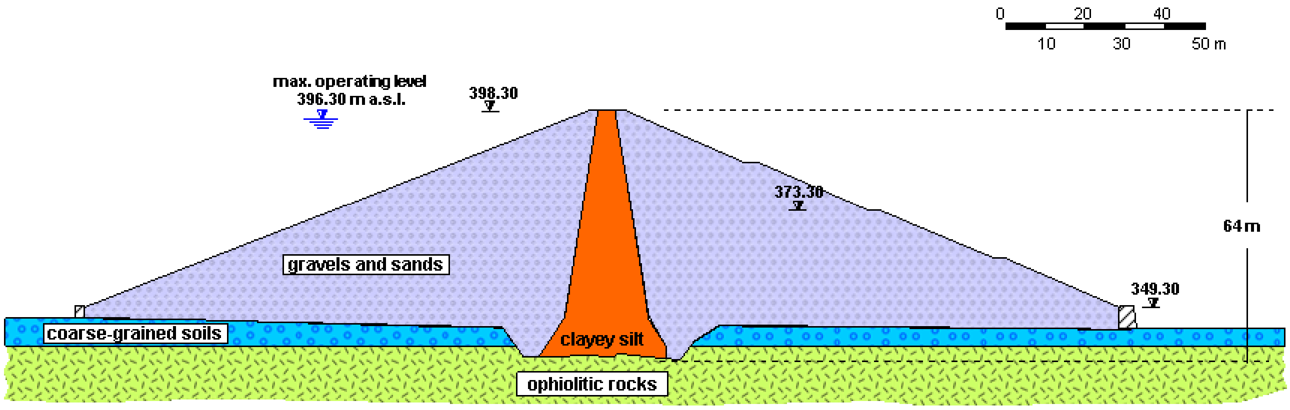

Figure 5.2 Main cross-section of Montedoglio dam

5.2 GEOTECHNICAL CHARACTERIZATION

The Montedoglio dam was extensively investigated during years, specifically during the design, construction and service life. Table 5.1 summarises the geotechnical investigations carried out since 1963, for the design of the dam, up to 2013 whose geotechnical campaign was conducted for the seismic reassessment studies. The main purposes of the investigations are also summarized in the Table 5.1. Only some test results are presented here, which are essential to model the construction and impoundment phases of the dam.

Table 5.1 Geotechnical campaigns carried out for the characterization of the dam and foundation materials

Year	**Type of test**
1963	Seismic refraction tests and laboratory tests for design of the dam
1967	Seismic refraction tests on the foundation materials of the dam
1971	Seismic refraction tests on the left bank
1977-1986	In situ and laboratory tests during construction
1982	Cross-hole test within the dam body during construction (dam height was 18 m)
1994-1995	In situ and laboratory tests during service life for maintenance problems
2013	In situ and laboratory tests for the seismic revaluation of the dam

5.2.1 In situ tests

Before the construction of the dam, in the period 1963-1971, three geotechnical campaigns were carried out, consisting essentially in field tests. A plain view of the location of the in situ tests is illustrated in Figure 5.3. During the first campaign (1963), seismic refraction tests were carried out with the purpose of determining the P-waves velocity of the foundation soils. Other seismic refraction tests were conducted in 1967 on the foundation materials, along the cross-sections A, B, C and D (Fig. 5.3). Seismic refraction tests were further executed in 1971 to investigate the dynamic properties of the alluvial soil layer (Fig. 5.3 A-A3 and B1-B3) and those of the left bank (Fig. 5.3 C1-C17 and D1-D4) of the dam. The results of all tests are summarized in Table 5.2. Three different layers can be identified, that is a 5-6 m thick layer of alluvial deposit, the altered portion of the bedrock, which is located in the surficial part of the subsoil, and the intact bedrock constituted by ophiolitic rocks. The values of P-wave velocities are summarized in Table 5.2 and are pretty consistent among the three different tests performed.

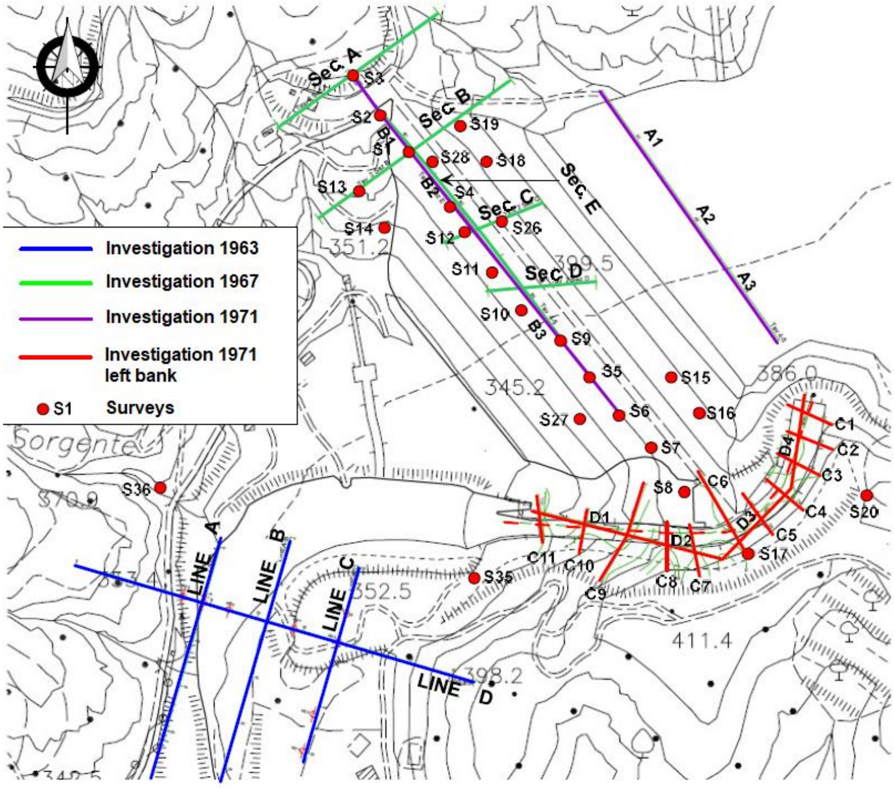

Figure 5.3 Plain view of seismic refraction tests and surveys before the construction of the dam

Table 5.2 P- waves velocities of the foundation materials determined using seismic refraction tests

Year	V_p (m/s)				
	Superficial layer	**Altered rock (shoulders)**	**Alluvial layer**	**Altered rock (riverbed)**	**Bedrock**
1963	500	1400	1900	-	3500-4500
1967	500	-	1500	2400-3200	3500-4700
1971	300-500	800-1200	1500-1600	2500-3000	3500-4500

In 1982 the embankment dam was partially constructed up to the elevation of 358 m a.s.l., corresponding to about 18 m dam height from the base. Cross hole tests were performed in six boreholes along the main axis of the dam in both upstream and downstream shells and in the core (see Fig. 5.4). In Fig. 5.5 profiles of P-waves and S-waves velocities, and Poisson's ratio are shown. The S-waves velocity V_s remains pretty uniform in the downstream shell with values of about 530 m/s up to 15 m deep (345 m a.s.l.), where the values increase gradually from 530 to 900 m/s, corresponding to a 4-5 m thick alluvial layer above the foundation rock. In the upstream shell the V_s values are similar to those of the downstream shell, disregarding the first 4-5 m with about 400 m/s. In the core V_s is pretty constant and equal to 300 m/s with depth down to 337 m a.s.l., where it reaches 700 m/s because of the presence of foundation soil. The P-waves velocity V_p is similar in the upstream and downstream shells and equal to about 1000 m/s in the 13 m below ground level while between 13 and 18 m it increases gradually up to 3000 m/s. In the core V_p is 800 m/s up to 343 m a.s.l., where it starts to increase reaching 1000 m/s. The Poisson's ratio is defined from theory of elasticity as:

$$\nu = \frac{1}{2}\frac{\left(\frac{V_p}{V_s}\right)^2 - 2}{\left(\frac{V_p}{V_s}\right)^2 - 1} \tag{5.1}$$

In the core ν is uniform value with depth from 0.35 to 0.45, while in the shells varies between about 0.2 to 0.4.

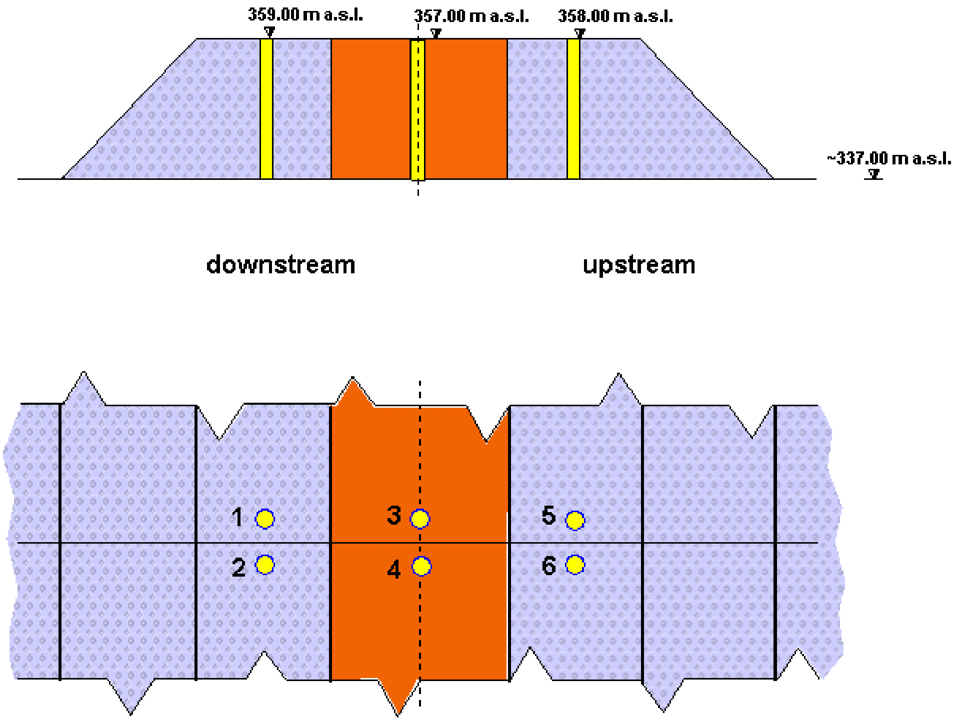

Figure 5.4 A schematic plain view and a cross section of the dam with bore holes for cross-hole tests in the core and in the shells in 1982

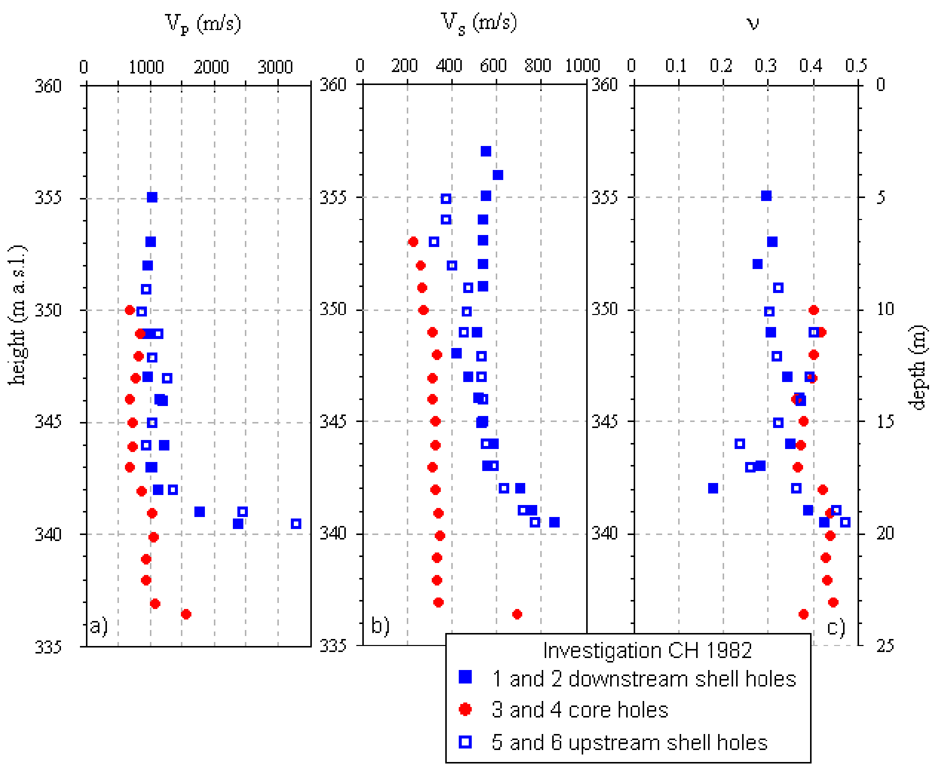

Figure 5.5 Profiles of P-waves and S-waves velocities and Poisson's ratio from cross-hole tests in the 1982

In 2013, an additional geotechnical campaign was carried out, aiming primarily at completing the dynamic characterization of dam body and foundation materials. In Fig. 5.6 the location of in situ tests is shown. Specifically, a seismic refraction test, two cross-hole tests and five HVSR (Horizontal to Vertical Spectral Ratio) tests were performed. The seismic refraction test was carried out on the downstream berm at elevation of 373.30 (see Fig. 5.6); the instruments covered a length of 110 m and allowed to investigate the subsoil up to a depthof 40 m. The results are presented in Figure 5.7 and indicate the presence of a 2-4 m thick superficial layer with V_p less than 1000-1200 m/s, a 30 m thick layer with V_p between 1200 m/s and 1600 m/s, a 32 m depth alluvial soil with 1800-2000 m/s and the rock substratum with 3200-3600 m/s.

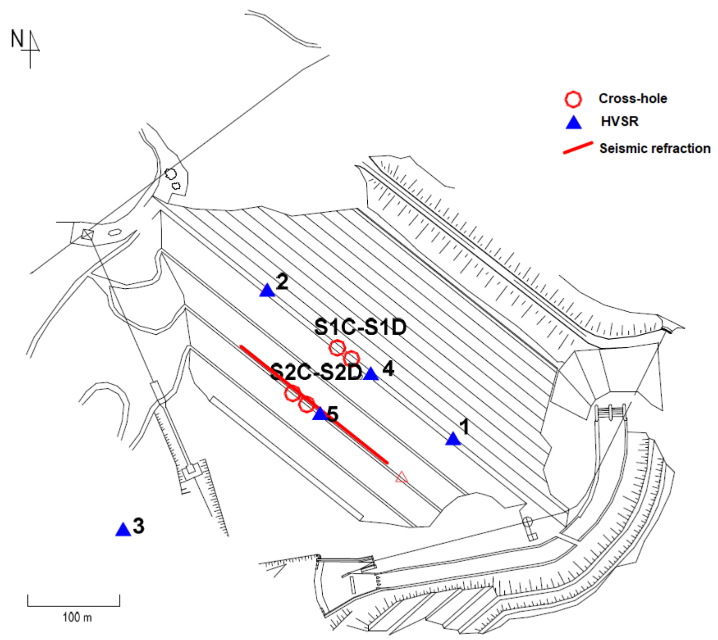

Figure 5.6 Plain view of field tests carried out in 2013

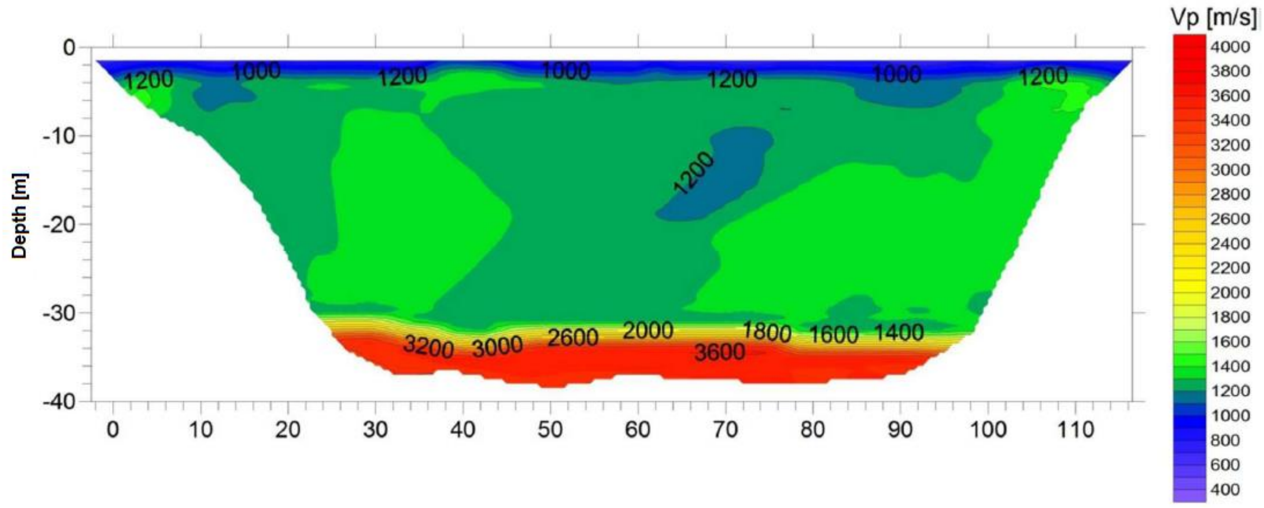

Figure 5.7 Cross-section of the dam with the values of P-waves velocity obtained from the seismic refraction test carried out in 2013

The cross-hole tests were made into the boreholes S1C-S1D and S2C-S2D (see Fig. 5.6), localized at the crest of the dam and at the downstream berm, respectively. The results presented in Fig. 5.8 and 5.9 show that the core is characterized by a S-waves velocity of 300 m/s and a P-waves velocity of 1200 m/s at the crest, which increases with depth to reach the values of 350 m/s and 1800 m/s of V_s and V_p, respectively. In the downstream shell the profile of V_s increases from 500 m/s at the top to 800-900 m/s in the alluvial layer and to 1700 m/s in the foundation rocks. A similar trend is shown by V_p with values starting from 1000 m/s at the top and reaching 4000 m/s in the bottom.

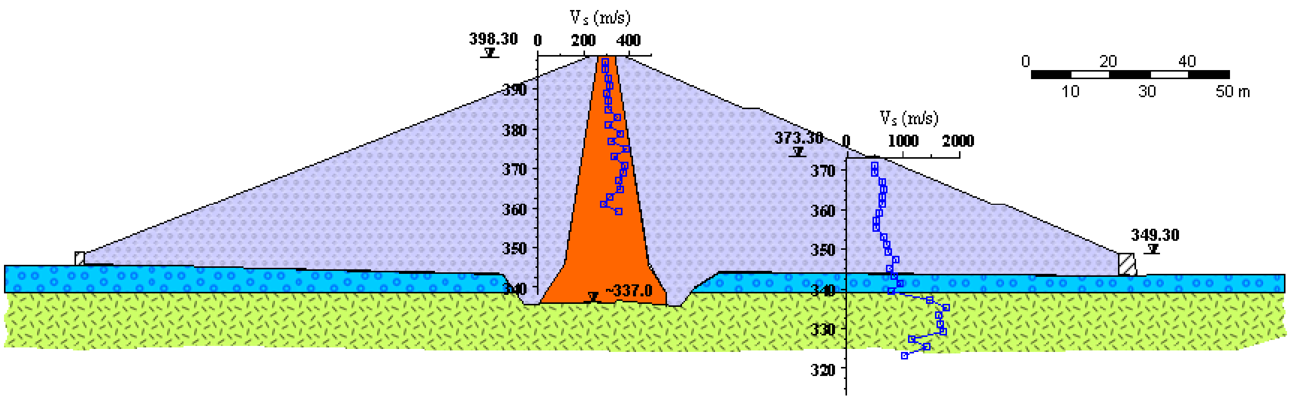

Figure 5.8 Profiles of S-waves velocity in the core and in the downstream shell from cross-hole tests carried out in the 2013 campaign

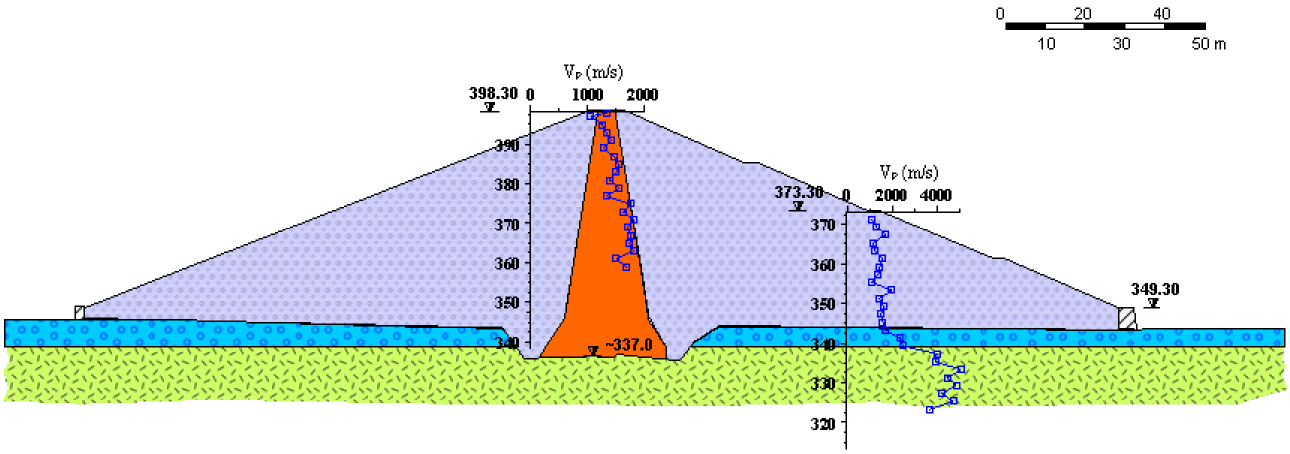

Figure 5.9 Profiles of P-waves velocity in the core and in the downstream shell from cross-hole tests carried out in the 2013 campaign

In Fig. 5.10 and 5.11 a comparison between the 1982 and 2013 cross-hole tests are presented. In the core (see Fig. 5.10) values of S-waves velocity from both investigations are similar, while the values of the 2013 P-waves velocity are higher than those of the 1982 campaign. In the downstream shell the 2013 velocities are slightly greater than those of 1982, probably due to the influence of the overburden pressure.

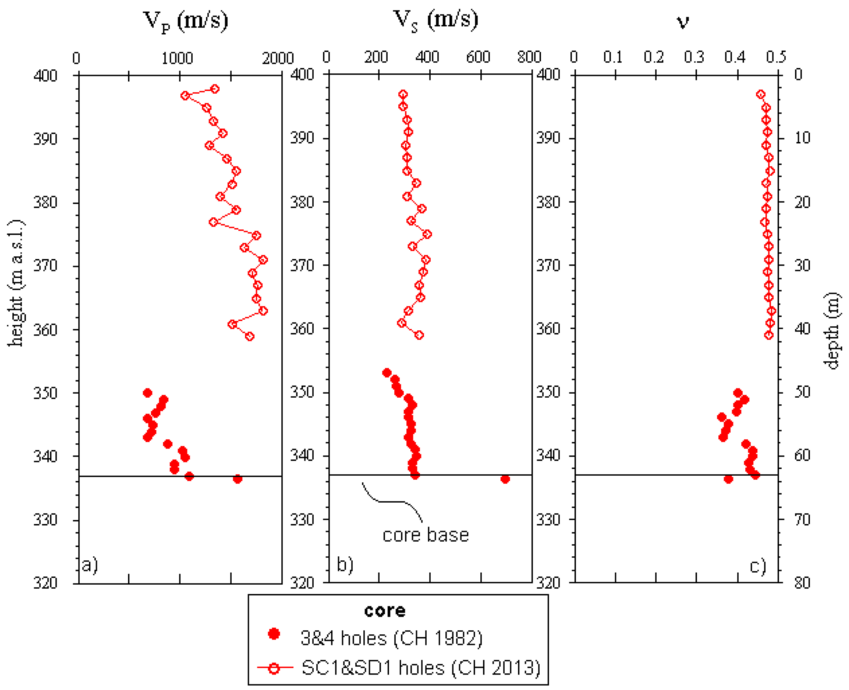

Figure 5.10 Profiles of Vs, Vp and ν for the core from cross-hole tests of 2013 and 1982

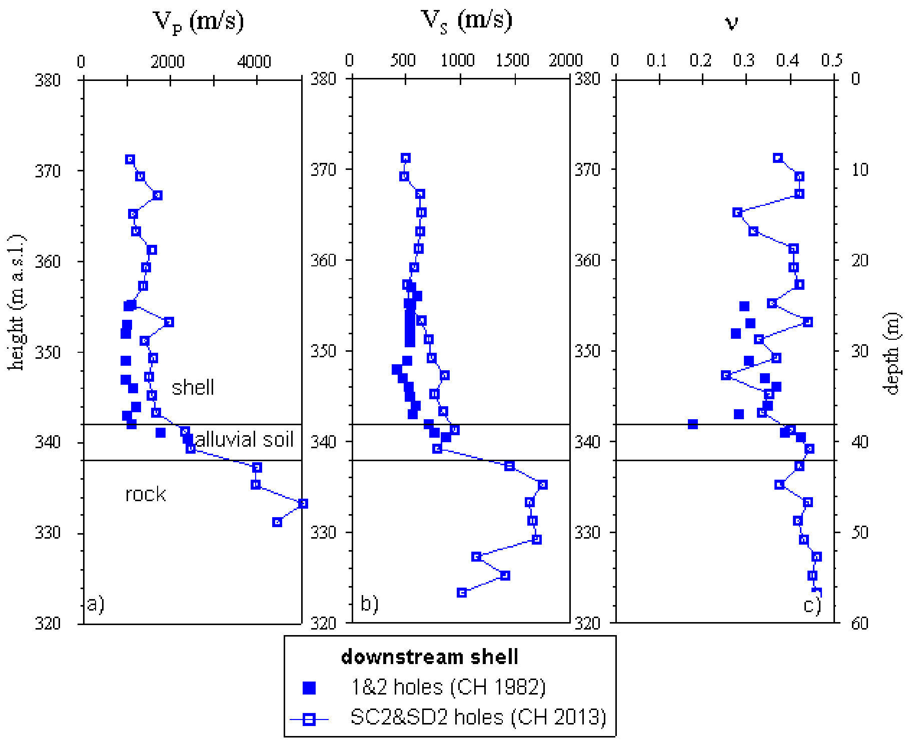

Figure 5.11 Profiles of Vs, Vp and ν for the downstream shell from cross-hole tests of 2013 and 1982

The experimental profile of Vs in the core is in accordance to the literature review (Lanzo, 2018), that is Vs slightly increases with depth due to the overconsolidation of the core material. This behaviour is also observed for the shell material. Anyway, these data have not been utilized in the thesis which concerns exclusively with the static dam behaviour.

In the borehole S1D within the core, a permeability test of Lefranc type was made in 2013, obtaining permeability coefficient $k = 9 \cdot 10^{-8}$ cm/s.

The main other in situ tests during construction and in 1994 for both the dam materials are summarized in Table 5.3 for the core and 5.4 for the shells.

Table 5.3 Mechanical and physical parameters for core material obtained from in situ tests

Type of test	**Tests number**	γ_d (kN/m^3)	$w - w_{opt}$ (%)
Density (during construction)	810	18-19	12-20

Table 5.4 Mechanical and physical parameters for shells material obtained from in situ tests

Type of test	Test number	γ_d (kN/m^3)	$w - w_{opt}$ (%)	k (cm/s)
Proctor (during construction)	25	21.8-22.8	6-8.58	-
Density (during construction)	777	22-24	5-10	-
Permeability (during construction)	10	-	-	2.3-3.21$\cdot 10^{-4}$
Density (1994)	-	-	2.69-4.62	-
Permeability (1994)	-	-	-	1.0-4.0$\cdot 10^{-3}$

5.2.2 Laboratory tests

For core and shells materials laboratory tests were carried out before, during and after the dam construction. According to the design of the dam, core and shells materials should have fulfil grain size distribution within the prescribed ranges indicated respectively in Fig. 5.12 and 5.13.

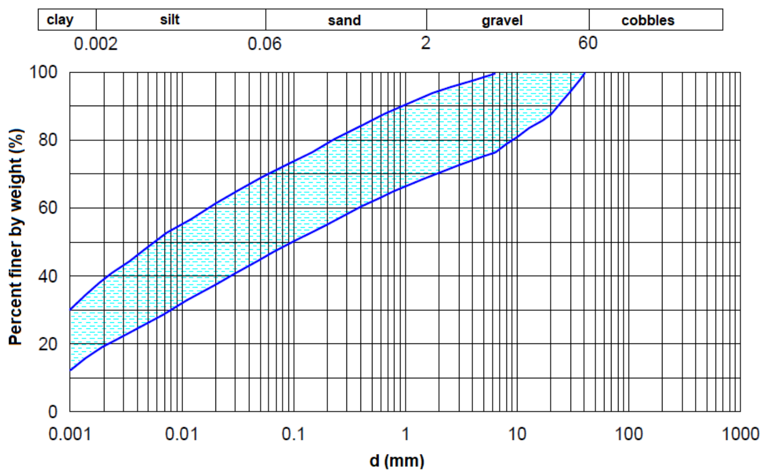

Figure 5.12 Grain size distribution of core material according to design prescriptions

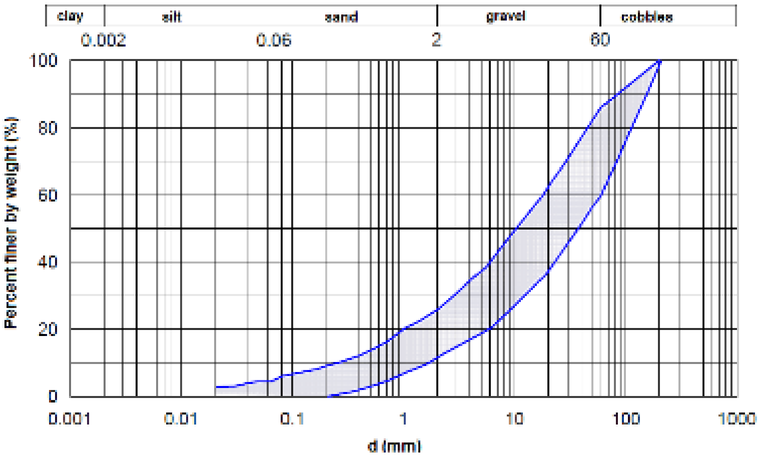

Figure 5.13 Grain size distribution of shell material according to design prescriptions

For the design of the dam, mechanical and physical parameters for core and shells materials were obtained by laboratory tests on reconstituted samples reported in Table 5.5 and 5.6 for core and shells, respectively. The permeability coefficient in the shell material was lower than expected, consequently layers of pervious material have been interposed within the shells. Stability analysis of the dam in the original design was performed assuming the smaller values obtained in laboratory tests, which are presented in Table 5.7 and Table 5.8.

Table 5.5 Mechanical and physical parameters for core material assumed for the design of the dam

γ_d (kN/m^3)	w_{opt} (%)	k (cm/s)	c' (kPa)	φ' (°)
20.4	9.5	$2.16 \cdot 10^{-8}$	60	35
18.0	15.7	$3.18 \cdot 10^{-9}$	55	16
19.1	11.3	$1.80 \cdot 10^{-8}$	50	24

Table 5.6 Mechanical and physical parameters for shells material assumed for the design of the dam

γ_d (kN/m^3)	w_{opt} (%)	k (cm/s)	c' (kPa)	φ' (°)
22.15	6.3	$1.67 \cdot 10^{-3}$	40	42
22.45	6.1	$1.91 \cdot 10^{-3}$		
-	-	$6.39 \cdot 10^{-4}$		

-	-	$5.09 \cdot 10^{-4}$		

Table 5.7 Mechanical and physical assumed parameters for core material for the stability analysis

γ_d (kN/m^3)	c (kPa)	φ (°)
18.0	50	16

Table 5.8 Mechanical and physical assumed parameters for shells material for the stability analysis

γ_d (kN/m^3)	c (kPa)	φ (°)
22	0	40

During construction, several laboratory tests were carried out on undisturbed samples for the core and on reconstituted samples for the shells. The main results are presented in Table 5.9 and 5.10, respectively. The grain size curves obtained for both core and shells are in the prescribed range. The dry unit weight and the water content of core lie in the range $\gamma_d = 18 - 20$ kN/m^3, $w = 10 - 18$ %, while for the shells $\gamma_d = 21.66 - 22.4$ kN/m^3, $w = 5.5 - 8.0$ %.

During construction, two consolidated drained triaxial tests were made on reconstituted samples of shell material, using apparatus of different diameter in two different laboratories. The first test was carried out in 1980 on samples of diameter $d = 10$ cm and height $h = 20$ cm; the reconstituted samples had grain size less than 25 mm and $\gamma_d = 21.6$ kN/m^3. This test resulted in $c' = 0$ kPa and $\varphi' = 41°$. The second test was made in 1983 on samples with diameter $d = 25$ cm and height $h = 60$ cm; grain size particle was less than 80 mm. The test led to $c' = 10$ kPa and $\varphi' = 48°$.

Table 5.9 Mechanical and physical parameters for core material obtained from tests during construction

Type of test	Test number	γ_d (kN/m^3)	$w - w_{opt}$ (%)	w_L (%)	I_p (-)	k (cm/s)
Grain size	156	-	-	-	-	-
Proctor	65	18-20	10-18	-	-	-

Cons. Limits	104	-	-	20-40	5-20	-
Permeability	103	-	-	-	-	$5.09 \cdot 10^{-9}$- $6.07 \cdot 10^{-8}$

Table 5.10 Mechanical and physical parameters for shells material obtained from tests during construction

Type of test	Test number	γ_d (kN/m^3)	$w - w_{opt}$ (%)	k (cm/s)	c' (kPa)	φ' (°)
Grain size	307	-	-	-	-	-
Proctor	2	21.6-22.4	5.5-8	-	-	-
CD Triaxial test	-	-	-	-	0	41
CD Triaxial test	2	-	-	1.26-1.43 $\cdot 10^{-4}$	10	48

During years 1994-1995, 21 undisturbed samples were taken from the core and 4 samples were taken from the shells. The range of grain size distribution of the core samples is different from the prescribed variation as Fig. 5.14 shows, while the average grain size distribution of the shell samples is on the lower bound of the prescribed range (Fig. 5.15).

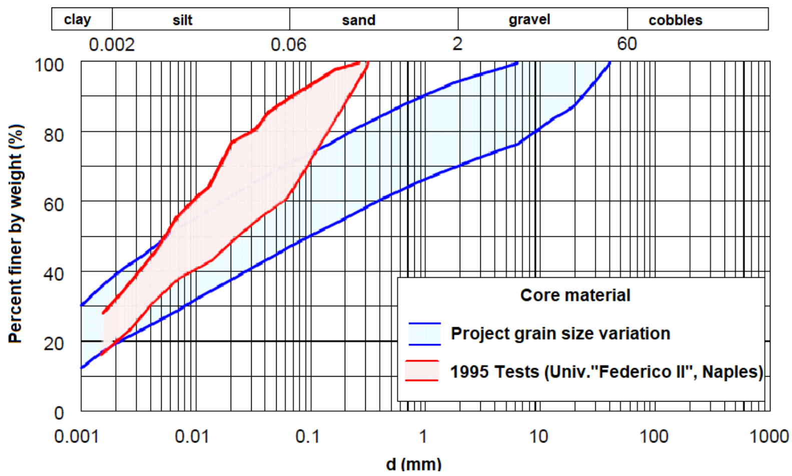

Figure 5.14 Comparison of grain size distribution from 1995 tests and prescribed grain size range from project for core material

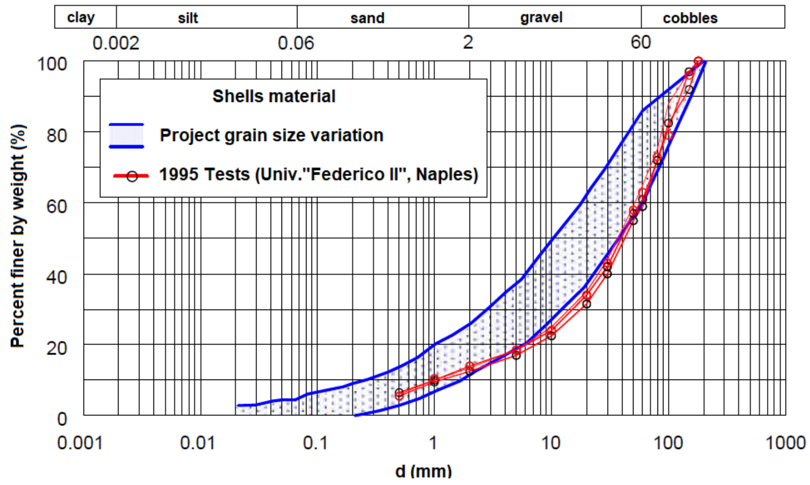

Figure 5.15 Comparison of grain size distribution from 1995 tests and design prescription in terms of grain size range for shells material

In Fig. 5.16 results from tests during 1995 on undisturbed samples from core are summarized in terms of variation of main physical and state properties with depth, while in Fig. 5.17 Casagrande plasticity and activity charts are presented. The average proprieties can be summarized as follows: unit weight is $\gamma = 20.7\ \mathrm{kN/m^3}$, water content $w = 19.2\%$, dry unit weight $\gamma_d = 17.4\ \mathrm{kN/m^3}$, void ratio $e = 0.54$ and porosity $n = 0.35$, plastic limit $w_p = 50.5$, the plasticity index $I_p = 23.28$ and the consistency index $I_c = 1.31$. Five permeability tests were carried on core samples obtaining values of coefficient of permeability between $0.4 \cdot 10^{-9}$ and $1.2 \cdot 10^{-9}\ \mathrm{cm/s}$ with the average value of $0.78 \cdot 10^{-9}\ \mathrm{cm/s}$ (Fig. 5.18). Seven isotropic consolidated undrained triaxial tests were carried out on undisturbed core samples showing a value of friction angle in the range of 23.5-28.7° (average value 25.5°) assuming cohesion $c' = 0$, and a distribution of undrained cohesion with depth as indicated in Fig. 5.19. The triaxial tests were processed again giving back values of $\varphi' \approx 20°$ and $c' = 40\ \mathrm{kN/m^2}$. In Table 5.11 physical and mechanical average core parameters are summarized resulting from tests during construction and during years 1994-1995.

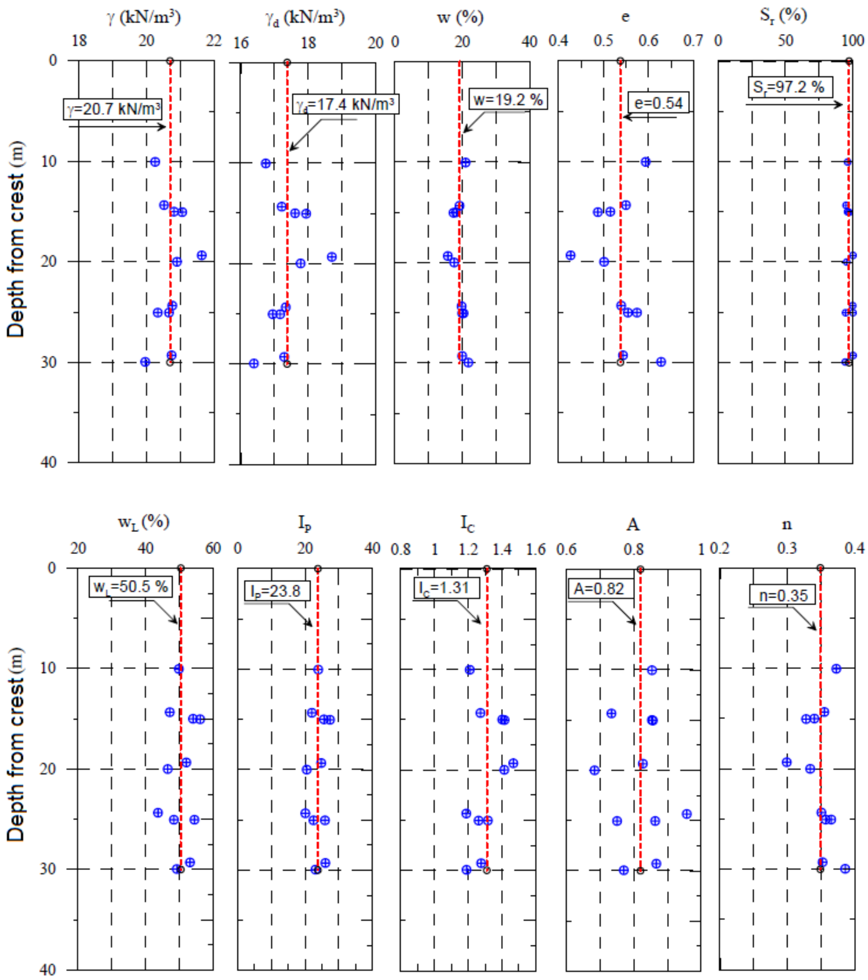

Figure 5.16 Variation of the main physical and state properties of the core material with depth from laboratory tests in 1995

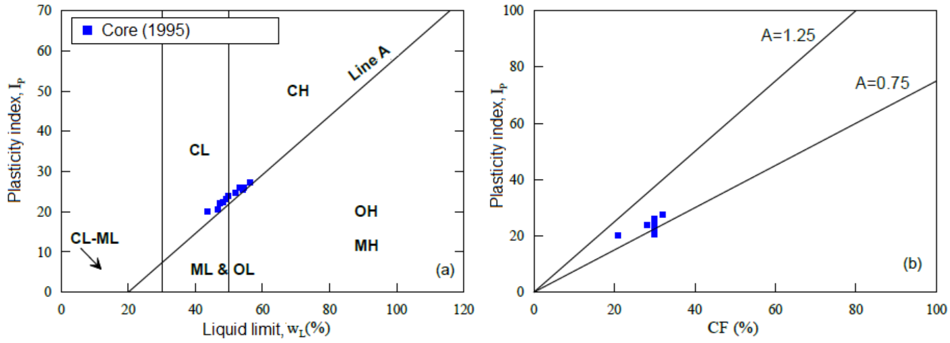

Figure 5.17 a) Casagrande plasticity chart b) Activity chart of core material based on laboratory tests carried out in 1995

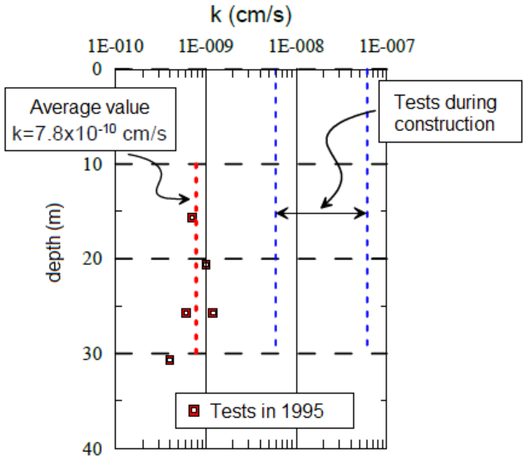

Figure 5.18 Values of permeability coefficient for the core soil

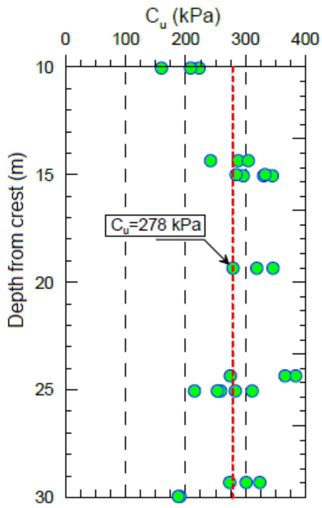

Figure 5.19 Profile of undrained cohesion c_u from laboratory tests on undisturbed core samples carried out in 1995

Table 5.11 Physical and mechanical average core parameters

Core parameter	**Average value**
γ (kN/m^3)	20.7
γ_d (kN/m^3)	17.4
w (%)	19.2
e	0.54
n	0.35
w_L (%)	50.5

I_p	23.8
I_c	1.3
k (cm/s)	$3 \cdot 10^{-8}$
c' (kPa)	0
φ' (°)	23.5-28.7
C_u (kPa)	278

In 1994 in situ tests were conducted for the measurement of the permeability coefficient obtaining values varying between 1 cm/s and $4 \cdot 10^{-3}$cm/s, (average value of $2.9 \cdot 10^{-3}$cm/s). In Fig. 5.20 these test results are compared with those from design and from in situ and laboratory tests during construction.

In 1993 consolidated drained triaxial test was carried out on a sample with diameter $d = 35.5$ cm and height $h = 82.5$ cm. The samples were compacted at approximately optimum water content and density (6.5% e 20.5 kN/m^3). The resulting strength parameters are $c' = 0$ kPa and $\varphi' = 42.4°$ for $\sigma_3' \leq 100$ kPa, and $c' = 35.9$ kPa and $\varphi' = 39.4°$ for $100 \leq \sigma_3' \leq 500$ kPa. Results are presented in Fig. 5.21 for three values of confining pressures $\sigma_3' = 100, 200, 300$ kPa. The Poisson ratio was calculated using the following elastic relation:

$$\nu' = \frac{1}{2}\left(1 - \frac{\varepsilon_v}{\varepsilon_a}\right) \quad (5.2)$$

After applying σ_3', constant head permeability tests were made obtaining permeability coefficients of $k = 1.45 \cdot 10^{-2}$ cm/s and $k = 0.74 \cdot 10^{-3}$ cm/s for $\sigma_3' = 100$ kPa and $\sigma_3' = 200$ kPa, respectively. In Table 5.12 physical and mechanical average shells parameters resulting from tests during construction and during years 1993-1995 are summarized.

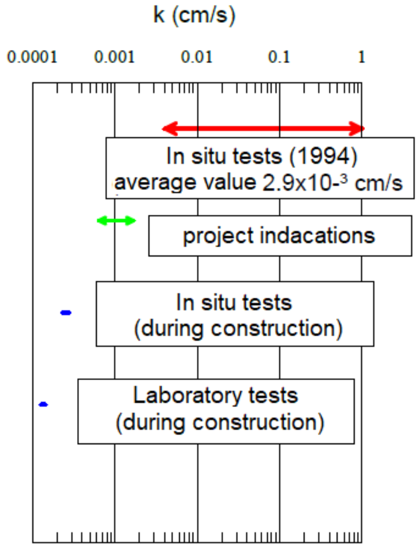

Figure 5.20 Values of permeability coefficient for the shells soil

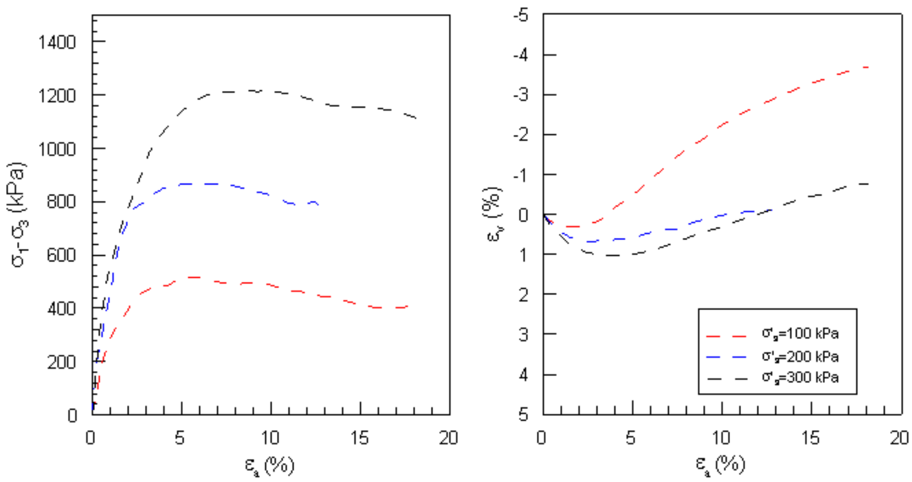

Figure 5.21 Results from large consolidated drained triaxial test on shell material carried out in 1993

Table 5.12 Physical and mechanical average shells parameters

Shells parameter	**Average value**
γ $(\mathrm{kN/m^3})$	24.2
k (cm/s)	$3 \cdot 10^{-3}$
c' (kPa)	0
φ' (°)	40

In the 2013 geotechnical campaign, several tests were conducted to characterize mechanical and seismic behaviour of dam materials. Tests on core material provided physical and mechanical parameters reported in Table 5.13. The core material showed a grain size distribution comparable to that obtained from 1994 tests as it can observed in Fig. 5.22. Variation of main characteristics with depth resulting from tests during 1995 and 2013 on core samples are presented in Fig. 5.23, while in Fig. 5.24 Casagrande plasticity chart is presented. The distribution of characteristics of core material with depth is uniform. The average properties are the following: unit weight is $\gamma = 20.7\,\mathrm{kN/m^3}$, water content is $w = 19\%$, the liquid limit is $w_L = 48.2\%$, the plasticity index is $I_p = 22.8$ and consistency index is $I_c = 1.28$.

Table 5.13 Physical parameters for core material obtained from tests in 2013

Sample	Depth (m)	γ $(\mathrm{kN/m^3})$	γ_s $(\mathrm{kN/m^3})$	w (%)	w_L	w_p	I_p	S_r (%)	e	A	I_c
S1C/CI1	4.50-4.80	20.2	26.7	23.3	55	26	29	100	0.629	0.83	1.09
S1C/CI2	8.50-8.80	21.6	26.7	15.0	37	22	15	97.1	0.421	0.88	1.46
S1C/CI3	16.50-16.80	20.4	26.7	18.5	47	25	22	91.4	0.549	0.71	1.30
S1C/CI4 (high part)	23.00-23.35	21.3	26.7	17.2	37	21	16	99.8	0.469	0.70	1.24
S1C/CI4 (lower part)	23.00-23.35	20.8	26.7	19.6	54	26	28	99.3	0.537	0.70	1.23
S1D/CI1	30.00-30.30	21.2	26.7	15.4	34	19	15	91.9	0.456	0.50	1.24
S1C/CI5	36.00-36.45	20.5	26.7	21.5	48	24	24	99.9	0.584	0.86	1.11

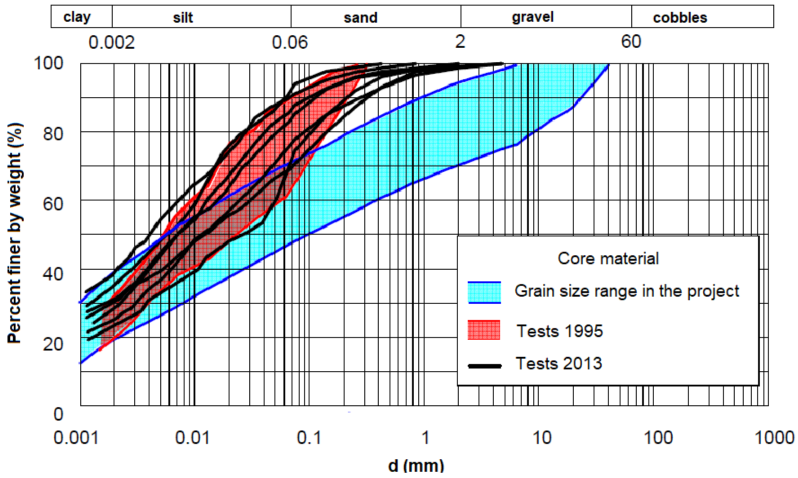

Figure 5.22 Comparison of grain size distributions from 1995 and 2013 tests and prescribed grain size range for core material

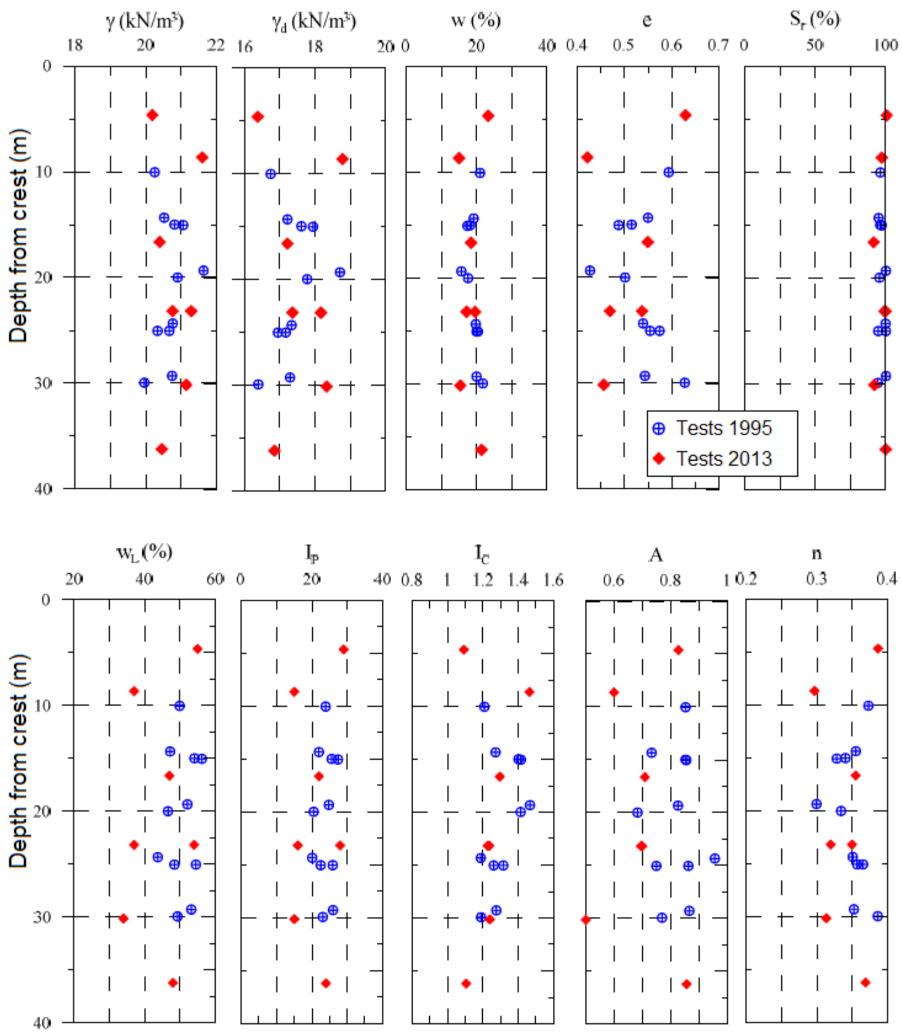

Figure 5.23 Comparison of variation of the main characteristics of the core with depth from laboratory tests in 1995 and in 2013

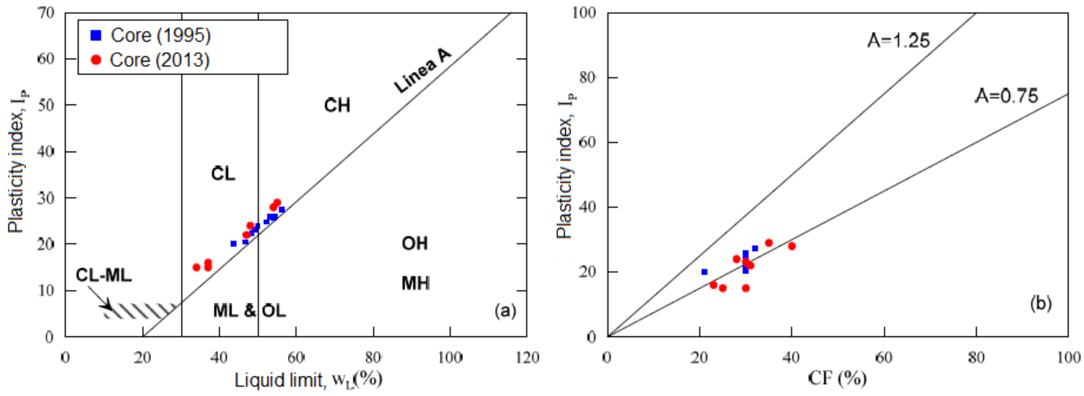

Figure 5.24 a) Casagrande plasticity chart b) Activity chart of core laboratory tests in 1995 and in 2013

On undisturbed samples retrieved from core one dimensional, direct shear, consolidated drained triaxial and cyclic tests were carried out in 2013, while on reconstituted samples from shells only dynamic and cyclic tests were performed. Results in terms of curves $e - \log \sigma_v'$ are illustrated in Fig. 5.25, while the estimated permeability values varies from $3 \cdot 10^{-9}$ and $6 \cdot 10^{-9}$ cm/s, which are very similar to those obtained from tests in 1995.

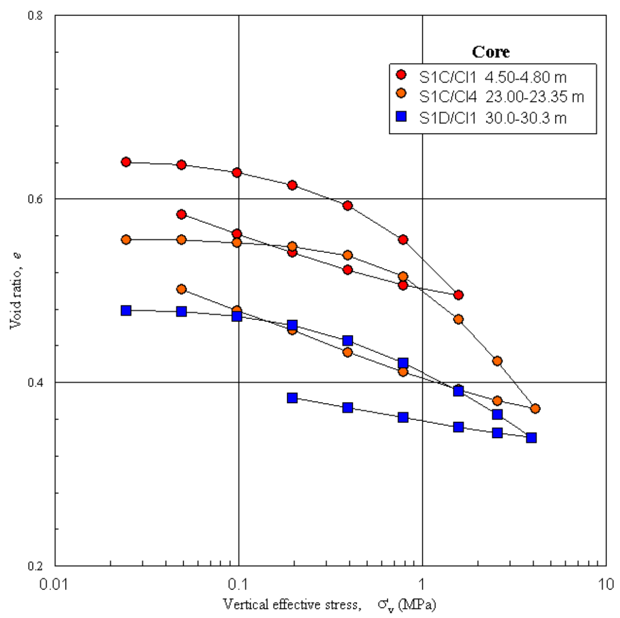

Figure 5.25 Oedometer curves for core soils from one dimensional test in 2013

In Fig. 5.26 results of consolidated drained triaxial tests and the derived strength envelope are illustrated, resulting in shear strength parameters $c' = 40$ kPa and $\varphi' = 25.7°$. Based on direct shear test, the values $c' = 50$ kPa and $\varphi' = 22.3°$ were obtained, as indicated in with the failure envelope in Fig. 5.26b.

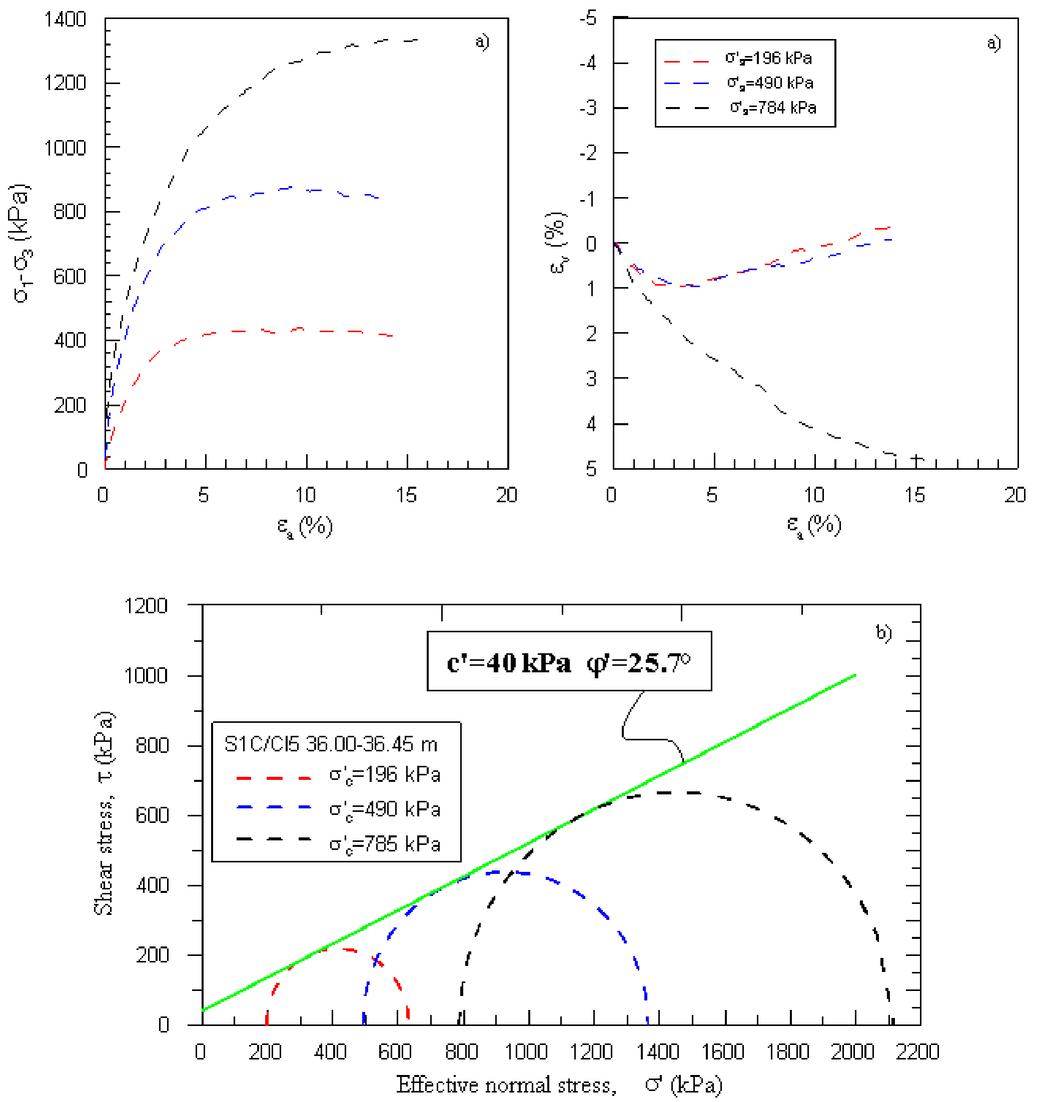

Figure 5.26 a) Results of consolidated drained triaxial test in 2013 on core soil and b) the strength envelope

5.3 GEOTHECNICAL MODEL

Considering all the results of in situ and laboratory tests performed during the years, the input values of the physical and mechanical parameters in the numerical analyses for the soils of dam's body and dam's foundation were chosen and summarized in Table 5.14.

Table 5.14 Physical and mechanical soils parameters

Parameters	Core	Shoulders	Alluvial layer	Rock basement
γ $(\mathrm{kN/m^3})$	20.7	24.2	22.0	25.0
k $(\mathrm{m/s})$	$3 \cdot 10^{-10}$	$3 \cdot 10^{-5}$	$3 \cdot 10^{-5}$	$3 \cdot 10^{-10}$
c' (kPa)	-	-	0	-
φ' (°)	-	-	40	-
E' (MPa)	-	-	200	12550
ν $(-)$	-	-	0.25	0.35

The unit weights (γ) of core and shoulders represent the average values obtained from the tests (Tables 5.11 and 5.12). For the alluvial layer and the rock basement, there are no data to determine the unit weights, therefore, the assumed values are representative of soils with similar characteristics. The permeability (k) from laboratory and in situ tests showed pretty similar values and they are fixed for core and shoulders as the average values obtained from in situ tests. The choice of the cohesion (c') and the friction angle (φ') of the soils of dam's body depends on the employed constitutive model and it is referred to the respective sections of this thesis (6.2.1, 6.2.2 and 7.2). For the alluvial layer, in all the numerical analyses the Mohr-Coulomb model is used and the strength parameters are taken as average values obtained from laboratory tests for shoulders material (Table 5.12), assuming that the shells and alluvial layer soils are similar. The rock basement is modelled as linear elastic material, therefore, only elastic parameters (E', ν) are required, which are selected as the values at small strain. The elastic parameters of the alluvial layer were chosen to match the observed settlements at the top of the foundation and for the dam's body are referred to the respective employed constitutive relationship.

5.4 MONITORING MEASUREMENTS

During the construction and reservoir impounding of Montedoglio dam several types of measurements have been conducted to monitor its behaviour. The instruments installed mainly aim to measure pore water pressures, vertical and horizontal displacements and reservoir levels. In this thesis it will be referred to data collected during construction and impounding from 1979 to 2001.

5.4.1 Vertical displacement

Altogether, 11 verticals are installed within the dam to obtain settlement profiles. Three main cross-sections are examined, namely B, C and D. For each cross-section, three verticals are monitored, one located in the upstream shell, one in the downstream shell and at the latter at the contact core-downstream shell. Section B is characterized by instrumented verticals A3, A6 and A9, Section C corresponds to verticals A2, A5 and A8, and finally Section D to verticals A1, A4 and A7. Verticals A4, A5 and A6 are positioned in the downstream shell at about 374.0 m a.s.l., while verticals A7, A8 and A9 are mostly in the downstream shell with about 10 m inside the core, and verticals A1, A2 and A3 are located in the upstream shell at about 375 m a.s.l. In Fig. 5.28 an example of the evolution of the embankment and the impounding height with time is shown, in particular for the vertical A8 in Section C, which corresponds to the selected cross-section to be studied. Fig. 5.29, 5.30 and 5.31 indicate the vertical settlements profiles recorded in time for each section evaluated. The settlements at the bottom of the verticals A7, A8 and A9 are near zero due to the presence of the deep rock layer, while in the other verticals settlements are different from zero because of the presence of the foundation alluvial layer. Settlement profiles are parabolic with a maximum of about 110 cm along verticals A7, A8 and A9, and of about 20 cm in the others.

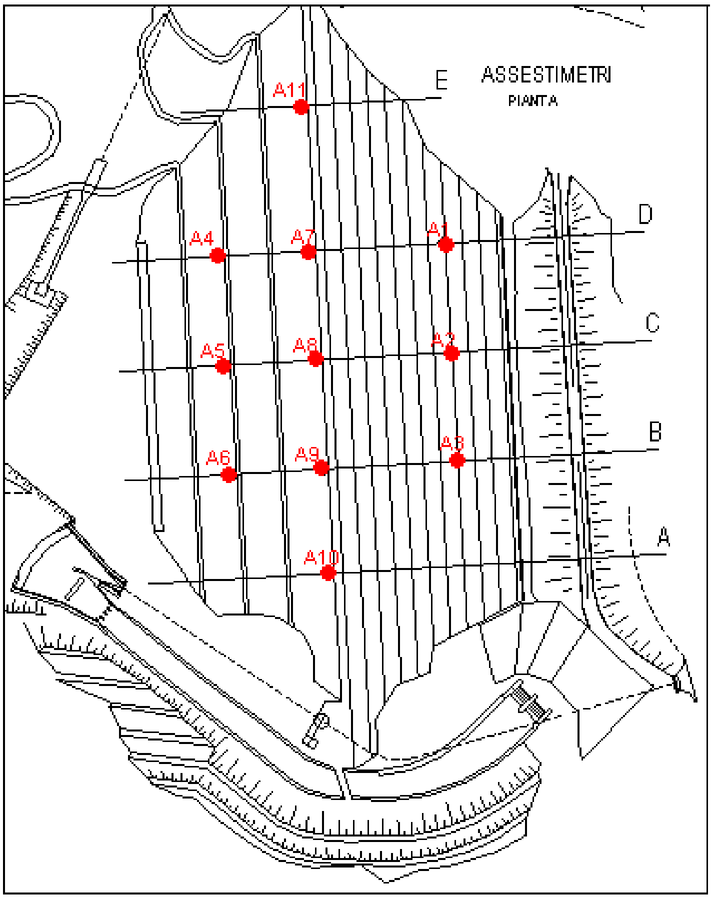

Figure 5.27 Plain view of the Montedoglio dam with the location of vertical displacement measurements

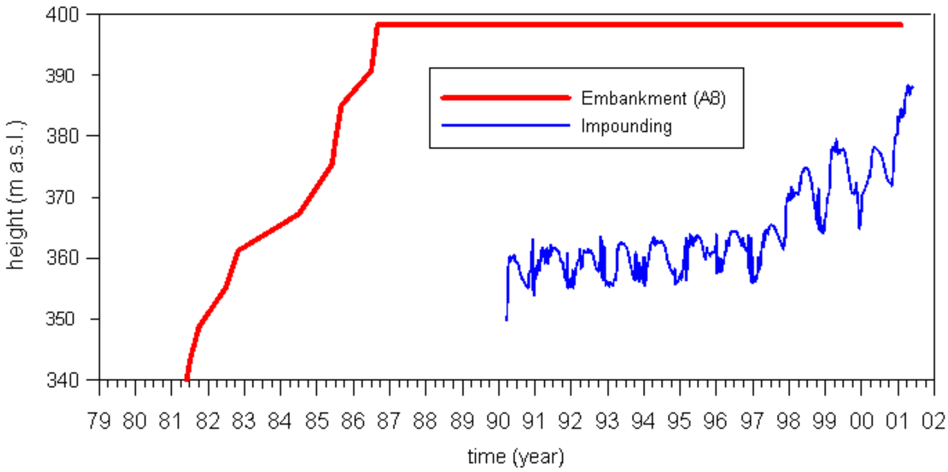

Figure 5.28 Evolution of embankment height and reservoir level

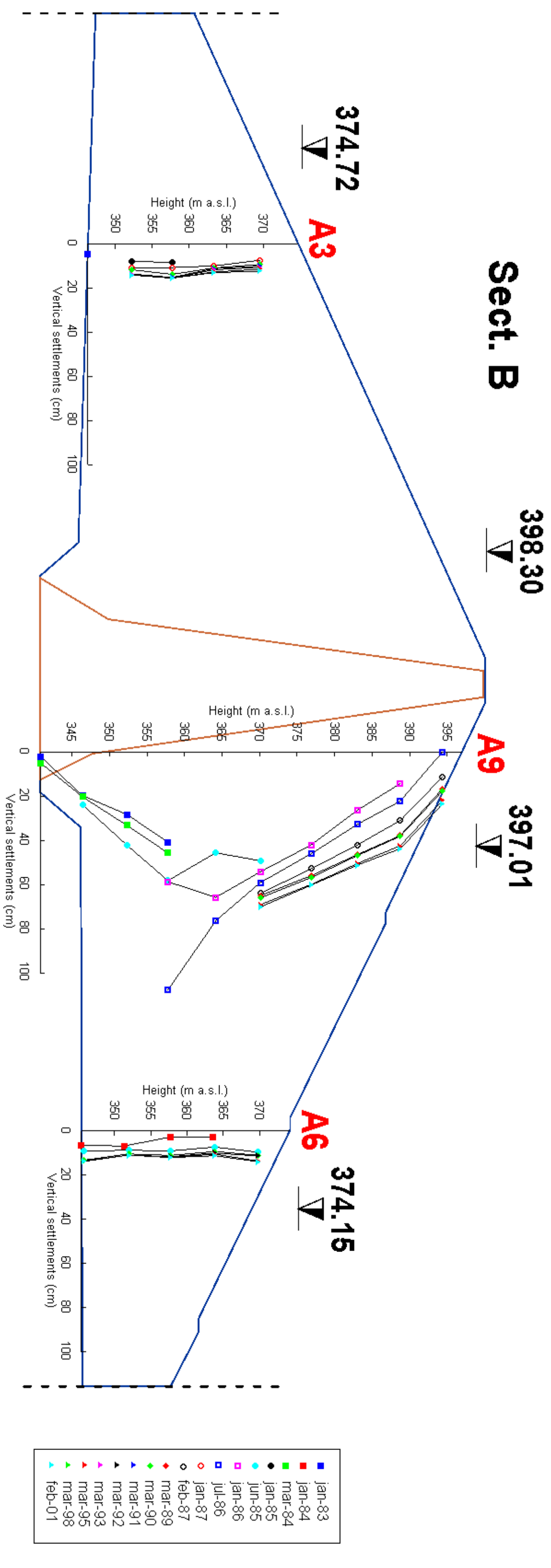

Figure 5.29 Vertical settlement profiles of vertical A3-A9-A6 Section B

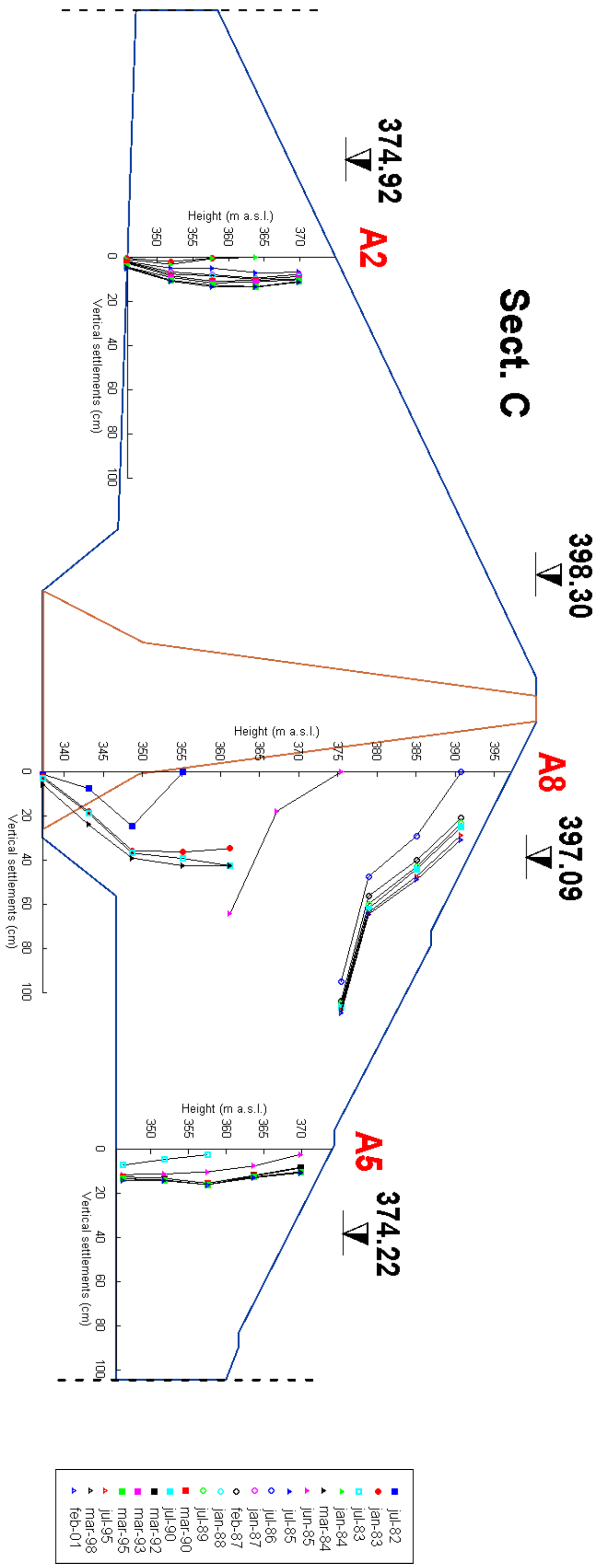

Figure 5.30 Vertical settlement profiles of vertical A2-A8-A5 Section C

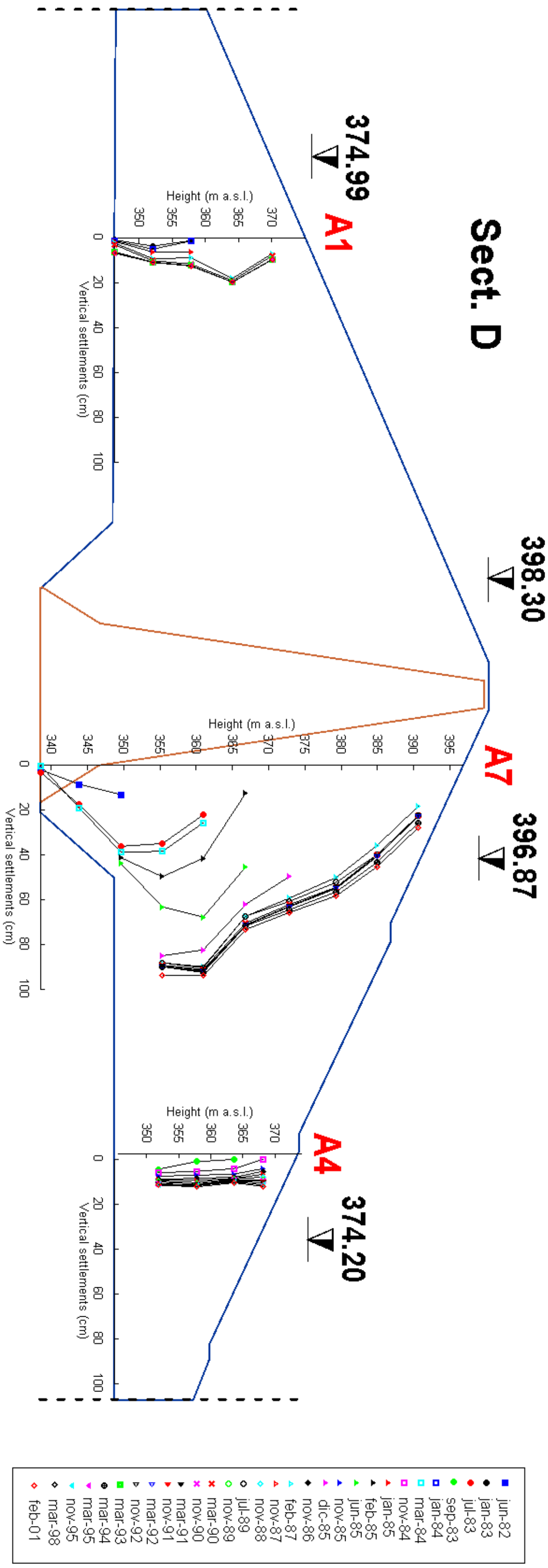

Figure 5.31 Vertical settlement profiles of vertical A1-A7-A4 Section D

5.4.2 Piezometers measurements

The evolution of the hydraulic head with time during first filling and service life is presented for gauges installed in the core and at the contact between the core and the rock basement. In Fig. 5.32 the location of the vibrating wire piezometers along the dam axis corresponding to the sections A, B, C and E is shown. In Fig. 5.33, 3 vertical cross-sections of the core with the positions of vibrating wire piezometers are presented. In total 5 piezometers are located for each section, 3 of which were introduced in 2004 (M19, M20, M21) for atypical measurements in piezometers M7, M8 and M9. In Fig. 5.34, 5.35 and 5.36 for sections B, C and D the evolution of piezometric head with time for the installed gauges and the variation of the reservoir level are reported. The piezometer heads measured at the upstream toe of the core (M1, M2, M3) follow the respective variation of the impounding level with time, those measured at the downstream toe of the core (M4, M5, M6) are pretty constant and are located above the installation height. The piezometric measurements of the gauges installed in the upstream core at height of 373 m a.s.l. (M16, M17, M18) are slightly influenced by the fluctuation of the impounding level. The hydraulic heads of the piezometers at about the upstream (M7, M8, M9) and downstream (M19, M0, M21) core base are quite similar, even though the measurements of the newer gauges (M19, M0, M21) are lower, probably because the installation height is greater and is localized at downstream core face.

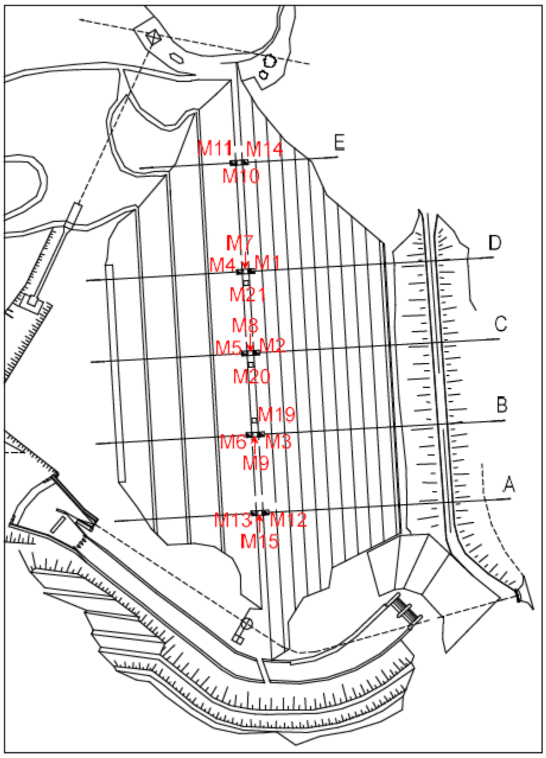

Figure 5.32 Planimetry of the Montedoglio dam with the location of vibrating wire piezometers in the core

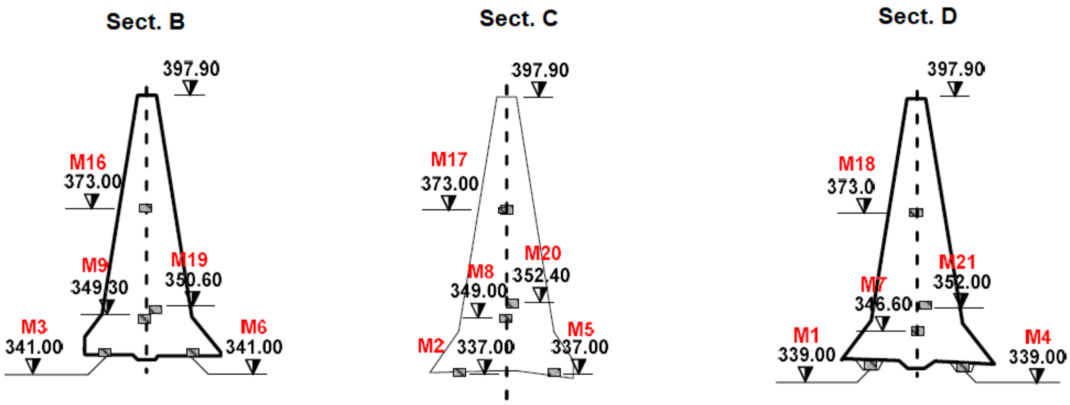

Figure 5.33 Location of vibrating wire piezometers in the core for vertical sections B, C and D

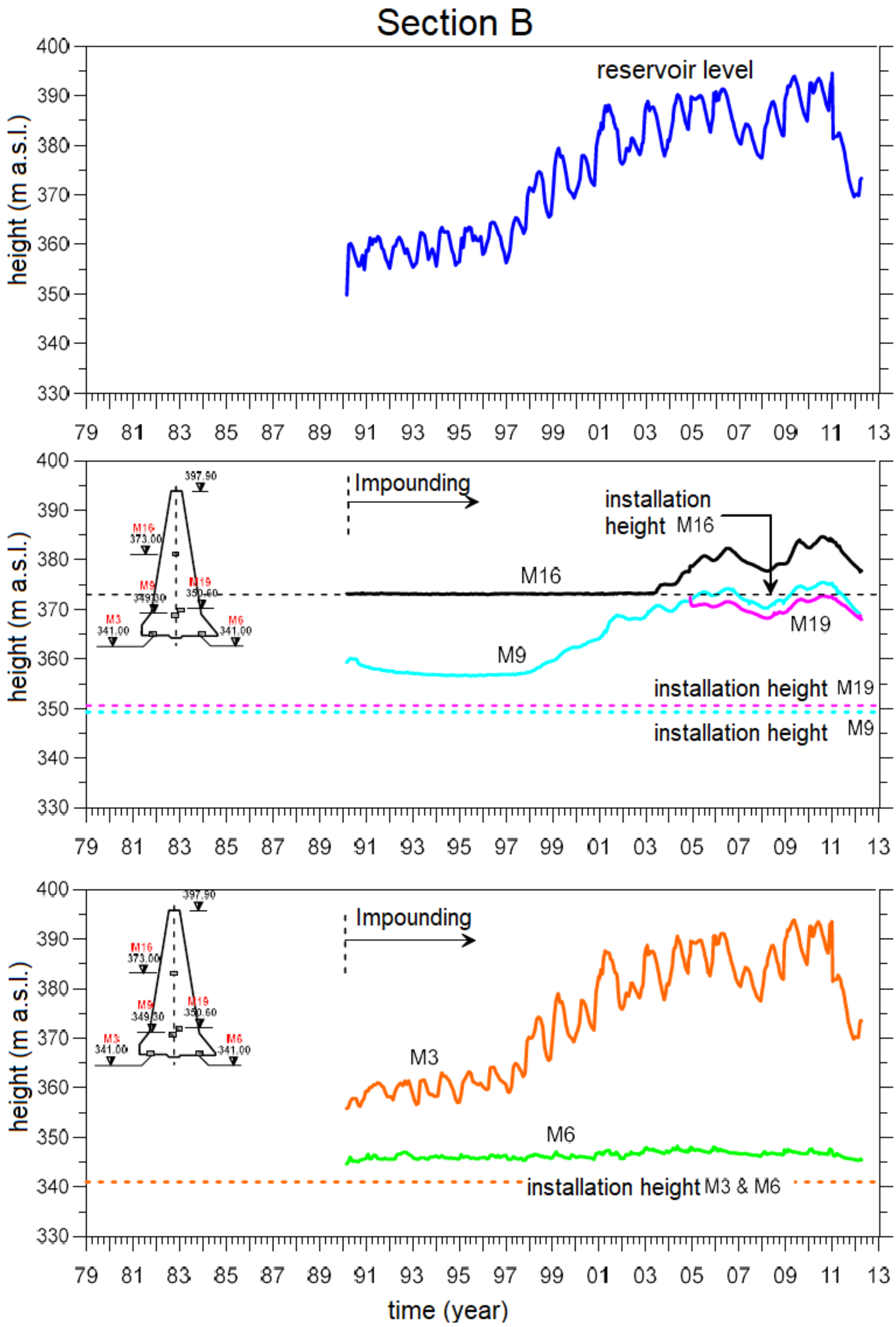

Figure 5.34 Piezometric head with time in the core (Sect. B)

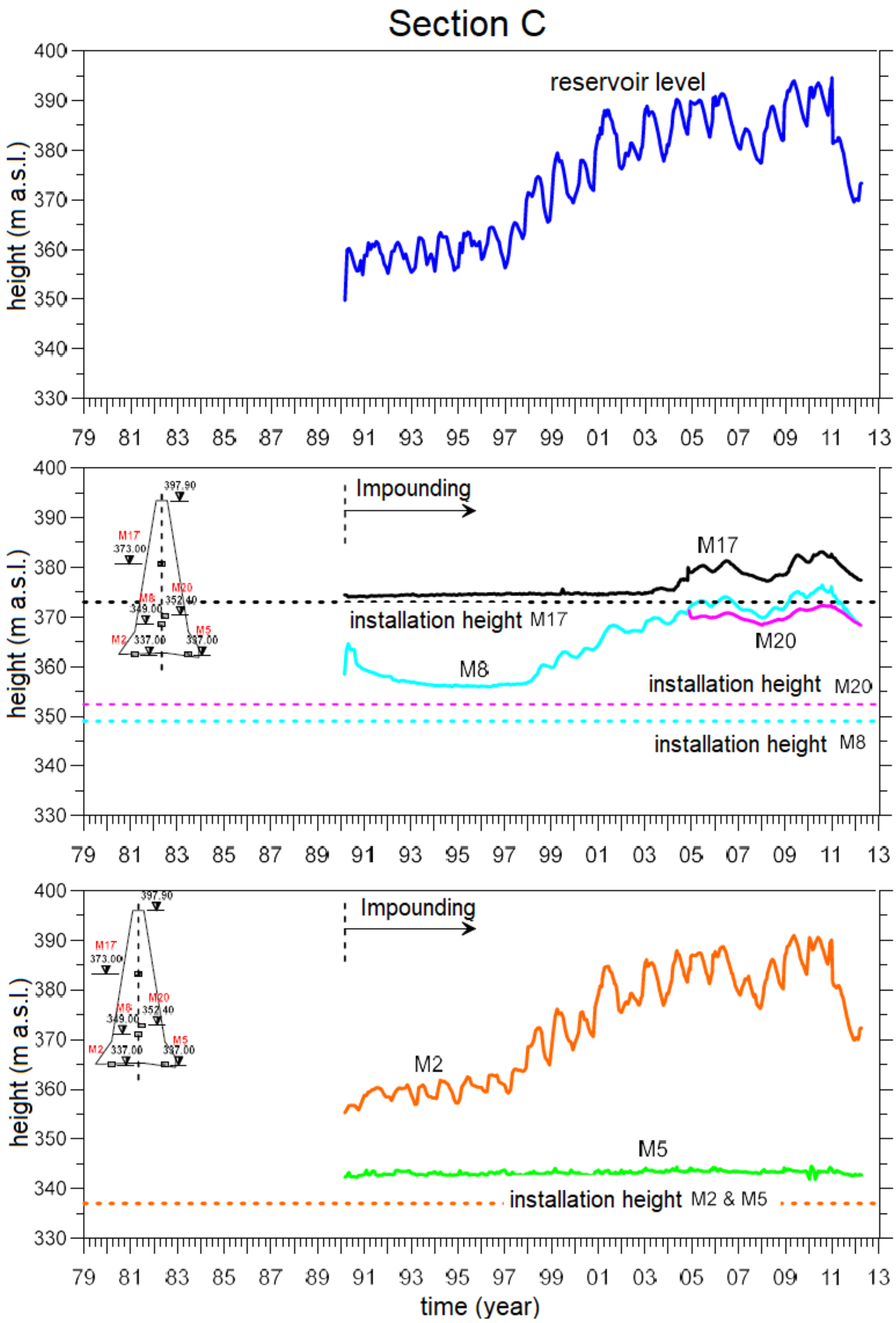

Figure 5.35 Piezometric head with time in the core (Sect. C)

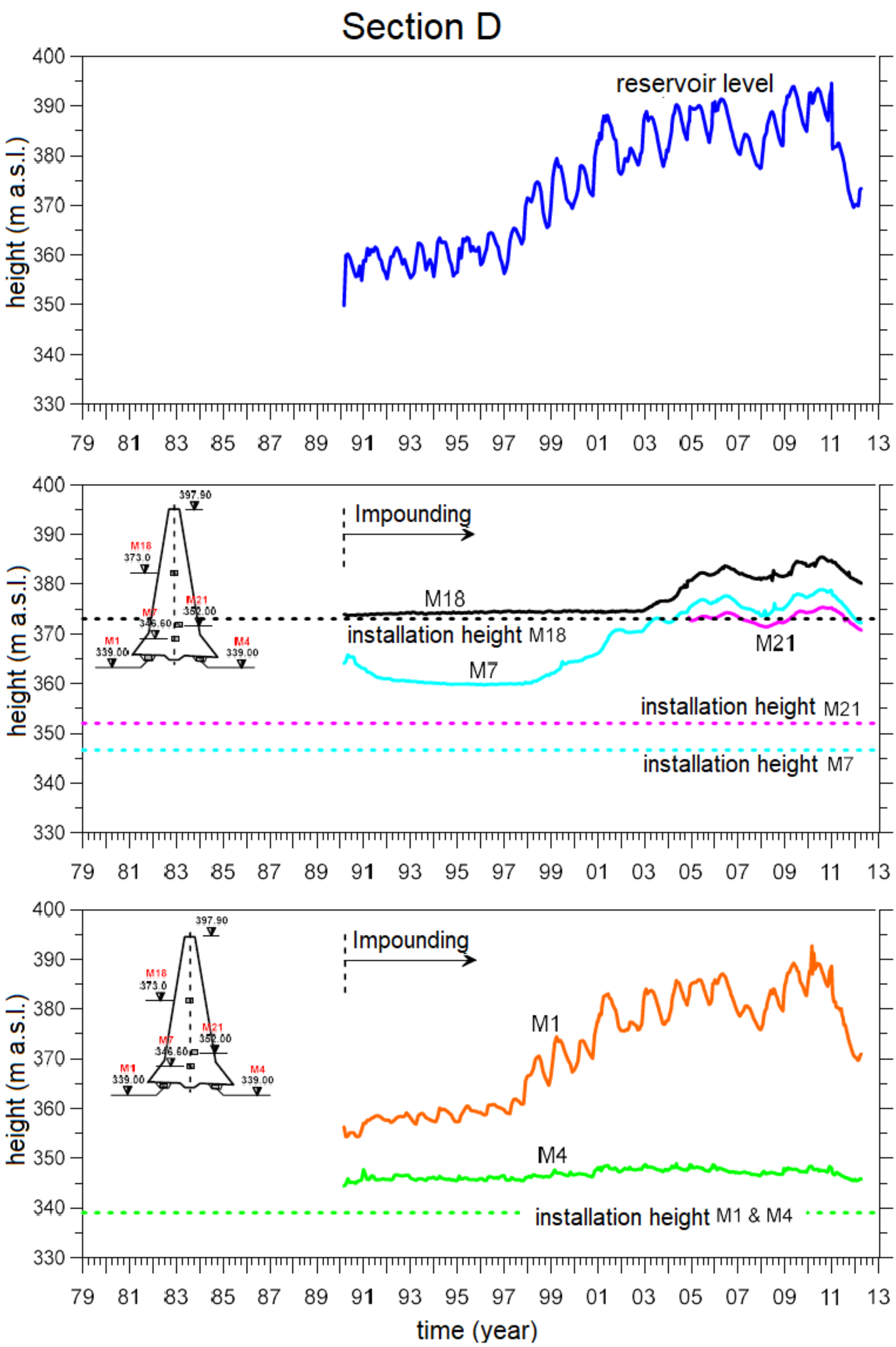

Figure 5.36 Piezometric head with time in the core (Sect. D)

6. STRESS-DEFORMATION ANALYSIS OF THE MONTEDOGLIO DAM WITH FLAC

6.1 INTRODUCTION

The remarkable results of the numerical analyses obtained by several authors, employing elasto-plastic hardening models to simulate the phases of construction and impoundment of embankment dams, highlight the capability of this class of models to reproduce correctly the deformational behaviour of this type of dams.

In this section, the hardening plasticity model Cysoil implemented in FLAC 7.0 and already described in Section 3.3, was chosen to reproduce the stress and strain state of the Montedoglio zoned earth dam during the construction phase. Further, numerical simulations have also been carried out using a simple elastic perfectly plastic analysis with Mohr-Coulomb model for comparison.

6.2 DETERMINATION OF MODEL PARAMETERS

Two simulations of the construction phase with different constitutive models for the dam's body have been carried out. In a first analysis the elastic perfectly plastic Mohr-Coulomb model was employed for both core and shells, while a second analysis was performed using the Cysoil model. The Cysoil model parameters were defined through results from laboratory tests, while the Mohr-Coulomb model parameters were determined through both results from laboratory tests and a back-analysis, in order to reproduce the field measurements obtained at the end of the construction.

6.2.1 Mohr-Coulomb model

As already mentioned, in this analysis the elastic perfectly plastic Mohr-Coulomb model was employed for both core and shells. For the alluvial layer below the shoulders and for the rock basement, the Mohr-Coulomb model and the linear elastic model were employed, respectively (see Sect. 5.3 for the models parameters). The mechanical parameters for the dam soils using Mohr-Coulomb models are summarized in Table 6.1.

Table 6.1 Mohr-Coulomb model parameters

Parameters	**Core**	**Shoulders**
c' (kPa)	10	0
φ' (°)	25	40
E' (MPa)	10	50
ν $(-)$	0.25	0.25

The cohesion and the friction angle of the core were chosen conservatively in the intervals obtained from different laboratory tests, while those of the shells were taken as average values obtained from laboratory tests (Table 5.12). The elastic parameters (E', ν) for the dam's body were chosen in the intervals of values obtained from field and laboratory tests in the context of back analysis. The chosen parameters are capable to reproduce throughout the numerical analysis the field measurements of vertical displacements of the dam at the end of the construction.

6.2.2 Cysoil model

The Cysoil model was employed only for the dam's body and it was calibrated on the results from one-dimensional test and consolidated drained triaxial test on intact samples for the core, and on results of large consolidated drained triaxial test on reconstituted samples for the shells. As we discussed before, the model is characterized by a deviatoric plastic surface and a volumetric plastic surface. The model parameters which characterize the deviatoric plastic surface are: the ultimate friction angle φ_f', the ultimate dilatancy angle ψ_f, the mobilized friction angle φ_m', the cohesion c', the failure ratio R_f, the calibration factor β, the reference effective pressure p_{ref}, the constant m_1, and the elastic tangent shear modulus at reference effective pressure G_{ref}^e. The elastic tangent shear modulus at reference effective pressure G_{ref}^e could be expressed as:

$$G_{ref}^e = \frac{E_{ur}^{ref}}{2(1+\nu)} \tag{6.1}$$

where ν is the Poisson's ratio and E_{ur}^{ref} is the unloading-reloading modulus at reference effective pressure p_{ref}.

The model parameters which characterize the volumetric plastic surface are: the dimensionless parameter α, the cap pressure p_c', the slope of the laboratory curve for p' versus ε_v at reference effective pressure K_{ref}^{iso}, the constant m_2, the reference effective pressure p_{ref}, and the ratio between the rates of elastic and plastic volumetric strain R. The ratio R can be expressed as a function of E_{ur}^{ref} and K_{ref}^{iso}:

$$R = \frac{E_{ur}^{ref}}{3\,(1-2\nu)\,K_{ref}^{iso}} - 1 \tag{6.2}$$

The total model parameters are 14: φ_f', ψ_f, φ_m', c', R_f, β, p_{ref}, m_1, E_{ur}^{ref}, ν, α, p_c', K_{ref}^{iso}, m_2. The reference effective pressure p_{ref} is defined as 100 kPa, while the constant m_1 was initially set to a FLAC default value of 1 for both materials and then checked and confirmed by the simulation of the single element triaxial test The initial values of φ_m' for both materials were determined from the following expression:

$$\sin\varphi_m' = \frac{1-K_0}{1+K_0} \tag{6.3}$$

where the value of K_0 is defined as:

$$K_0 = 1 - \sin\varphi' \tag{6.4}$$

Considering φ' as friction angles used in the Mohr-Coulomb analysis reported in Table 6.1, for the core $\varphi' = 25°$, $K_0 = 0.577$ and $\varphi_m' = 15.56°$, while for the shells $\varphi' = 40°$, $K_0 = 0.357$ and $\varphi_m' = 28.28°$.

The cap pressure p_c' was determined based on the assumption that the process of mechanical compaction induces a characteristic yield stress in the compacted soil mass similar to that exhibited by the soil masses subjected to natural processes of over consolidation during their geological life time (Prakash et al., 2014). The effect of compaction is an increase of the lateral stresses and of the lateral earth pressure. Using an empirical relationship (Schmidt, 1966; Alpan, 1967) the over consolidation ratio can be fixed as:

$$OCR^m = \frac{K_{01}}{K_{00}} \tag{6.5}$$

Where K_{00} and K_{01} are the coefficient of lateral earth pressure before and after compaction, respectively, and m is an empirically parameter. For the value of m, Schmertmann (1985) recommended m = 0.42, the value of K_{00} was determined from Eq. (6.4) and the value of K_{01} for compacted soil was assumed as 1 (Potts & Zdravkovic, 1999; Massarsch, 2002). For the core, $K_{00} = 0.577$ and the calculated $OCR = 3.7$. Each constructed layer is about 6 m thick, hence it is possible to approximate the vertical effective stress in the half of layer ($z = 3\ m$) as $\sigma'_{vo} = 62.1\ kPa$. The preconsolidation stress can be determined as:

$$\sigma'_P = OCR \cdot \sigma'_{vo} = 229.8\ kPa \tag{6.6}$$

According to the previous hypotheses, the position of the initial deviatoric surface is known and the values of p'_0 and q_0 can be evaluated as:

$$p'_0 = \frac{\sigma'_P + 2\ K_{00}\ \sigma'_P}{3} = 164.9\ kPa \tag{6.7}$$

$$q_0 = p_0{}'\ \frac{3(1-K_{00})}{(1+2K_{00})} = 97.2\ kPa \tag{6.8}$$

The point with coordinates (p'_0, q_0) belongs also to the initial volumetric surface (Eq. (6.9)) from which it is possible to determine the cap pressure p'_c (Eq. 6.10)

$$q^2 + p'^2 = p_c{}'^2 \tag{6.9}$$

$$p_c{}' = \sqrt{p_0{}'^2 + q_0{}'^2} = 191.5\ kPa \tag{6.10}$$

The value of $p_c{}'$ assumed for the core in the numerical analyses is set to $190\ kPa$.

The remaining deviatoric and volumetric parameters can be determined using results from triaxial test and from one-dimensional test, respectively. Starting with the core material, a numerical simulation of one-dimensional test was carried out and the results were compared with real results from one-dimensional test (Fig. 6.1). The same procedure was made for the triaxial test (Fig. 6.2), obtaining all model parameters summarized in Table 6.2 for the core.

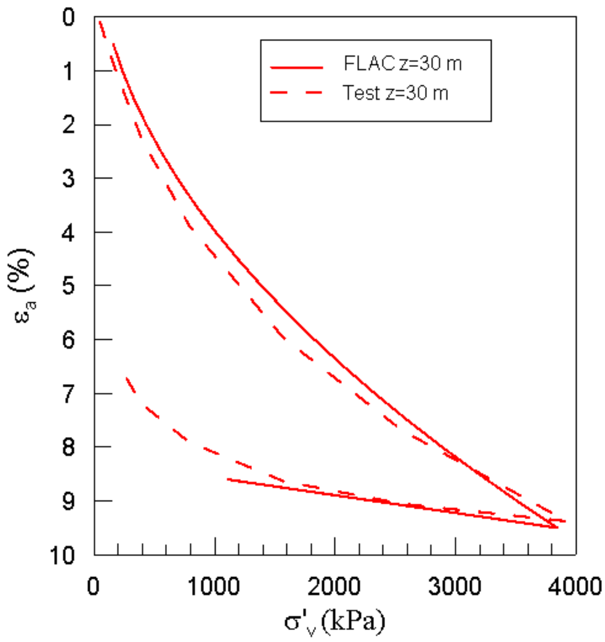

Figure 6.1 Comparison of results from simulation and from one-dimensional test for core material

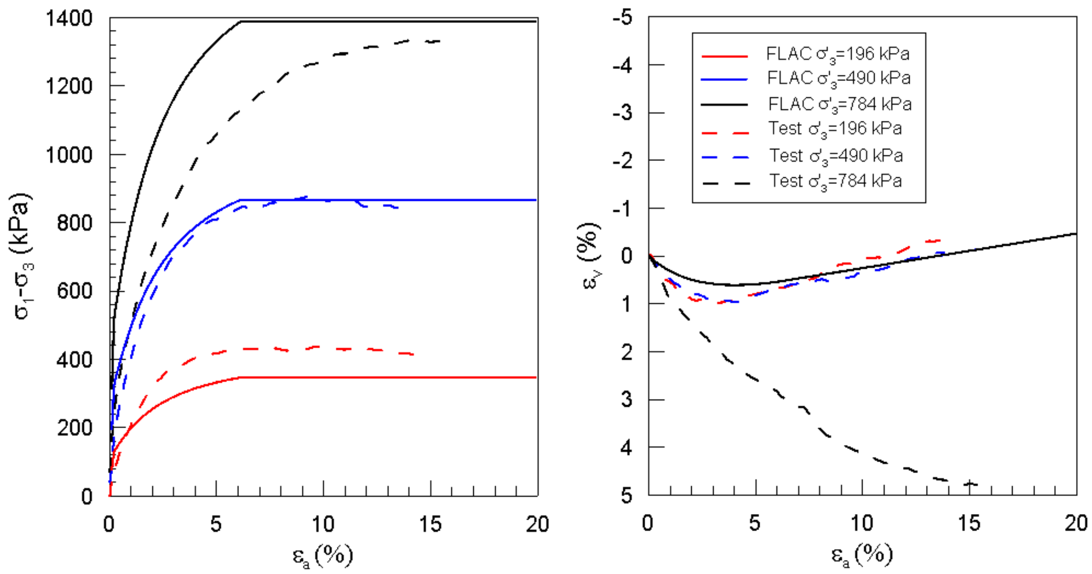

Figure 6.2 Comparison of results from simulation and from triaxial test for core material

Table 6.2 Cysoil model parameters for core material

Parameter	**Value**
K_{ref}^{iso} (MPa)	9
E_{ur}^{ref} (MPa)	40
ν (-)	0.3
α (-)	1
p_c' (kPa)	190
φ_f' (°)	28
φ_m' (°)	15
ψ_f (°)	2
c' (kPa)	0
R_f (-)	0.9
β (-)	0.5
p_{ref} (kPa)	100
m_1 (-)	1
m_2 (-)	0.5

The granular nature of the shell material makes difficult carrying out one-dimensional test, for this reason there are no data about this type of test. In this context, only the deviatoric model parameters on triaxial test could be determined, therefore, it was chosen to active only the shear envelope of the model considering a high value of the cap pressure $p_c = 1E20$ kPa. The comparison between results of simulation and test is presented in Fig. 6.3, and model parameters for shells are summarized in Table 6.3.

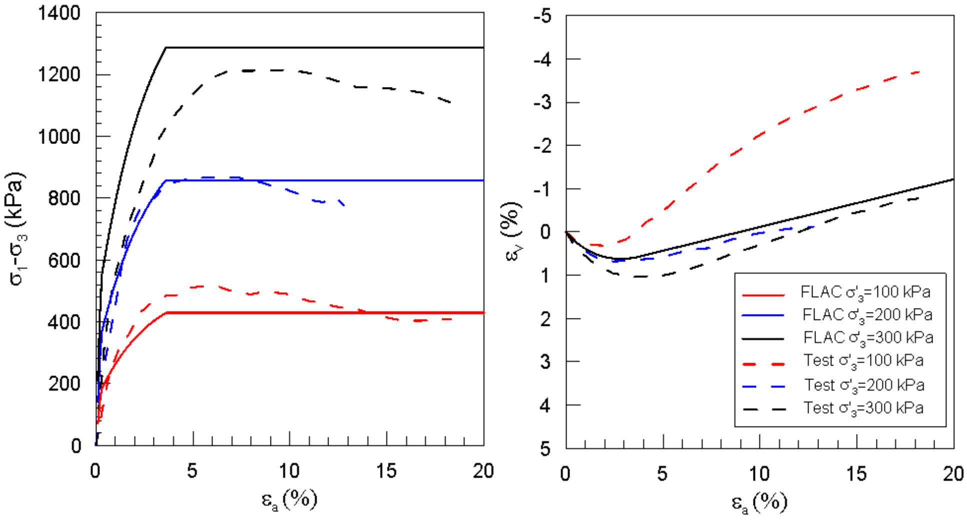

Figure 6.3 Comparison of results from simulation and from triaxial test for shell material

Table 6.3 Cysoil model parameters for shell material

Parameter	**Value**
K_{ref}^{iso} (MPa)	-
E_{ur}^{ref} (MPa)	70
ν (-)	0.25
α (-)	-
p_c (kPa)	1E20
φ_f' (°)	43
φ_m' (°)	28
ψ_f (°)	3
c' (kPa)	0
R_f (-)	0.9
β (-)	0.7
p_{ref} (kPa)	100
m_1 (-)	1
m_2 (-)	-

As shown in Fig. 6.1, a good match between the numerical simulation and experimental data is highlighted for the one dimensional test on core material. The overall behaviour of both materials is well described by the model in the triaxial tests, although the laboratory results for the confining pressure of 490 kPa for the core and 200 kPa for the shell materials are more outlined. The model is able to describe only volumetric behaviour for $\sigma_3' = 196$ and 490 kPa for the core (Fig. 6.2) and for $\sigma_3' = 200$ for the shell (Fig. 6.3). This behaviour indicates that the volumetric strains variations with axial strains are not captured by the model. Actually, this similar trend at all confining pressures in terms of axial versus volumetric strains is clearly a drawback of the Cysoil model.

6.3 FINITE DIFFIRENCE ANALYSIS

In this Section, the results of the numerical analyses of the construction phase of Montedoglio dam using the finite difference code FLAC are presented and discussed. The analysed cross-section is the main cross-section C of the zoned dam. The mesh is characterized by elements with height between 1 and 1.5 m and it is presented in Fig. 6.4. The boundaries of the analysed section were defined as 60 m below the dam’s base and 150 m away from the dam’s toe. The boundary conditions are characterized by zero horizontal and vertical displacements along the bottom boundary, and zero horizontal displacement on the lateral boundaries. It was assumed implicitly that the tested samples were representative of the fill materials in the field. In the simulation the shells include also filters and drained layers. The analysis is drained and the water table was assumed at the top of the alluvial layer downstream at 342.2 m a.s.l..

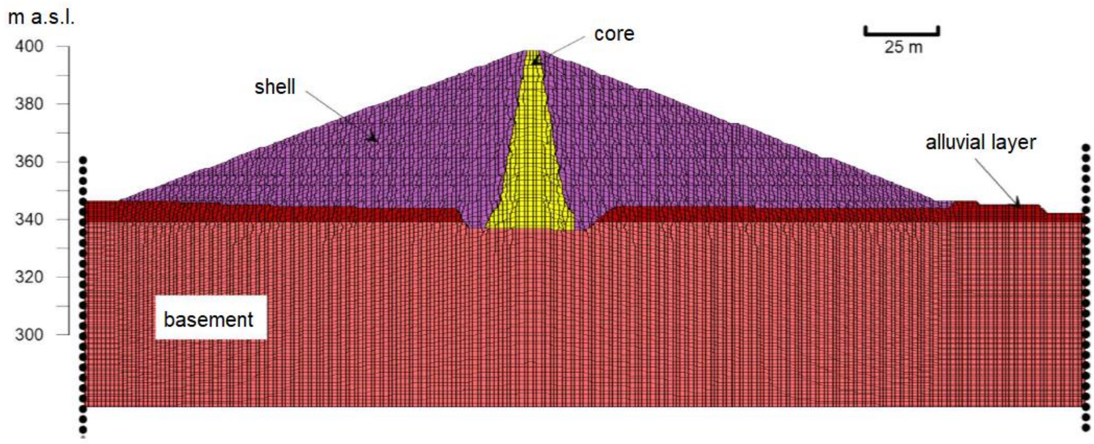

Figure 6.4 Finite difference mesh of the dam's cross-section

6.3.1 Analysis during construction

As explained before, two analyses of the construction phase of Montedoglio dam have been carried out: a first analysis with Mohr-Coulomb model for the dam’s body, and a second one with Cysoil model. The foundation soil was modelled for both simulations as elastic perfectly plastic Mohr-Coulomb material for the alluvial layer and as linear elastic material for the rock basement. The excavation of the alluvial layer to found the core directly on the rock foundation was simulated removing groups of elements in horizontal layers. The construction of the dam’s body was simulated adding groups of elements in horizontal layers through a gravity 'turn-on' analysis: 10 horizontal layers of about 6 m thick were added in 10 increments. The results which are presented in this Section refer to the Cysoil analysis, even though the observed settlements at the end of the construction also for the Mohr-Coulomb analysis are shown for comparison. The vectors of cumulated displacement at the end of the construction are presented in Fig. 6.5, the maximum value of the displacements is 79.7 cm and it was reached in the core. In Fig. 6.6 the contours of cumulated vertical and horizontal displacements at the end of the construction are showed. The contours of cumulated vertical and horizontal total stress level at the end of the construction are defined in Fig. 6.7, while the contours of cumulated vertical and horizontal effective stress level at the end of the construction are presented in Fig. 6.8. The contours of cumulated fluid stress at the end of the construction are presented in Fig. 6.9. From the contours of total vertical stress, a transmission of forces from core to shoulders caused by different stiffness is visible due to the great stress difference at the contact between the two materials. To highlight the arching in the dam, the arching ratio in the middle core along the dam height was calculated (Fig. 6.10) from the results of the simulation at the end of construction. The arching ratio is less than one, as Fig. 6.10 shows, indicating that stress transmission between the shell and the core occurred. The minimum value of arching ratio corresponds to about 14.6 m of dam height from the base of the core. The more pronounced effect is between dam base and 40 m of dam elevation, which is in contrast with the general rule that the arching ratio decreases as the dam height increases with a mean effect in upper high dam. From 45 m of dam elevation to the top of the core, the arching ratio value remains around 0.7. The contours of cumulated total volumetric and maximum shear strain are showed in Fig. 6.11, and the contours of cumulated plastic volumetric and deviatoric strain follow in Fig. 6.12. The observed settlements at the end of the construction in the upstream shell (A1-A2-A3) (see Section 5.4.1), at the contact core-downstream shell (A7-A8-A9), and in the downstream shell (A5-A6-A7) are presented in Fig. 6.13 in comparison with predicted settlements using FLAC and the Cysoil model. For completeness, the results of the Mohr-Coulomb analysis were added. The results of numerical analyses are in good agreement with the measured vertical displacements at the end of the construction. The differences between the two models, as Fig. 6.13 shows, are very small in the shells and more pronounced in the core, where the Mohr-Coulomb analysis underestimates the measured settlements with respect to Cysoil one.

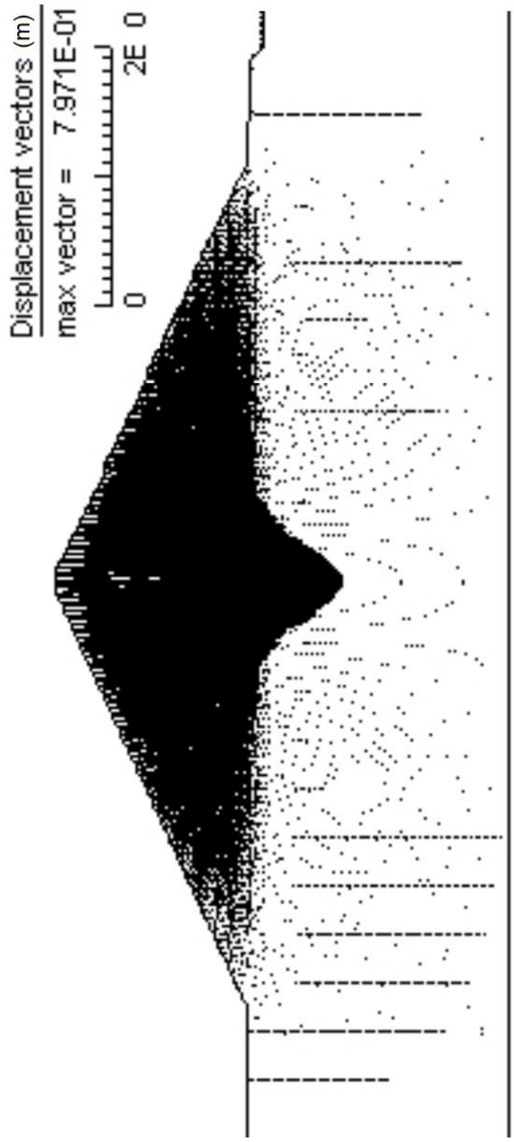

Figure 6.5 Vectors of cumulated displacement at the end of the construction

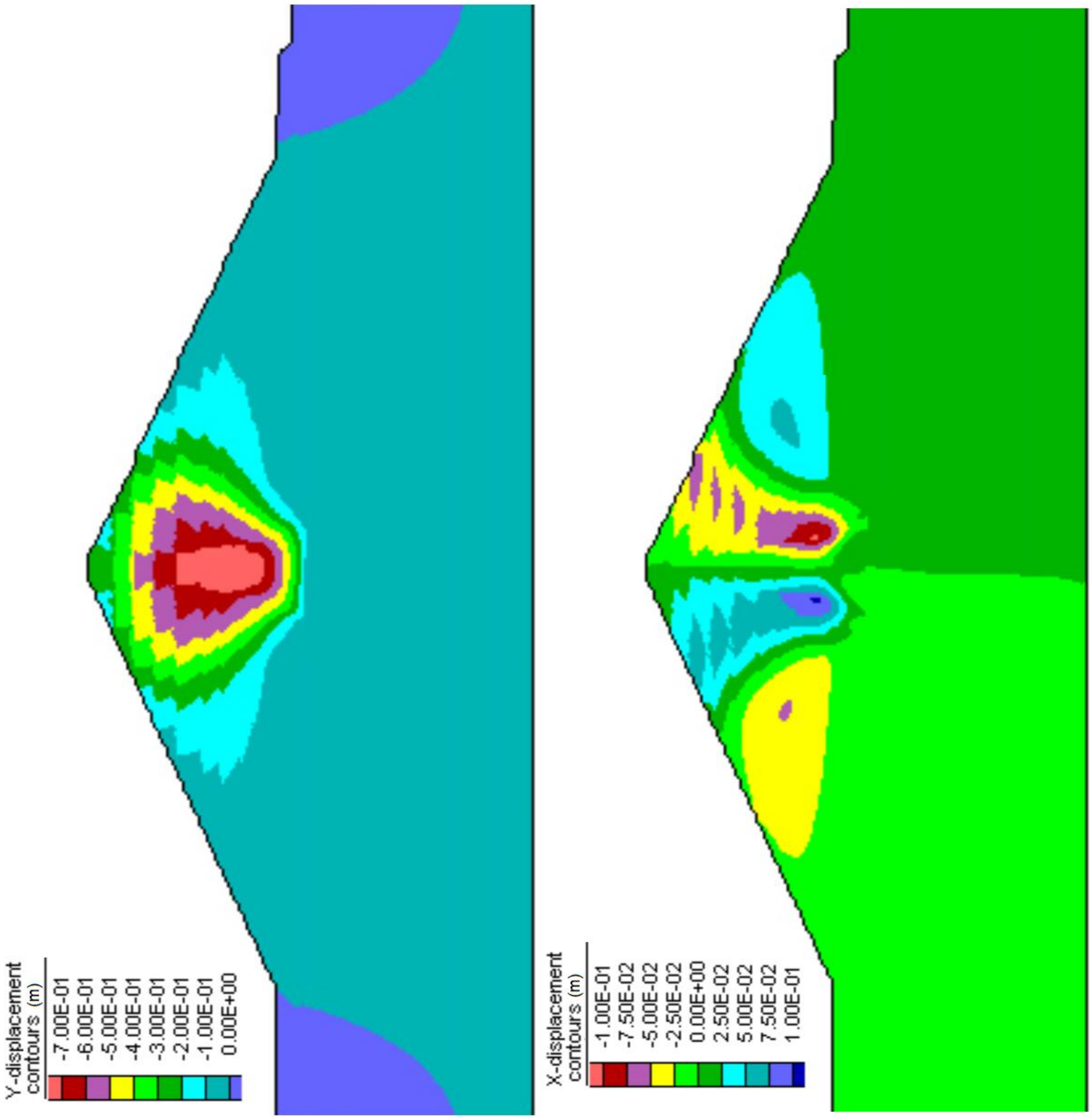

Figure 6.6 Contours of cumulated left) vertical displacements v (m) and right) horizontal displacements u (m) at the end of the construction

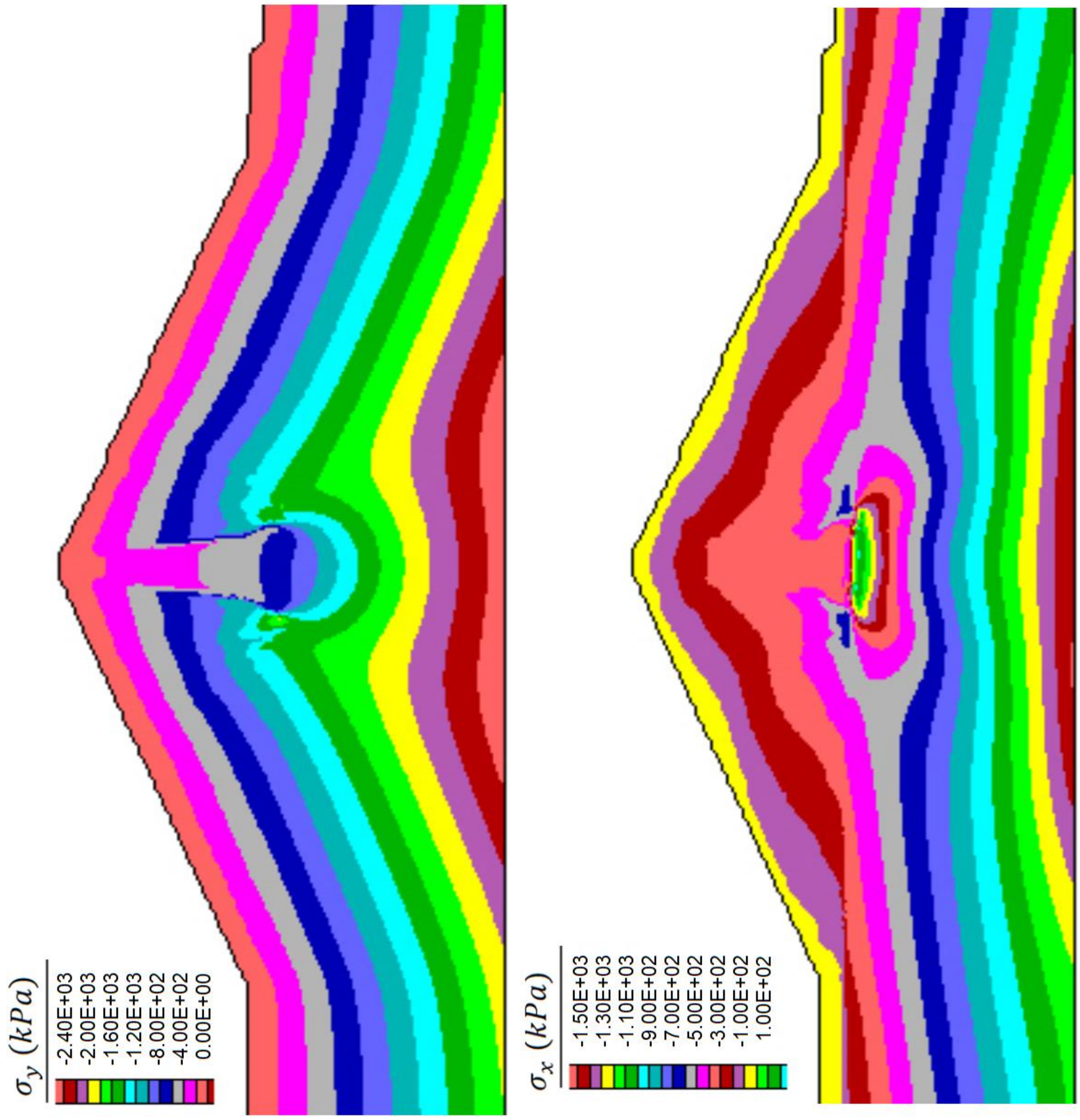

Figure 6.7 Contours of cumulated left) vertical total stress level $\sigma_y\ (kPa)$ and right) horizontal total stress level $\sigma_x\ (kPa)$ at the end of the construction

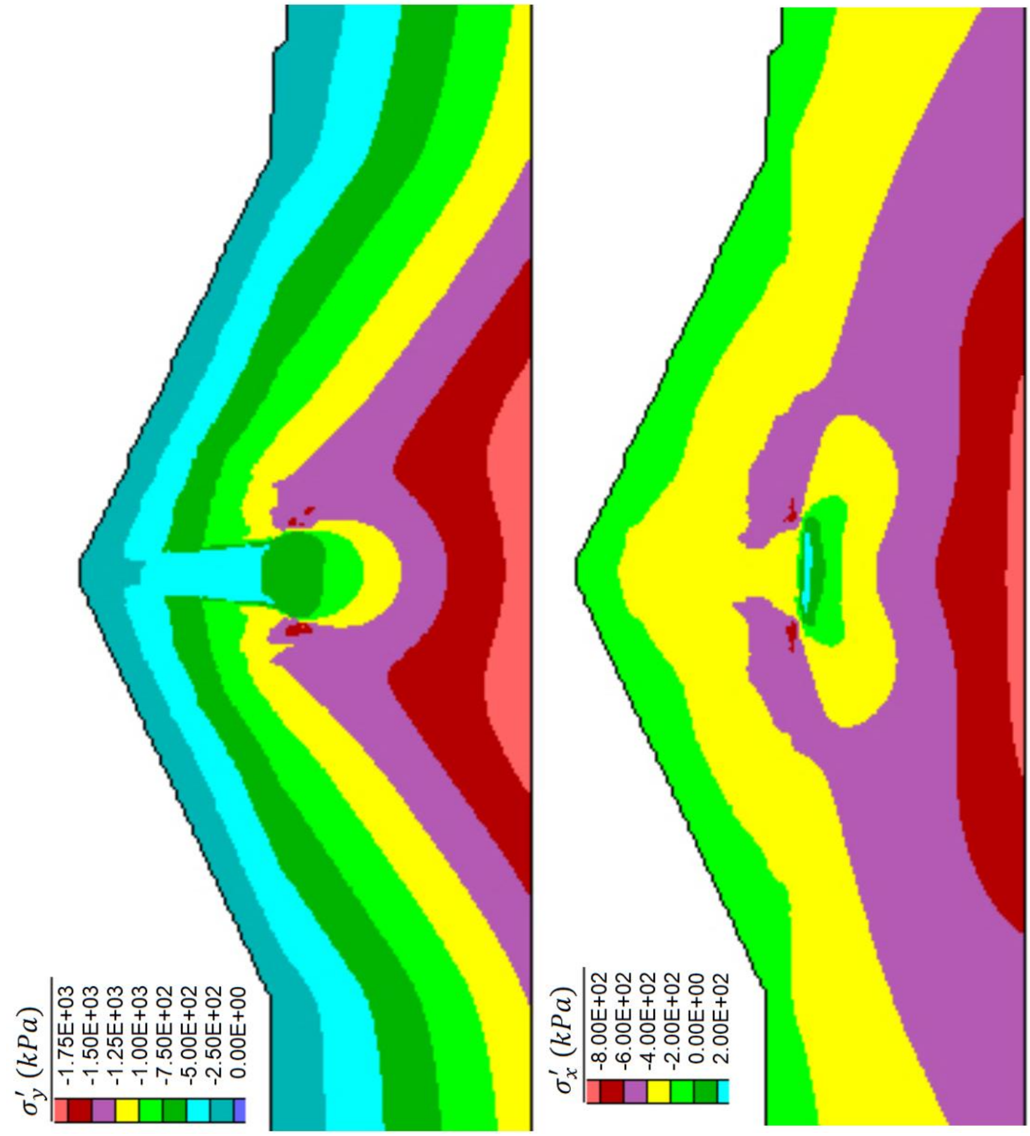

Figure 6.8 Contours of cumulated left) vertical effective stress level $\sigma'_y\ (kPa)$ and right) horizontal effective stress level $\sigma'_x\ (kPa)$ at the end of the construction

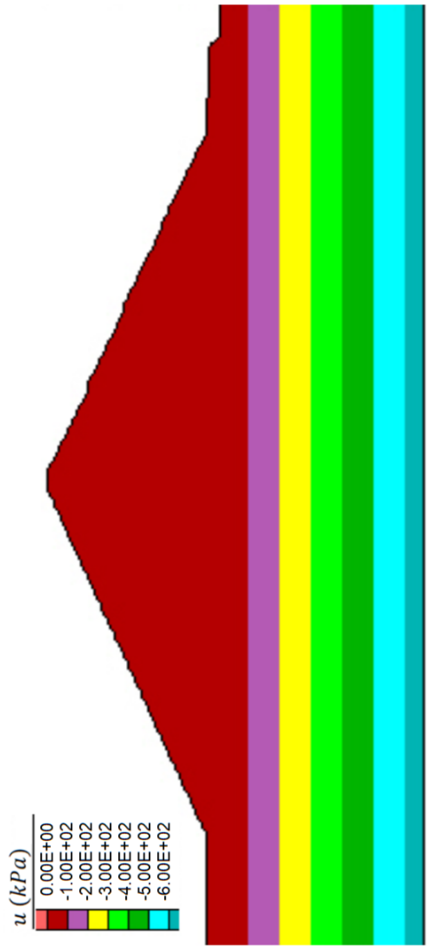

Figure 6.9 Contours of cumulated fluid stress $u\ (kPa)$ at the end of the construction

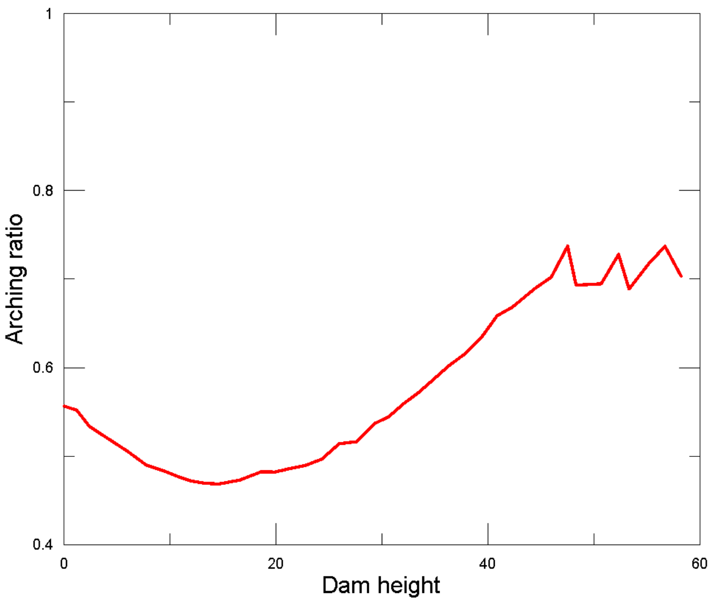

Figure 6.10 Calculated arching ratio versus dam height in the middle core

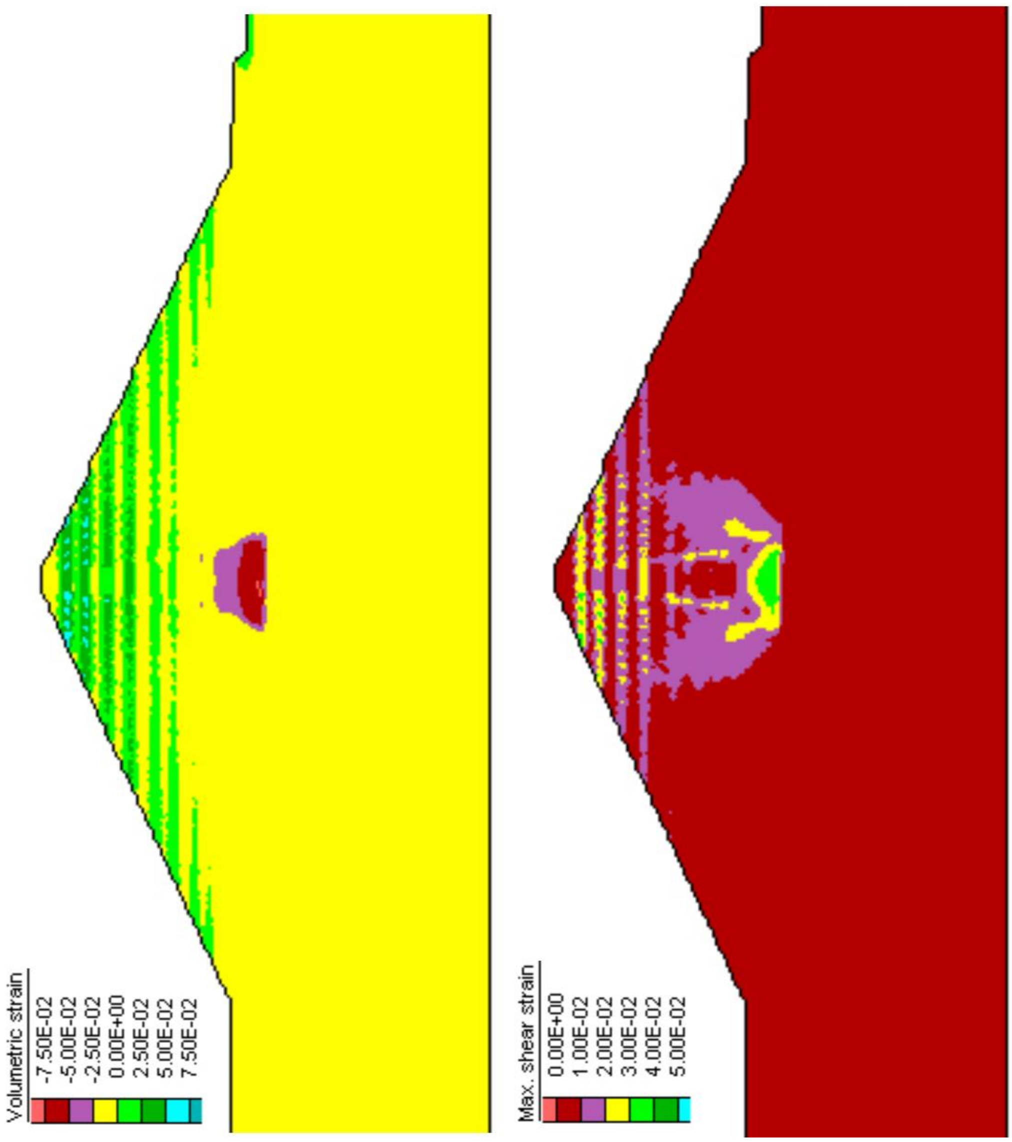

Figure 6.11 Contours of left) total volumetric strain ε_v (-) and right) maximum shear strain γ (-) at the end of the construction

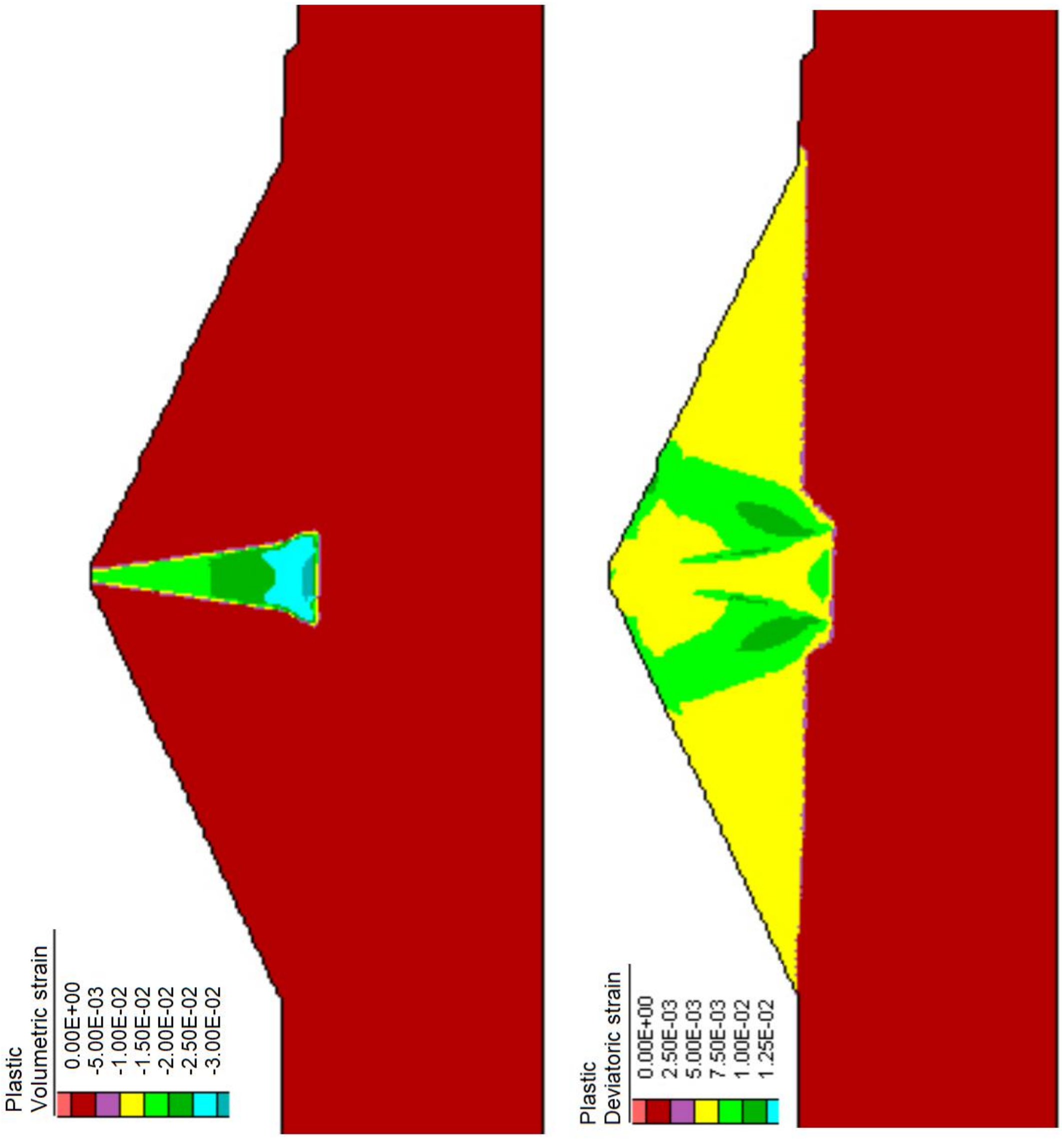

Figure 6.12 Contours of cumulated left) plastic volumetric strain ε_v (-) and right) plastic deviatoric strain ε_s (-) at the end of the construction

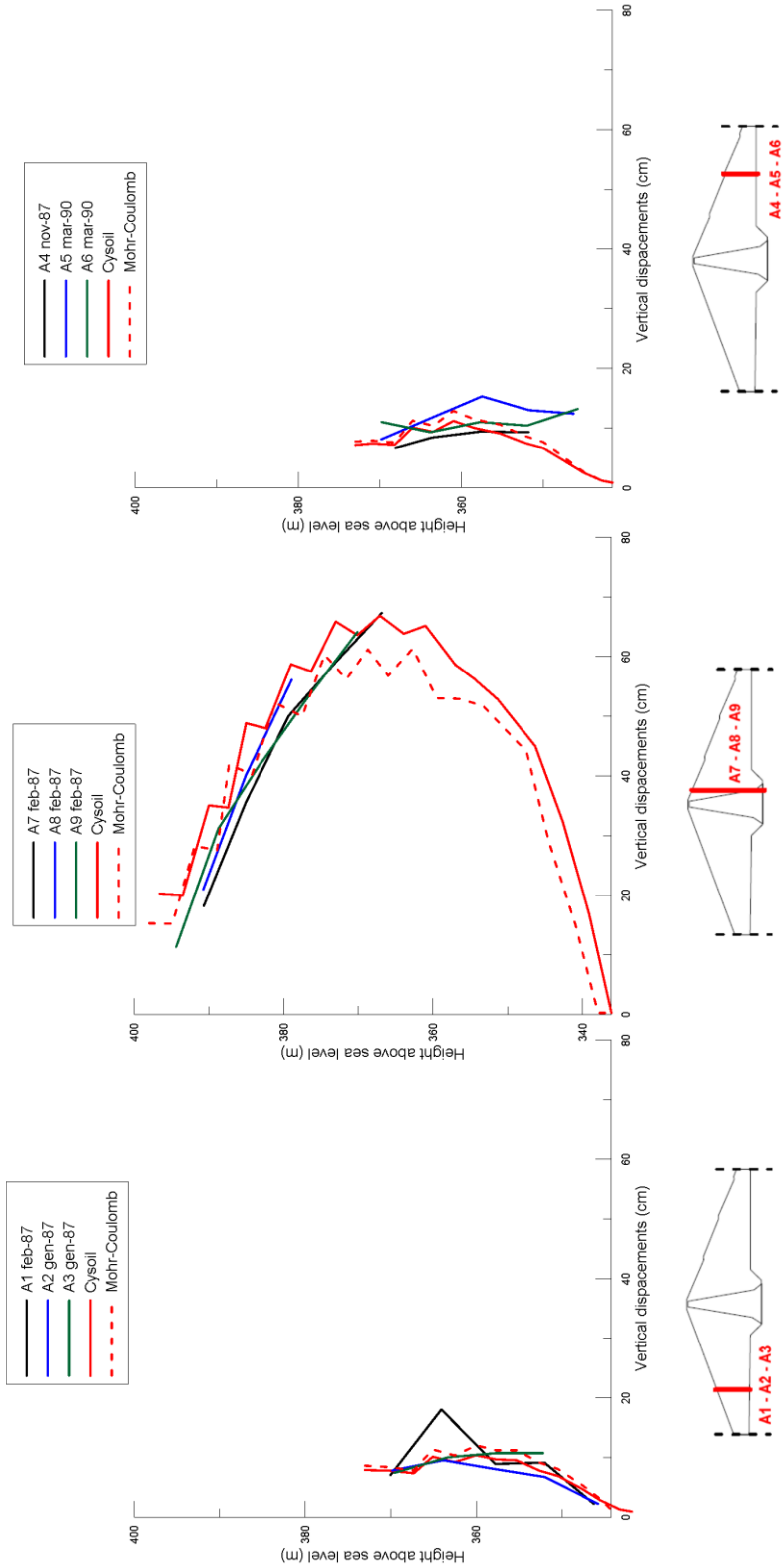

Figure 6.13 Comparison between observed and predicted vertical settlements at the end of the construction in the upstream shell (A1-A2-A3), at the contact core-downstream shell (A7-A8-A9), and in the downstream shell (A5-A6-A7) using FLAC, the Cysoil and Mohr-Coulomb models

7. STRESS-DEFORMATION ANALYSIS OF THE MONTEDOGLIO DAM WITH ICFEP

7.1 INTRODUCTION

As mentioned before, Kovacevic (1994) and Kovacevic et al. (2008) illustrated that the Lade's double hardening model is well-suited to reproduce the deformation behaviour of rockfill dams during construction and reservoir impounding. The case study of the Montedoglio dam was analysed with the finite element code ICFEP, in which the Lade's double hardening model was already implemented by Kovacevic (1994). The numerical analysis involves the simulation of the dam construction and the reservoir impounding and it is fully coupled. The capability of the model to predict the deformation behaviour is highlighted comparing the observed settlements with those predicted through the numerical modelling at the end of the construction and during impounding. The model is applicable to general three-dimensional stress conditions, but the parameters required to characterize the soil behaviour can be derived entirely from results of isotropic compression and conventional drained triaxial compression tests (Lade, 1977). The available laboratory tests for the dam's body include one dimensional and drained triaxial tests for the core material and only a drained triaxial test for the shell material. Kovacevic (1994) explored the possibility to use a one-dimensional test instead of an isotropic compression test to derive model parameters using some artifices. Some of the model parameters of the shell soil were defined on a triaxial test, while some were assumed from literature on similar material. For the core, the model parameters were based on both one-dimensional and triaxial tests.

7.2 DETERMINATION OF MODEL PARAMETERS

The determination of the model parameters is based, as discussed earlier, on the results of one-dimensional and drained triaxial tests (Lade, 1977; Kovacevic, 1994). A preliminary set of the double-hardening model parameters were first determined from laboratory results as described by Lade (1977) and were then adjusted based on the finite element simulation of the triaxial test.

The elastic strain increments, which are recoverable upon unloading, are calculated from Hooke's law which requires two independent elastic parameters: a stress dependent Young's modulus E and a constant value of Poisson's ratio ν. As reported in Sect. 4.3.3, the unloading-reloading modulus is defined as:

$$E_i = MPa\left(\frac{\sigma_3'}{Pa}\right)^n \tag{7.0}$$

The constant M and exponent n could be determined from triaxial compression tests performed with various values of the confining pressure σ_3'. By estimating the Young's modulus on the basis of the initial slope of the triaxial compression stress-strain curves, it is possible to plot the E_i/Pa versus σ_3'/Pa relationship for different values of σ_3' (Kovacevic, 1994). The values of M and n can be determined fitting the data with a power function. The value of the Poisson's ratio was calculated using the initial slope of the curves $\varepsilon_v - \varepsilon_a$ from triaxial compression tests through the relation:

$$\nu = \frac{1}{2}\left(1 - \frac{\varepsilon_v}{\varepsilon_a}\right) \tag{7.1}$$

For Lade (1977), the value of the Poisson's ratio has to be close to 0.2 for the elastic parts of unloading-reloading stress-paths. The value obtained for the core from the results of the triaxial test was too high, therefore it was decided to adopt a smaller value. In Fig. 7.1 the graph E_i/Pa versus σ_3'/Pa obtained from data of triaxial tests for core and shells is presented, while in Table 7.1 the determined elastic model parameters are summarized.

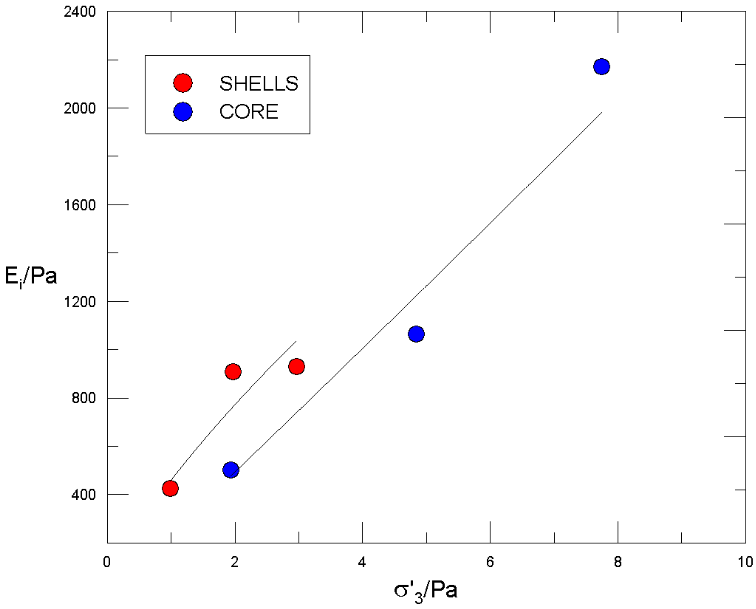

Figure 7.1 Elastic parameters M and n for core and shells

Table 7.1 Elastic parameters for core and shells

Elastic parameters	**Core**	**Shells**
M	242.5	459.4
n	1.03	0.75
ν	0.30	0.25

As mentioned in Sect. 4.3.4, the failure criterion is represented by the following relationship:

$$\eta_1 = \left(\frac{I_1^3}{I_3} - 27\right)\left(\frac{I_1}{Pa}\right)^m \tag{4.24}$$

The failure parameters m and η_1 can be determined by plotting $(I_1^3/I_3 - 27)$ versus (Pa/I_1) at failure on a log-log diagram (Fig. 7.2), where η_1 is the intercept with $(Pa/I_1) = 1$ and m is the slope of the straight line. The determined failure parameters for core and shell materials are presented in Table 7.2.

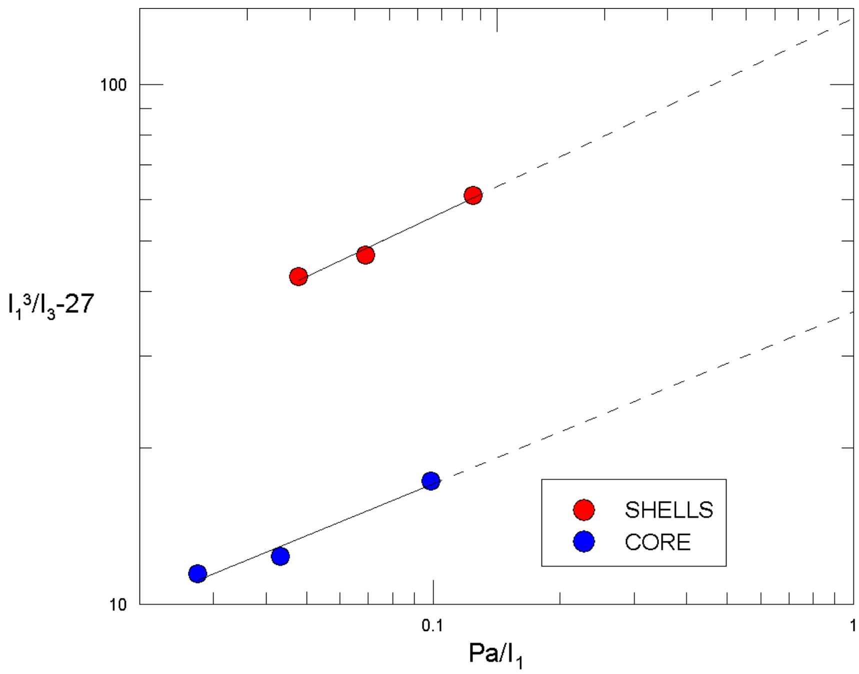

Figure 7.2 Failure parameters m and η_1 for core and shells

Table 7.2 Failure parameters for core and shells

Failure parameters	**Core**	**Shells**
η_1	36.5	133.3
m	0.33	0.38

The cap yield surface is characterized by the plastic collapse parameters p and C, which define the work-hardening parameter H_c as:

$$H_c = Pa^2 \left[\frac{W_{p,c}}{CPa}\right]^{\frac{1}{p}} \tag{4.29}$$

$W_{p,c}$ is the accumulated plastic work and can be calculated for isotropic compression test as follows:

$$W_{p,c} = \sum(\Delta W_{p,c}) = \sum(\sigma^T \Delta\varepsilon^{p,c}) = 3\sum(\sigma_3' \Delta\varepsilon_3^{p,c}) \tag{7.2}$$

The plastic collapse strains are calculated from the assumed isotropic compression test by subtracting the corresponding elastic strains to the total ones:

$$\Delta\varepsilon^{p,c} = \Delta\varepsilon - \Delta\varepsilon^e \tag{7.3}$$

The work-hardening parameter H_c for isotropic compression test can be determined using Eq. (4.27) obtaining:

$$H_c = 3\sigma_3'^2 \tag{7.4}$$

The relationship between $W_{p,c}$ and H_c can be described by:

$$W_{p,c} = CPa\left(\frac{H_c}{Pa^2}\right)^p \tag{7.5}$$

Plotting $W_{p,c}/Pa$ versus H_c/Pa^2 and fitting the data with a power function is possible to determine C and p.

Although there are no isotropic compression tests, it is possible to use the data of a one-dimensional test if appropriate assumptions are made. There is some experimental evidence suggesting that the compressibility in isotropic compression is lower than in one-dimensional compression (Kovacevic, 1994). Kovacevic (1994) assumed, firstly for the rockfill of Roadford dam, that the compressibility of the rockfill depends only on mean effective stress p' and a value of $K_0 = 0.40$. The resulting response (after all parameters were determined) in one-dimensional compression was too stiff, and to obtain better agreement a value of $K_0 = 0.30$ was assumed and that the compressibility in an isotropic compression test was some 20% lower than in a one-dimensional compression test.

For the core material of the Montedoglio dam, initially a similar assumption to Kovacevic (1994) on rockfill material was made, that its compressibility in an isotropic compression test was set 20% lower than in a one-dimensional compression test. However, as the resulting response was still too stiff, the percentage of reduction was increased to 40% obtaining with the resulting model parameters a good agreement between the observed and the simulated behaviour. In Fig. 7.3 $W_{p,c}/Pa$ versus H_c/Pa^2 is plotted for the core material and fitting the data with a power function the plastic collapse parameters are determined and reported in Table 7.3. The values of the plastic collapse parameters for the shell material presented in Table 7.3 were taken from the calculated values of the

Roadford rockfill analysed by Kovacevic (1994) with the Lade's double hardening model, because there are no one dimensional or isotropic compression tests for this material.

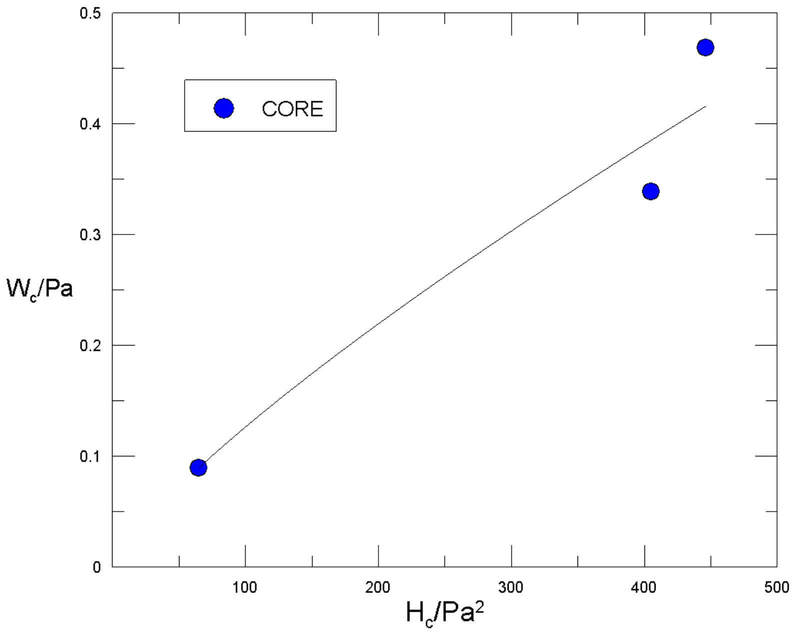

Figure 7.3 Work-hardening parameters p and C for core material

Table 7.3 Plastic collapse parameters for core and shells

Plastic collapse parameters	**Core**	**Shells**
C	0.0032	0.00045
p	0.769	1

The relationship between the work-hardening (or softening) parameter H_p and the accumulated plastic expansive work $W_{p,p}$ can be expressed by:

$$H_p = a\, e^{-b\, W_{p,p}} \left(\frac{W_{p,p}}{Pa}\right)^{1/q} \tag{4.35}$$

To define this relationship from a triaxial test it is necessary to follow some steps. First of all, determining H_p according to Eq. (7.6) and $W_{p,p}$ according to Eq. (4.36) and plotting H_p versus $W_{p,p}/Pa$.

$$H_p = \left(\frac{I_1^3}{I_3} - 27\right)\left(\frac{I_1}{Pa}\right)^m \tag{7.6}$$

$$W_{p,p} = \sum\left(\Delta W_{p,p}\right) = \sum(\sigma^T \Delta\varepsilon^{p,p}) \tag{4.36}$$

The plastic expansive strain increments $\Delta\varepsilon^{p,p}$ are calculated by subtracting the elastic $\Delta\varepsilon^e$ and plastic collapse strain increments $\Delta\varepsilon^{p,c}$ from the total strain increments $\Delta\varepsilon$ according to Eq. (4.13) and (4.14):

$$\Delta\varepsilon^{p,p} = \Delta\varepsilon - \Delta\varepsilon^e - \Delta\varepsilon^{p,c} \tag{7.7}$$

The parameter q is calculated for a particular value of the confining pressure σ_3' according to (Lade, 1977; Kovacevic, 1994):

$$q = \frac{\log\frac{W_{p,peak}}{W_{p,60}} - \left(1 - \frac{W_{p,60}}{W_{p,peak}}\right)\log e}{\log\left(\frac{\eta_1}{H_{p,60}}\right)} \tag{7.8}$$

where e is the base of the natural logarithm, $\left(W_{p,peak}, \eta_1\right)$ and $\left(W_{p,60}, H_{p,60}\right)$ are two sets of corresponding values from the relation between H_p-$W_{p,p}$. These two points are the values which correspond to the peak point and the point at 60% of η_1 on the work-hardening part of the H_p-$W_{p,p}$ relation. The representation of the H_p-$W_{p,p}/Pa$ relation of core and shell materials is reported in Fig. 7.4.

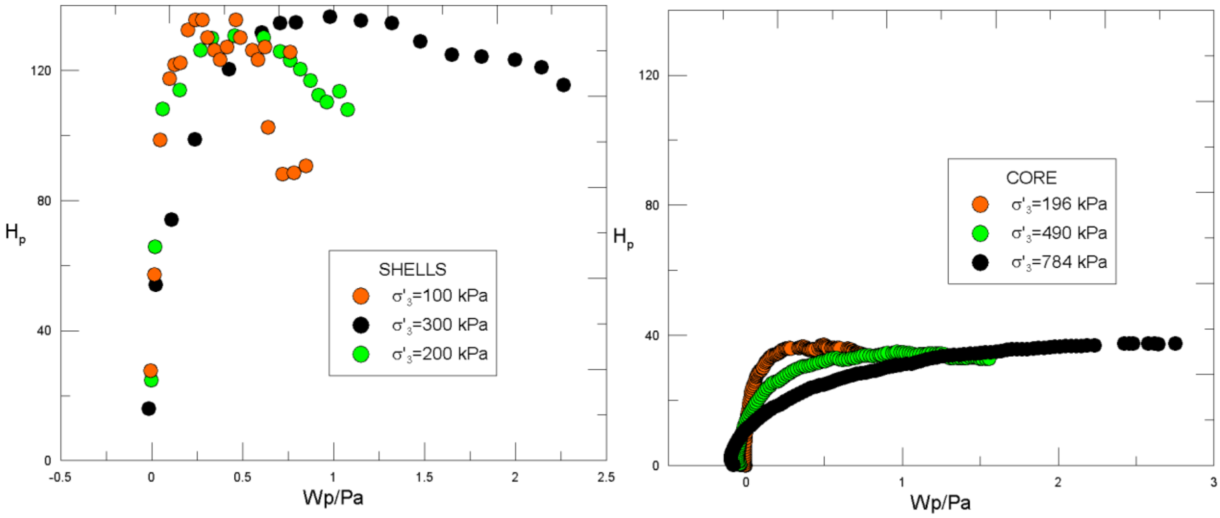

Figure 7.4 Variation of accumulated expansive plastic work $W_{p,p}$ with hardening parameter H_p and confining pressure σ_3'

The parameter q varies with confining pressures σ_3' according to Eq. (4.39) and once determined q for different values of the confining pressure, plotting q versus (σ_3'/Pa) is possible to evaluate the work-hardening parameters α and β (Fig. 7.5).

$$q = \alpha + \beta \frac{\sigma_3'}{Pa}, \; q \geq 1 \tag{4.39}$$

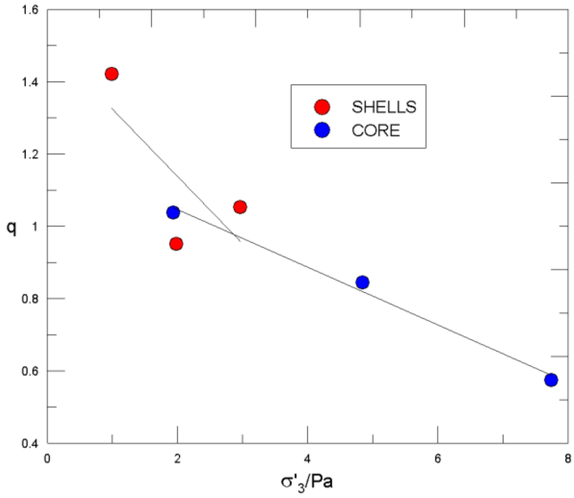

Figure 7.5 Work-hardening parameters α and β for core and shells

The parameters a and b from Eq. (4.35) are dependent on the minimum principal effective stress σ_3' as follows:

$$a = \eta_1 \left(\frac{e\,Pa}{W_{p,peak}}\right)^{1/q} \tag{4.37}$$

$$b = \frac{1}{q\,W_{p,peak}} \tag{4.38}$$

$$W_{p,peak} = Pa\,P \left(\frac{\sigma'_3}{Pa}\right)^{I} \tag{4.40}$$

Plotting the values of $(W_{p,peak}/Pa)$ versus (σ'_3/Pa) and fitting the data by a power function as in Fig. 7.6, the parameters P and I can be determined.

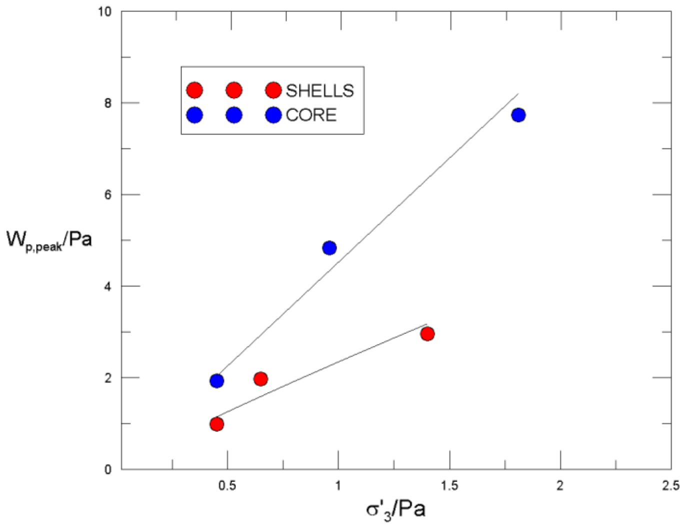

Figure 7.6 Work-hardening parameters P and I for core and shells

The value η_2 of the non-associative flow rule (Eq. (4.33)) can be evaluated from the results of triaxial compression tests using the following expression (Lade, 1981):

$$\eta_2 = \frac{3\,(1+\nu^p)\,I_1^2 - 27\,\sigma'_3\,(\sigma'_1 + \nu^p\,\sigma'_3)}{\left(\frac{Pa}{I_1}\right)^m \left[\sigma'_3\,(\sigma'_1 + \nu^p\,\sigma'_3) - \left(\frac{I_3}{I_1}\right) m\,(1+\nu^p)\right]} \tag{7.9}$$

where ν^p is a function of the plastic expansive strain increments determined by subtracting the elastic and plastic collapse strain increments from the total ones as before:

$$\nu^p = -\frac{\Delta\varepsilon_3^{p,p}}{\Delta\varepsilon_1^{p,p}} \tag{7.10}$$

The variation of the calculated η_2 is plotted against H_p in Fig. 7.7 from data of drained triaxial tests on core and shell materials determining the model parameters S, R and t on which η_2 depends (Eq. (4.34). The plastic expansive parameters of core and shell materials are summarized in Table 7.4.

$$\eta_2 = S\, H_p + R\left(\frac{\sigma_3'}{Pa}\right)^{1/2} + t \tag{4.34}$$

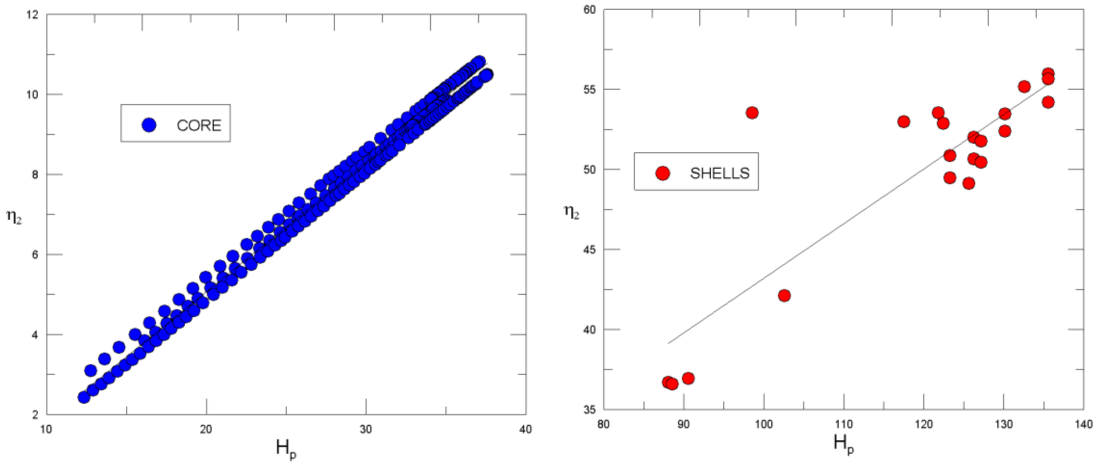

Figure 7.7 Plastic potential parameters S, R and t for core and shells

Table 7.4 Plastic expansive parameters for core and shells

Plastic expansive parameters	**Core**	**Shells**
α	1.2	1.5
β	-0.08	-0.19
P	0.23	0.42
I	0.98	0.98
S	0.33	0.32
R	0	0
t	-1.4	10.2

7.3 MODEL PREDICTIONS FOR IDEALIZED SINGLE ELEMENT TESTS

The model parameters determined in the previous Section are employed herein to predict the response of the core and shells materials in drained triaxial compression tests, comparing the predicted and the observed behaviour. The predictions were made assuming that the laboratory tests have no end or side imperfections and that the soil behaves in a uniform manner throughout the sample (Kovacevic, 1994). The soil sample was modelled as a single axisymmetric finite element, on which increments of compressive axial strain $\Delta\varepsilon_a$ were applied with a constant confining pressure σ_3'. The results of the triaxial tests are plotted in terms of deviatoric stress $\sigma_1 - \sigma_3$ versus the volumetric strain ε_v and versus the axial strain ε_a.The comparison between the results from finite element simulations and laboratory tests are presented in Fig. 7.8 for drained triaxial compression test on core material at different values of confining pressure $\sigma_3' = 196, 490, 785$ kPa, and in Fig. 7.10 for large drained triaxial compression test on shell material at $\sigma_3' = 100, 200, 300$ kPa. In Fig. 7.9 a 7.1, particulars of the triaxial test on the core and shell material in a lower range of axial strain are presented.

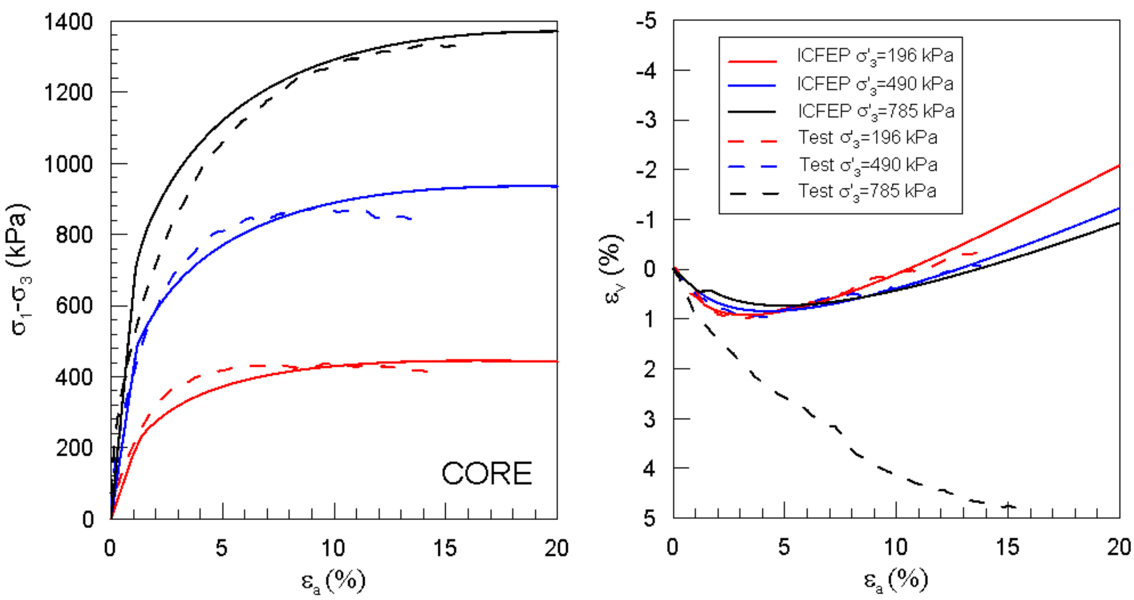

Figure 7.8 Comparison of predicted and measured behaviour in drained triaxial tests on core material with Lade's double hardening model

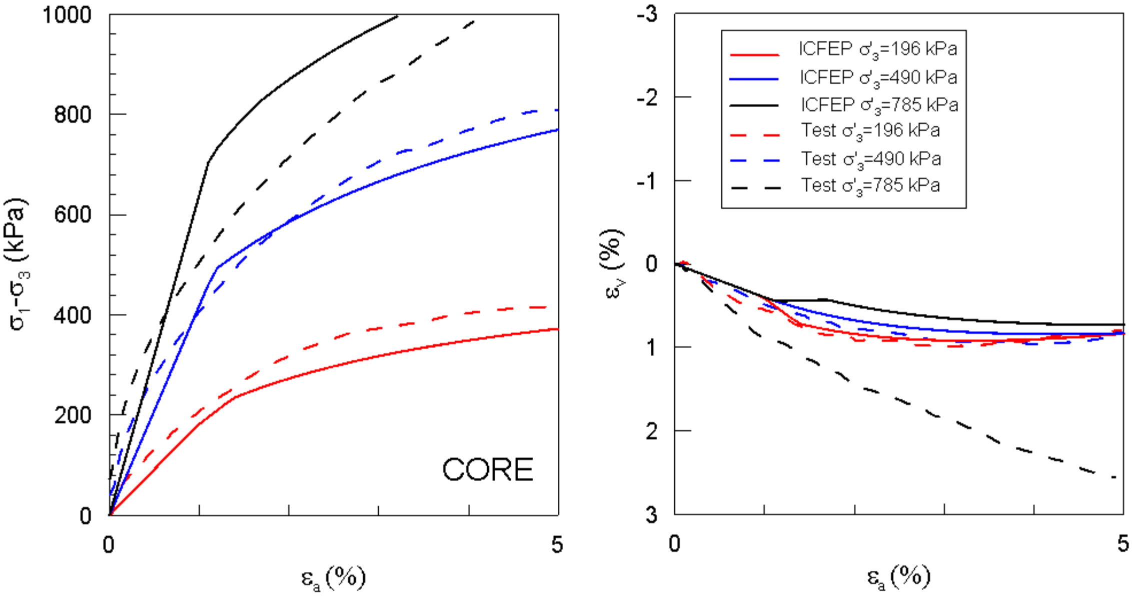

Figure 7.9 Particular of the comparison of predicted and measured behaviour in drained triaxial tests on core material with Lade's double hardening model where the axial strain is lower than 5%

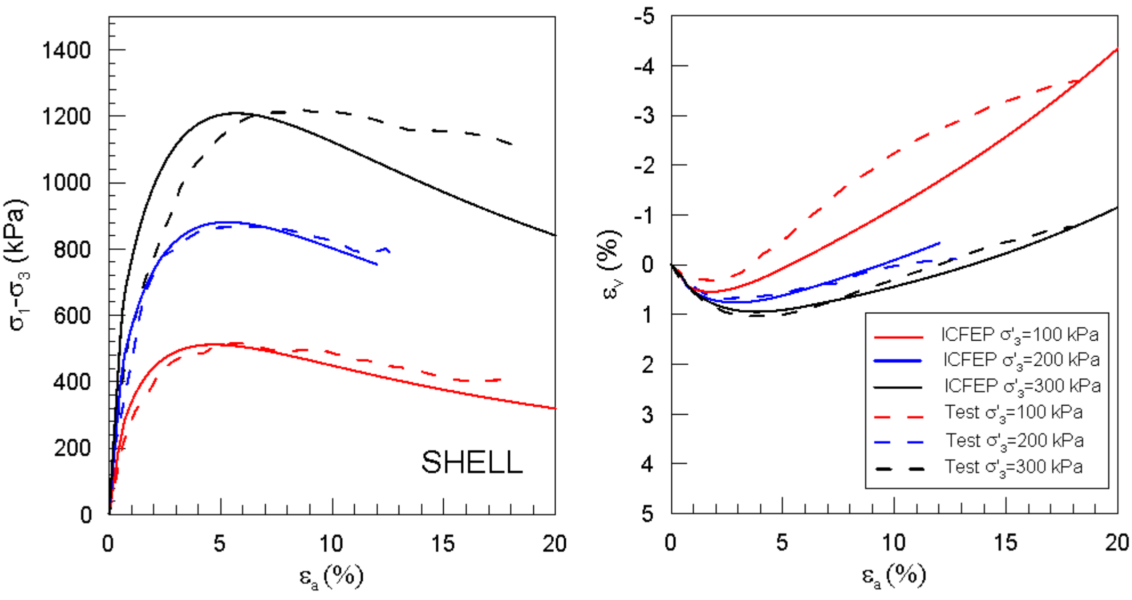

Figure 7.10 Comparison of predicted and measured behaviour in drained triaxial tests on shell material with Lade's double hardening model

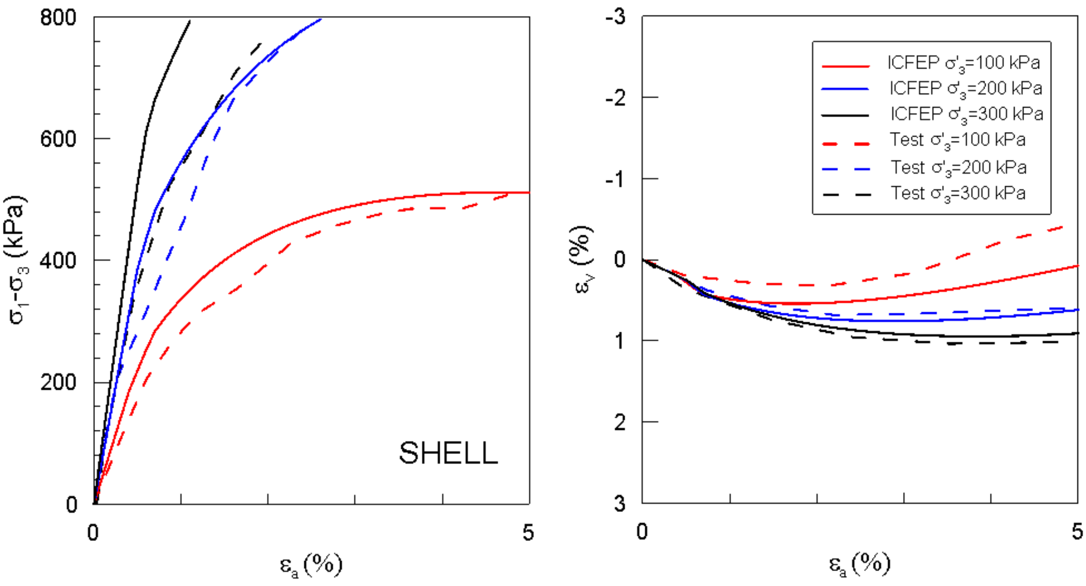

Figure 7.11 Particular of the comparison of predicted and measured behaviour in drained triaxial tests on shell material with Lade's double hardening model where the axial strain is lower than 5%

As it can be seen in Fig. 7.9, for core material there is a good agreement between observed and predicted initial elastic stiffness for axial strain lower than 2%. In about the range of 2-5 % the stiffness is slightly underestimated for $\sigma_3' = 196$ and 490 kPa and slightly overestimated for $\sigma_3' = 785$ kPa. The volumetric behaviour is overall well described for $\sigma_3' = 196$ and 490 kPa (Fig. 7.8), where the volumetric strains at low stress levels are captured and the variation with axial strains as well. At high confining pressure ($\sigma_3' = 785$ kPa) the analysis is not able to represent the compressive behaviour (Fig. 7.8) and the variation of volumetric strains is characterized by a step (see Fig. 7.9) which could probably related to numerical problems. For the shell material (Fig. 7.10), the observed behaviour in the $q - \varepsilon_a$ plane is well captured by the model for $\sigma_3' = 100$ and 200 kPa, while for $\sigma_3' = 300$ kPa the stiffness is quite overestimated (Fig. 7.11) and also the softening curve is more accentuated than the real one. The variation of volumetric strains with axial strains in general is quite well described, but the maximum value of volumetric strain is slightly overestimated for the small value of confining pressure $\sigma_3' = 100$ kPa (Fig. 7.11).

Some of the 14 model parameters which were determined based on laboratory tests following the calibration procedure described in Section 7.2, were modified through the numerical simulation of the single element tests to fit better the measured curves. In Tables 7.5 and 7.6 the model parameters determined from tests and used in the finite element simulation of both materials are summarised, respectively (in bold are indicated the parameters modified).

Table 7.5 Model parameters determined from laboratory tests for core and shells

Model parameters	Core	Shells
M	242.5	459.4
n	1.03	0.75
ν	0.30	0.25
η_1	36.5	133.3
m	0.33	0.38
C	0.0032	0.00045
p	0.769	1
α	1.2	1.5
β	-0.08	-0.19
P	0.23	0.42
I	0.98	0.98
S	0.33	0.32
R	0.0	0.0
t	-1.4	10.2

Table 7.6 Model parameters modified from single element tests for core and shells

Model parameters	Core	Shells
M	**100.0**	459.4
n	**0.9**	0.75

ν	0.30	0.25
η_1	36.5	133.3
m	**0.31**	0.38
C	0.0032	0.00045
p	0.769	1
α	**3.5**	**3.0**
β	**0.0**	**0.0**
P	**0.25**	**0.15**
I	**1.0**	0.98
S	**0.39**	**0.27**
R	0.0	0.0
t	**2.8**	**12.0**
OCR	**2**	**3**

7.4 FINITE ELEMENT ANALYSIS

In this paragraph the results of the numerical analyses of the construction phase and reservoir impounding of the Montedoglio dam using the finite element code ICFEP are presented and discussed. The analysed cross-section is the Section C of the zoned dam, whose finite element mesh is presented in Fig. 7.12. The boundaries of the geometrical model were defined as 5 m below the dam's base and 150 m away from the dam's toes. The boundary conditions are characterized by zero horizontal and vertical displacements along the bottom boundary, and zero horizontal displacement on the lateral boundaries. It was assumed implicitly that the tested samples were representative of the fill materials in the field. Filters and drained layers were included in the shells for the entire simulation. The analysis is fully coupled but only the core was considered as consolidating material. The water table during construction was assumed to be in the rock foundation below the core at 335.97 m a.s.l. and it was raised before the reservoir impounding to reach the top of the alluvial layer upstream at 346.6 m a.s.l. and downstream at 342.2 m a.s.l.. The phases of the analysis in terms of increments, time, embankment and water levels are described in Table 7.7.

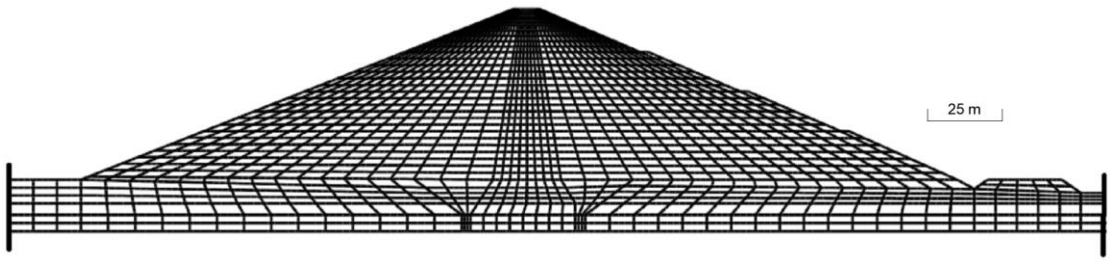

Figure 7.12 Finite element mesh of the dam's cross-section

Table 7.7 Description of the phases of the analysis in terms of increments, time, embankment and water levels

Phase	Increment number	Time (year)	Embankment level (m a.s.l.)	Water level upstream (m a.s.l.)	Water level downstream (m a.s.l.)
Excavation	1	0.1875	342.61	335.97	335.97
	2	0.1875	341.00		
	3	0.1875	339.43		
	4	0.1875	335.97		
Construction	5 - 36	6	398.30	335.97	335.97
Rising water level	37	0.3	398.30	346.60	342.20
Reservoir impounding	38	0.083	398.30	350.00	342.20
	39	0.083		360.00	
	40 - 69	7.5		360.00	
	70	0.5		374.00	
	71 - 90	2.7		374.00	
	91	0.25		385.00	
	92 - 102	11		385.00	

7.4.1 Analysis during construction

The analysis of the construction phase of the Montedoglio dam was carried out using the Lade’s double hardening model for the materials of the dam’s body. The constitutive models employed for the foundation soil are the elastic perfectly plastic Mohr-Coulomb model and a linear elastic model, for the alluvial layer and the rock basement, respectively. The physical parameters for all materials are summarized in Table 5.14, which also contains the mechanical parameters for the linear elastic and Mohr-Coulomb models. The elastic parameters of the alluvial layer were chosen to match the observed settlements at the top of the foundation. The double-hardening model parameters for the core and shell materials were already presented in the previous section in Table 7.6. The precipitation boundary condition (Section 4.2.5) was prescribed on both sides of the core, prescribing no flow from the core. The value of the permeability in the core was considered isotropic and variable with mean effective stress, using a nonlinear model described before in Sect. 4.2.6 Eq. 4.12. The value of the coefficient of permeability at zero mean effective stress was $k_0 = 3 \cdot 10^{-10}$ m/s, while the choise of the constant $a = 0.002\ m^2/kN$ was based on the existing literature on London clay (Schroeder et al. 2004; Gawecka et al. 2017)).

Table 7.8 Physical and mechanical soils parameters

Parameters/Materials	**Core**	**Shoulders**	**Alluvial layer**	**Rock basement**
γ_{sat} (kN/m^3)	20.7	25.0	22.0	25.0
γ_d (kN/m^3)	20.7	24.2	22.0	25.0
c' (kPa)	-	-	0	-
φ' (°)	-	-	40	-
E' (MPa)	-	-	200	12550
ν (−)	-	-	0.25	0.35

Before the construction, a distribution of a stress state in K_0 conditions was given to the foundation layers through an user defined subroutine and assuming the water level in the rock foundation below the core at height of 335.97 m a.s.l.. The excavation of the alluvial layer to found the core directly on the rock foundation was simulated removing groups of elements in 4 horizontal layers (Table 7.7), one layer per increment. The construction started adding groups of elements through a gravity 'turn-on' analysis. The entire construction was simulated through 32 horizontal layers in 32 increments as Table 7.7 summarily shows. More specific details about the increments, the time and the embankment level for each increment are reported in Table 7.9.

Table 7.9 Description of construction phase in terms of increments, time, embankment and water levels

Phase	Increment number	Time (year)	Embankment level (m a.s.l.)	Water level (m a.s.l.)
Construction	5	0.1875	339.43	335.97
	6	0.1875	341.00	335.97
	7	0.1875	342.61	335.97
	8	0.1875	344.19	335.97
	9	0.1875	346.6	335.97
	10	0.1875	348.7	335.97
	11	0.1875	350.8	335.97
	12	0.1875	352.9	335.97
	13	0.1875	355.0	335.97
	14	0.1875	357.1	335.97
	15	0.1875	359.2	335.97
	16	0.1875	361.3	335.97
	17	0.1875	363.3	335.97
	18	0.1875	365.3	335.97
	19	0.1875	367.3	335.97
	20	0.1875	369.3	335.97
	21	0.1875	371.3	335.97
	22	0.1875	373.3	335.97
	23	0.1875	375.3	335.97
	24	0.1875	377.3	335.97
	25	0.1875	379.3	335.97
	26	0.1875	381.3	335.97
	27	0.1875	383.3	335.97
	28	0.1875	385.3	335.97
	29	0.1875	386.9	335.97
	30	0.1875	388.6	335.97
	31	0.1875	390.2	335.97
	32	0.1875	391.8	335.97
	33	0.1875	393.4	335.97
	34	0.1875	395.1	335.97
	35	0.1875	396.7	335.97
	36	0.1875	398.3	335.97

An initial value of suction was assigned to the dam’s body during construction, in particular 10 kPa to the shells and 50 kPa to the core were defined. The effect of mechanical compaction on the new constructed layers was taken into account selecting a value of $K_0 = 1$ (Potts et al., 2001; Massarsch, 2002) in order to simulate the increase of horizontal stress in the soil. The mesh of the dam's body with cumulated displaced shape and the vectors of cumulated displacement at the end of the construction are presented in Fig. 7.13. The maximum value of the displacements is 88.7 cm and it was reached in the core. In Fig.7.14 the contours of cumulated vertical and horizontal displacements at the end of the construction are showed. The contours of cumulated vertical and horizontal total stress level at the end of the construction are defined in Fig. 7.15, while the contours of cumulated vertical and horizontal effective stress level at the end of the construction are presented in Fig. 7.16. As it can be seen in Fig. 7.15 the trend of the vertical total stress highlights a step at the contact between shell and core, with a reduction of the vertical total stress in the core. The reason could be probably due to a load transfer from core to shell. The presence of arching is highlighted by the finite element analysis and it could be explained by a great difference between core and shells elastic moduli. The variation of Young's modulus with confining pressure of both materials according to Lade's double hardening model is shown in Fig. 7.17. As the confining pressure increases, the difference between the two Young's moduli becomes greater. The contours of accumulated pore fluid stress (Fig. 7.18) show that at the end of the construction there is still a suction of 10 kPa in the shells and that an excess of pore pressure was developed in the core. The contours of cumulated total volumetric and deviatoric strains are showed in Fig. 7.19, and the contours of cumulated plastic volumetric and deviatoric strain follow in Fig. 7.20. The observed settlements at the end of the construction in the upstream shell (A1-A2-A3) (see Section 5.4.1), at the contact core-downstream shell (A7-A8-A9), and in the downstream shell (A5-A6-A7) are presented in Fig. 7.21 in comparison with calculated settlements using ICFEP and the Lade's double hardening model. The measured settlements at the end of the construction are well captured in terms of absolute values and in terms of vertical displacements profiles. Along the verticals A7-A8-A9 there is a very good match from predicted and measured displacements. The measured settlements are slightly overestimated in the upstream shell (A1-A2-A3), while in the downstream shell (A5-A6-A7) the settlements of the foundation layer are underestimated. On the whole, the comparison shows that the Lade's double hardening model seems well-suited to predict the settlements of the dam during construction for both core and shells.

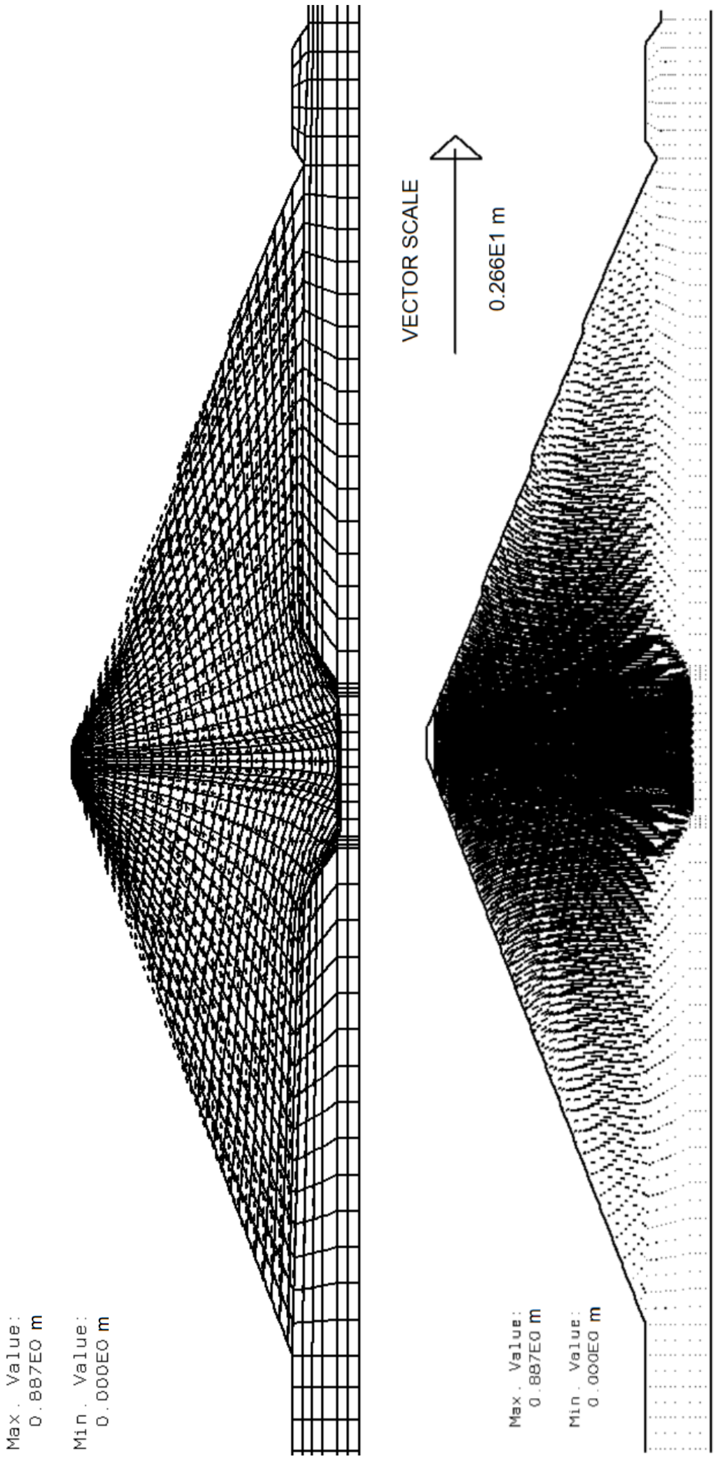

Figure 7.13 left) Mesh of the dam’s body with cumulated displaced shape at the end of the construction; right) vectors of cumulated displacement at the end of the construction

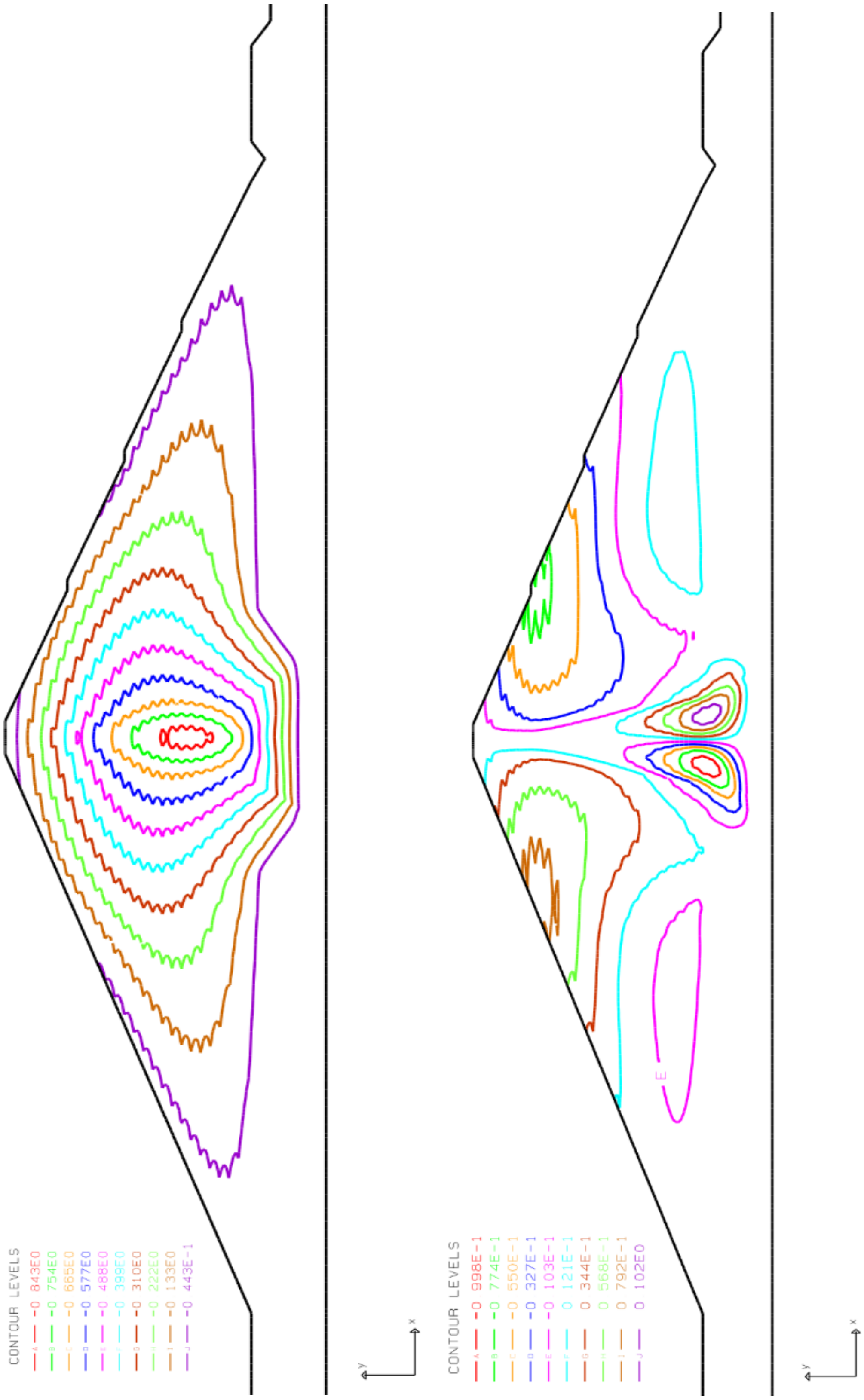

Figure 7.14 Contours of cumulated left) vertical displacements v (m) and right) horizontal displacements u (m) at the end of the construction

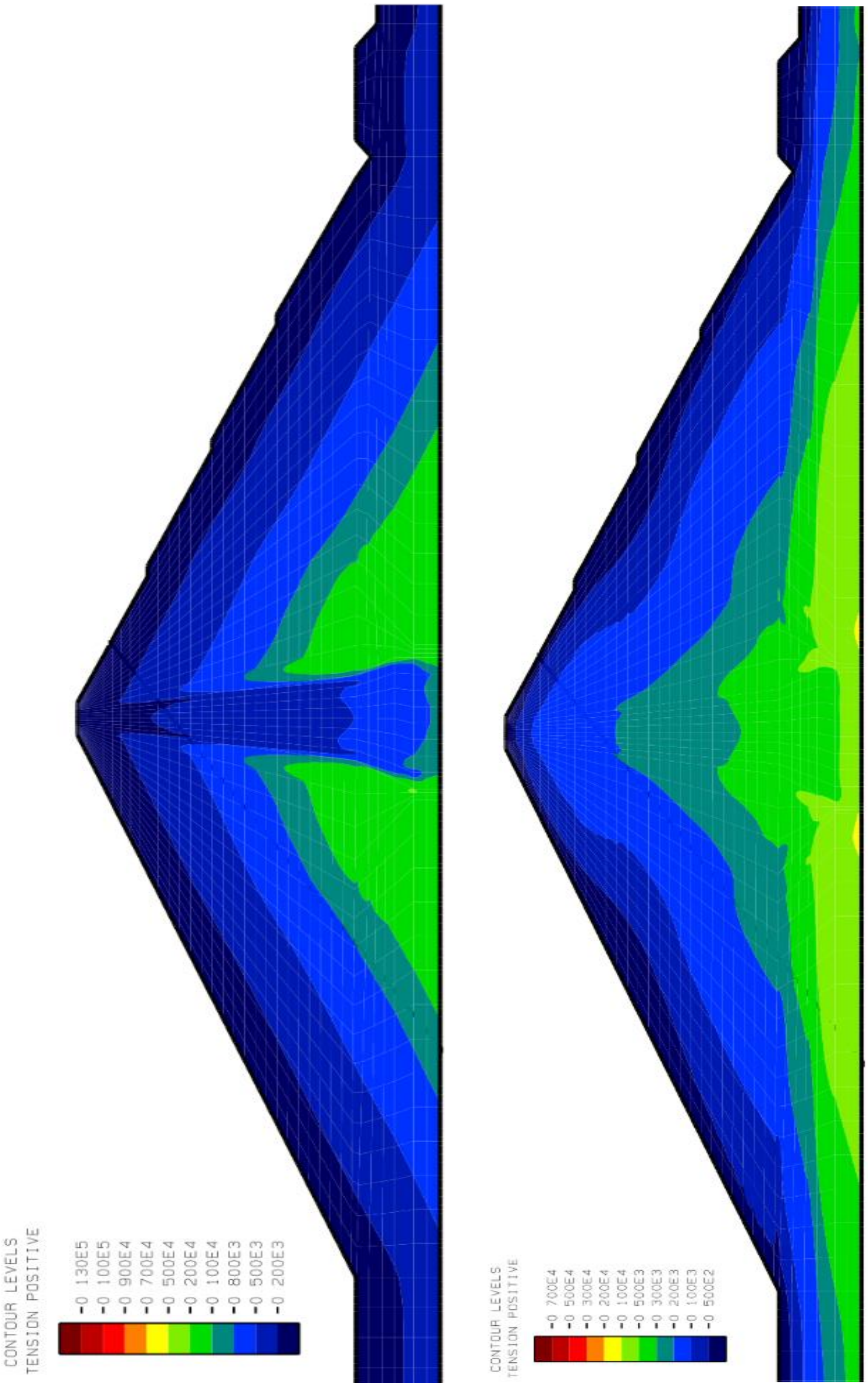

Figure 7.15 Contours of cumulated left) vertical total stress level σ_y (kPa) and right) horizontal total stress level σ_x (kPa) at the end of the construction

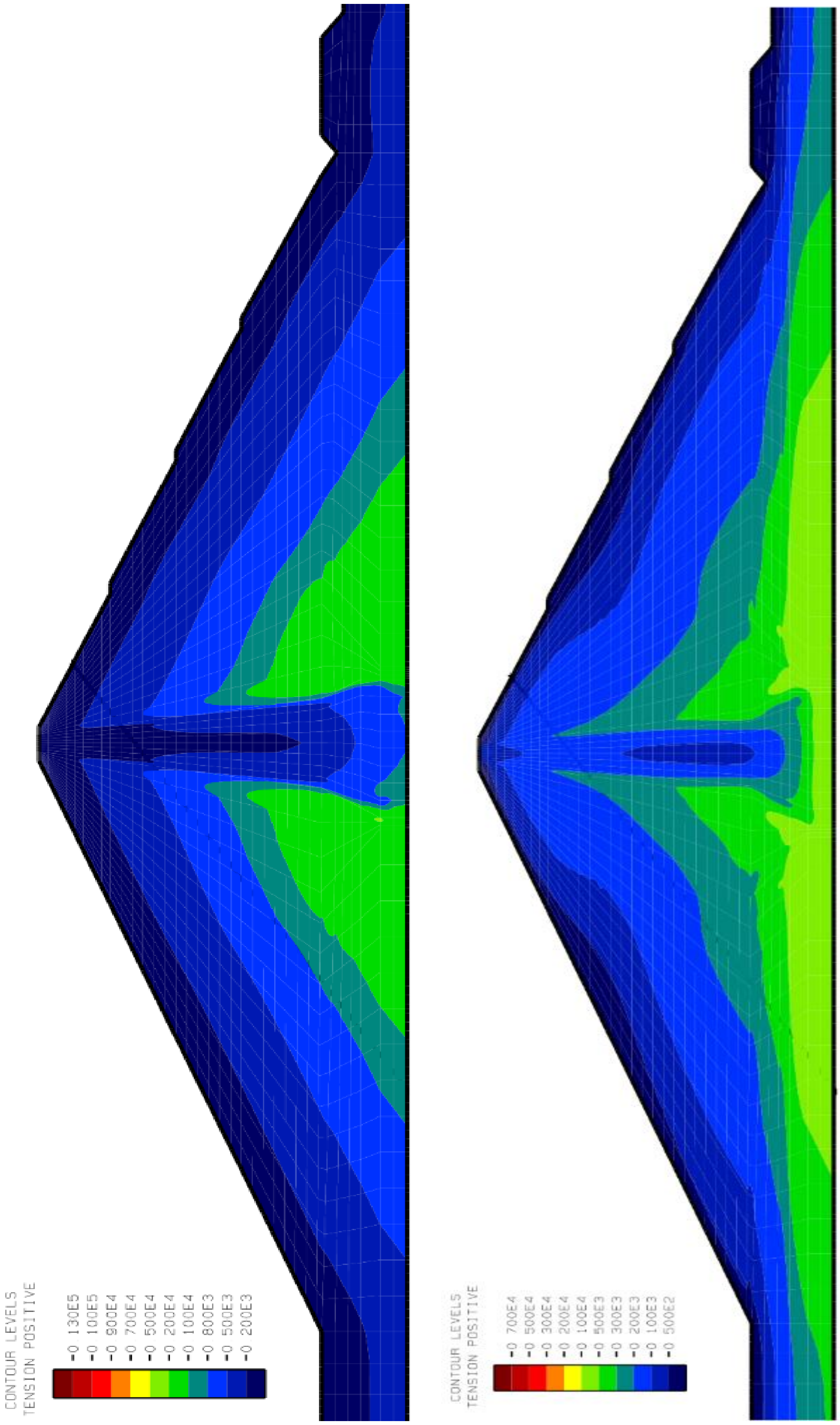

Figure 7.16 Contours of cumulated left) vertical effective stress level σ'_y (kPa) and right) horizontal effective stress level σ'_x (kPa) at the end of the construction

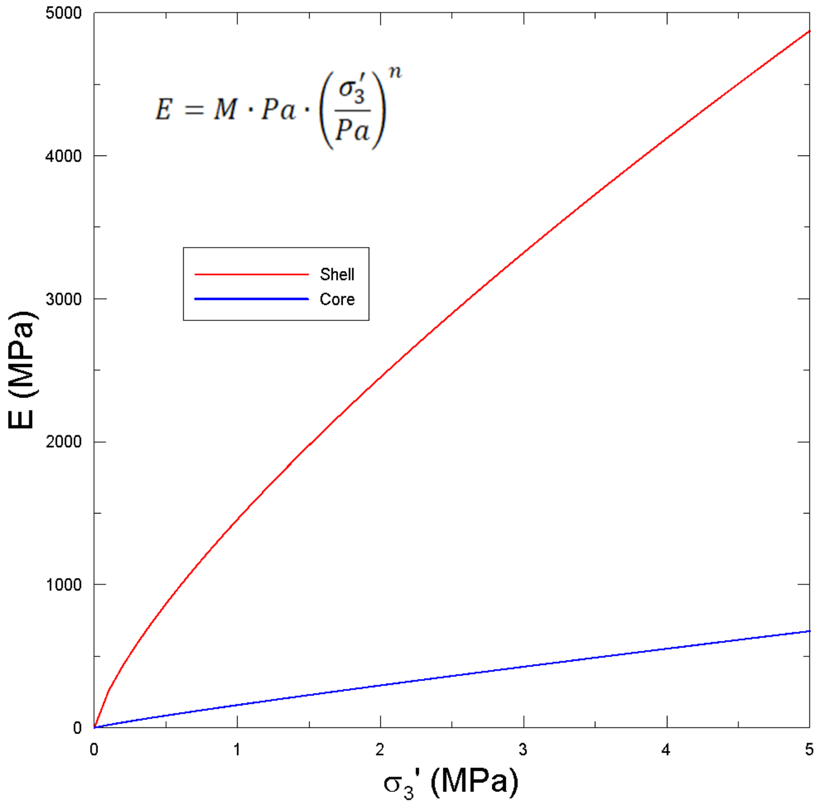

Figure 7.17 Variation of elastic modulus with confining pressure for core and shell

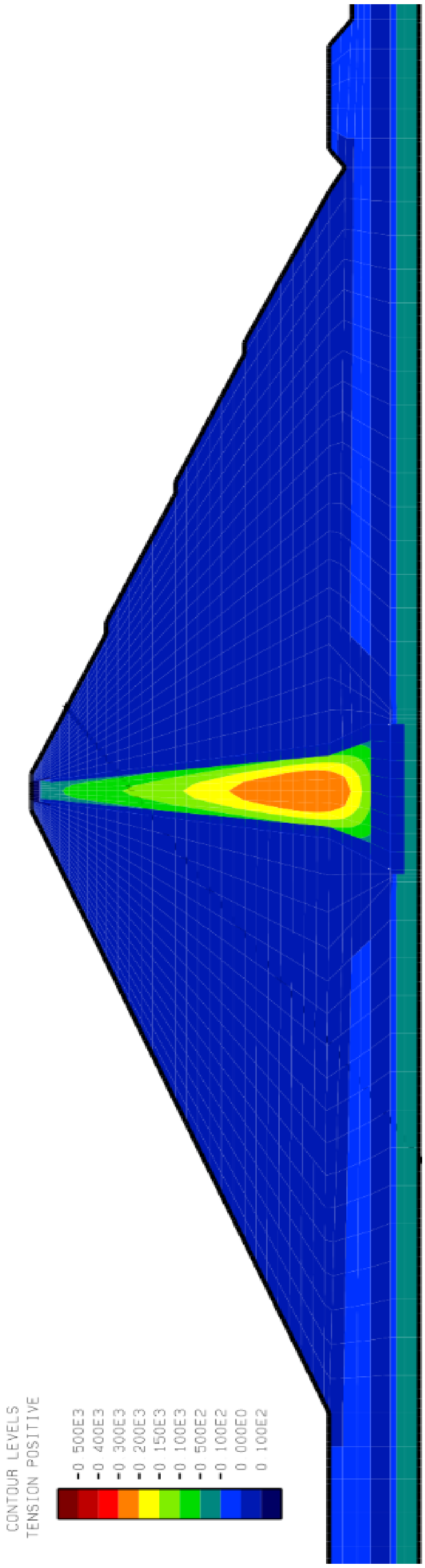

Figure 7.18 Contours of cumulated fluid stress u (kPa) at the end of the construction

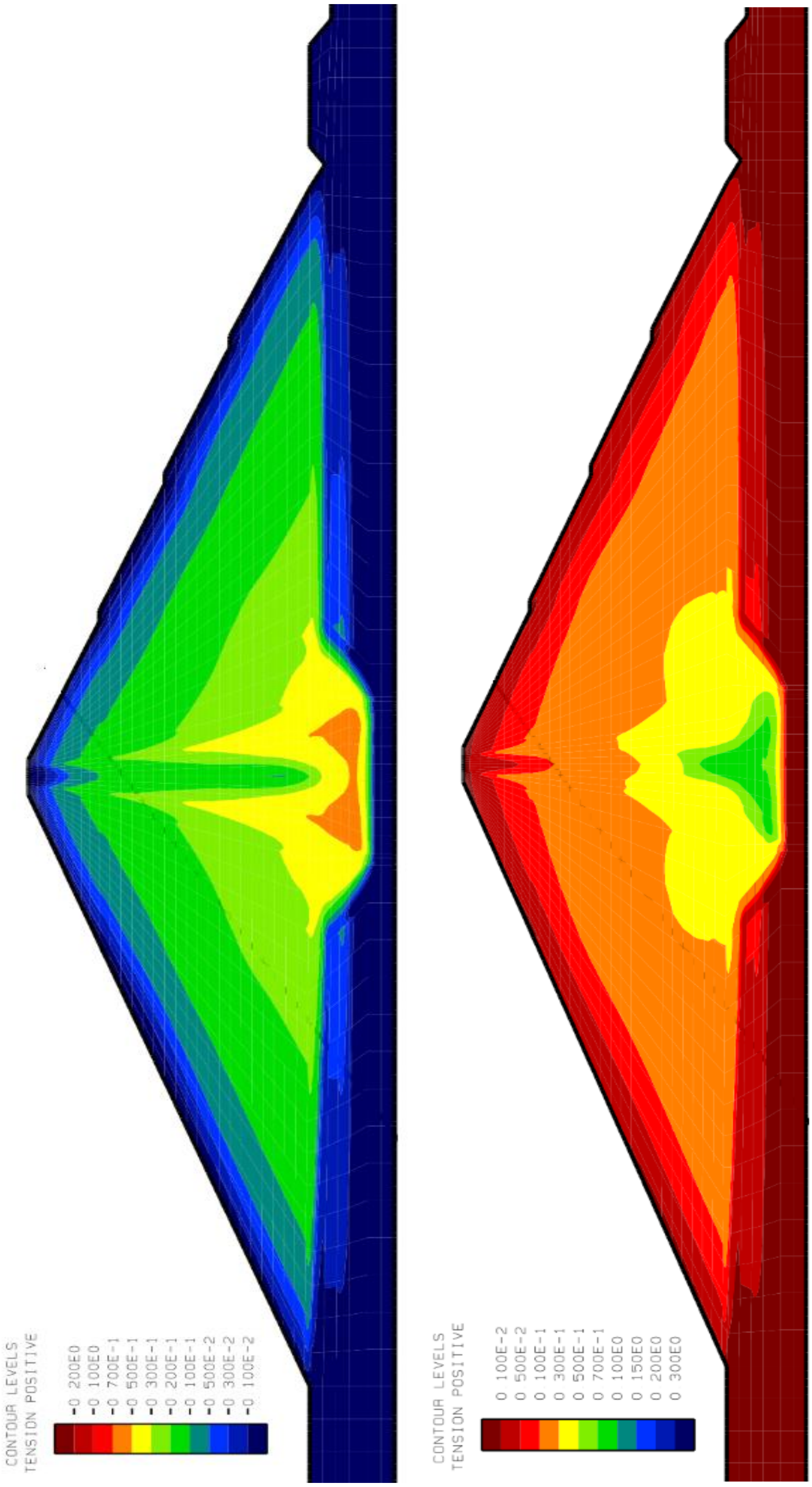

Figure 7.19 Contours of cumulated left) total volumetric strain ε_v $(-)$ and right) total deviatoric strain E $(-)$ at the end of the construction

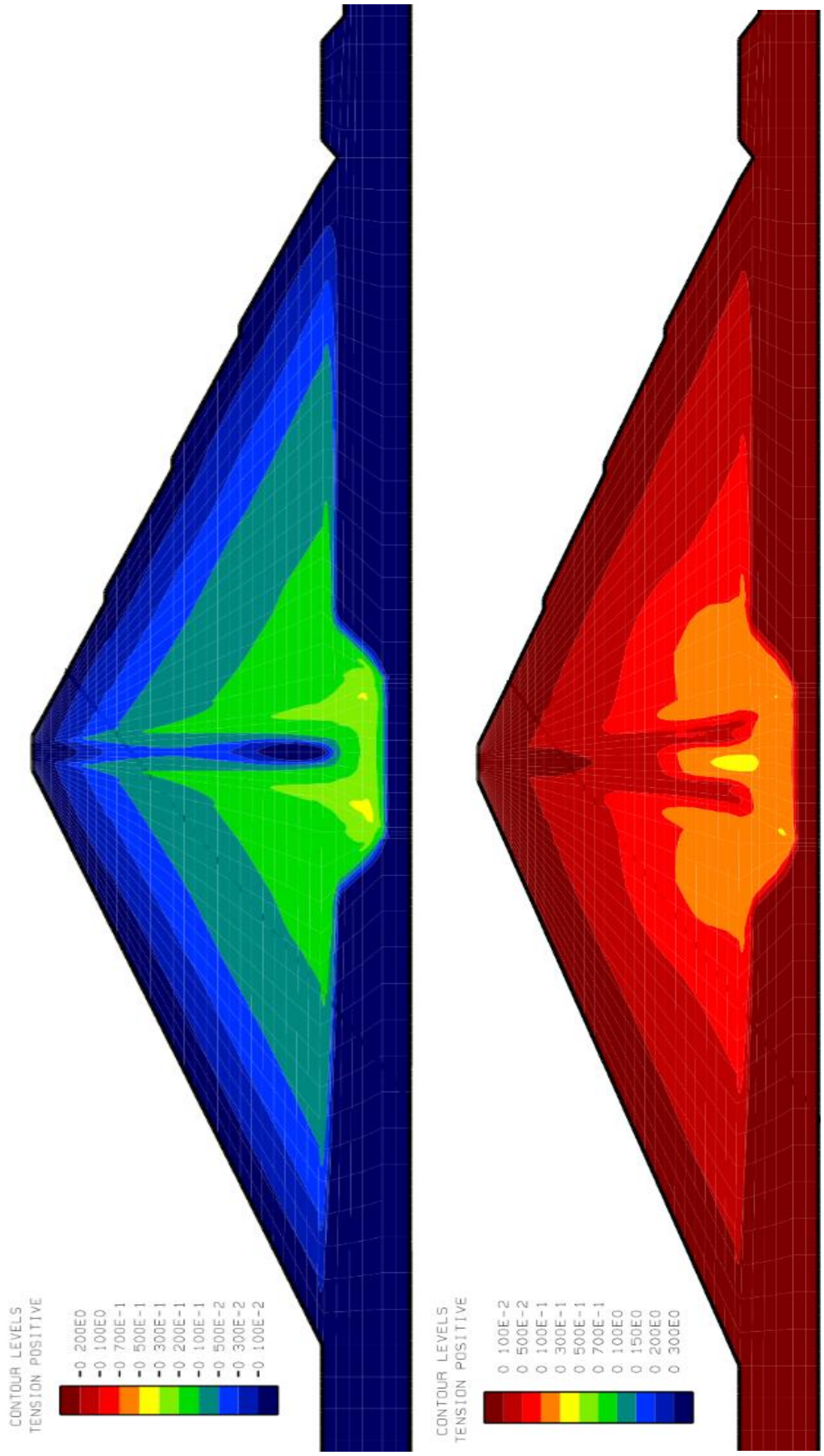

Figure 7.20 Contours of cumulated left) plastic volumetric strain ε_v $(-)$ and right) plastic deviatoric strain E $(-)$ at the end of the construction

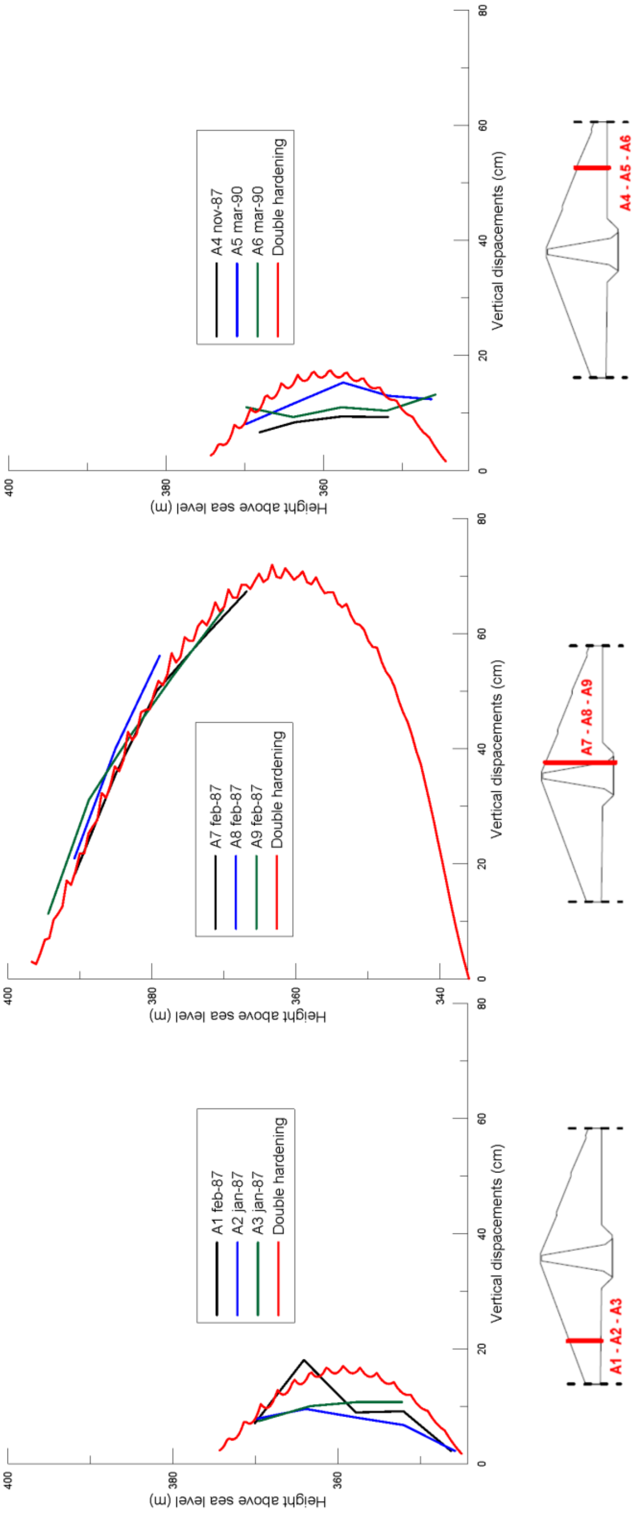

Figure 7.21 Comparison between observed and predicted settlements at the end of the construction in the upstream shell (A1-A2-A3), at the contact core-downstream shell (A7-A8-A9), and in the downstream shell (A5-A6-A7) using ICFEP, the Lade's double hardening and the linear elastic models

7.4.2 Rising of water level

Before the beginning of the impoundment, the water level was raised from the level at the base of the core to the top of the alluvial layer at maximum height of 346.6 m a.s.l. upstream and 342.2 m a.s.l. downstream. The rising of water level was simulated through the hydraulic boundaries applying the water level as “internal” pore fluid pressure in the elements of the mesh. The pore fluid pressure was applied as hydraulic boundary in one increment to the upstream side of the model and then modified incrementally during reservoir impounding, while in the downstream side it was applied in one increment and left unchanged until equilibrium was reached at the end of the analysis (see Table 7.7). The water level was raised to the top of the foundation soil at the end of the construction in the increment number 37. The plot of the contours of cumulated fluid stress in Fig. 7.22 show that compared to Fig. 7.18 the water level was increased correctly.

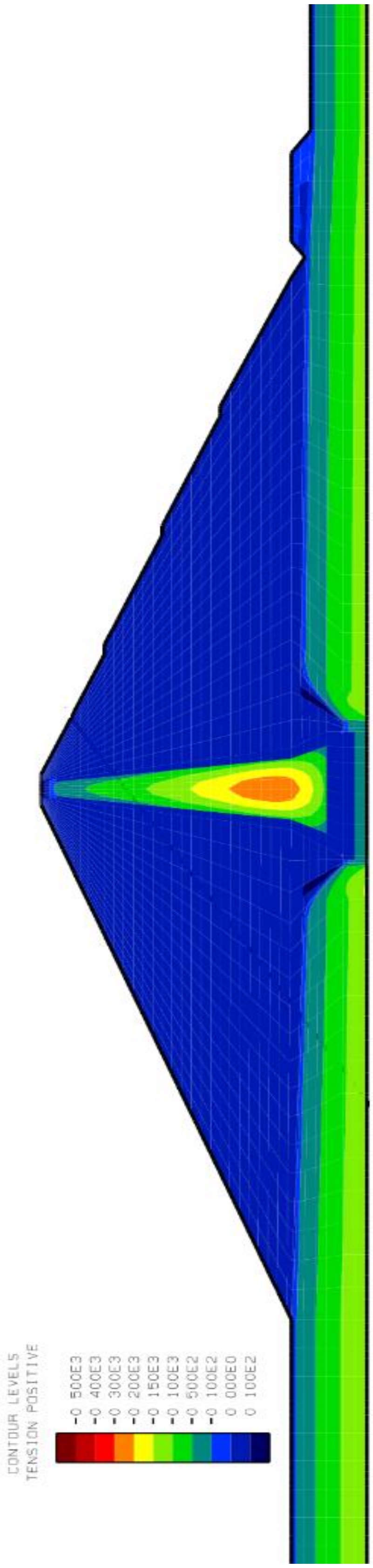

Figure 7.22 Contours of cumulated fluid stress u (kPa) after the rising of water level

7.4.3 Analysis during reservoir impounding

The reservoir impounding was simulated by applying the water load as an "internal" pore fluid pressure on the upstream face and as an "external" pore fluid pressure on the consolidating element, the core. The mechanical effect of the water load was reproduced by applying stress boundary conditions on the upstream face of the dam. The reservoir level was raised in stages and Fig. 7.23 shows the time sequence of the real reservoir impounding compared to the modelled one. As Table 7.7 shows, the water level was increased initially to 360 m a.s.l. in two increments of one month per increment (increments number 38 and 39), then the dam was left consolidating for 7 years and 6 months in 30 increments of 3 months per increment (increments from 40 to 69). After that, the water level was raised to 374 m a.s.l. in one increment (increment number 70) of 6 months and then it was left to consolidate for 2 years and about 9 months in 20 increments (from 71 to 90). In the last stage, the water level reached 385 m a.s.l. in one increment of 3 months (increment number 91) and then the consolidation continued for 11 years in 11 increments (from 92 to 102) of one year per increment. In the time sequence of reservoir impounding (Fig. 7.24) five dates were chosen in function of the available measured data, to compare observed and predicted settlements: April 1990, May 1990, May 1993, September 1996, and Febbruary 2001. The observed settlements at each of these dates in the upstream shell (A1-A2-A3), at the contact core-downstream shell (A7-A8-A9), and in the downstream shell (A5-A6-A7) are presented in comparison with the predicted settlmements using ICFEP and the Lade's double hardening model. A very good agreement between observed and predicted settlements for each of the five dates is highlighted in Fig. 7.25, 7.26, 7.27, 7.28 and 7.29, proving that the Lade's model is well suited not only for the simulation of the construction but also for the reservoir impounding. The contours of vertical and horizontal total stress level (Fig. 7.30), vertical and horizontal effective stress level (Fig. 7.31), cumulated fluid stress (Fig. 7.32), total volumetric and deviatoric strain (Fig. 7.33), and plastic volumetric and deviatoric strain (Fig. 7.34) are presented for the increment which corresponds to February 2001.

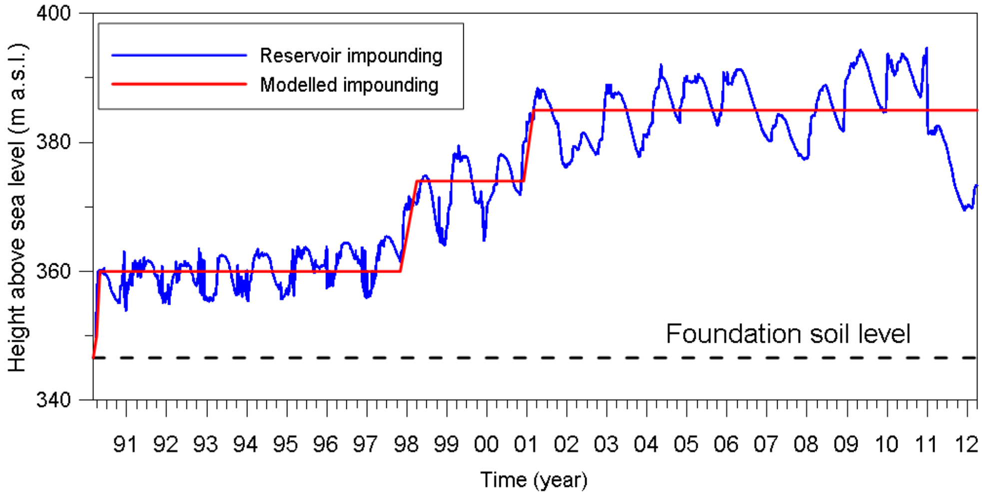

Figure 7.23 The representation of the dam reservoir impounding during time in comparison with modelled one

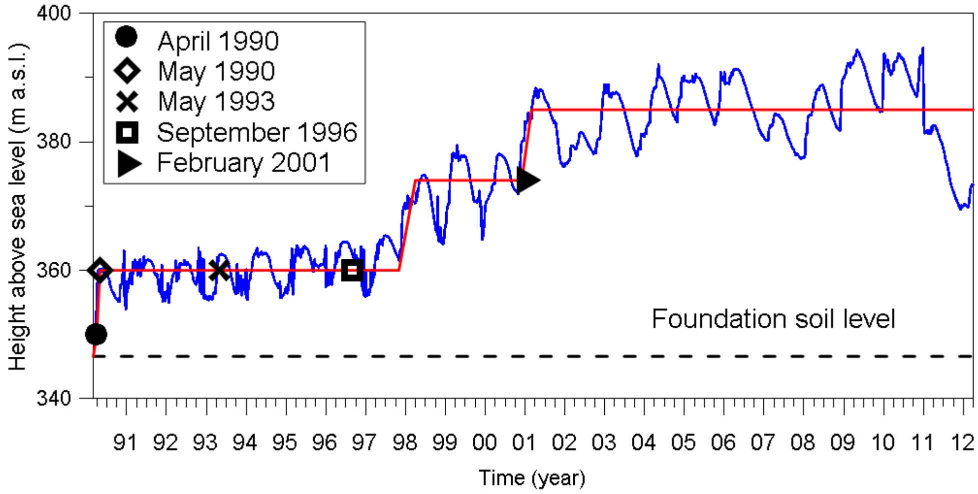

Figure 7.24 The representation of the five points during dam reservoir impounding

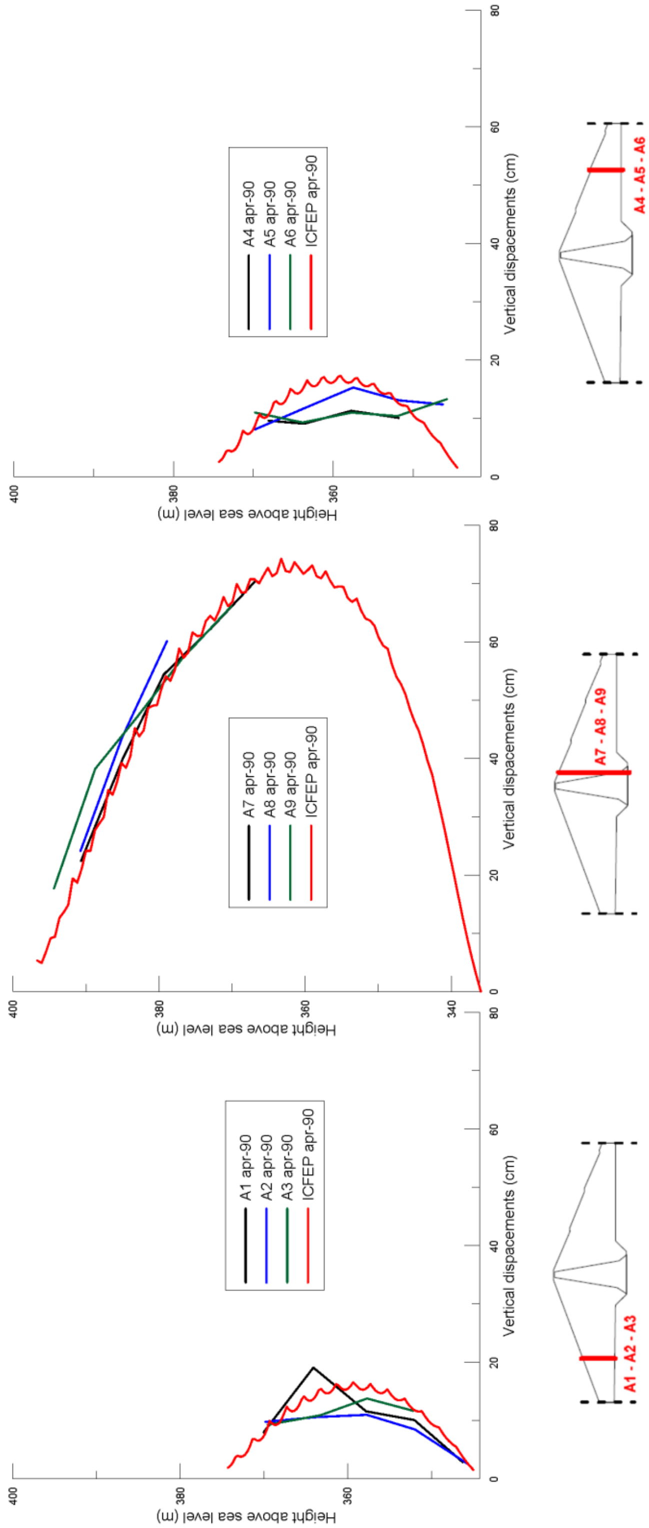

Figure 7.25 Comparison between observed and predicted vertical settlements at April 1990 in the upstream shell (A1-A2-A3), at the contact core-downstream shell (A7-A8-A9), and in the downstream shell (A5-A6-A7) using ICFEP and the Lade's double hardening model

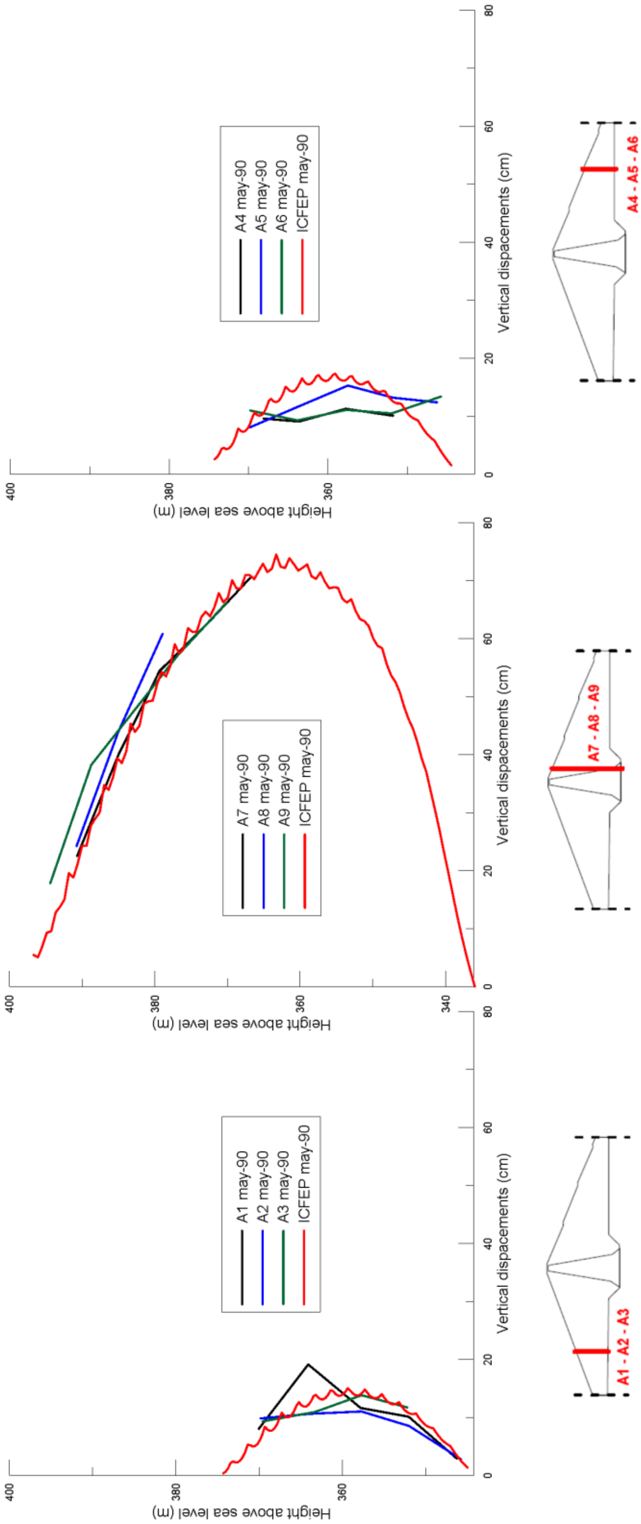

Figure 7.26 Comparison between observed and predicted vertical settlements at May 1990 in the upstream shell (A1-A2-A3), at the contact core-downstream shell (A7-A8-A9), and in the downstream shell (A5-A6-A7) using ICFEP and the Lade's double hardening model

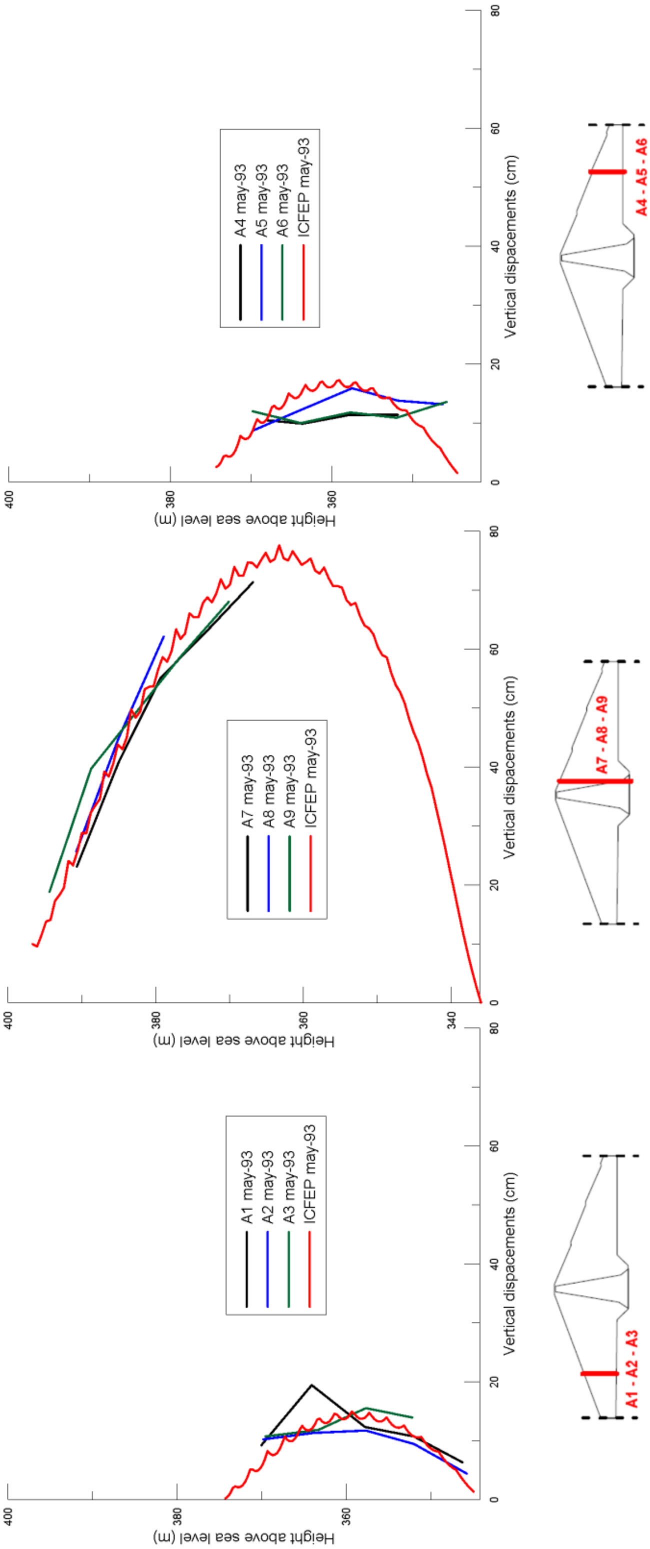

Figure 7.27 Comparison between observed and predicted vertical settlements at May 1993 in the upstream shell (A1-A2-A3), at the contact core-downstream shell (A7-A8-A9), and in the downstream shell (A5-A6-A7) using ICFEP and the Lade's double hardening model

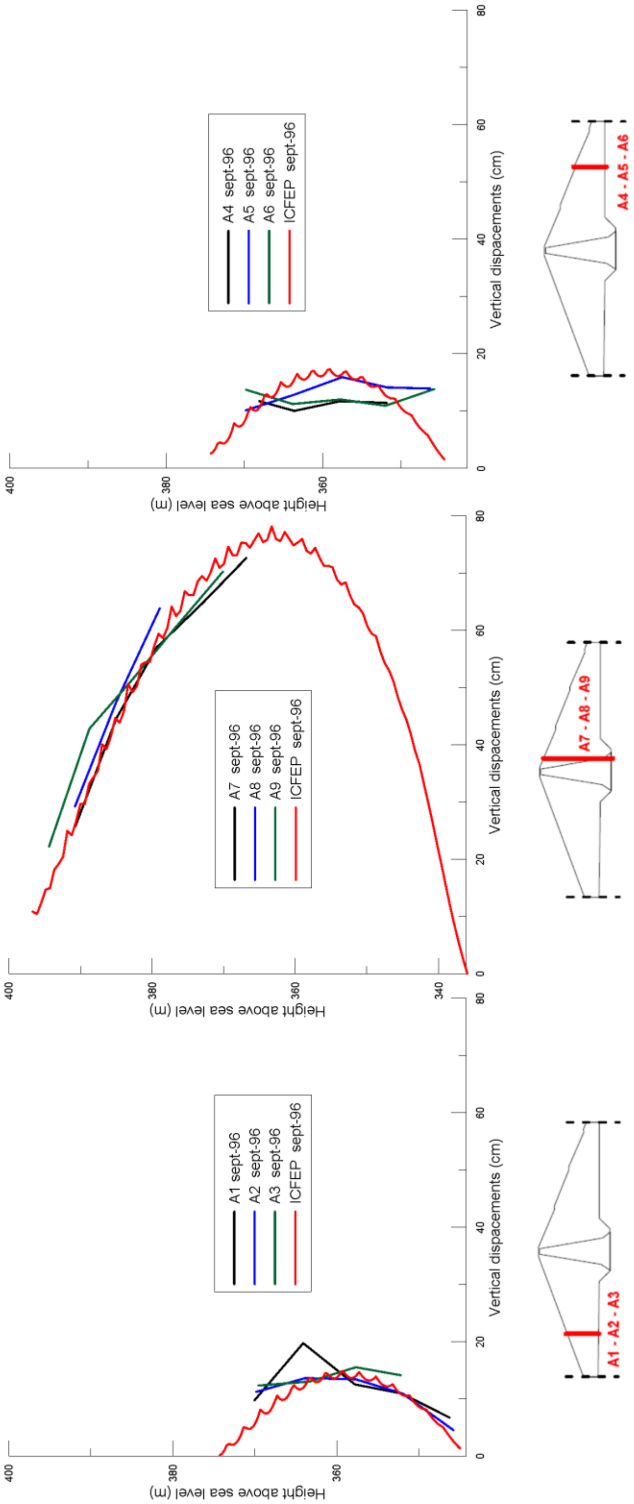

Figure 7.28 Comparison between observed and predicted vertical settlements at September 1996 in the upstream shell (A1-A2-A3), at the contact core-downstream shell (A7-A8-A9), and in the downstream shell (A5-A6-A7) using ICFEP and the Lade’s double hardening model

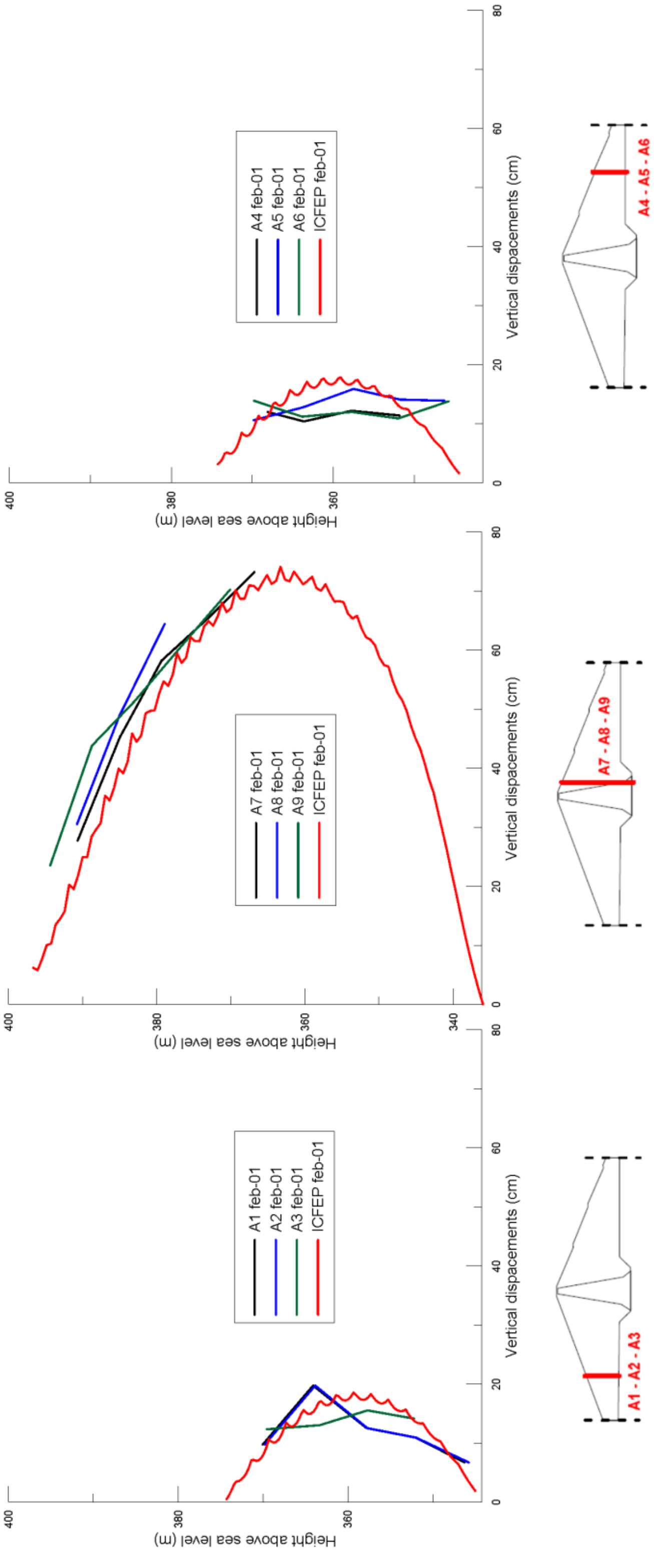

Figure 7.29 Comparison between observed and predicted vertical settlements at February 2001 in the upstream shell (A1-A2-A3), at the contact core-downstream shell (A7-A8-A9), and in the downstream shell (A5-A6-A7) using ICFEP and the Lade's double hardening model

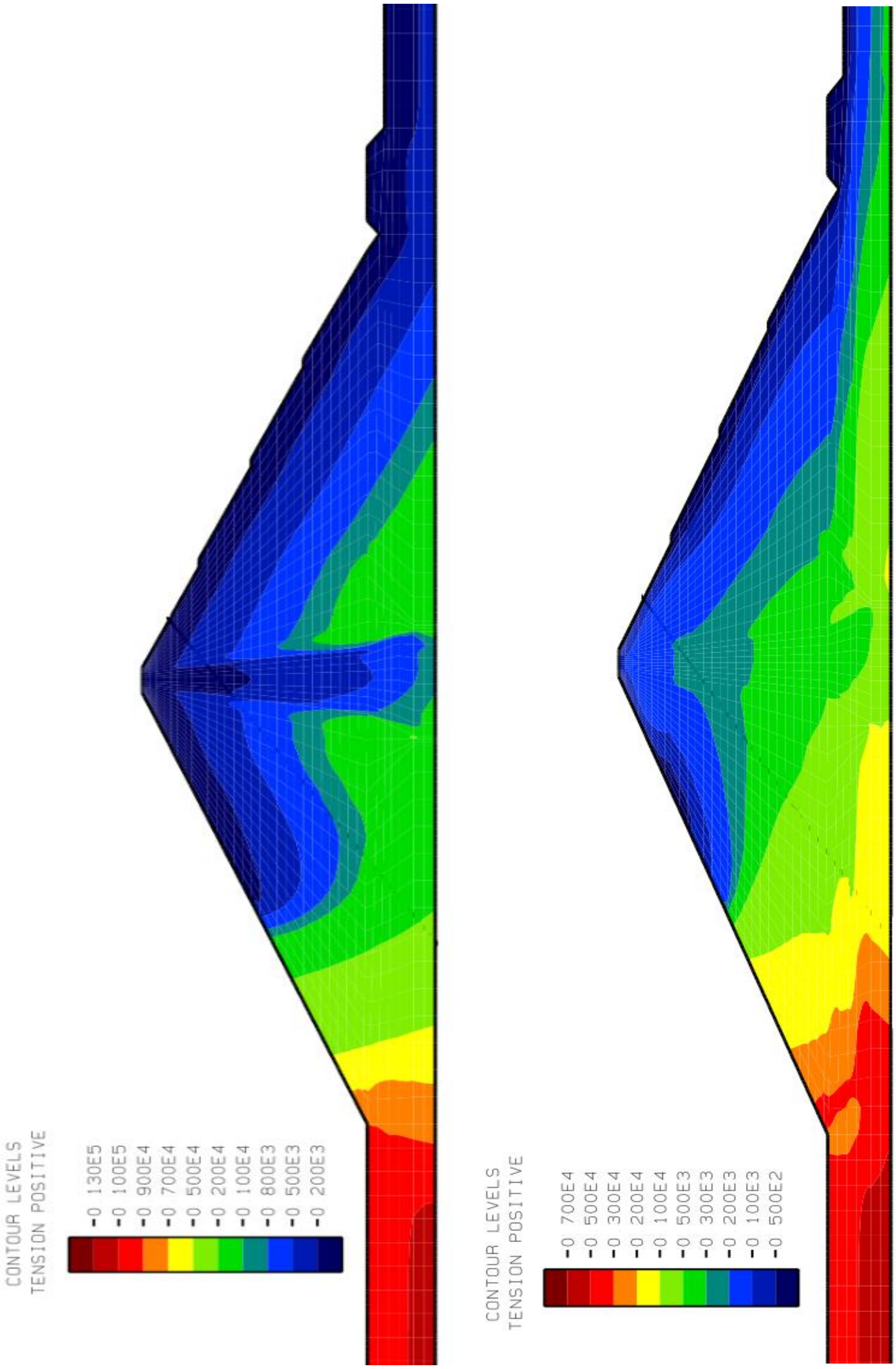

Figure 7.30 Contours of cumulated left) vertical total stress level σ_y (kPa) and right) horizontal total stress level σ_x (kPa) at February 2001

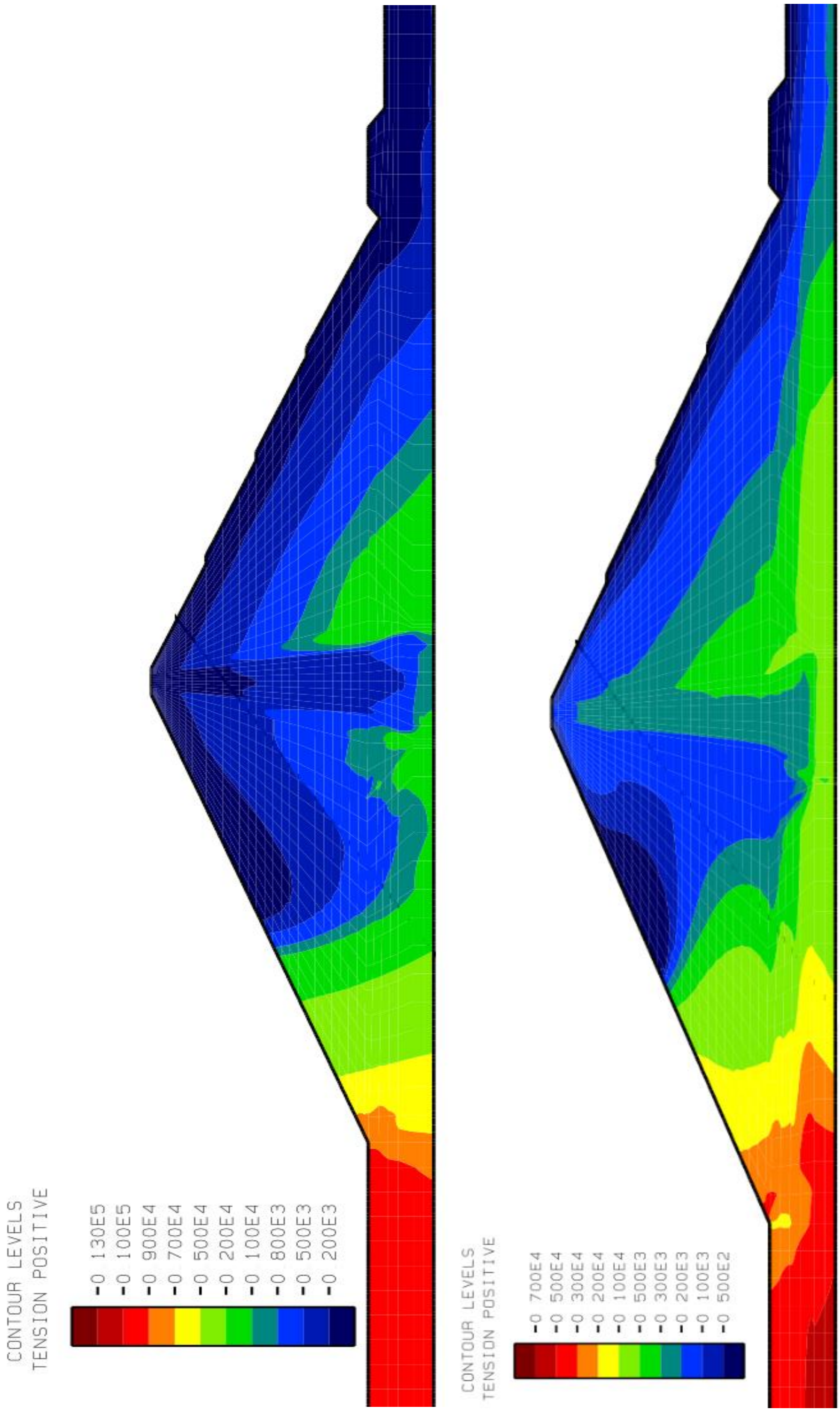

Figure 7.31 Contours of cumulated left) vertical effective stress level σ'_y (kPa) and right) horizontal effective stress level σ'_x (kPa) at February 2001

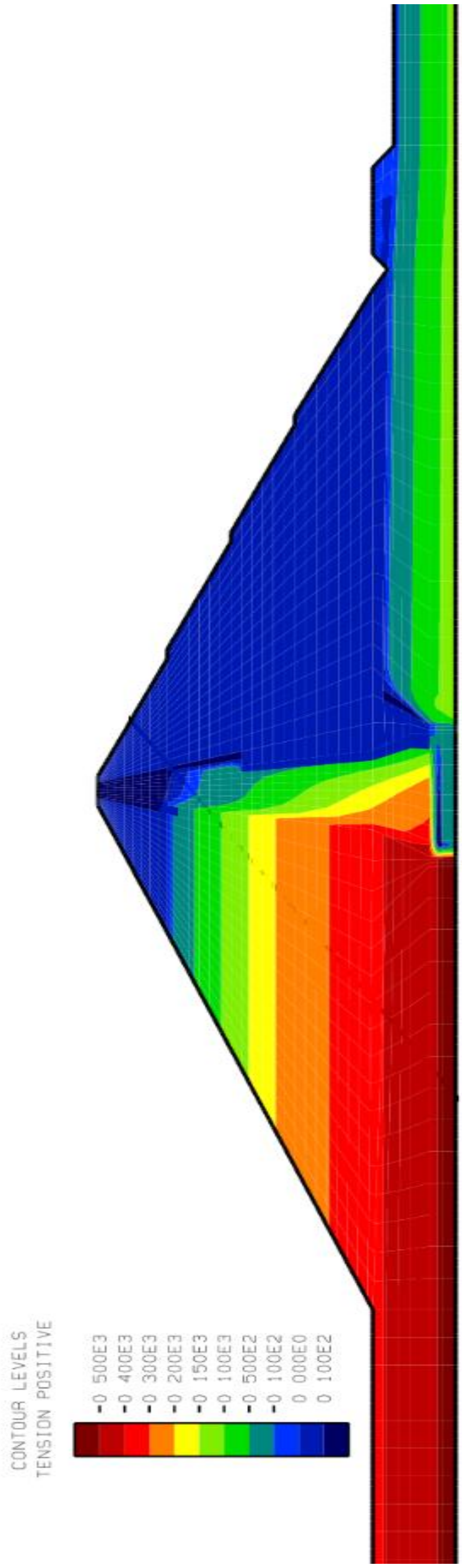

Figure 7.32 Contours of cumulated fluid stress u (kPa) at February 2001

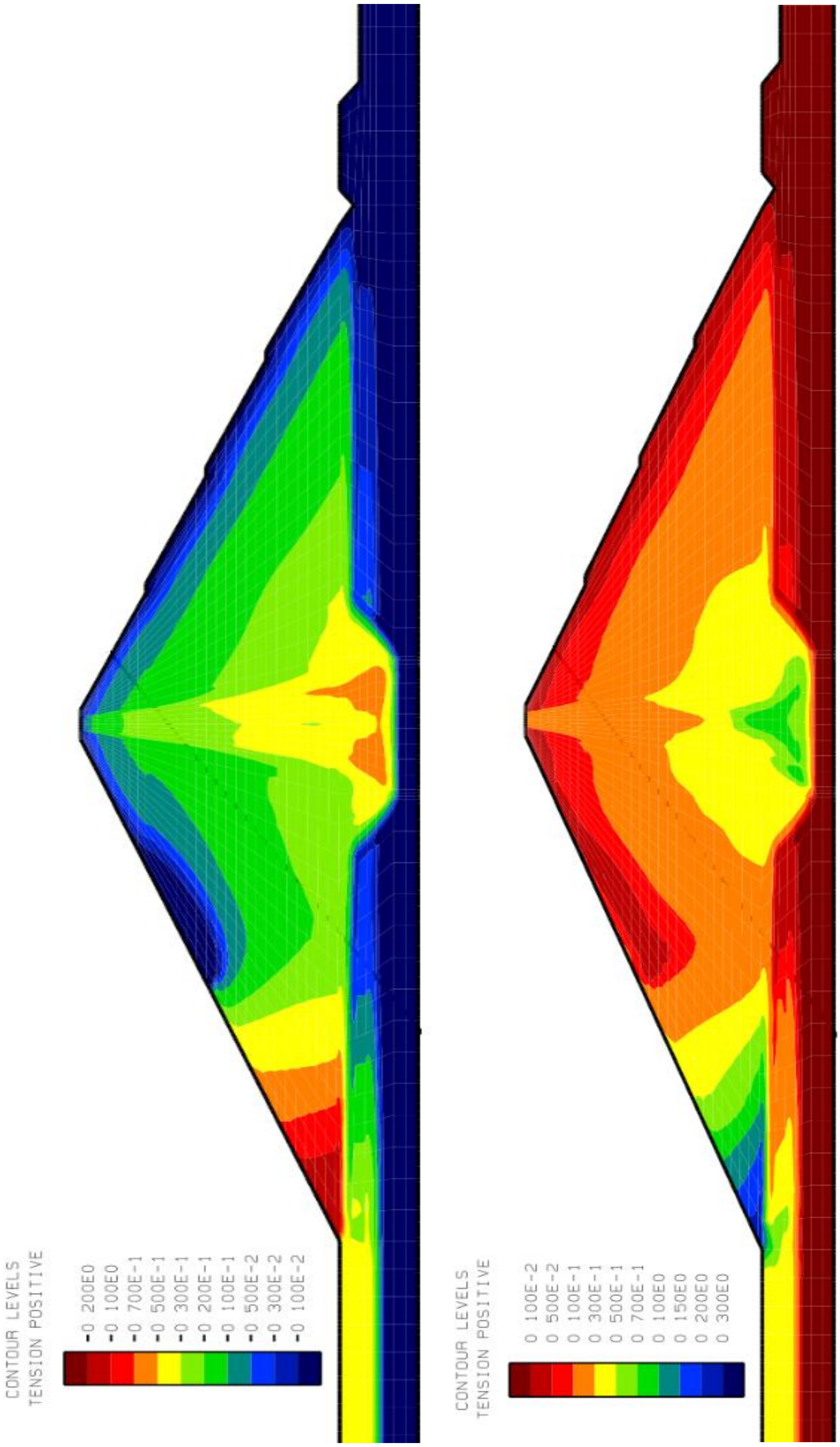

Figure 7.33 Contours of cumulated left) total volumetric strain ε_v $(-)$ and right) total deviatoric strain E $(-)$ at February 2001

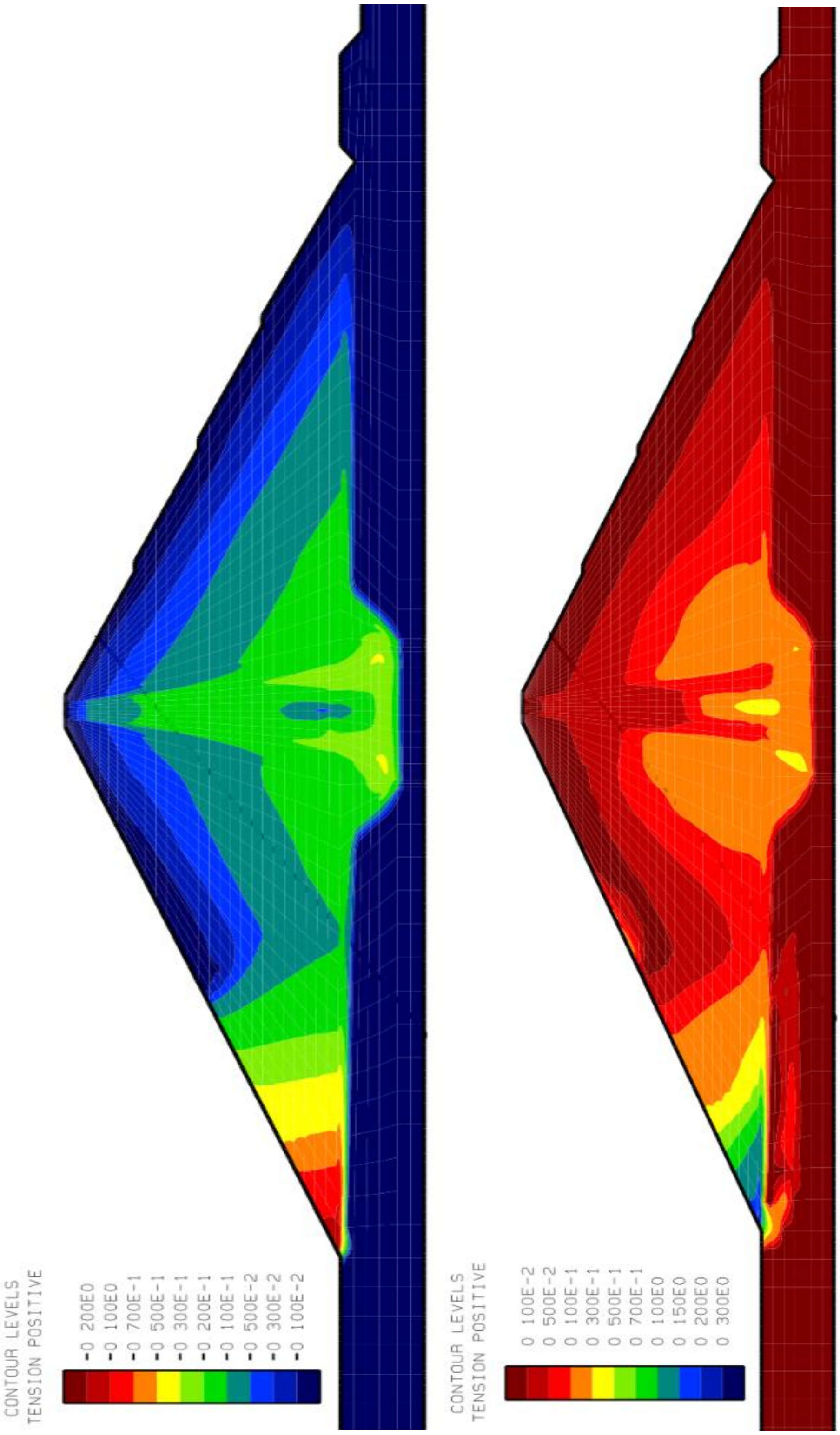

Figure 7.34 Contours of cumulated left) plastic volumetric strain ε_v $(-)$ and right) plastic deviatoric strain E $(-)$ at February 2001

8. COMPARISON BEWTEEN NUMERICAL RESULTS OBTAINED WITH THE TWO CODES

8.1 ANALYSIS DIFFERENCES

The results of numerical analyses of construction phase and reservoir impounding of Montedoglio dam were presented in the two previous chapters. The finite difference code FLAC 7.0 and the finite element code ICFEP were employed to analyse the construction phase of the dam. Through a comparison it is possible to figure out the mean differences between the two procedures and the respective results. In this Section, the common and different features of the two analyses were described. The geometrical model is characterized by boundaries defined as 150 m away from the dam's toes for both analyses, 60 m and 5 m below the dam's base for the FLAC and ICFEP analyses, respectively. The mechanical boundary conditions are identical for both codes. Filters and drained layers were included in the shells for both analyses. The finite element analysis is fully coupled but only the core was considered as consolidating material, while the finite difference analysis is completely drained. The position of the water table in the construction phase bewteen the two analyses is different: the simulation with FLAC is characterized by a water table at the top of the alluvial layer downstream at 342.2 m a.s.l., while with ICFEP the water table was assumed in the rock foundation below the core at 335.97 m a.s.l.. Therefore, these two assumptions (no consolidation for the finite difference analysis and different position of the water table) bring to a different distribution of the fluid stress. The construction consists of adding groups of elements in horizontal layers through a gravity 'turn-on' analysis. The numbers and the thickness of layers are different between the two simulations. The construction was simulated with FLAC adding 10 horizontal layers of about 6 m thick in 10 increments, and with ICFEP through 32 horizontal layers in 32 increments. From the point of view of constitutive models, for the foundation soil the same models with the same mechanical and physical parameters were employed for both codes: elastic perfectly plastic Mohr-Coulomb model for the alluvial layer, and a linear elastic model for the rock basement. For the dam's body two constitutive models of the same class of elasto-plastic hardening models were applied: the Cysoil model for the finite difference analysis, and the Lade's double-hardening model for the finite element analysis. The parameters of both models were determined from the same results of laboratory tests. The models are characterized by double plastic surfaces which control volumetric and deviatoric plastic strains. No one-dimensional tests were available for the shells material, therefore, some parameters assumptions were made for each model. For the Lade's double-hardening model, the missing parameters were obtained from literature of similar rockfill material (Sect. 7.2). For the Cysoil model, only the deviatoric hardening was activated through the introduction of a high value of the cap pressure p_c, avoiding plastic volumetric strain in the shells (Sect. 6.2.2).

8.2 COMPARISON OF THE RESULTS OF SIMULATIONS

The simulation results of the construction phase of Montedoglio dam with the two codes are compared and analysed. In all subsequent figures used for comparison, the upper and lower plots refer to the FLAC and ICFEP simulations, resectively. The vectors of cumulated displacement at the end of construction obtained through FLAC and ICFEP simulations are presented in Fig. 8.1. The trend of the vectors is similar and the core is settled more than shells. The maximum values of displacement are 79.7 cm with FLAC and 88.7 cm with ICFEP. Hence, the constructed dam model with ICFEP is characterized by 9 cm of displacement more than that obtained with FLAC. The comparison between the results of the two simulations in terms of cumulated vertical and horizontal displacements at the end of the construction are presented in Fig. 8.2 and 8.3. The displacements obtained using FLAC are generally less than those obtained with ICFEP. The vertical displacements (Fig. 8.2) of ICFEP model are more pronounced in the shells than those obtained with FLAC. The trend of the horizontal displacements (Fig. 8.3) is comparable between the two analyses, though in the ICFEP simulation at the core base the displacements are different. The contours of cumulated vertical and horizontal total stresses at the end of the construction are compared in Fig. 8.4 and 8.5, respectively. The variation of the total stresses observed in the two simulations is comparable, but the horizontal total stress in the core base of the FLAC model is characterized by a reduction as compared to the ICFEP representation. A wide stress variation at the contact between core and shells highlights an arching effect, more pronounced in the lower part of the core. The comparison of cumulated vertical and horizontal effective stresses at the end of the construction are shown in Fig. 8.6 and 8.7. The trend seems similar but some differences exist: in the ICFEP analysis the effective stress in the core is lower, while in the foundation soil it is higher. The reason of such differences could be ascribed to the pore fluid pressure distribution, which is different between the two simulations at this stage as show in Fig. 8.8. As mentioned, the water table in the FLAC simulation was assumed at the top of the alluvial layer downstream at 342.2 m a.s.l. and the analysis is drained, while for ICFEP the water table was assumed in the rock foundation below the core at 335.97 m a.s.l., the core is considered a consolidating material and a suction of 10 kPa and 50 kPa were applied in the shells and in the core, respectively. Clearly the resulting pore water pressure distribution reflects these assumptions and the effective stress as well. Fig. 8.8 highlights that at the end of the construction with ICFEP a suction of 10 kPa is present in the shells and that an excess of pore pressure was developed in the core, both effects are not present in the fluid stress distribution obtained with FLAC. 8.8. The volumetric and deviatoric strains from the two simulation are different. The total volumetric strain (Fig. 8.9) in the FLAC simulation, reflects a volume reduction in the lower part of core and a volume increase of some layers in the higher part of the dam, while in the ICFEP simulation the result shows only a volume reduction. The contours of plastic volumetric strain (Fig. 8.11) obtained with FLAC show a volume reduction of the core and null values in the shells for the model assumption, while the contours obtained with ICFEP are characterized by the same trend of the total volumetric strain. The deviatoric strain (Fig. 8.10 and 8.12) of the two simulations are determined through different formulations and only a qualitative comparison is possible. The observed settlements at the end of the construction in the upstream shell (A1-A2-A3), at the contact of core-downstream shell (A7-A8-A9), and in the downstream shell (A5-A6-A7) are presented in Fig. 8.13 in comparison with calculated ones using the Lade's double hardening and Cysoil models. Although both models capture the deformation behaviour of the dam, the vertical displacements obtained with Lade's double hardening model are more accurate in the core than those obtained with Cysoil. In the shells, the Cysoil model seems to underestimate the observed displacements, especially in the downstream shell. From the analysis of the simulations results, the Lade's double hardening model is clearly more well-suited to predict the observed behaviour of the dam.

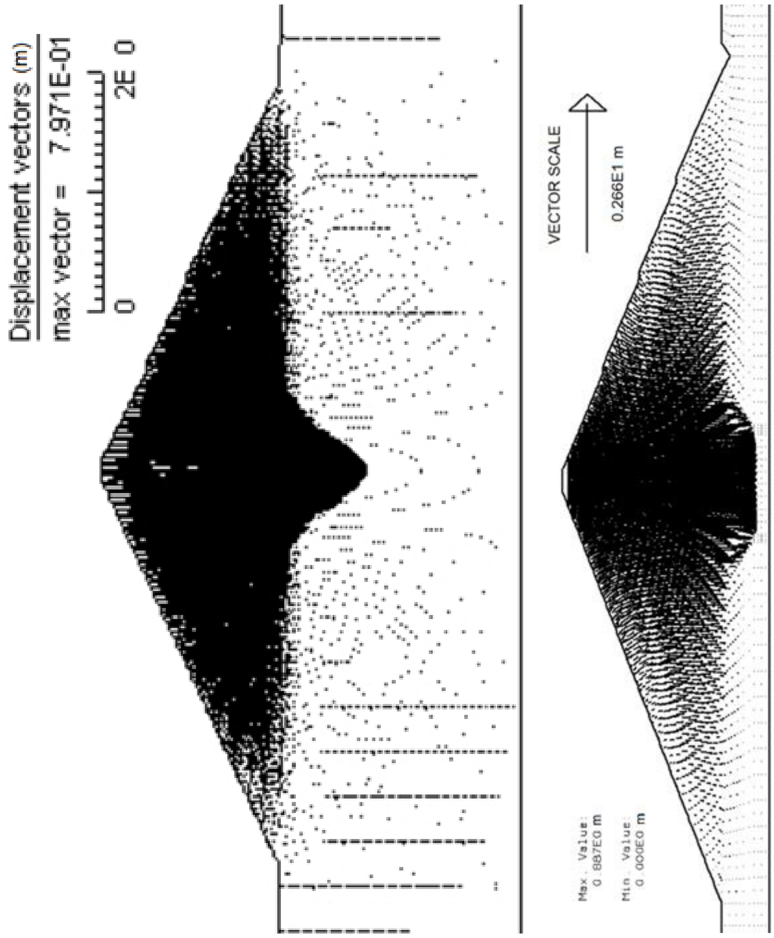

Figure 8.1 Vectors of cumulated displacement at the end of the construction obtained with left) FLAC right) ICFEP

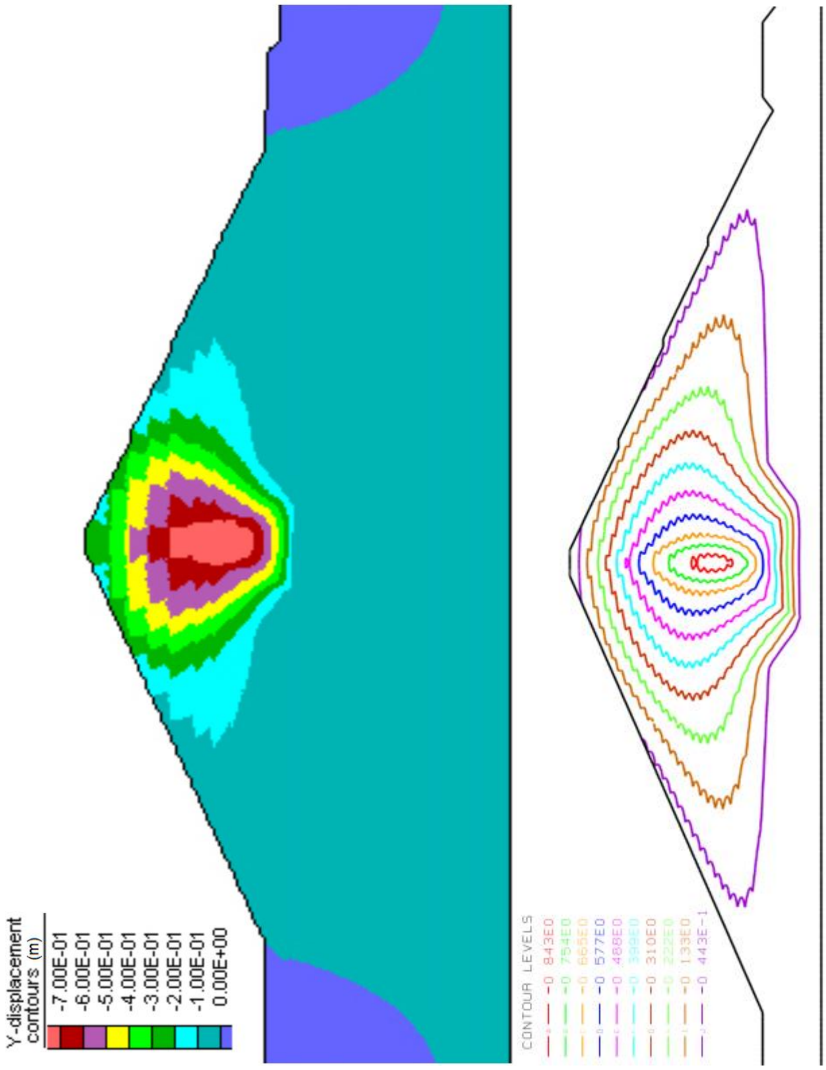

Figure 8.2 Contours of cumulated vertical displacements v (m) at the end of the construction obtained using left) FLAC and right) ICFEP

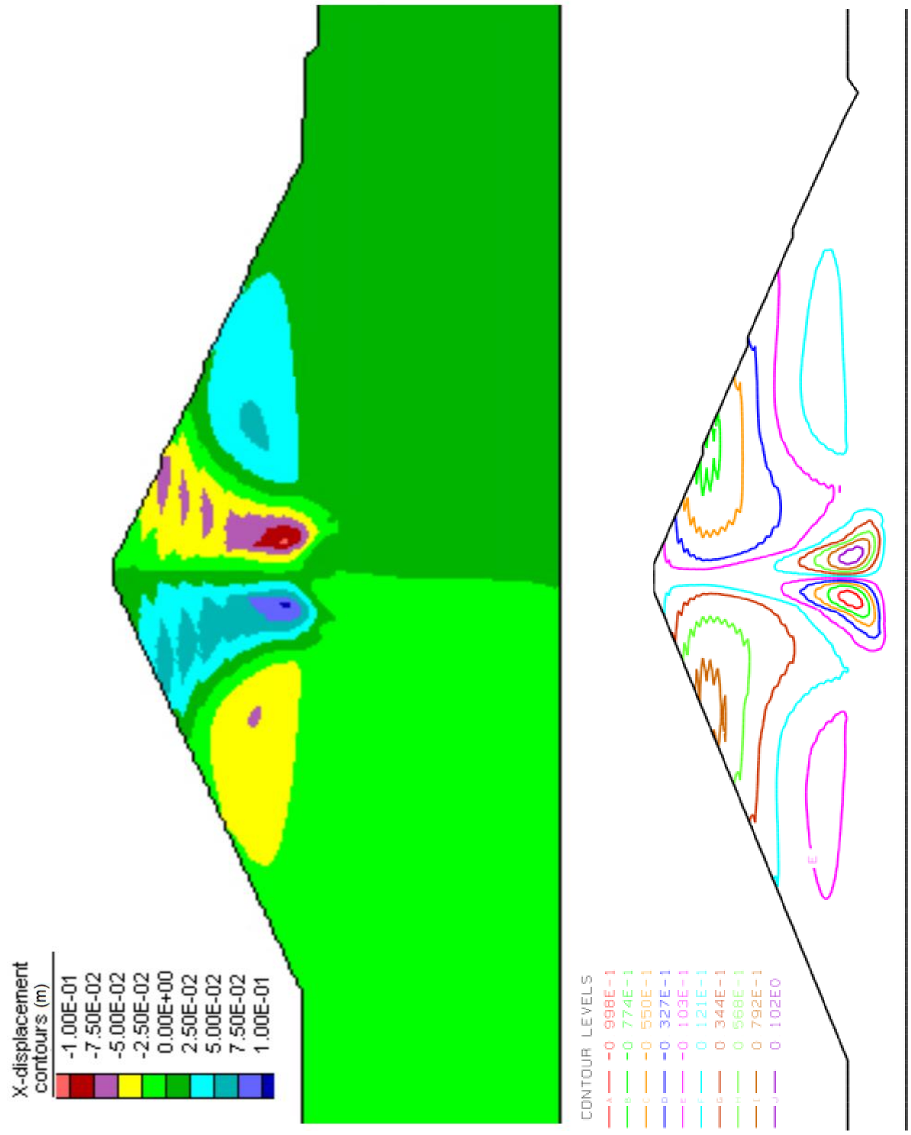

Figure 8.3 Contours of cumulated horizontal displacements u (m) at the end of the construction obtained using left) FLAC and right) ICFEP

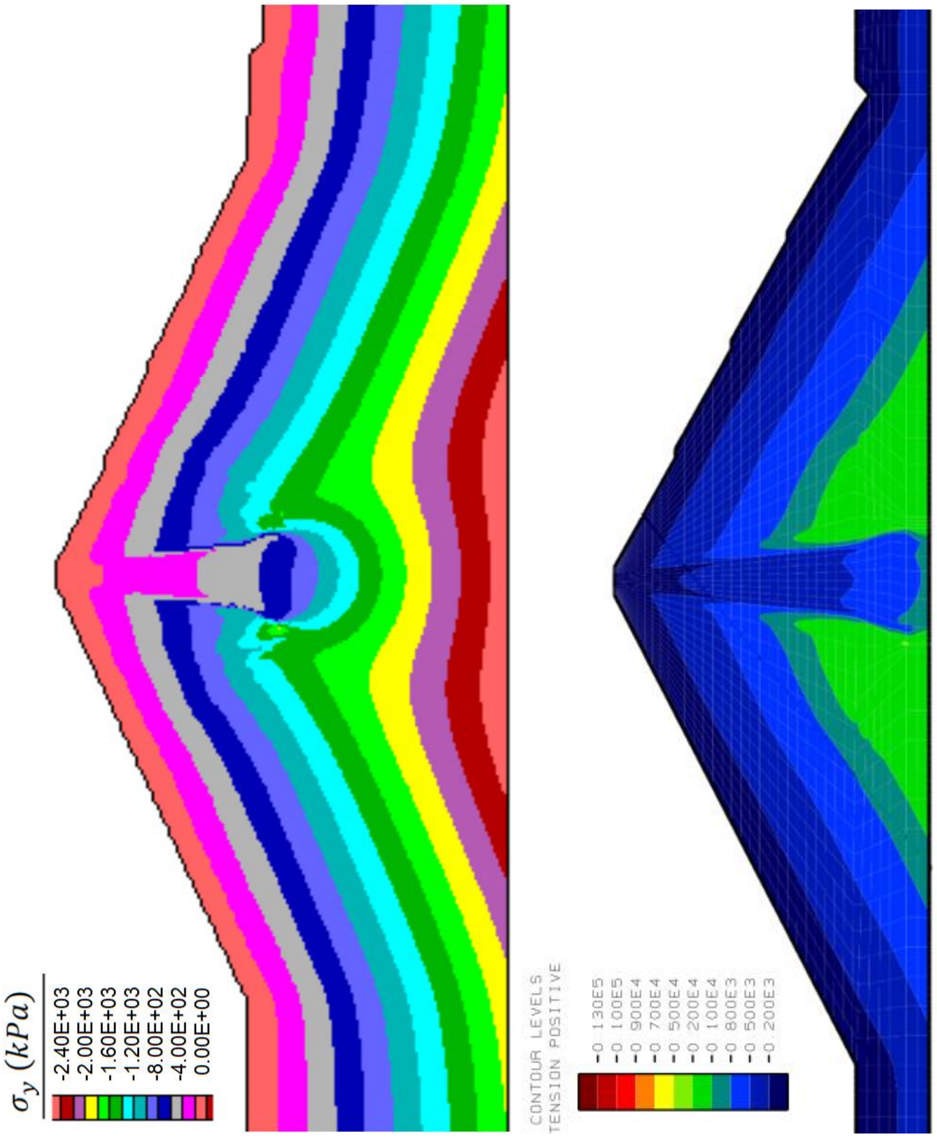

Figure 8.4 Contours of cumulated vertical total stress level σ_y (kPa) at the end of the construction obtained using left) FLAC and right) ICFEP

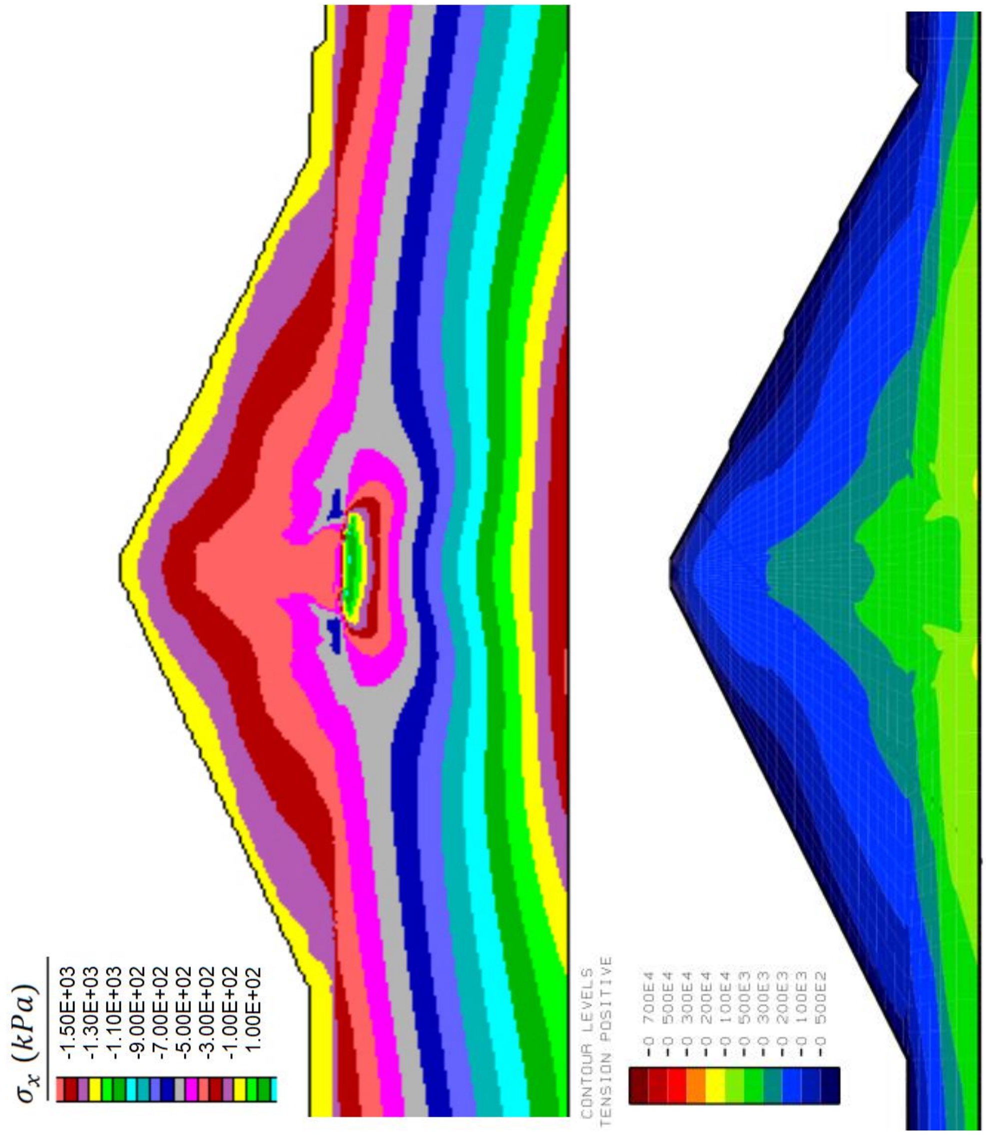

Figure 8.5 Contours of cumulated horizontal total stress level σ_x (kPa) at the end of the construction obtained using left) FLAC and right) ICFEP

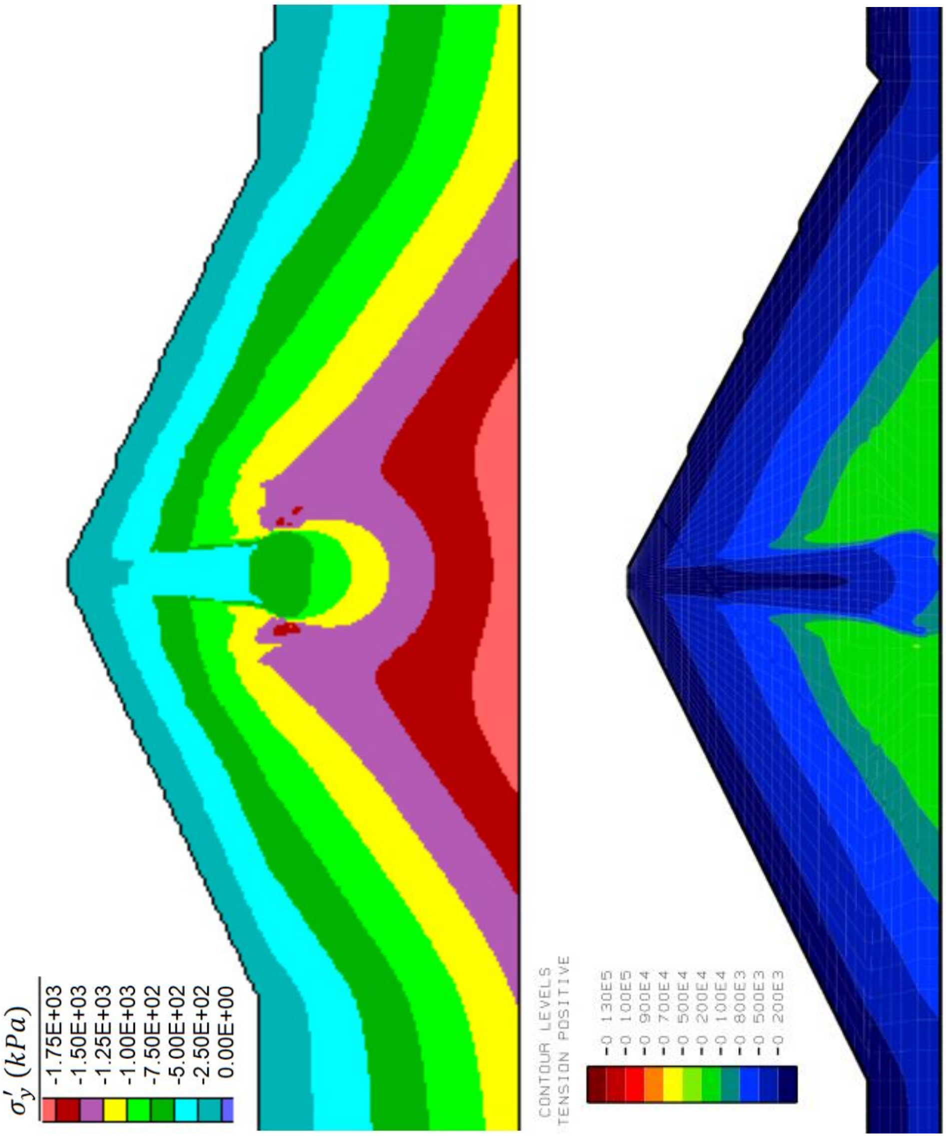

Figure 8.6 Contours of cumulated vertical effective stress level σ'_y (kPa) at the end of the construction obtained using left) FLAC and right) ICFEP

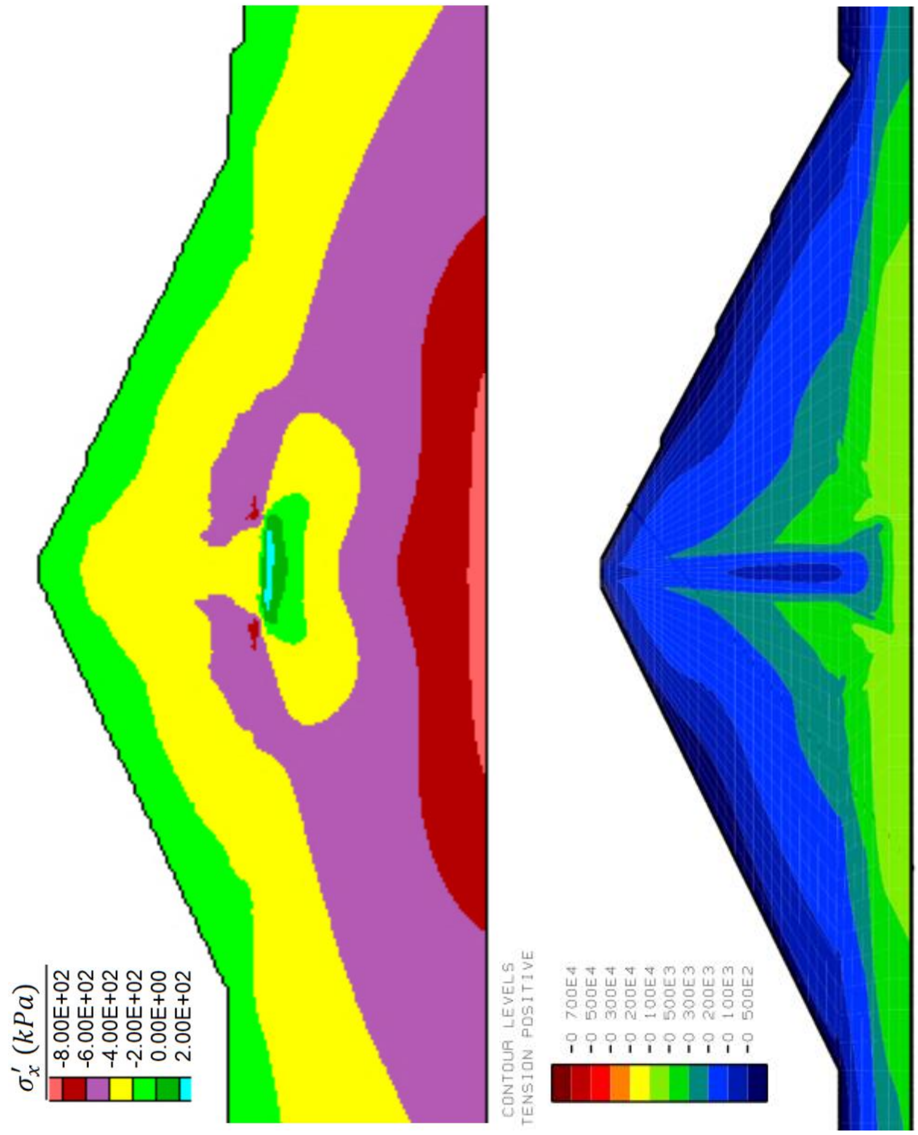

Figure 8.7 Contours of cumulated horizontal effective stress level σ'_x (kPa) at the end of the construction obtained using left) FLAC and right) ICFEP

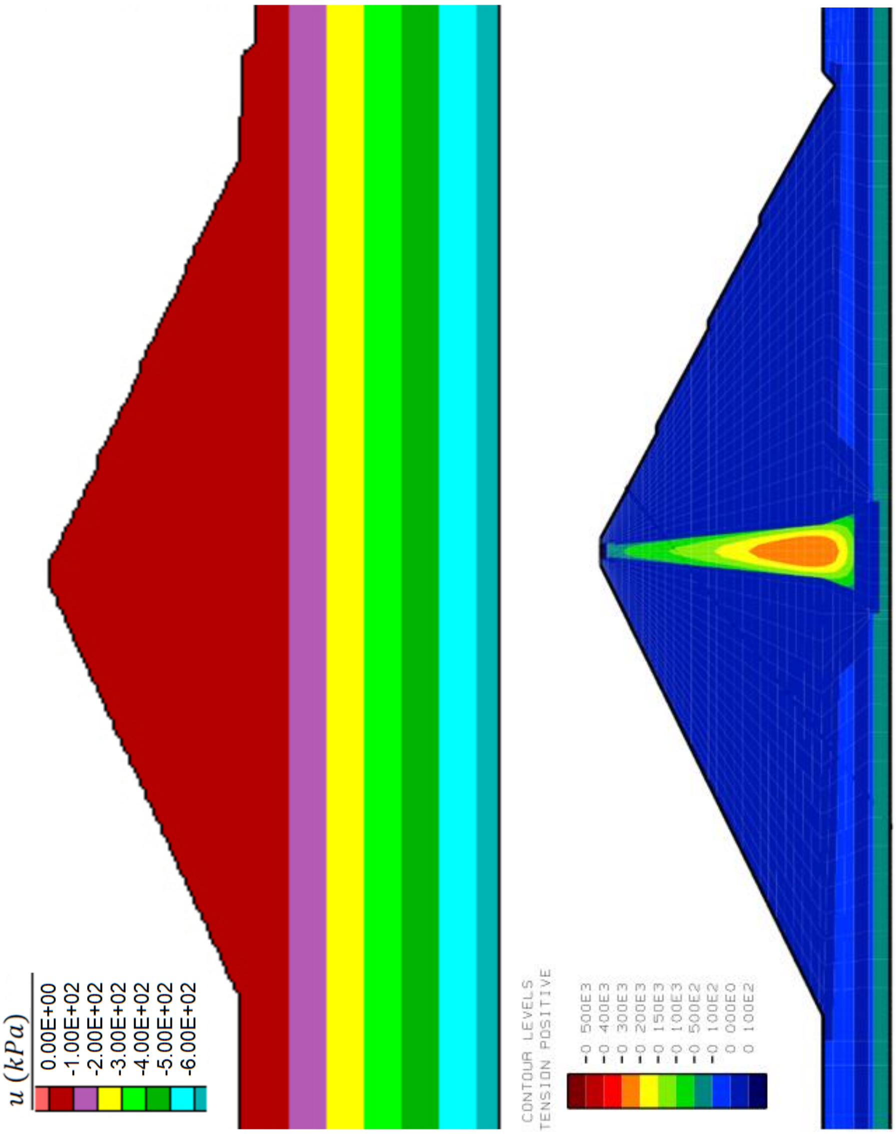

Figure 8.8 Contours of cumulated fluid stress u (kPa) at the end of the construction obtained using left) FLAC and right) ICFEP

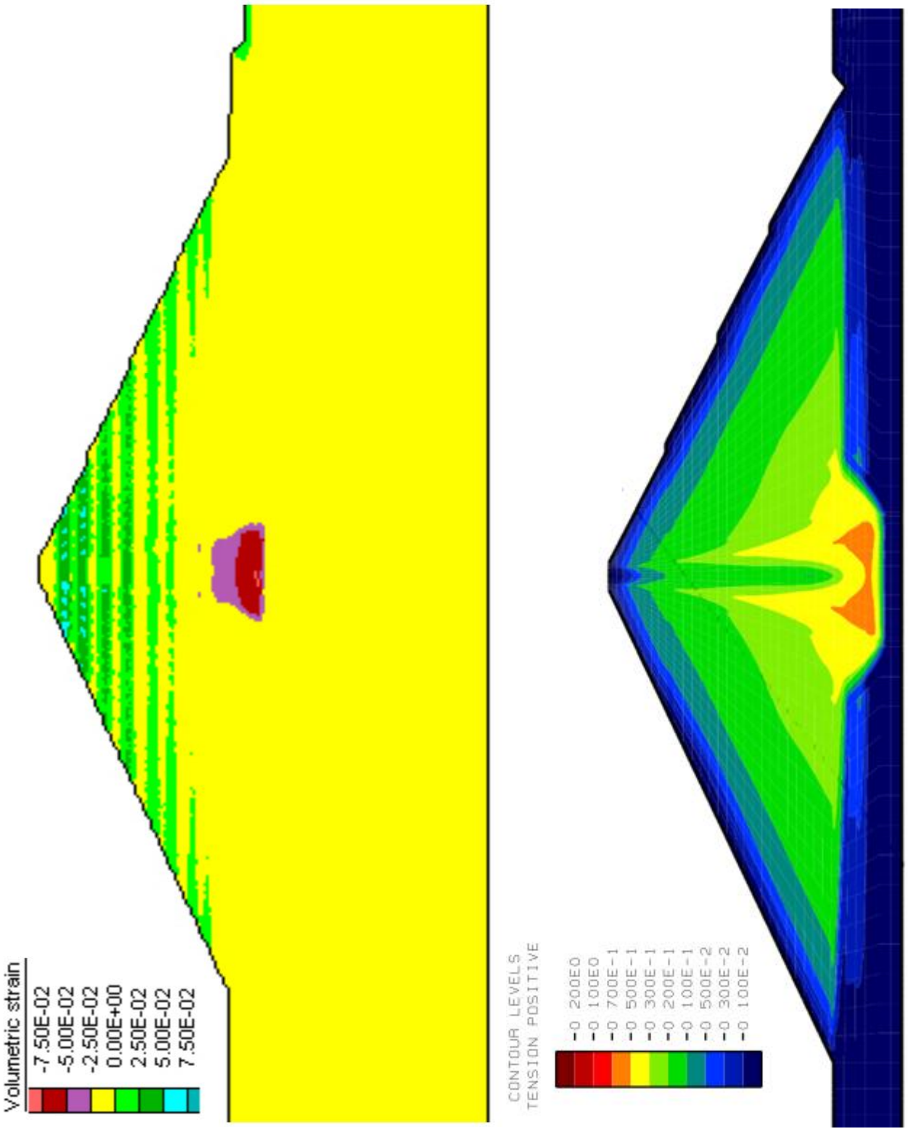

Figure 8.9 Contours of total volumetric strain ε_v (-) at the end of the construction obtained using a) FLAC and b) ICFEP

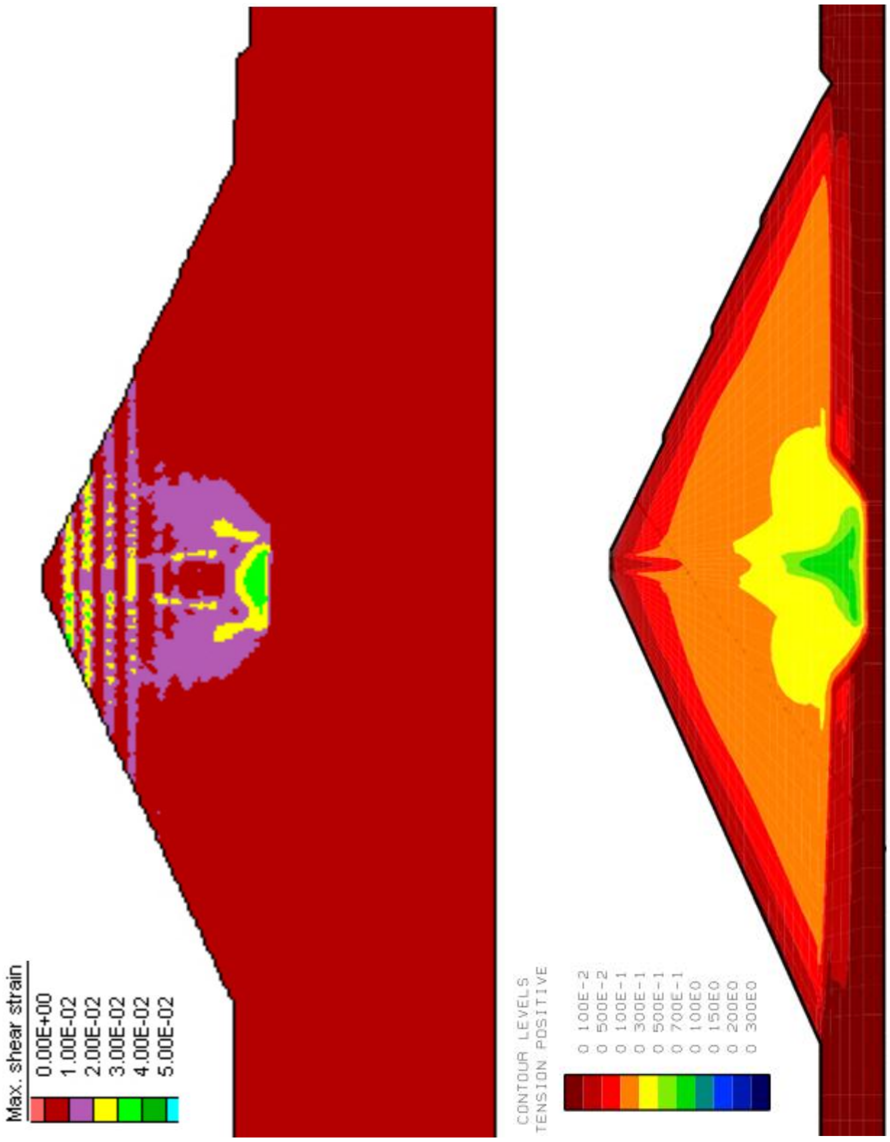

Figure 8.10 Contours of a) maximum shear strain γ (-) obtained using FLAC and b) total deviatoric strain E $(-)$ obtained using ICFEP at the end of the construction

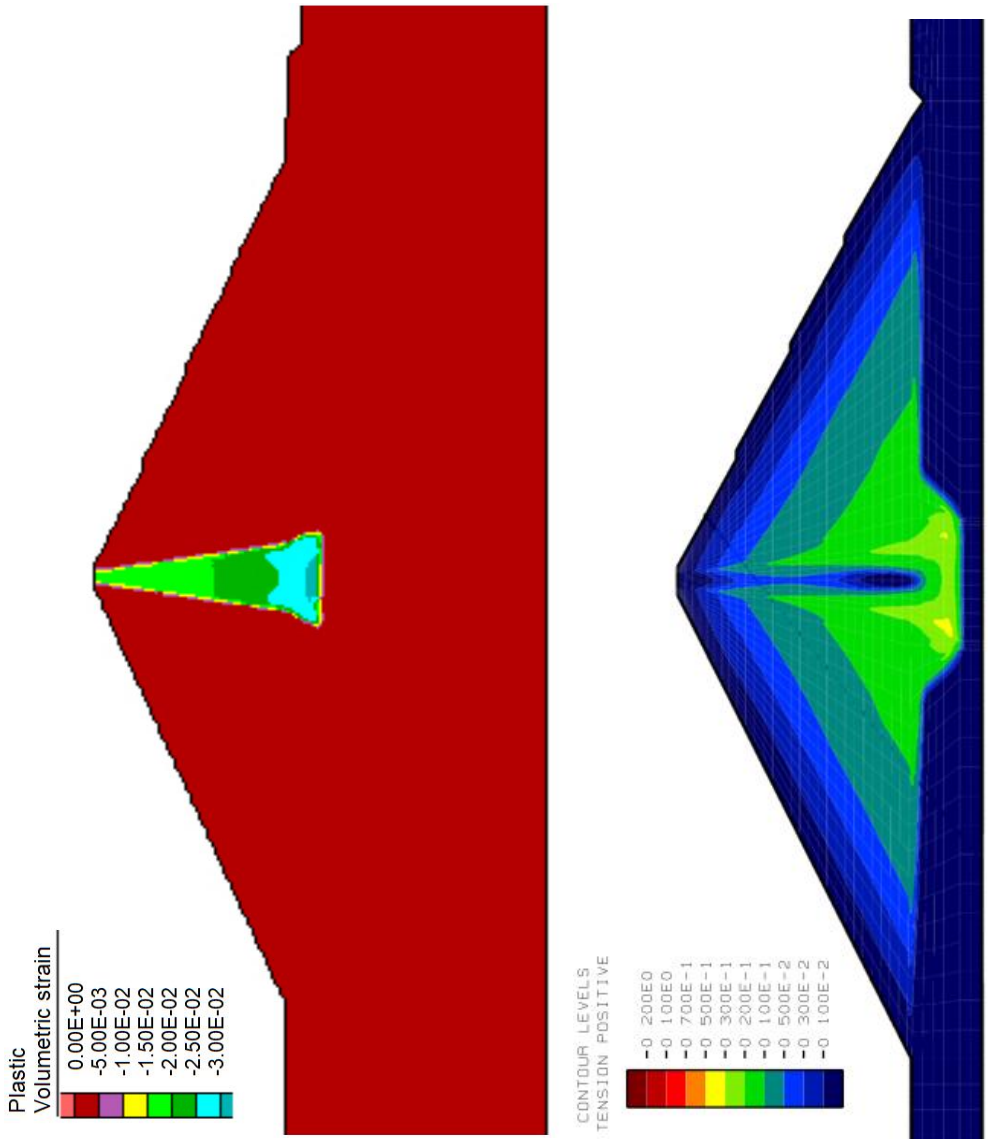

Figure 8.11 Contours of cumulated plastic volumetric strain ε_v at the end of the construction obtained using left) FLAC and right) ICFEP

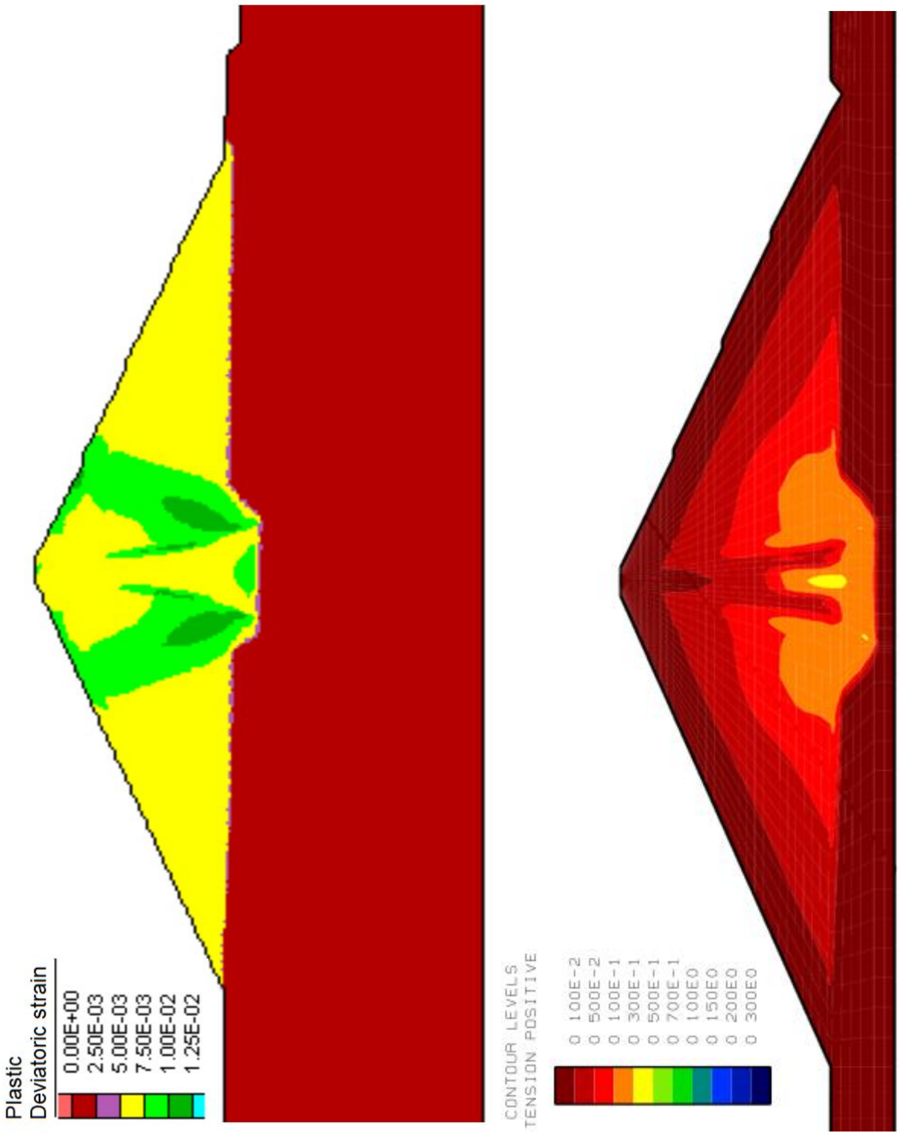

Figure 8.12 Contours of cumulated left) plastic deviatoric strain ε_s (-) obtained using FLAC and right) plastic deviatoric strain E $(-)$ obtained using ICFEP at the end of the construction

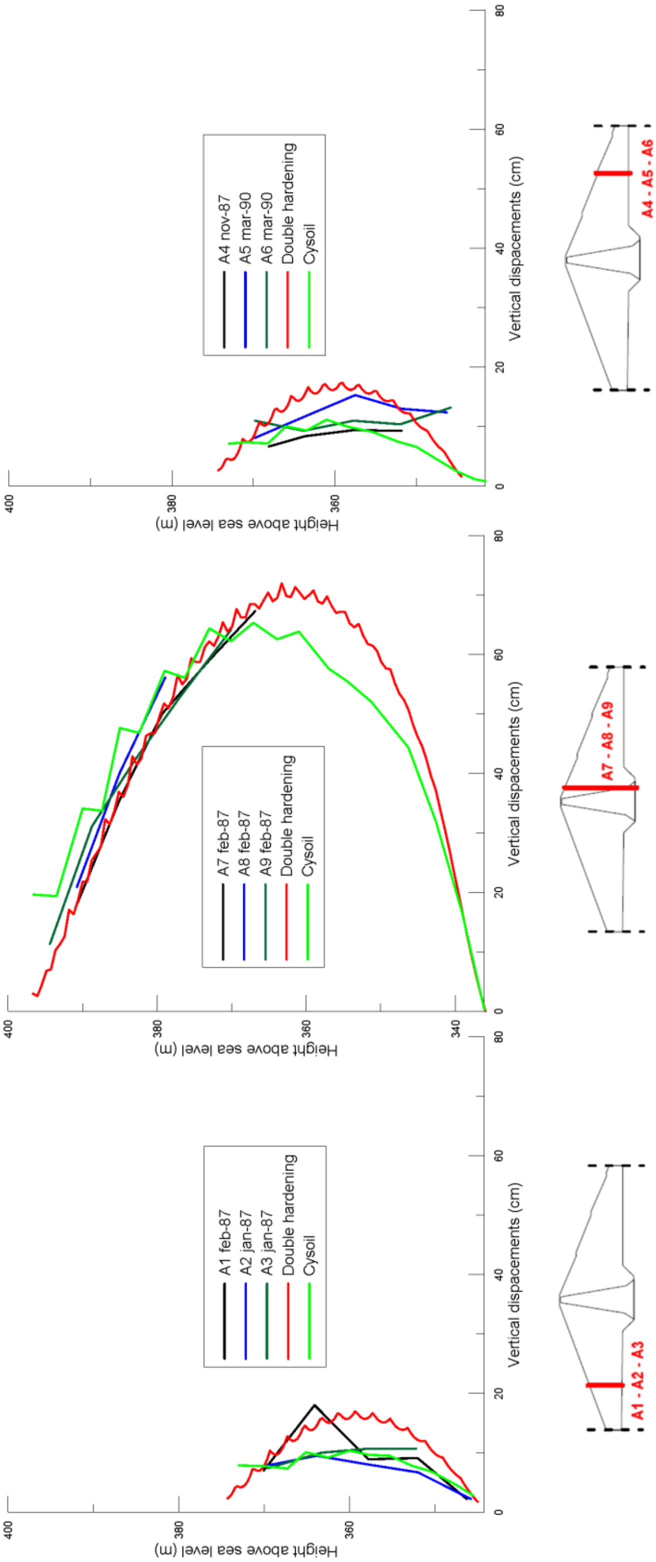

Figure 8.13 Comparison between observed and predicted vertical settlements at the end of the construction in the upstream shell (A1-A2-A3), at the contact core-downstream shell (A7-A8-A9), and in the downstream shell (A5-A6-A7) using the Lade's double hardening and Cysoil models

9. SUMMARY AND CONCLUSIONS

The deformation behaviour of embankment dams during construction and reservoir operations was extensively studied in the last fifty years, due to the growing capability of computational tools and the consequent increasing possibility to perform advanced numerical analyses. Methods from existing literature which can help to identify abnormal deformations were discussed, simple procedures to estimate strains and displacements were presented, helpful techniques of interpreting the field measurements were described and some strain related problems which could occur during these dam's phases were briefly explained. Multiple numerical analyses of the construction and reservoir impounding of embankment dams, which include rockfill and zoned dams, were performed by many authors, numerous significant aspects of the simulations were highlighted, as construction or excavation adding or removing layers and the critical role of stress-strain relationships. The simple elastic models do not account for many aspects of real soil behaviour, like the influence of the stress path and the presence of irreversible strains, and they can become insufficient to describe the deformation behaviour. The elasto-plastic constitutive models could represent the real soil behaviour more reliably when the conditions are closer to failure and when the relative stiffness between different embankment materials is strongly different (stiff shell and soft core in a zoned dam). From the class of elasto-plastic constitutive models, more complex hardening/softening models of the critical state type with multi yield surfaces could be defined as advance constitutive models. They can account for the stress path dependency, the plasticity effect of grain crushing and rearrangement and the decrease in stiffness accompanied by irreversible deformation. They were widely employed by several authors to analyse these phases of various embankment dams, representing accurately the field data. However, these types of models are not commonly used in practice, because they are complex and include large number of parameters to be determined. The model parameters could be determined from standard and advanced tests on the core and rockfill materials. However, these are challenging issues as undisturbed samples from core are barely available. Further, the experimental determination of the rockfill material is generally limited by the high-dimension granular nature of the shell which renders difficult and highly expensive the experimental investigations on this type of materials. Therefore, the difficulty to perform laboratory tests on core and rockfill materials make the parameters determination problematic.

In the present thesis, the case study of Montedoglio earth-core zoned dam was analysed with two advanced constitutive models. The background of the research is characetrized by a well-documented case study with high-quality monitoring data of the construction and impoundment phases. This is combined with high-quality laboratory tests on both core and rockfill materials, which is not ordinary for largest part of existing dams, as already mentioned, and which allowed to made detailed calibration and comparisons of the model parametrs assumed. The simulations have been carried out with two different codes which implement two different constitutive models with two intersective yield surfaces employed for the numerical simulations. The first model is denoted as Cysoil (or cap-yield) model, a strain-hardening constitutive model implemented in the finite difference code FLAC 7.0, which is characterized by an elastic domain closed by a frictional and cohesive Mohr-Coulomb shear envelope and an elliptic volumetric cap. The second model is the double hardening model, a strain-hardening/softening model implemented in the finite element code ICFEP, which is characterized, as well, by an elastic domain closed by the conical and the cap yield surfaces. The determination of the models parameters was based on the results of standard laboratory tests on intact core samples and reconstituted shells samples. The Cysoil model was employed to analyse the construction phase of Montedoglio dam with the code FLAC 7.0. The predicted values of settlements at the end of the construction along specific verticals in the dam's body were compared with high-quality field measurements, obtaining a good agreement. The Lade's double hardening model was used to simulate the phases of construction and first reservoir impounding of the same case study with the code ICFEP. Also in this case, a satisfactory comparison between observed and computed settlements at the end of the construction and during first filling was obtained.

The results of both numerical modelling demonstrate that both models were capable to represent the dam deformation behaviour, providing a good prediction of stresses and strains in the zoned dam. Even though the Lade's model seems more accurate in predicting the measured settlements, both results are highly satisfactory in terms of stresses and strains, showing that both models are remarkably capable to describe the dam behaviour. Furthermore, the superiority of this class of models with respect to more simple models was also demonstrated.

Finally, while the capability of the Lade's double hardening model in reproducing the static stress-deformation behaviour of dams has already been demonstrated in the literature, conversely the use of Cysoil is generally very limited and no simulations have been found in the literature regarding the static analysis of dams. Therefore, the conclusions made are particularly important for the Cysoil model implemented in FLAC as it can be used with confidence for the simulation of embankment dams, as long as high-quality data on material properties are available.

10. Bibliography

Alonso, E. E., & Oldecop, L. A. (2000). Fundamentals of rockfill collapse. In *Unsaturated soils for Asia. Proceedings of the Asian Conference on Unsaturated Soils, UNSAT-ASIA 2000, Singapore, 18-19 May, 2000* (pp. 3-13). AA Balkema.

Alonso, E. (2003). Exploring the limits of unsaturated soil mechanics: The behavior of coarse granular soil and rockfill. *The 11th Buchanan Lecture. University of Texas A&M.*

Alonso, E. E., Olivella, S., & Pinyol, N. M. (2005). A review of Beliche Dam. *Géotechnique, 55*(4), 267-285.

Alonso, E. E., Pinyol, N. M., & Gens, A. (2013). Compacted soil behavior: initial state, structure and constitutive modelling. *Géotechnique, 63*(6), 463-478.

Alpan, I. (1967). The empirical evaluation of the coefficient K_0 and K_{0R}. *Soils and foundations, 7*(1), 31-40.

Al-Tabbaa, A., & Wood, D. M. (1989). An experimentally based 'bubble' model for clay. In *International Symposium on Numerical Models in Geomechanics (3rd: 1989).* (pp. 91-99). Elsevier Applied Science Publishers.

Biot, M. A. (1941). General theory of three-dimensional consolidation. *Journal of applied physics, 12*(2), 155-164.

Booker, J. R., & Small, J. C. (1975). An investigation of the stability of numerical solutions of Biot's Eqations of consolidation. *International Journal of Solids and Structures, 11*(7-8), 907-917.

Byrne, P. M., Park, S. S., & Beaty, M. (2003). Seismic liquefaction: Centrifuge and numerical modelling. In *FLAC and numerical modelling in geomechanics-2003* (pp. 321-331).

Cathie, D. N., & Dungar, R. (1978). Evaluation of finite element predictions for constructional behaviour of a rockfill dam. *Proceedings of the Institution of Civil Engineers, 65*(3), 551-568.

Chang, C. Y., & Duncan, J. M. (1970). Analysis of soil movement around a deep excavation. *Journal of Soil Mechanics & Foundations Div.*

Clough, R. W. and Woodward, R. J. (1967) "Analysis of Embankment Stresses and Deformations," *Journal of the Soil Mechanics and Foundations Division*, ASCE, Vol. 93, No. SM4, July, 1967, pp. 529-549.

Da Silva, A. F., & de Assis, A. P. (2014). Effect of the Valley Shape on the Embankment Behavior of Concrete Face Rockfill Dams. *Journal of Software Engineering, 19*, 1855-1862.

Derakhshandi, M., Pourbagherian, H. R., Baziar, M. H., Shariatmadari, N., & Sadeghpour, A. H. (2014). Numerical analysis and monitoring of a rockfill dam at the end of construction (case study: Vanyar dam). *International Journal of Civil Engineering, 12*(4), 326-337.

Dounias, G. T., Potts, D. M., & Vaughan, P. R. (1996). Analysis of progressive failure and cracking in old British dams. *Geotechnique, 46*(4), 621-640.

Duncan, J. M., & Chang, C. Y. (1970). Nonlinear analysis of stress and strain in soils. *Journal of Soil Mechanics & Foundations Div*. ASCE, Vol.96, No. SM5, pp. 1629-1653

Duncan, J. M. (1980). Strength, stress-strain and bulk modulus parameters for finite element analysis of stresses and movements in soil. *Geotech. Engrg. Research Report* UCB/GT/80-01.

Duncan, J.M. (1992), "Static stability and deformation analysis", *Proc. Spec. Conf. Stability and Performance of Slopes and Embankments - II, Goat. Eng. Div.*, ASCE, Vol.1, (eds. Seedand Boulanger), pp.222-266

Duncan, J.M. (1994), "The role of advanced constitutive relations in practical applications", *Proc. 13th mt. Conf. Soil Mechs. Found. Eng.*, New Delhi, Vol.5, pp.31-48

Duncan, J. M. (1996). State of the art: limit Eqilibrium and finite-element analysis of slopes. *Journal of Geotechnical engineering, 122*(7), 577-596.

Eisenstein, Z. (1974) "Application of Finite Element Method to Analysis of Earth Dams," tate of the Art Report, First Brazilian Seminar on “Application of Finite Element Method in Soil Mechanics, -Universidade Federal do Rio de Janeiro, September, 1974

Fell, R., Wan, C. F., Cyganiewicz, J., & Foster, M. (2003). Time for development of internal erosion and piping in embankment dams. *Journal of geotechnical and geoenvironmental engineering, 129*(4), 307-314.

Fell, R., Mac Gregor, P., & Stappledon, D. (2005). Geotechnical Engineering of Embankment dams, book. *AA Balkema, Netherlands*.

Fontanella, E. M., & Pagano, L. (2008). Approcci semplificati per l’interpretazione delle misure in dighe in terra. *Ital Geotechn J*, 3, 95-108.

Foster, M. A., Spannagle, M., & Fell, R. (1998). *Analysis of embankment dam incidents*. University of New South Wales, School of Civil Engineering.

Foster, M., Fell, R., & Spannagle, M. (2000a). The statistics of embankment dam failures and accidents. Canadian Geotechnical Journal, 37(5), 1000-1024.

Foster, M., Fell, R. and Spannagle, M. (2000b). A method for estimating the relative likelihood of failure of embankment dams by internal erosion and piping. Canadian Geotechnical Journal, 37 (5), 1025–1061.

Gawecka, K. A., Taborda, D. M., Potts, D. M., Cui, W., Zdravković, L., & Haji Kasri, M. S. (2017). Numerical modelling of thermo-active piles in London Clay.

Proceedings of the Institution of Civil Engineers-Geotechnical Engineering, 170(3), 201-219.

Grammatikopoulou, A., Zdravkovic, L., & Potts, D. M. (2006). General formulation of two kinematic hardening constitutive models with a smooth elastoplastic transition. *International Journal of Geomechanics, 6*(5), 291-302.Hunter, G., & Fell, R. (2002). *The deformation behaviour of rockfill*. University of New South Wales, School of Civil and Environmental Engineering.

Hunter, G., & Fell, R. (2003). *The deformation behaviour of embankment dams*. University of New South Wales, School of Civil and Environmental Engineering.

ICOLD (1974) Lessons from Dam Incidents, Paris, France, International Commission on Large Dams.

ICOLD (1995) Dam Failures Statistical Analysis. Bulletin 99, Paris, France, International Commission on Large Dams

Itasca Consulting Group, Inc. (2011). FLAC – Fast Lagrangian Analysis of Continua, Ver. 7.0 User’s Manual. Minneapolis: Itasca.

Jennings, J. E., & Knight, K. (1957). The prediction of total heave from the double oedometer test. *Transactions of the South African Institution of Civil Engineers, 7*(9), 285-291.

Justo, J.L. (1991) Collapse: Its importance, fundamentals and modelling. In *Advances in Rockfill Structures* (Maranha das Neves ed.), Kluwer Academic Publishers, Netherlands, pp. 97-152.

Kim, M. K., & Lade, P. V. (1988). Single hardening constitutive model for frictional materials: I. Plastic potential function. Computers and Geotechnics, 5(4), 307-324.

Kim, Y. S., Seo, M. W., Lee, C. W., & Kang, G. C. (2014). Deformation characteristics during construction and after impoundment of the CFRD-type Daegok Dam, Korea. Engineering geology, 178, 1-14.

Kondner, R. L. (1963). Hyperbolic stress-strain response: cohesive soils. *Journal of the Soil Mechanics and Foundations Division, 89*(1), 115-143.

Kovacevic, N. (1994). Numerical analyses of rockfill dams, cut slopes and road embankments. *PhD Thesis*, Imperial College, University of London.

Kovacevic, N. (1997). Assessing the safety of old embankment dams by observing and analysing movement during reservoir operation. In *Inter. Conf. on Large Dams* (pp. 551-566).

Kovacevic, N., Potts, D. M., & Vaughan, P. R. (2008). Recent advances in the numerical modelling of embankment dams. In *Ensuring reservoir safety into the future: Proceedings of the 15th Conference of the British Dam Society at the University of Warwick from 10–13 September 2008* (pp. 164-176). Thomas Telford Publishing.

Kovacevic, N. and Potts, D.M. (2011). Use of advanced constitutive models in numerical analysis of embankment dams, *Proc. 2nd Int. Symp. Computational Geomechanics (ComGeo 2011),* Cavtat, Croatia.

Kovacevic, N., Hight, D. W., Potts, D. M., & Carter, I. C. (2013). Finite-element analysis of the failure and reconstruction of the main dam embankment at Abberton Reservoir, Essex, UK. *Geotechnique, 63*(9), 753-767.

Lade, P. V. (1977). Elasto-plastic stress-strain theory for cohesionless soil with curved yield surfaces. *International journal of solids and structures*, *13*(11), 1019-1035.

Lade, P. V. (1981). Elasto-plastic stress-strain model for sand. In *Limit Eqilibrium, Plasticity and General Stress-Strain in Geotechnical Engineering* (pp. 628-648). ASCE.

Lade, P. V. (1984). Failure criterion for frictional materials. Mechanics of engineering materials, 385-402.

Lade, P. V., & Nelson, R. B. (1984). Incrementalization procedure for elasto-plastic constitutive model with multiple, intersecting yield surfaces. *International Journal for Numerical and Analytical Methods in Geomechanics, 8*(4), 311-323.

Lade, P. V., & Nelson, R. B. (1987). Modelling the elastic behaviour of granular materials. *International journal for numerical and analytical methods in geomechanics*, *11*(5), 521-542.

Lade, P. V., & Kim, M. K. (1988a). Single hardening constitutive model for frictional materials II. Yield criterion and plastic work contours. *Computers and geotechnics*, *6*(1), 13-29.

Lade, P. V., & Kim, M. K. (1988b). Single hardening constitutive model for frictional materials III. Comparisons with experimental data. *Computers and geotechnics, 6*(1), 31-47.

Lanzo, G. (2018). Alcune considerazioni sulla rivalutazione della sicurezza sismica delle dighe di materiali sciolti. *Proc. of Conferenze di Geotecnica di Torino-XXV Ciclo, Analisi e Progetto delle Opere Geotecniche in Zona Sismica. Politecnico di, Torino, Italy, November, 8-9.*

Lawton, E. C., Fragaszy, R. J., & Hetherington, M. D. (1992). Review of wetting-induced collapse in compacted soil. *Journal of geotechnical engineering, 118*(9), 1376-1394.

Marachi, N. D. (1969). Strength and Deformation. Characteristics of Rockfill Materials. Report No. TE-69-5, University of California, Department of Civil Engineering.

Marsal, R. J. (1958). Analisis de asentamientos en la presa Presidente Aleman. *Instituto de Ingenieria, National Autonomous University of Mexico, Mexico City, Mexico, Oaxaca*, (5).

Marsal, R. J. (1973). Mechanical properties of rockfill. Embankment dam engineering, Casagrande volume. John Wiley and Sons, New York, pp. 109-200.

Massarsch, K. R. (2002). Effects of vibratory compaction. In *International Conference on Vibratory Pile Driving and Deep Soil Compaction, Louvain-la-Neuve, Keynote Lecture* (pp. 33-42).

McCook, D. K. (2004). A comprehensive discussion of piping and internal erosion failure mechanisms. In *Proceedings, annual dam safety conference, ASDSO. Phoenix, Arizona*.

Mori, R. T., & Pinto, N. D. S. (1988). Analysis of deformations in concrete face rockfill dams to improve face movement prediction. In *Proceedings of the 16th International Congress on Large Dams* (pp. 27-34).

Naylor, D. J., Maranha das Neves, E., Mattar, D., & Veiga Pinto, A. A. (1986). Prediction of construction performance of Beliche Dam. *Geotechnique, 36*(3), 359-376.

Naylor, D. J., Tong, S. L., & Amir Shahkarami, A. (1989). Numerical modelling of saturation shrinkage. In *International symposium on numerical models in geomechanics.* 3 (NUMOG III) (pp. 636-648).

Naylor, D. J. (1991). Finite element methods for fills and embankment dams. In *Advances in rockfill structures* (pp. 291-340). Springer, Dordrecht.

Naylor, D. J., Maranha, J. R., Neves, E. M. D., & Pinto, A. V. (1997). A back-analysis of Beliche Dam. *Geotechnique, 47*(2), 221-233.

Nobari, E. S., & Duncan, J. M. (1972a). Effect of reservoir filling on stresses and movements in earth and rockfill dams: a report of an investigation. *Waterways Experiment Station. University of California, Department of Civil Engineering.*

Nobari, E. S., & Duncan, J. M. (1972b). Movements in dams due to reservoir filling. In *Performance of earth and earth-supported structures* (p. 797). ASCE.

Pagano, L., Desideri, A., & Vinale, F. (1998). Interpreting settlement profiles of earth dams. *Journal of geotechnical and geoenvironmental engineering, 124*(10), 923-932.

Pelecanos, L., Skarlatos, D., & Pantazis, G. (2018, June). Finite element analysis of the monitored long-term settlement behaviour of Kouris earth dam in Cyprus. In *9th European Conference on Numerical Methods in Geotechnical Engineering.*

Penman, A. D. M., Burland, J. B., & Charles, J. A. (1971). Observed and predicted deformations in a large embankment dam during construction. *Proceedings of the Institution of Civil Engineers*, *49*(1), 1-21.

Penman, A. D. M., & Charles, J. A. (1975). Predicted deformation of the upstream membrane of a rockfill dam. *Ground Engng*, 8(6), 47-48.

Penman, A. M., & Charles, J. A. (1985). Behaviour of rockfill dam with asphaltic membrane. In *International conference on soil mechanics and foundation engineering. 11* (pp. 2011-2014).

Penman, A. D. M. (1986). On the embankment dam. *Geotechnique*, *36*(3), 303-348.

Plaxis 2D Manual Version 9.0.

Potts, D. M., & Zdravkovic, L. (1999). Finite Element analysis in geotechnical engineering: Theory, London: Thomas Telford.

Potts, D. M., Zdravković, L., Addenbrooke, T. I., Higgins, K. G., & Kovačević, N. (2001). Finite element analysis in geotechnical engineering: application (Vol. 2). London: Thomas Telford.

Poulos, H. G., Booker, J. R., & Ring, G. J. (1972). Simplified calculation of embankment deformations. *Soils and Foundations, 12*(4), 1-17.

Prakash, K., Sridharan, A., & Prasanna, H. S. (2014). Compaction induced yield stress. *Geotechnical and Geological Engineering, 32*(2), 311-319.

Pramthawee, P., Jongpradist, P., & Kongkitkul, W. (2011). Evaluation of hardening soil model on numerical simulation of behaviors of high rockfill dams. *Songklanakarin Journal of Science & Technology, 33*(3).

Qoreishi, S. M. (2013). Numerical modeling of the behavior of Rockfill Dams during construction and impoundment.

Rezaee, H., Hajihassani, H., & Mahzarnia, S. (2017). Evaluation of Long-Term Settlement of Ghoocham Dam by Numerical Analysis. In *Proceedings of the 4th international conference, Published by Verlag der Technischen Universität Graz, Graz University of Technology, Graz, Austria.*

Rezaei, M. M., & Salehi, B. (2011). The effect of changing the geometry and compaction degree on arching of earth dams. In *Geo-Frontiers 2011: Advances in Geotechnical Engineering* (pp. 3207-3216).

Roscoe, K. H., Schofield, A., & Wroth, A. P. (1958). On the yielding of soils. *Geotechnique, 8*(1), 22-53.

Roscoe, K., & Burland, J. B. (1968). On the generalized stress-strain behaviour of wet clay. *Engineering Plasticity*, (eds. Heyman and Leckie), Cambridge University Press, Cambridge, pp.535-609

Rowe, P. W. (1962). The stress-dilatancy relation for static equilibrium of an assembly of particles in contact. *Proceedings of the Royal Society of London. Series A. Mathematical and Physical Sciences, 269*(1339), 500-527.

Rowe, P. W. (1971). Theoretical meaning and observed values of deformation parameters for soils. In *Proc. of Roscoe Memorial Symposium, Cambridge Univ.* (pp. 170-192).

Saboya Jr, F., & Byrne, P. M. (1993). Parameters for stress and deformation analysis of rockfill dams. *Canadian Geotechnical Journal, 30*(4), 690-701.

Schmertmann, J. H. (1985). Measure and use of the in situ lateral stress. *Practice of Foundation Engineering, A Volume Honoring Jorj O. Osterberg. Edited by RJ Krizek, CH Dowding, and F. Somogyi. Department of Civil Engineering, The Technological Institute, Northwestern University, Evanston,* 189-213.

Schmidt, B. (1966). Earth pressures at rest related to stress history. *Canadian Geotechnical Journal, 3*(4), 239-242.

Schanz, T., Vermeer, P. A., & Bonnier, P. G. (1999). The hardening soil model: formulation and verification. *Beyond 2000 in computational geotechnics*, 281-296.

Schroeder, F. C., Potts, D. M., & Addenbrooke, T. I. (2004). The influence of pile group loading on existing tunnels. Geotechnique, 54(6), 351-362.

Sharma, R. P., & Kumar, A. (2013). Case histories of earthen dam failures. In *Proc., 7th Int. Conf. on Case Histories in Geotechnical Engineering.* St. Louis, MO: Missouri Univ. of Science and Technology.

Sherard, J.L. (1973) Embankment dam cracking. In Embankment Dam Engineering (Casagrande Volume) (Hirschfeld and Poulos ed.), John Wiley and Sons, New York, pp. 271-353.

Sloan, S. W. (1987). Substepping schemes for the numerical integration of elastoplastic stress–strain relations. *International journal for numerical methods in engineering*, *24*(5), 893-911.

Sukkarak, R., Pramthawee, P., & Jongpradist, P. (2017). A modified elasto-plastic model with double yield surfaces and considering particle breakage for the settlement analysis of high rockfill dams. *KSCE Journal of Civil Engineering, 21*(3), 734-745.

Tanchev, L. (2014). *Dams and appurtenant hydraulic structures*. CRC Press.

Ti, K. S., Huat, B. B., Noorzaei, J., Jaafar, M. S., & Sew, G. S. (2009). A review of basic soil constitutive models for geotechnical application. *Electronic Journal of Geotechnical Engineering, 14*, 1-18.

Tschernutter, P., Seiwald, S., & Kainrath, A. (2011). Rheological behavior of an embankment dam after heightening. In *Proceedings of the 6th International Conference on Dam Engineering. LNEC, Lisboa* (pp. 1193-1219).

USACE(2004). Construction Considerations for Earth and Rock-Fill Dams. US Army Corps of Engineers.

Vaughan, P. R., Kovacevic, N., & Potts, D. M. (2004). Then and now: some comments on the design and analysis of slopes and embankments. In *Advances in geotechnical engineering: The Skempton conference: Proceedings of a three day conference on advances in geotechnical engineering, organised by the Institution of Civil Engineers and held at the Royal Geographical Society, London, UK, on 29–31 March 2004* (pp. 241-290). Thomas Telford Publishing.

Ventrella, C., Pelekanos, L., Skarlatos, D., & Pantazis, G. (2019). Finite element analysis of earth dam settlements due to seasonal reservoir level changes. *Proceedings of the XVII ECSMGE-2019 Geotechnical Engineering Foundation of the Future, Reykjavik, Iceland*, 1-7.

Zytynski, M., Randolph, M. F., Nova, R., & Wroth, C. P. (1978). On modelling the unloading-reloading behaviour of soils. *International Journal for Numerical and Analytical Methods in Geomechanics, 2*(1), 87-93.